Appariement et mouvement collectif dans des systèmes à N corps fermioniques : gaz d'atomes froids et étoiles à neutrons

Michael Urban

IPNO-T-12-01

Appariement et mouvement collectif dans des systèmes à N corps fermioniques : gaz d'atomes froids et étoiles à neutrons

Habilitation à diriger des recherches

Michael Urban (IPN Orsay)

Soutenue le 27 janvier 2012

Jury :
- M. Roland Combescot (rapporteur)
- M. Dany Davesne
- M. Elias Khan (président)
- M. Artur Polls (rapporteur)
- M. Giancarlo Strinati (rapporteur)

Table des matières

Chapitre I

Introduction

Après une thèse dans un domaine situé à mi-chemin entre la physique hadronique et la physique nucléaire, je me suis orienté vers la physique des gaz ultrafroids, en abordant notamment des questions liées au mouvement collectif des systèmes fermioniques superfluides. Pendant toute cette période, j'étais dans un environnement de physique nucléaire, et c'est donc naturellement que je me suis rendu compte des nombreux analogies qui existaient entre ces disciplines. Au cours des années, je me suis de plus en plus réorienté vers la physique nucléaire, et notamment vers la physique des étoiles à neutrons.

Dans ce mémoire, au lieu de présenter mes travaux par discipline, j'ai essayé au contraire de les regrouper de façon à bien souligner les analogies et ainsi démontrer que chaque discipline peut profiter des connaissances et méthodes développées dans l'autre.

Dans cette introduction, je vais tout d'abord rappeler quelques informations très générales sur les atomes piégés, pour donner au lecteur plus familier avec la physique nucléaire quelques notions que j'estime utiles pour mieux comprendre les travaux concernant les gaz d'atomes froids. Ensuite, j'expliquerai brièvement les analogies entre les noyaux, la matière nucléaire et les étoiles à neutrons d'une part et la physique des gaz quantiques d'autre part.

Atomes piégés comme gaz quantiques

Les gaz d'atomes froids représentent une discipline très jeune dans le domaine de la physique théorique à N corps. Ce sujet a en effet essentiellement émergé depuis la réalisation expérimentale de condensats de Bose-Einstein (Bose-Einstein condensate, BEC) en 1995 [17, 55, 89].

En quelques mots, ce genre d'expérience consiste à piéger et refroidir une vapeur d'atomes neutres à l'aide d'une combinaison de lasers et de champs magnétiques. Le potentiel ainsi créé peut être développé autour du minimum et on ne considère souvent que le terme quadratique, que l'on écrit comme $V(\mathbf{r}) = \sum_{i=x,y,z} m\omega_i^2 r_i^2/2$, où m est la masse de l'atome et les ω_i sont les "fréquences du piège." Le refroidissement à des températures extrêmement basses est crucial si l'on veut atteindre la condensation de Bose-Einstein. En effet, la statistique quantique des atomes ne se manifeste que lorsque la longueur d'onde de de Broglie correspondant au mouvement thermique, $\lambda = 2\pi\hbar/\sqrt{2mk_BT}$, devient au moins comparable à la distance moyenne entre les atomes, $d = n^{-1/3}$ (où $\hbar$ est la constante de Planck réduite, k_B est la constante de Boltzmann, et n est la densité du gaz). Il faut savoir que les densités typiques dans ces gaz piégés sont très faibles. À titre d'exemple, si l'on considère un gaz de $N = 10^6$ atomes de ^{23}Na dans un volume de $(100\,\mu\text{m})^3$, on trouve $d = 1\,\mu$m et une température correspondant à $d = \lambda$ de 400 nK. Cela illustre les échelles typiques de longueur et d'énergie dans ce domaine. Il faut par ailleurs noter que la distance d entre les atomes est de plusieurs ordres de grandeur plus grande que la taille des atomes et la portée de leur interaction (interaction van der Waals) qui sont de quelques

Å. Pour cette raison, c'est une excellente approximation de traiter les atomes comme des particules ponctuelles et leur interaction comme une interaction de portée nulle. Les températures de l'ordre du nK sont de plusieurs ordres de grandeur plus basses que toutes les températures que l'on trouve dans la nature (pour comparaison, la température du fond diffus cosmologique est d'environ 2.7 K).

Pour parvenir à de telles températures, la technique du refroidissement laser, qui est utilisée pour piéger les atomes, n'est pas suffisante et il faut avoir recours à un autre mécanisme : le refroidissement évaporatif. Le principe consiste à laisser sortir du piège les atomes les plus énergétiques, et à attendre ensuite que le système se rethermalise. Pour cela, il est indispensable qu'il y ait des collisions entre les atomes du gaz. Dans le cas d'atomes bosoniques, cela ne représente pas de problème, mais pour les fermions, la situation est différente. En effet, si l'on piège des atomes fermioniques dans un seul état hyperfin, ils ne peuvent pas collisionner en onde s à cause du principe de Pauli. Mais la section efficace pour une collision en onde p est proportionelle à $|\mathbf{p}_1 - \mathbf{p}_2|^2$, où $\mathbf{p}_1$ et $\mathbf{p}_2$ sont les impulsions des deux atomes, et le taux de collision décroît donc fortement quand la température baisse. Pour cette raison, cela a été plus difficile d'atteindre le régime dégénéré dans les gaz fermioniques que le BEC dans les gaz bosoniques. La pression de Pauli due à la dégénérescence d'un gaz de Fermi n'a été observée qu'en 1999 [92], en piégeant dans un même piège des isotopes bosoniques (^{7}Li) et fermioniques (^{6}Li) du même élément (refroidissement sympathique). Il est surprenant de voir que la présence d'un neutron de plus où de moins dans le noyau (qui n'a aucune importance pour les propriétés chimiques de l'atome) peut complètement modifier le comportement du gaz à des températures très basses.

Gaz de Fermi à deux composantes

Si l'on piège des atomes fermioniques dans un seul état hyperfin, comme mentionné ci-dessus, on obtient un gaz de Fermi pratiquement parfait à cause de l'absence d'interaction en onde s. Ceci n'est pas très intéressant du point de vue théorique puisqu'une des motivations pour étudier les gaz piégés est de comprendre les effets à N corps générés par l'interaction. L'étape suivante a donc été d'étudier les gaz contenant des atomes fermioniques dans deux états hyperfins [177]. Dans ce mémoire, on parlera d'ailleurs souvent de deux états de "spin" $\uparrow$ and $\downarrow$, même si cela n'a rien avoir avec le vrai spin des atomes qui est souvent supérieur à $1/2$.

Deux fermions de spin opposé peuvent donc interagir en onde s. Cette interaction peut être attractive ou répulsive, ce qui se traduit respectivement par une longueur de diffusion a négative ou positive. Comme la portée de l'interaction est vraiment petite, la connaissance de la longueur de diffusion est suffisante pour caractériser l'interaction. Par ailleurs, la particularité de ces systèmes est que la longueur de diffusion peut être ajustée par les expérimentateurs. Ceci est une nouveauté absolue : Dans les systèmes à N corps étudiés précédemment (noyaux atomiques, solides, etc.), l'interaction entre les particules était en effet donnée par la nature et il était impossible de la changer. Pour les atomes froids, l'effet qui permet de changer l'interaction est lié à ce que l'on appelle la "résonance de Feshbach" [204]. Le champ magnétique dans les pièges est suffisamment fort pour changer légèrement la structure électronique des atomes. Par conséquent, il peut arriver qu'un état faiblement lié de deux atomes ne soit plus lié pour une valeur différente du champ magnétique. Concrètement, quand on change le champ magnétique, la longueur de diffusion passe successivement d'une valeur $a > 0$ (dans le cas de l'existence d'un état faiblement lié) à une divergence (lorsque l'énergie de liaison est nulle) et enfin à une valeur $a < 0$.

Afin de caractériser l'intensité de l'interaction, on utilise souvent le paramètre adimensionné $k_F a$, où k_F est le module du vecteur d'onde de Fermi, défini par $k_F = (3\pi^2 n)^{1/3}$ (même à $T > 0$). Du fait de la divergence de la longueur de diffusion à la résonance de Feshbach, on préfère souvent donner la valeur $1/k_F a$ au lieu de $k_F a$. À la résonance, on a donc $1/k_F a = 0$. Dans ce cas, l'amplitude de diffusion (matrice T) atteint la limite imposée par l'unitarité de la matrice S, et on parle donc d'un gaz de Fermi "à l'unitarité."

Ainsi que nous l'avons mentionné ci-dessus, lorsque $1/k_F a > 0$, l'interaction entre les atomes de spin $\uparrow$ et

de spin $\downarrow$ possède un état faiblement lié que l'on appelle un dimère ou une molécule. Mais il ne faut pas oublier que ces molécules sont si faiblement liées qu'elles ne ressemblent pas à des molécules ordinaires : Leur taille est donnée par la longueur de diffusion a et peut atteindre plusieurs μm. Néanmoins, comme elles sont formées de deux fermions, ces molécules sont des bosons. Par conséquent, en dessous d'une température critique, elles forment un BEC comme les atomes bosoniques.

Regardons maintenant l'autre côté de la résonance, où l'interaction est attractive ($1/k_F a < 0$). Dans ce cas, par analogie avec la théorie de Bardeen-Cooper-Schrieffer (BCS) de la supraconductivité [32], il existe une température critique T_c en-dessous de laquelle les fermions près de la surface de Fermi forment des "paires de Cooper." Par conséquent, le gaz devient superfluide en-dessous de T_c.

Nous avons donc vu qu'à température suffisamment basse, le gaz de Fermi devenait superfluide, indépendamment du signe de $1/k_F a$: Soit il forme un BEC de molécules, soit il devient un superfluide de type BCS formé de paires de Cooper. Ce qui est surprenant, c'est que lorsque l'on passe de $1/k_F a > 0$ à $1/k_F a < 0$, les propriétés du système varient de façon continue, même si la longueur de diffusion a diverge. Cette transition continue s'appelle le "cross-over BEC-BCS." Mes travaux concernant les atomes piégés présentés ci-après concernent surtout le côté BCS du cross-over, donc le cas $1/k_F a < 0$.

Appariement et superfluidité en physique nucléaire

En physique nucléaire, il y a plusieurs phénomènes qui montrent que les nucléons dans les noyaux sont appariés et que les noyaux sont superfluides. La manifestation la plus évidente de l'appariement dans les noyaux est le fait que les noyaux ayant un nombre impair de protons ou de neutrons ont systématiquement une énergie de liaison plus faible que les noyaux pairs ("even-odd mass staggering"). Un autre exemple est le "gap" dans le spectre d'excitation des noyaux pairs. Il est intéressant de noter que l'analogie entre les supraconducteurs et les noyaux [47] a déjà été remarquée en 1958, immédiatement après l'apparition de la théorie BCS en 1957.

L'appariement désigne une corrélation entre les particules. Mais quand on parle de superfluidité, on pense d'abord à un fluide parfait, sans aucune viscosité, et donc aux conséquences de l'appariement sur les propriétés dynamiques. Et en fait, on connaît depuis très longtemps de telles manifestations de la superfluidité en ce qui concerne les noyaux. L'exemple le plus connu est certainement le moment d'inertie des noyaux [169], qui est fortement réduit par rapport à celui d'un corps rigide.

Dans les noyaux, les neutrons s'apparient entre eux, et les protons aussi. L'appariement entre neutrons et protons, par contre, est supprimé parce que les fonctions d'onde au niveau des surfaces de Fermi respectives sont trop différentes. Cependant, dans la matière nucléaire, l'appariement neutron-proton est possible. La matière nucléaire est une idéalisation qui n'existe pas dans la nature, mais qui a, en plus de son intérêt théorique, une importance dans la modélisation de la formation des étoiles à neutrons. Dans la matière nucléaire symétrique (où les densités de protons et de neutrons sont identiques) à basse densité, on s'attend à ce que l'appariement neutron-proton soit dominant par rapport à l'appariement neutron-neutron et proton-proton, parce qu'il existe un état lié neutron-proton, le deuton, tandis que deux neutrons ou deux protons ne sont jamais liés. En augmentant la densité (cf. chapitre II), on peut donc passer d'un gaz de deutons à la matière nucléaire avec des paires de Cooper neutron-proton, en analogie avec le crossover BEC-BCS dans les atomes froids discuté ci-dessus.

La matière de neutrons (sans protons) est un autre cas intéressant d'un système superfluide en physique nucléaire. Elle intervient notamment dans le contexte des étoiles à neutrons mais également quand on étudie des noyaux exotiques très riches en neutrons. Comme nous l'avons déjà mentionné, deux neutrons ne forment pas d'état lié mais la longueur de diffusion neutron-neutron est cependant très grande ($a_{nn} = -18.7 \pm 0.6$ fm [116]). À basse densité, il est donc possible de satisfaire $k_F a_{nn} > 1 > k_F R$ (R étant la portée de l'interaction, qui est de l'ordre de $1 - 2$ fm). Il existe par conséquent une analogie directe entre la matière de neutrons de basse densité et le gaz de Fermi dans la limite unitaire [129].

Superfluidité dans les étoiles à neutrons

Les étoiles à neutrons sont des objets fascinants qui sont formés lors d'une supernova à la fin de la vie d'une étoile [219]. Leur densité est comparable à la densité des noyaux, et leur masse qui est supérieure à la masse solaire est concentrée dans un rayon de l'ordre de 10 km. Comme l'indique leur nom, les étoiles à neutrons sont essentiellement formées de neutrons. En moins d'un mois après leur formation, elles se refroidissent (par émission de neutrinos) à des températures de l'ordre de 10^9 K $\simeq$ 100 keV [115]. Comparée aux énergies typiques dans la matière nucléaire, cette température peut être considérée comme presque nulle. Une autre propriété importante des étoiles à neutrons est leur rotation rapide : on les observe comme des pulsars avec des périodes de plusieurs ms jusquà quelques s.

La modélisation des étoiles à neutrons nécessite de réunir des connaissances de nombreux domaines : physique hadronique, physique nucléaire, physique de la matière condensée, astrophysique, etc. Sans entrer dans les détails, une étoile à neutrons possède une croûte externe, une croûte interne et un cœur. Aux températures typiques de moins de 10^9 K, la matière est probablement superfluide de la croûte interne jusqu'au centre du cœur. La rotation de l'étoile nécessite donc l'existence de vortex, comme dans l'hélium superfluide en rotation [107], dans les supraconduteurs de type II dans un champ magnétique [3] ou dans les BEC [1] et gaz de fermions superfluides [275] dans les pièges en rotation.

La croûte externe consiste en un réseau cristallin de noyaux riches en neutrons dans un gaz d'électrons dégénéré. Plus on descend vers le centre de l'étoile, plus la densité et l'excès de neutrons augmentent. Quand l'excès de neutrons devient trop grand, les neutrons ne sont plus liés dans les noyaux et ils forment un gaz de neutrons entre les noyaux. Ceci définit la croûte interne. Le gaz de neutrons est superfluide, ce qui a des conséquences importantes. L'effet le plus spectaculaire est probablement le phénomène de "glitch" : De temps en temps, la vitesse de rotation de l'étoile change brusquement, tandis que normalement elle diminue très régulièrement. On pense que ce phénomène est une conséquence d'un arrachement ("depinning") des vortex du réseau cristallin de la croûte interne [19].

À partir d'une certaine densité (à peu près la densité de saturation de la matière nucléaire), la matière devient homogène. C'est ce qui définit la transition entre la croûte et le cœur. Ensuite, à l'intérieur du cœur, la densité augmente jusqu'à plusieurs fois la densité de saturation. À ce jour, on ne sait pas bien en quoi consiste la matière à ces densités extrêmes, mais il ne s'agit très probablement pas de matière formée uniquement de neutrons et protons. Une possibilité est que la matière baryonique, formée donc de baryons, c'est-à-dire de neutrons, protons et autres particules composées de trois quarks, se transforme en matière de quarks, dans laquelle les quarks ne sont plus "confinés." Dans les étoiles hybrides (à cause de la présence de quarks on ne parle plus d'étoiles à neutrons), trois types de quarks peuvent exister : les quarks u ("up"), d ("down") et s ("strange" = étrange). Ils portent non seulement une charge électrique, mais ils ont aussi une "couleur," qui est à l'origine de leur interaction *via* l'échange de gluons. Si, comme on le pense, les quarks sont également appariés, alors on parlera de la "supraconductivité de couleur" [222]. Une question très intéressante est de savoir s'il y a de l'appariement entre les quarks légers (u, d) et les quarks s qui sont beaucoup plus lourds. Des éléments de réponse concernant l'appariement entre particules de masses différentes pourront peut-être bientôt être apportés grâce aux mélanges d'atomes différents dans un piège [229].

Plan du mémoire

La suite du présent mémoire est organisée en quatre chapitres. Le chapitre II donne quelques exemples pour la description de l'appariement dans des différents systèmes. Dans le chapitre III, je discuterai les effets de la superfluidité dans les gaz de fermions en rotation (sans vortex). Dans le chapitre IV, je donnerai des exemples concernant la description des modes collectifs dans des systèmes fermioniques superfluides et normaux. Chaque chapitre contient un résumé et une sélection d'articles publiés. Finalement, le chapitre V contient des perspectives.

Chapitre II

Corrélations d'appariement

Les corrélations d'appariement jouent un rôle important dans des systèmes fermioniques très variés : l'hélium 3 superfluide, les supraconducteurs, les noyaux atomiques, la matière nucléaire, la matière de neutrons, et, dans l'hypothèse où elle existe, la matière de quarks. Les gaz fermioniques ultrafroids, créés récemment dans les pièges, sont donc d'un grand intérêt dans le sens où ils permettent d'étudier ce phénomène dans des conditions bien contrôlées. Dans ce chapitre, je donnerai quelques exemples concernant la description théorique de l'appariement dans les gaz d'atomes piégés, dans la matière de quarks, et dans la matière nucléaire.

Appariement dans des systèmes finis : équations de Hartree-Fock-Bogoliubov / Bogoliubov de Gennes (publication n° 1, p. 10)

Les trois premières publications choisies dans ce chapitre concernent la description de l'appariement dans le régime BCS, où l'appariement est considéré comme faible. L'accent est mis sur la description de systèmes de taille finie en résolvant les équations Bogoliubov-de Gennes (BdG). En physique nucléaire, on s'est naturellement intéressé dès le début aux systèmes à petit nombre de particules (le noyau stable le plus lourd est le plomb 208 avec 82 protons et 126 neutrons), et un formalisme standard utilisé pour décrire l'appariement dans les noyaux est le formalisme Hartree-Fock-Bogoliubov (HFB). Ecrites dans l'espace des coordonnées, les équations HFB sont identiques aux équations BdG. Dans la limite d'un système infini et uniforme, le formalisme BdG (ou HFB) est également identique au formalisme BCS.

L'objectif est de calculer le paramètre d'ordre Δ ("gap"), qui est une mesure de l'appariement. Dans un système non-uniforme, il dépend des coordonnées spatiales : $\Delta = \Delta(\mathbf{r})$. Une difficulté à laquelle on se heurte dans le cas des atomes froids est liée à l'interaction de portée nulle. En effet, à cause de cette interaction indépendante de l'impulsion, la fonction d'onde des paires de Cooper possède une contribution non nulle jusqu'à des impulsions très importantes. Ceci donne lieu à une divergence dans l'équation de gap. Dans le cas d'un système uniforme, cette divergence peut être évitée si l'on exprime la constante de couplage dans l'équation du gap en fonction de la longueur de diffusion a [207] : la longueur de diffusion a divergeant également, les deux divergences s'annulent. Cette idée a été généralisée pour des systèmes piégés par Bruun et al. [59]. Dans la publication [119] (publication n° 1 ci-après), nous avons développé une méthode, similaire à la méthode introduite par Bulgac et Yu [67] dans le cadre de la physique nucléaire, qui utilise l'approximation Thomas-Fermi (TF) pour les états très loin de la surface de Fermi. C'est une excellente approximation et beaucoup plus simple à implémenter dans les calculs numériques que la méthode de la réf. [59]. De plus, nous avons introduit une modification qui améliore considérablement la convergence (c'est-à-dire, le résultat indépendant du cut-off numérique est déjà obtenu pour des valeurs beaucoup plus petites du cut-off).

Ayant résolu ce problème technique, nous avons calculé $\Delta(\mathbf{r})$ et comparé les résultats avec ce que l'on

obtient avec l'approximation de densité locale ("local density approximation", LDA). Cette approximation consiste à faire le calcul en chaque point $\mathbf{r}$ comme si le système était uniforme avec un "potentiel chimique local" $\mu(\mathbf{r}) = \mu - V(\mathbf{r})$, où μ est le vrai potentiel chimique du système et $V(\mathbf{r})$ le potentiel du piège. Nous avons trouvé que lorsque le nombre de particules était faible, la LDA surestimait fortement l'appariement, et notamment ne reproduisait pas les effets de couche qui existent dans un système piégé. Par contre, à partir du moment où Δ devient plus grand que la distance entre les couches ($\hbar\omega$), les effets de couche disparaissent et l'accord entre LDA et BdG devient meilleur. Cependant, même si l'accord est bon à température nulle, il est moins bon à des températures $T > 0$: par exemple, le profil de $\Delta(\mathbf{r})$ n'a pas la bonne forme près de la température critique T_c à laquelle l'appariement disparaît, et la LDA surestime la valeur de T_c. Nous avons montré que cet écart est en parfait accord avec des prédictions qui ont été faites dans le cadre de l'équation de Ginzburg-Landau [30].

Appariement dans un gaz de fermions polarisé (publication n° 2, p. 24)

Jusqu'à maintenant, on a supposé que les deux états de spin des atomes qui forment les paires de Cooper sont occupés de manière égale. Cependant il existe une autre situation intéressante, qui a été étudiée dans plusieurs expériences [171, 182, 220] : c'est le cas d'un gaz polarisé, c'est-à-dire, un gaz dans lequel il y a plus d'atomes de spin $\uparrow$ (par exemple) que de spin $\downarrow$.

Comme dans l'état BCS tous les atomes sont appariés, il est clair que l'appariement BCS n'est pas possible dans un gaz uniforme et polarisé. Cependant, la phase BCS peut supporter un petit écart $\delta\mu = \mu_\uparrow - \mu_\downarrow$ des deux potentiels chimiques. Cela permet d'avoir, au sein d'un système piégé, un cœur non-polarisé dans la phase BCS au centre, entouré d'une couche polarisée dans laquelle se trouvent les atomes de l'espèce majoritaire ($\uparrow$) non appariés. Néanmoins, on espère trouver des situations où les atomes s'apparient dans une phase polarisée. Si l'on applique les formules BCS au cas $\delta\mu > 2\Delta$, on trouve les mêmes nombres d'occupation, $n_\uparrow(k) = n_\downarrow(k)$ pour les particules de spin $\uparrow$ et $\downarrow$, sauf dans un intervalle de k correspondant à des énergies autour de $\bar{\mu} = (\mu_\uparrow + \mu_\downarrow)/2$, où l'on trouve $n_\uparrow(k) = 1$ et $n_\downarrow(k) = 0$ (pour $T = 0$). On appelle cela la phase de Sarma [209] ou "breached pairing."

Un autre exemple de phase polarisée avec appariement est la phase dite de LOFF ou FFLO (Fulde-Ferrel-Larkin-Ovchinnikov), qui a été prédite pour des supraconducteurs en présence d'un champ magnétique [111, 146]. Dans le cas d'un système uniforme, les paires de Cooper dans la phase LOFF ont une impulsion totale non-nulle. Ceci permet un appariement de particules des deux surfaces de Fermi, le paramètre d'ordre $\Delta(\mathbf{r})$ n'étant plus constant mais faisant des oscillations dans l'espace. Une autre forme d'appariement "exotique" dans des gaz polarisés, proposée dans la réf. [216], est la déformation des surfaces de Fermi.

Ce qui a été dit ci-dessus concerne les systèmes uniformes. Cependant, dans le cas d'un système piégé, l'appariement exotique peut prendre des formes différentes. Par exemple, la généralisation de l'idée derrière la phase LOFF à un système piégé implique qu'il faut permettre un appariement entre des états possédant des nombres quantiques principaux différents. Dans le cas d'un système sphérique, ceci implique des oscillations radiales du paramètre d'ordre. Tous les effets comme des phases d'appariement exotique, des interfaces entre deux phases, etc. sont contenus dans la théorie BdG et doivent donc apparaître naturellement si l'on résout les équations BdG. Dans la publication [77] (publication n° 2), nous avons donc généralisé notre travail précédent au cas où les nombres d'atomes des deux spin sont différents, $N_\uparrow \neq N_\downarrow$.

Comme précédemment, nous avons comparé nos résultats avec les prédictions obtenues dans le cadre de la LDA. De manière générale, la LDA prédit le scénario suivant : Au centre du piège il existe une région superfluide de type BCS, où les densités des deux états de spin sont égales ; cette région est éventuellement entourée d'une couche de phase LOFF, où les deux densités sont différentes, et à l'extérieur on trouve une phase non appariée. Les transitions entre ces phases étant du premier ordre, la LDA prédit des discontinuités

aux interfaces entre les phases. Les résultats que nous avons obtenus avec notre calcul BdG montrent que cette notion est fortement simplifiée. Qualitativement, il est vrai qu'au centre du piège la différence entre les deux densités est fortement réduite à cause de l'appariement, tandis qu'à l'extérieur l'appariement est très faible et la différence entre les deux densités est donc proche de la prédiction de la LDA. Pour certaines valeurs des paramètres, nous avons effectivement trouvé des oscillations du paramètre d'ordre, que nous avons interprétées comme des signes de la phase LOFF. Mais, contrairement à la prédiction de la LDA, les densités et le paramètre d'ordre ne présentent pas de discontinuité. Si l'on veut retenir la notion de plusieurs phases, il faut admettre que l'interface entre les phases est si épais que l'on ne peut pas le négliger lorsque l'on traite un système piégé qui n'est pas vraiment macroscopique. Des travaux récents [36] suggèrent que les oscillations que nous avons trouvées ne représentent en réalité pas de signe de la phase LOFF, mais qu'elles font partie de l'interface entre la phase BCS et la phase non-appariée.

Appariement entre particules de masses différentes : matière de quarks (publication n° 3, p. 29)

Comme la polarisation, la différence entre les masses des deux constituants d'une paire de Cooper crée un obstacle à l'appariement BCS. On s'attend par conséquent à des effets similaires à ceux discutés précédemment pour les phases exotiques dans le contexte de la polarisation. Il est déjà possible de piéger des atomes de masses différentes dans le même piège, p.ex., ^{6}Li and ^{40}K [229]. Il sera donc bientôt possible d'étudier l'appariement entre atomes de masses différentes dans les expériences. Du point de vue théorique, cette question a déjà été étudiée, mais dans un contexte différent : celui de la matière de quarks [53, 76, 221].

La matière de quarks à haute densité et basse température constitue également un système dans lequel l'appariement entre les fermions joue un rôle important (supraconductivité de couleur). On pense que la matière de quarks se forme à très haute densité, par exemple à l'intérieur d'une étoile à neutrons ou éventuellement lors de collisions d'ions lourds, dès que les nucléons, dans lesquels les quarks sont normalement confinés, commencent à se recouvrir. Si l'on considère non seulement les quarks u et d, qui constituent les nucléons, mais également les quarks étranges s, qui sont plus lourds, il n'est pas exclu que la "matière de quarks étrange" soit plus stable que la matière nucléaire [45, 266]. Sous cette hypothèse, il pourrait y avoir des "étoiles étranges" constituées entièrement de matière de quarks étranges [6, 127], ou même des petites gouttes de matière de quarks étranges, nommées "strangelets."

À cause de leur masse élevée, la densité des quarks s (masse ~ 100 MeV, charge $-\frac{1}{3}e$) est normalement supposée inférieure à celle des quarks u et d (masses quelques MeV, charges $+\frac{2}{3}e$ et $-\frac{1}{3}e$, respectivement). Par conséquent, la matière de quarks possède une charge électrique positive. Dans le cas d'une étoile à quarks, la charge positive est globalement compensée par la charge négative des électrons, mais à la surface de l'étoile il reste un très fort champ électrique qui peut éventuellement être détecté [180, 255]. Cependant, dans ce scénario, la supraconductivité de couleur n'a pas été prise en compte. Comme dans le cas du gaz de fermions polarisé, l'appariement cherche à réduire la différence entre les densités. L'état le plus symétrique et probablement le plus stable, dans lequel tous les quarks sont appariés, s'appelle l'état "color-flavor locked" (CFL). Dans cet état, la densité des quarks s est égale aux densités des quarks u et d, et par conséquent la charge électrique est nulle. Dans ce scénario là, il n'y a donc pas d'électrons dans l'étoile et le champ électrique à la surface est nul. La supraconductivité de couleur peut également avoir des conséquences importantes sur la stabilité des "strangelets" [162].

Le fait que la matière de quarks dans l'état CFL soit électriquement neutre est un résultat qui a été obtenu dans le cas de la matière infinie et uniforme. On se demande donc si ce résultat est aussi valable dans un petit "strangelet" ou à la surface d'une étoile à quarks. Dans la publication [176] (publication n° 3), nous avons donc fait un calcul de type HFB (= BdG) pour calculer le gap $\Delta(\mathbf{r})$, les densités $n(\mathbf{r})$ etc. dans un système fini.

Pour décrire la matière de quarks, nous avons utilisé le modèle du sac du MIT [83]. Ce modèle simule

le confinement des quarks d'une façon schématique en les enfermant dans un "sac," sur lequel le vide non perturbatif de QCD à l'extérieur exerce une pression que l'on appelle la constante de sac. À ce modèle, nous avons rajouté une interaction d'appariement de type delta (avec un cut-off) afin de décrire l'appariement entre les quarks. De plus, nous avons inclu l'interaction Coulombienne entre les quarks qui a des effets importants sur la distribution de charge. Les différences principales par rapport aux atomes piégés sont que les quarks dans le sac sont relativistes tandis que les atomes sont non relativistes, et que dans le cas des quarks il y a plusieurs canaux d'appariement tandis que dans le cas des atomes piégés (avec deux états de spin) il n'y en a qu'un.

Notre premier résultat intéressant est que les équations HFB permettent plusieurs solutions qualitativement différentes et que suivant les paramètres la solution la plus stable n'est pas toujours la même. Par exemple, il existe des solutions où tous les quarks sont appariés, de sorte que la charge électrique totale du strangelet est nulle, et des solutions qui sont telles qu'à la surface du strangelet il reste quelques quarks légers (u et d) qui ne sont pas appariés, de sorte que la charge totale est positive. Dans la plupart des cas cependant, la solution neutre est la plus stable. Mais même si la charge totale est nulle, la distribution de la charge dans le strangelet n'est pas triviale. À cause des différentes conditions aux bords pour les quarks légers et les quarks étranges, il y a toujours une densité de charge positive à la surface, qui est compensée par un excès de charge négative à l'intérieur. La plupart de cette charge est localisée directement sous la surface dans une couche d'environ 1 fm d'épaisseur, correspondant à la longueur de cohérence, c'est-à-dire, l'extension des paires de Cooper. Quand on s'éloigne de la surface (vers l'intérieur), la densité de charge décroît exponentiellement, la longueur caractéristique étant la longueur d'écrantage de Debye. En plus de la distribution de charge, nous avons également étudié l'énergie des strangelets en fonction du nombre baryonique A. Nous avons ainsi déterminé les paramètres d'une formule de type goutte liquide et la tension de surface.

Cross-over BEC-BCS dans la matière nucléaire dans le cadre de la théorie de Nozières et Schmitt-Rink (publication n^o 4, p. 47)

Le formalisme HFB (ou BdG) n'est valable que dans le régime BCS. Ainsi, et ceci d'autant plus que $T > 0$, il faut un autre formalisme si l'on veut décrire le cross-over BEC-BCS. Par exemple, dans la théorie BCS, la température critique T_c est la température de dissociation des paires, tandis que dans le régime BEC, les paires sont fortement liées et T_c est la température critique de la condensation de Bose-Einstein de ces paires, qui est beaucoup plus basse que la température de dissociation. Sauf dans la limite de couplage faible, la température critique obtenue dans le cadre de la théorie BCS est donc trop élevée parce que la théorie BCS ne tient pas compte de la présence de paires non condensées. Il faut considérer des corrélations de paire déjà au-dessus de T_c, comme dans la théorie de Nozières et Schmitt-Rink (NSR) [174].

Le cross-over du régime BEC vers le régime BCS est actuellement étudié dans les gaz d'atomes froids, mais ce phénomène apparaît aussi dans d'autres systèmes. Dans la publication n^o 4 [137], nous discuterons l'exemple de la matière nucléaire symétrique. À des basses densités, protons et neutrons forment un gaz de deutons, et T_c est donc donnée par la température de condensation des deutons. Quand la densité augmente, la matière nucléaire passe du régime BEC au régime BCS. Ceci est différent du cas des atomes froids, où le cross-over ne dépend que du paramètre $1/k_F a$. En effet, dans la matière nucléaire, on ne peut pas négliger la portée de l'interaction, qui est comparable avec la distance entre les nucléons. Les éléments de matrice de l'interaction diminuent donc avec le transfert d'impulsion, qui est typiquement de l'ordre de k_F pour des nucléons qui forment une paire de Cooper.

La méthode que nous avons utilisée pour décrire le cross-over BEC-BCS dans la matière nucléaire est un peu différente de la théorie NSR originale, parce que dans la matière nucléaire il faut tenir compte du champ Hartree-Fock (HF) qui donne lieu à un décalage des énergies de quasiparticules et donc du potentiel chimique, à une masse effective m^*, etc. Pour inclure ces effets, nous avons utilisé la force de Gogny, une interaction

effective qui décrit très bien la matière nucléaire au niveau HF [91]. Ensuite, nous avons inclu les corrélations de paire en calculant la self-énergie dans l'approximation d'échelle, avec une paramétrisation séparable de l'interaction nucléon-nucléon (potentiel de Yamaguchi [269]). Ce qui est différent du traitement NSR standard, c'est que dans les diagrammes en échelle, nous n'avons pas utilisé les fonctions de Green libres, mais les fonctions de Green HF. Comme la force de Gogny est une interaction effective, elle est faite pour décrire de manière effective, déjà au niveau HF, l'effet des corrélation sur les énergies de quasiparticules, et il faut donc faire une soustraction afin d'éviter un double comptage quand on rajoute la self-énergie dans l'approximation d'échelle. De cette façon, nous avons calculé T_c en fonction de la densité de la matière nucléaire, et, à part pour des densités élevées, la température critique obtenue est bien plus basse que celle prédite par la théorie BCS.

Dans la matière symétrique, il y a à basse température une transition de phase liquide-gaz qui est beaucoup étudiée théoriquement et expérimentalement (p.ex. dans des expériences de multifragmentation [48, 84, 97, 98, 158, 159]). La matière nucléaire homogène n'est donc stable qu'à très basse densité (phase "gazeuse") et à des densités au-dessus de la densité de saturation environ (phase "liquide"). À des densités intermédiaires, des gouttes liquides se forment dans le gaz (construction de Maxwell). Notre étude a montré qu'après l'inclusion des corrélations de paire, la phase gazeuse reste stable jusqu'à des densités beaucoup plus élevées qu'au niveau HF. Ce résultat est très plausibe : En incluant explicitement la formation de clusters dans la phase gazeuse, ceux-ci jouent le rôle des gouttes liquides et poussent l'instabilité de la phase gazeuse vers une densité plus élevée.

1 Hartree-Fock-Bogoliubov theory versus local-density approximation for superfluid trapped fermionic atoms

Marcella Grasso and Michael Urban, Phys. Rev. A 68, 033610 (2003)

We investigate a gas of superfluid fermionic atoms trapped in two hyperfine states by a spherical harmonic potential. We propose a new regularization method to remove the ultraviolet divergence in the Hartree-Fock-Bogoliubov equations caused by the use of a zero-range atom-atom interaction. Compared with a method used in the literature, our method is simpler and has improved convergence properties. Then we compare Hartree-Fock-Bogoliubov calculations with the semiclassical local-density approximation. We observe that for systems containing a small number of atoms shell effects, which cannot be reproduced by the semiclassical calculation, are very important. For systems with a large number of atoms at zero temperature the two calculations are in quite good agreement, which, however, is deteriorated at non-zero temperature, especially near the critical temperature. In this case the different behavior can be explained within the Ginzburg-Landau theory.

1.1 Introduction

In the last few years an increasing interest has been directed towards ultracold gases of trapped fermionic atoms. Many experimental efforts are made to develop and improve the techniques for trapping and cooling fermionic atoms like, for instance, ^{40}K and ^{6}Li. An interesting aspect of trapped fermionic atoms in comparison with other Fermi systems is that parameters such as the temperature, the density, the number of particles, and even the interaction strength are tunable experimentally. By tuning the magnetic field in the vicinity of a Feshbach resonance [204], the scattering length, which is related to the interaction strength, can be changed. This offers a wide range of possibilities to investigate the behaviour of these systems in different experimental conditions. By using optical or magnetic traps, temperatures of about $\frac{1}{4}T_F$ have been achieved [92, 93, 214, 245], where $T_F = \epsilon_F/k_B$ is the Fermi temperature.

All these efforts are mainly directed to the realization and detection of a phase transition to the superfluid phase below some critical temperature T_C. In order to have a s-wave attractive interaction among the atoms, which can give rise to s-wave pairing correlations below T_C, the atoms have to be trapped and cooled in two different hyperfine states. This has been achieved in a recent experiment [177], where also the Feshbach resonance in the ^{6}Li scattering amplitude has been used to enhance the scattering length. It seems that in the same experiment some signals indicating a superfluid phase transition have been observed.

From the theoretical point of view many calculations have been performed in order to predict and study the equilibrium properties of the trapped system when the phase transition takes place. So far all these calculations are based on the mean-field approach. In Ref. [131] the trapped Fermi gas was treated in local-density approximation (LDA), where the system is locally treated as infinite and homogeneous. In Ref. [30] some corrections to the LDA for temperatures near T_C were obtained in the framework of the Ginzburg-Landau (GL) theory. The first approach fully taking into account the finite system size was introduced in Ref. [59] and studied further in Refs. [60, 63]. It consists in a Hartree-Fock-Bogoliubov (HFB) calculation, analogous to calculations done in nuclear physics, where the mean field and the pairing properties of the system are treated self-consistently. In Ref. [59] also a regularization prescription for the pairing field was developed: Since the densities in the traps are very low, the atom-atom interaction can be approximated by a zero-range interaction. However, this leads to an unphysical ultraviolet divergence of pairing correlations which has to be removed.

In spite of the possibility to perform full HFB calculations, it should be mentioned that these calculations are numerically very heavy and therefore limited to moderate numbers of particles. Another shortcoming of present HFB calculations is that they are restricted to the case of spherical symmetry, while the traps used in

the experiments are usually strongly deformed. Hence, to describe trapped systems under realistic conditions, one has to rely on calculations within the LDA. This is a quite embarrassing situation, since even for large numbers of particles the results of HFB and LDA calculations have not always been in good agreement (see results shown in Ref. [59]).

In this paper we will present a detailed comparison between HFB and LDA calculations. In particular, we will show that the disagreement between HFB and LDA calculations which has been found in Ref. [59] is to a certain extent caused by the use of an unsuitable regularization prescription for the pairing field in the HFB calculations. We will present a modified regularization prescription which was originally developed for HFB calculations in nuclear physics [67] and which is much easier to implement numerically. (As we learned after sending the first version of our manuscript, Nygaard et al. used the same prescription in their calculation of a vortex line in a dilute superfluid Fermi gas [175], without giving a description of this scheme.) Due to its improved convergence properties, this scheme leads to more precise results for the pairing field, which in the case of large numbers of atoms agree rather well with the results of the LDA at least at zero temperature. At non-zero temperature, however, the differences between HFB and LDA results turn out to be important even for very large numbers of particles. For example, we find that the critical temperature obtained within the LDA is too high, and that the pairing field profile near the critical temperature is not well described by a LDA calculation: we show with the HFB approach that it actually has a Gaussian shape, as it was predicted in the framework of the GL theory in Ref. [30].

The paper is organized as follows: In Sec. 1.2 we will present the adopted formalism with a particular attention on the description of the regularization techniques. In Sec. 1.3 we will show some comparisons between HFB and LDA calculations and illustrations of the results obtained with different choices for the regularization method. We will also discuss results obtained for non-zero temperatures and verify the quantitative predictions of the GL theory. Finally, in Sec. 1.4 we will draw our conclusions.

1.2 Formalism

In this paper we will consider a spherically symmetric harmonic trap with trapping frequency ω, where N atoms of mass m populate equally two different spin states $\uparrow$ and $\downarrow$, i.e., $N_\uparrow = N_\downarrow$. As mentioned in the introduction, the low density of the system allows to introduce a contact interaction for the atoms, caracterized by the s-wave scattering length a. The hamiltonian reads

$$H = T + \sum_{j=1}^{N} \frac{1}{2} m\omega^2 \mathbf{r}_j^2 + \frac{4\pi\hbar^2 a}{m} \sum_{i<j} \delta^3(\mathbf{r}_i - \mathbf{r}_j)\,, \tag{1.1}$$

where T is the kinetic term. For convenience let us introduce a coupling constant g defined as:

$$g = \frac{4\pi\hbar^2 a}{m}\,. \tag{1.2}$$

Since we are considering attractive interactions, we have $a < 0$ and, consequently, $g < 0$. To simplify the notation, we will use in what follows the "trap units", i.e.

$$m = \omega = \hbar = k_B = 1\,. \tag{1.3}$$

Thus, energies will be measured in units of $\hbar\omega$, lengths in units of the oscillator length $l_{ho} = \sqrt{\hbar/(m\omega)}$, and temperatures in units of $\hbar\omega/k_B$.

Before describing the HFB approach, let us add some comments on the validity of the hamiltonian (1.1). The parametrization of the interaction in terms of the free-space s-wave scattering length a is valid at very

low densities, where the distance between particles is much larger than $|a|$. However, if the distance between particles becomes comparable with $|a|$, the bare interaction has to be replaced by a density-dependent effective interaction, as it is done in nuclear physics (see also [129]). This is particularly important in the vicinity of a Feshbach resonance, where $|a|$ becomes very large. In this case it might be necessary to include the Feshbach resonance as a new degree of freedom into the Hamiltonian [240].

1.2.1 HFB approach and regularization procedure

The hamiltonian (1.1) will be treated within the mean-field approximation. We will not go into details here as the formalism has been introduced and extensively illustrated in Ref. [59]. The Hartree-Fock-Bogoliubov (HFB) or Bogoliubov-de Gennes [90, 201] equations read:

$$\begin{aligned}[H_0 + W(\mathbf{R})]u_\alpha(\mathbf{R}) + \Delta(\mathbf{R})v_\alpha(\mathbf{R}) &= E_\alpha u_\alpha(\mathbf{R})\,,\\ \Delta(\mathbf{R})u_\alpha(\mathbf{R}) - [H_0 + W(\mathbf{R})]v_\alpha(\mathbf{R}) &= E_\alpha v_\alpha(\mathbf{R})\,,\end{aligned} \tag{1.4}$$

where α collects all quantum numbers except spin (n, l, m), u_α and v_α are the two components of the quasi-particle wavefunction associated to the energy E_α, and H_0 is the following single-particle hamiltonian:

$$H_0 = T + U_0 - \mu\,, \tag{1.5}$$

where $U_0 = \frac{1}{2}r^2$ is the harmonic trapping potential and μ the chemical potential. The Hartree-Fock mean field $W(\mathbf{R})$ in Eq. (1.4) is expressed by

$$W(\mathbf{R}) = g\sum_\alpha \left\{\, |v_\alpha(\mathbf{R})|^2\,[1 - f(E_\alpha)] + |u_\alpha(\mathbf{R})|^2 f(E_\alpha)\right\}, \tag{1.6}$$

where $f(E_\alpha)$ is the Fermi function:

$$f(E_\alpha) = \frac{1}{e^{E_\alpha/T} + 1}\,. \tag{1.7}$$

With a zero-range interaction the pairing field $\Delta(\mathbf{R})$ appearing in Eq. (1.4) would usually be defined as $\Delta(\mathbf{R}) = -g\langle\Psi_\uparrow(\mathbf{R})\Psi_\downarrow(\mathbf{R})\rangle$, where $\Psi_{\downarrow\uparrow}$ is the field operator associated with the spin states $\downarrow$ and $\uparrow$. However, this expression is divergent and must be regularized. The regularization prescription proposed in Ref. [59] consists in using the pseudopotential prescription [132]:

$$\Delta(\mathbf{R}) = -g\lim_{r\to 0}\frac{\partial}{\partial r}\left[r\,\langle\Psi_\uparrow(\mathbf{R} + \tfrac{\mathbf{r}}{2})\Psi_\downarrow(\mathbf{R} - \tfrac{\mathbf{r}}{2})\rangle\right]. \tag{1.8}$$

In practice, Eq. (1.8) is evaluated as follows: It is possible to show that the expectation value $\langle\Psi_\uparrow(\mathbf{R} + \mathbf{r}/2)\Psi_\downarrow(\mathbf{R} - \mathbf{r}/2)\rangle$ diverges as $\Delta/(4\pi r)$ when $r \to 0$ if a zero-range interaction is used. Now one adds and subtracts from this expectation value the quantity $\frac{1}{2}\Delta(\mathbf{R})G^0_\mu(\mathbf{R}, \mathbf{r})$, where G^0_μ is the Green's function associated to the single-particle hamiltonian H_0, Eq. (1.5), and calculated for the chemical potential μ:

$$G^0_\mu(\mathbf{R}, \mathbf{r}) = \sum_\alpha \frac{\phi^0_\alpha(\mathbf{R} + \frac{\mathbf{r}}{2})\phi^{0*}_\alpha(\mathbf{R} - \frac{\mathbf{r}}{2})}{\epsilon^0_\alpha - \mu}\,, \tag{1.9}$$

where ϕ^0_α denotes the eigenfunction of H_0 with eigenvalue $\epsilon^0_\alpha - \mu$. One can demonstrate that this Green's function diverges as $1/(2\pi r)$ when $r \to 0$. Expressing $\langle\Psi_\uparrow\Psi_\downarrow\rangle$ in terms of the wave functions u and v, one can

write the pairing field Δ as

$$\Delta(\mathbf{R}) = -g \lim_{r\to 0} \frac{\partial}{\partial r}\Big[r \sum_{\alpha} \Big(u_\alpha(\mathbf{R}+\tfrac{\mathbf{r}}{2}) v^*_\alpha(\mathbf{R}-\tfrac{\mathbf{r}}{2}) \left[1-f(E_\alpha)\right] - v^*_\alpha(\mathbf{R}+\tfrac{\mathbf{r}}{2}) u_\alpha(\mathbf{R}-\tfrac{\mathbf{r}}{2}) f(E_\alpha) \\ - \frac{\Delta(\mathbf{R})}{2} \frac{\phi^0_\alpha(\mathbf{R}+\frac{\mathbf{r}}{2})\phi^{0*}_\alpha(\mathbf{R}-\frac{\mathbf{r}}{2})}{\epsilon^0_\alpha - \mu} \Big) + \frac{\Delta(\mathbf{R})}{2} G^0_\mu(\mathbf{R},\mathbf{r}) \Big] . \quad (1.10)$$

The sum over α is no longer divergent for $r \to 0$, since the divergent part of $-\frac{1}{2}\Delta G^0_\mu$ cancels the divergent part of $\langle \Psi_\uparrow \Psi_\downarrow \rangle$. Thus, we can take the limit $r \to 0$ of this sum. On the other hand, the divergence of the last term is removed by the pseudopotential prescription, which selects only the regular part of the Green's function G^0_μ:

$$\lim_{r\to 0} \frac{\partial}{\partial r}\big[r\, G^0_\mu(\mathbf{R},\mathbf{r})\big] \equiv G^{0\,reg}_\mu(\mathbf{R}) . \quad (1.11)$$

Finally, Δ can be expressed as follows:

$$\Delta(\mathbf{R}) = -g \sum_{\alpha} \Big(u_\alpha(\mathbf{R}) v^*_\alpha(\mathbf{R}) \left[1-2f(E_\alpha)\right] - \frac{\Delta(\mathbf{R})}{2} \frac{|\phi^0_\alpha(\mathbf{R})|^2}{\epsilon^0_\alpha - \mu} \Big) - \frac{g\Delta(\mathbf{R})}{2} G^{0\,reg}_\mu(\mathbf{R}) . \quad (1.12)$$

Once the regular part of the Green's function is calculated for a given chemical potential μ [59], the HFB equations are solved self-consistently.

In practice, it is of course impossible to extend the sum over all states α and one has to introduce some cutoff. However, since the sum over α converges, the cutoff should not affect the results if it is chosen sufficiently high. We will discuss about the rapidity of convergence of the regularization procedure presented here with respect to the introduced energy cutoff. We will show that the convergence is quite slow. Moreover, the calculations can become heavy when systems with a large number of atoms are treated, as the function $G^{0\,reg}_\mu$ has to be calculated for a large value of the chemical potential. A way to simplify the regularization procedure and to avoid to calculate $G^{0\,reg}_\mu$ is proposed in Ref. [67], where the procedure of [59] is extended to calculations for nuclear systems. We will describe this method in next subsection.

1.2.2 Thomas-Fermi approximation in the regularization procedure

In Ref. [67] a simpler regularization procedure was proposed where the Thomas-Fermi approximation (TFA) is used to calculate the regular part of the Green's function. To that end let us write the Green's function G^0_μ by adopting the TFA for the sum over the states corresponding to oscillator energies ϵ^0_{nl} above some suffiently large value $\epsilon_C = N_C + \frac{3}{2}$:

$$G^0_\mu(\mathbf{R},\mathbf{r}) \approx \sum_{\substack{nlm \\ \epsilon^0_{nl}\le\epsilon_C}} \frac{\phi^0_{nlm}(\mathbf{R}+\frac{\mathbf{r}}{2})\phi^{0*}_{nlm}(\mathbf{R}-\frac{\mathbf{r}}{2})}{\epsilon^0_{nl}-\mu} + \int_{k_C(R)}^{+\infty} \frac{d^3k}{(2\pi)^3} \frac{e^{i\mathbf{k}\cdot\mathbf{r}}}{\frac{k^2}{2}+\frac{R^2}{2}-\mu} , \quad (1.13)$$

where

$$k_C(R) = \sqrt{2\epsilon_C - R^2} = \sqrt{2N_C + 3 - R^2} . \quad (1.14)$$

Observing that

$$\int_0^{+\infty} \frac{d^3k}{(2\pi)^3} \frac{e^{i\mathbf{k}\cdot\mathbf{r}}}{\frac{k^2}{2}} = \frac{1}{2\pi r} \quad (1.15)$$

and using Eq. (1.13), we can write the regular part of the Green's function as follows:

$$G_\mu^{0\,reg}(\mathbf{R}) = \lim_{r\to 0}\Big(G_\mu^0(\mathbf{R},\mathbf{r}) - \frac{1}{2\pi r}\Big)$$
$$\approx \sum_{\substack{nlm\\ \epsilon_{nl}^0\le\epsilon_C}} \frac{\phi_{nlm}^0(\mathbf{R})\phi_{nlm}^{0*}(\mathbf{R})}{\epsilon_{nl}^0-\mu} + \int_{k_C(R)}^{+\infty}\frac{d^3k}{(2\pi)^3}\Big(\frac{1}{\frac{k^2}{2}+\frac{R^2}{2}-\mu}-\frac{1}{\frac{k^2}{2}}\Big) - \int_0^{k_C(R)}\frac{d^3k}{(2\pi)^3}\,\frac{1}{\frac{k^2}{2}}\,. \quad (1.16)$$

Evaluating the integrals over $\mathbf{k}$ and summing over the magnetic quantum number m, we obtain

$$G_\mu^{0\,reg}(\mathbf{r}) \approx \sum_{\substack{nl\\ \epsilon_{nl}^0\le\epsilon_C}} \frac{(2l+1)R_{nl}^2(r)}{4\pi(\epsilon_{nl}^0-\mu)} + \frac{k_F^0(r)}{2\pi^2}\ln\frac{k_C(r)+k_F^0(r)}{k_C(r)-k_F^0(r)} - \frac{k_C(r)}{\pi^2}\,, \quad (1.17)$$

where R_{nl} are the radial parts of the oscillator wave functions and

$$k_F^0(r) = \sqrt{2\mu - r^2} \quad (1.18)$$

is the local Fermi momentum. As noted in Ref. [67], this method can be used beyond the classical turning point (characterized by $k_F^0(r)=0$) by allowing for imaginary values of $k_F^0(r)$. The case that $k_C(r)$ becomes imaginary will not be considered, because we assume that N_C is sufficiently large such that the pairing field can be neglected in the regions where $k_C(r)$ is imaginary. It should also be pointed out that already for, say, $N_C \ge \mu + 10$, Eq. (1.17) is an extremely accurate approximation to $G_\mu^{0\,reg}$, and gives results which are almost undistinguishible from those obtained by the numerically heavy algorithm proposed in Ref. [59].

Now let us substitute Eq. (1.17) into Eq. (1.12). We have to choose a cutoff for the sum over single-particle states. Instead of choosing a cutoff for the quasiparticle energies E_α, as it is done in Ref. [67], we can likewise restrict the sum in Eq. (1.12) to the states corresponding to those appearing in the sum in Eq. (1.17). This is the natural choice if one obtains the wave-functions u_α and v_α and the quasiparticle energies E_α by solving Eq. (1.4) in a truncated harmonic oscillator basis containing the states satisfying $\epsilon_{nl}^0 \le \epsilon_C = N_C + \frac{3}{2}$. In this way we obtain the following simple formula for the gap:

$$\Delta(r) = -g\sum_{\substack{nl\\ \epsilon_{nl}^0\le\epsilon_C}} \frac{2l+1}{4\pi}u_{nl}(r)v_{nl}(r)\left[1-2f(E_{nl})\right] - g\frac{\Delta(r)}{2}\Big(\frac{k_F^0(r)}{2\pi^2}\ln\frac{k_C(r)+k_F^0(r)}{k_C(r)-k_F^0(r)} - \frac{k_C(r)}{\pi^2}\Big)\,. \quad (1.19)$$

Finally, this can be rewritten in terms of a position dependent effective coupling constant:

$$\Delta(r) = -g_{\mathit{eff}}(r)\sum_{\substack{nl\\ \epsilon_{nl}^0\le\epsilon_C}} \frac{2l+1}{4\pi}u_{nl}(r)v_{nl}(r)\left[1-2f(E_{nl})\right], \quad (1.20)$$

where

$$\frac{1}{g_{\mathit{eff}}(r)} = \frac{1}{g} + \frac{1}{2\pi^2}\Big(\frac{k_F^0(r)}{2}\ln\frac{k_C(r)+k_F^0(r)}{k_C(r)-k_F^0(r)} - k_C(r)\Big)\,. \quad (1.21)$$

We stress again that the results obtained with this regularization prescription, from now on called prescription (a), coincide with the results obtained with the prescription introduced in Ref. [59].

However, it will turn out that it is useful to introduce the following modification of the method: Let us replace everywhere $k_F^0(r)$ by the local Fermi momentum taking into account the full potential (trapping potential U_0 plus Hartree-Fock potential W):

$$k_F(r) = \sqrt{2\mu - r^2 - 2W(r)}\,. \quad (1.22)$$

Formally this replacement does not change anything: Instead of adding and subtracting the term $\frac{1}{2}\Delta(\mathbf{R})G^0_\mu(\mathbf{R},\mathbf{r})$ from the divergent expectation value $\langle\Psi_\uparrow(\mathbf{R}+\mathbf{r}/2)\Psi_\downarrow(\mathbf{R}-\mathbf{r}/2)\rangle$ with G^0_μ being the Green's function corresponding to the harmonic oscillator potential U_0, we can also add and subtract a similar term involving the Green's function G_μ corresponding to the full potential U_0+W. Also from Eq. (1.21) it is evident that in the limit $N_C\to\infty$ [i.e., $k_C(r)\to\infty$] the results will be independent of the choice of k_F. However, we will see that the convergence of this modified scheme, from now on referred to as scheme (b), is very much improved. Thus, it is possible to use a much smaller cutoff N_C without having a strong cutoff dependence of the results.

1.2.3 Local-density approximation

If the number of particles becomes very large, it is natural to assume that the system can be treated locally as infinite matter with a local chemical potential given by $\mu-U_0(\mathbf{r})$. This assumption leads directly to the local-density approximation (LDA). Formally, the LDA corresponds to the leading order of the Wigner-Kirkwood $\hbar$ expansion, which is at the same time an expansion in the gradients of the potential [201]. Thus it is the generalization of the standard Thomas-Fermi approximation (TFA), which also corresponds to the leading order of an $\hbar$ or gradient expansion, to the superfluid phase. Here we will adopt the name LDA in order to avoid confusion with the full HFB calculations using the TFA only in the regularization prescription, as discussed in Sec. 1.2.2. But in the literature also the name TFA is adopted.

In the case of a zero-range interaction, the LDA (or TFA) amounts to solving at each point $\mathbf{r}$ the following non-linear equations for the mean field $W(\mathbf{r})$ and the pairing field $\Delta(\mathbf{r})$:

$$W(\mathbf{r})=\frac{g}{2}\rho(\mathbf{r})=g\int\frac{d^3k}{(2\pi)^3}\Big(\frac{1}{2}-[1-2f(E(\mathbf{r},\mathbf{k}))]\frac{\epsilon(\mathbf{r},\mathbf{k})-\mu}{2E(\mathbf{r},\mathbf{k})}\Big)\,, \tag{1.23}$$

$$\Delta(\mathbf{r})=-g\int\frac{d^3k}{(2\pi)^3}\Big([1-2f(E(\mathbf{r},\mathbf{k}))]\frac{\Delta(\mathbf{r})}{2E(\mathbf{r},\mathbf{k})}-\frac{\Delta(\mathbf{r})}{2(\epsilon(\mathbf{r},\mathbf{k})-\mu)}\Big)\,, \tag{1.24}$$

where

$$\epsilon(\mathbf{r},\mathbf{k})=\frac{k^2}{2}+U_0(\mathbf{r})+W(\mathbf{r})\,, \tag{1.25}$$

$$E(\mathbf{r},\mathbf{k})=\sqrt{(\epsilon(\mathbf{r},\mathbf{k})-\mu)^2+\Delta^2(\mathbf{r})}\,. \tag{1.26}$$

The last term in Eq. (1.24) has been introduced in order to regularize the ultraviolet divergence. In fact, the pseudopotential prescription used in the previous subsections was originally motivated by the fact that it reduces to such a term if it is applied to a homogeneous system [59, 67]. A more rigorous justification of this term is that it appears if one renormalizes the scattering amplitude of two particles in free space [207].

Let us first consider the case of zero temperature, $T=0$. In this case, and if the gap Δ is small compared with the local Fermi energy $\epsilon_F=\frac{1}{2}k_F^2$, Eqs. (1.23) and (1.24) can be solved (almost) analytically. Under these conditions the density practically coincides with the density obtained for $\Delta=0$, where Eqs. (1.23), (1.25), and (1.26) can be transformed into a cubic equation for the local Fermi momentum:

$$g\frac{k_F^3(\mathbf{r})}{6\pi^2}+\frac{k_F^2(\mathbf{r})}{2}+U_0(\mathbf{r})-\mu=0\,. \tag{1.27}$$

For a given local Fermi momentum and under the assumption that corrections of higher order in Δ/ϵ_F are negligible, Eq. (1.24) can be solved analytically. The result is the well-known formula

$$\Delta(\mathbf{r})=8\epsilon_F(\mathbf{r})\exp\Big(-2-\frac{\pi}{2k_F(\mathbf{r})|a|}\Big)\,. \tag{1.28}$$

Now we turn to the case of non-zero temperature, but we want to consider only temperatures below the critical temperature, i.e., $0 < T < T_C$. Therefore, we can neglect the influence of the temperature on the density and have to consider only the temperature dependence of Δ. Let us denote the gap at $T = 0$ by Δ_0. Then the gap at non-zero temperature can be obtained from the approximate relation [153]

$$-\ln\frac{\Delta(\mathbf{r})}{\Delta_0(\mathbf{r})} = \int d\xi\,\frac{f\big(\sqrt{\xi^2+\Delta^2(\mathbf{r})}\big)}{\sqrt{\xi^2+\Delta^2(\mathbf{r})}}\,. \tag{1.29}$$

The solution of this equation leads to a universal function which gives the ratio Δ/Δ_0 as a function of T/T_C, with $T_C \approx 0.57\Delta_0$. Note that, within the LDA, the critical temperature is a local quantity, $T_C = T_C(\mathbf{r})$.

In order to compare the LDA with the HFB theory, with special emphasis on the regularization prescription, we will now introduce a regularization scheme for the gap equation within LDA which is slightly different from Eq. (1.24). First of all, if we want to investigate the cutoff dependence, we have to introduce a cutoff in Eq. (1.24). Secondly, the regularization term introduced in Eq. (1.24) corresponds to the regularization prescription (b) described at the end of the previous subsection, which is different from that introduced in Ref. [59] and from the regularization scheme (a). If we want to compare the LDA results with HFB results obtained with the original prescription or with the prescription (a), which involves the Green's function G^0_μ of the potential U_0 and not the Green's function G_μ of the full potential $U_0 + W$, we have to replace the energy $\epsilon(\mathbf{r},\mathbf{k})$ appearing in the regularization term by

$$\epsilon^0(\mathbf{r},\mathbf{k}) = \frac{k^2}{2} + U_0(\mathbf{r})\,. \tag{1.30}$$

Thus, the gap equation within LDA suitable for comparison with the regularization scheme (a) reads

$$\Delta(\mathbf{r}) = -g\int_0^{k_C(\mathbf{r})}\frac{d^3k}{(2\pi)^3}\Big([1-2f(E(\mathbf{r},\mathbf{k}))]\frac{\Delta(\mathbf{r})}{2E(\mathbf{r},\mathbf{k})} - \frac{\Delta(\mathbf{r})}{2(\epsilon^0(\mathbf{r},\mathbf{k})-\mu)}\Big)\,. \tag{1.31}$$

At zero temperature, $T = 0$, it is again possible to solve this equation analytically, with the result

$$\Delta(\mathbf{r}) = 8\epsilon_F(\mathbf{r})\sqrt{\frac{k_C(\mathbf{r})-k_F(\mathbf{r})}{k_C(\mathbf{r})+k_F(\mathbf{r})}}\exp\Big(-2-\frac{\pi}{2k_F(\mathbf{r})|a|}-\frac{k^0_F(\mathbf{r})}{2k_F(\mathbf{r})}\ln\frac{k_C(\mathbf{r})-k^0_F(\mathbf{r})}{k_C(\mathbf{r})+k^0_F(\mathbf{r})}\Big)\,. \tag{1.32}$$

The result corresponding to the regularization scheme (b), Eq. (1.28), is recovered from this result by replacing k^0_F by k_F. In this case there is no cutoff dependence at all, but one should remember that in deriving Eq. (1.32) we have implicitly assumed that the cutoff lies above the Fermi surface. A weak cutoff dependence would appear only if corrections to Eq. (1.32) of higher order in Δ/ϵ_F were included.

1.3 Numerical results

In this section we will present some numerical results. In particular, we will investigate the convergence properties of the different renormalization methods. Then, we will discuss the validity of the LDA at zero temperature. Finally, we will compare HFB and LDA calculations at non-zero temperature.

In our numerical calculations we will use for the coupling constant the value $g = -1$ (in units of $\hbar^2 l_{ho}/m$). If we consider ^{6}Li atoms with scattering length $a = -2160a_0$ [2], where $a_0 = 0.53\,$Å is the Bohr radius, this value of g corresponds to a trap with $\omega = 2\pi\times 817\,$Hz. (Before relating this to real experimental conditions, one should however remember that in the experiments the trap is usually axially deformed, with a low longitudinal trapping frequency ω_z and a high transverse trapping frequency $\omega_\perp$. For example, in the experiment described in Ref. [177], the trapping frequencies were given by $\omega_z = 2\pi\times 230\,$Hz and $\omega_\perp = 2\pi\times 6625\,$Hz.) The choice $g = -1$ also facilitates the comparison of our results with those from Ref. [59], where the same value for g was used.

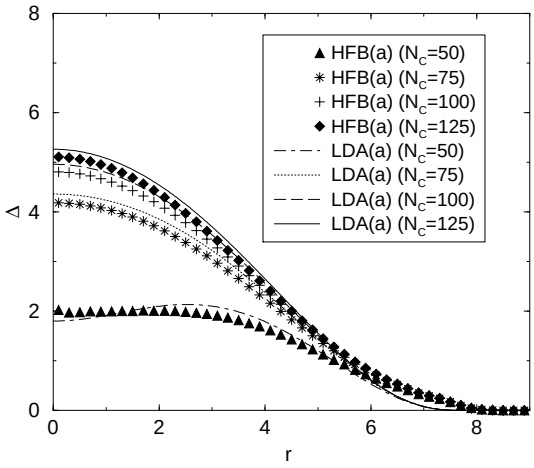

Figure 1.1: Pairing field Δ (in units of $\hbar\omega$) as a function of the distance r (in units of l_{ho}) from the center of the trap, calculated for the parameters $\mu = 32\hbar\omega$ and $g = -1\hbar^2 l_{ho}/m$, corresponding to $N \approx 1.7 \times 10^4$ particles in the trap. The different curves have been obtained within the HFB and LDA formalisms using the regularization prescription (a) for different values of the cutoff N_C.

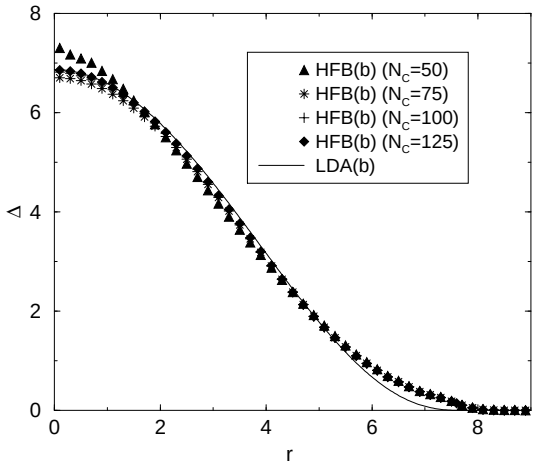

Figure 1.2: Same as Fig. 1.1, but with regularization prescription (b). Remember that with this prescription the LDA result [Eq. (1.32)] is independent of the cutoff N_C.

1.3.1 Convergence of the regularization methods

In this section we will discuss the convergence rates with respect to the cutoff used in the numerical calculations for different choices for the regularization procedure. As in Sec. 1.2 we denote by (a) the HFB calculations made with the choice of k_F^0 given by Eq. (1.18), and and by (b) the calculations made with the choice where k_F^0 is replaced by k_F as given by Eq. (1.22). For our comparison we use a chemical potential $\mu = 32\hbar\omega$, the corresponding number of atoms in the trap is $N \approx 1.7 \times 10^4$.

In Figs. 1.1 and 1.2 we present the pairing field Δ calculated at zero temperature within the HFB and LDA formalisms for different values of the cutoff N_C from 50 up to 125. The results shown in Fig. 1.1 have been obtained with the choice (a) for the regularization for both the HFB and LDA calculations. We verified that the HFB calculations with the exact Green's function ${G_\mu^0}^{reg}$ (without TFA) give practically the same results as the method HFB(a) for all the values of the cutoff. This means that the TFA in the regularization procedure is very satisfying and reproduces well the regular part of the oscillator Green's function.

We observe in Fig. 1.1 that the agreement between LDA and HFB is reasonable for all values of the cutoff N_C. We also notice that for $N_C = 125$, which is the maximum value that we considered, the convergence has not yet been reached and therefore the pairing field would grow further if we could increase the cutoff above 125. In Fig. 1.2 we present the same calculations made with the choice (b) for the regularization. Remember that with this choice, the pairing field within LDA is independent of N_C once N_C lies above the Fermi surface. On the other hand, the HFB results saturate quite fast and are already very close to convergence for $N_C = 75$. Again, the LDA and HFB results are in reasonable agreement.

By comparing Figs. 1.1 and 1.2 one observes clearly that the calculations (a), Fig. 1.1, are still quite far from convergence even for the highest considered cutoff. We argue that the convergence rate of method (a),

which is the same convergence rate as that of HFB without TFA in the regularization prescription [59], is much slower than that of method (b). This is more evident in Fig. 1.3 where we plot the HFB values of the pairing field in the center of the trap, $\Delta(0)$, for the two regularization prescriptions (a) (stars) and (b) (diamonds) as a function of the cutoff N_C. We also plot the results obtained within the LDA(a) (full line) and LDA(b) (dashed line) up to a cutoff of $N_C = 10^4$. In the inset of the figure we magnify the region of cutoff values between 50 and 150. We can observe in the inset that the LDA(a) curve fits well the calculated points for HFB(a). We noticed that the LDA(a) results converge slowly towards a pairing field of about $6.86\hbar\omega$, at a very high cutoff, $N_C = 10^6$. For $N_C = 10^3$ the pairing field in LDA(a) is still only $6.37\hbar\omega$. This very slow convergence rate can be understood within the LDA by taking the ratio of the pairing fields corresponding to the methods (a) and (b). Using Eq. (1.32) in the limit of very large k_C, one can derive the relation

$$\frac{\Delta_{LDA(a)}(\mathbf{r})}{\Delta_{LDA(b)}(\mathbf{r})} \approx 1 - \frac{|g|\sqrt{2}\,[\mu - W(\mathbf{r})]}{3\pi^2\sqrt{N_C}} + \cdots , \tag{1.33}$$

where $W(\mathbf{r})$ represents the Hartree field (in the present case, $W(0) \approx -16\hbar\omega$).

As the agreement between LDA(a) and HFB(a) is good in the region up to $N_C = 125$, we suppose that the convergence rate for HFB(a) is the same as for LDA(a). On the contrary, within HFB(b) the values of the pairing field in the center of the trap are $6.81\hbar\omega$ for $N_C = 100$ and $6.86\hbar\omega$ for $N_C = 125$: we conclude that the convergence in this case is much faster. In what follows we will always use the method (b) for the regularization procedure.

1.3.2 Validity of the LDA at zero temperature

As mentioned before, the parameters used for the calculations shown in Figs. 1.1, 1.2, and 1.3 correspond to a trap with about 1.7×10^4 atoms. In this case we found a good agreement between the numerical HFB results and the results obtained from the LDA. However, one might wonder under which conditions the LDA is valid. To study this question, one has to look at systems containing smaller numbers of particles, since in smaller systems the quantum effects (in particular shell effects) which are neglected in the LDA, are supposed to be more important.

In Fig. 1.4 we present the HFB (full line) and LDA (dashed line) results for the pairing field in the center of the trap, $\Delta(0)$, as a function of the number of atoms N. The calculations are done again at zero temperature and with a coupling constant $g = -1$ in trap units. We observe that the two calculations are in reasonable agreement for numbers of atoms greater than about 5000, which confirms the expectation that the LDA is a valid approximation for systems with a large number of atoms.

What is particularly interesting to look at in this figure is the region $N \lesssim 3000$. In this region the HFB results clearly show the shell structure: the pairing field becomes zero for $N = 240, 330, 440, \ldots$, which are the harmonic oscillator "magic numbers". One also realizes that the central value of the pairing field is smaller if the outer shell corresponds to odd-parity states, than in the case where the outer shell corresponds to even-parity states. This can be understood easily, since the main contribution to the pairing field comes from the states near the Fermi surface, and only s states can contribute to the pairing field at $r = 0$. Usually one expects that the LDA should at least reproduce the value of the pairing field if the fluctuations due to shell effects are averaged out, but our results show that the pairing field calculated within the LDA is systematically too high. This might be related to the fact that we are looking at the pairing field at one particular point ($\mathbf{r} = 0$) rather than at the average gap at the Fermi surface, as proposed in Ref. [104].

When the number of atoms grows, above a value of about 2500 the shell structure starts to be washed out and gradually disappears due to the stronger and stronger pairing correlations. This happens in the region

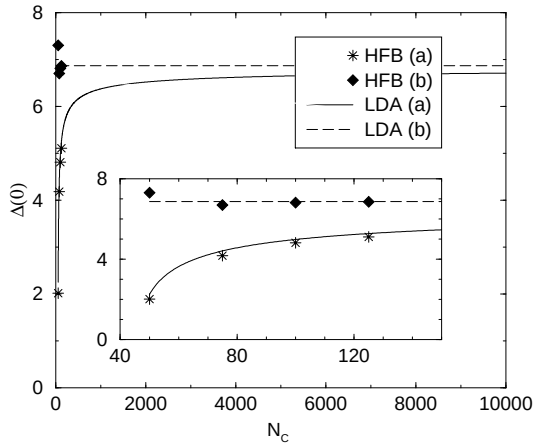

Figure 1.3: Value of the pairing field in the center of the trap, $\Delta(0)$ (in units of $\hbar\omega$), as a function of the cutoff N_C, obtained from HFB calculations with the regularization methods (a) (stars) and (b) (diamonds), and from the LDA, method (a) (solid line) and method (b) (dashed line). The parameters μ and g are the same as in Fig. 1.1.

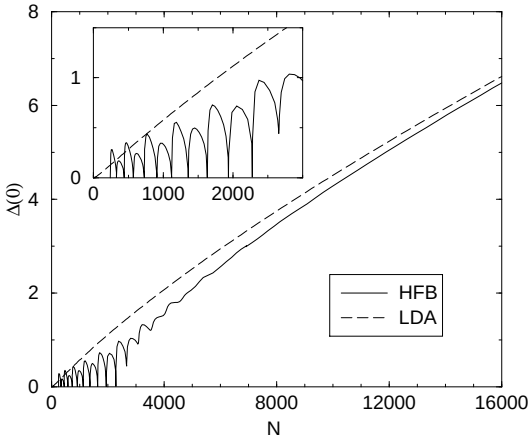

Figure 1.4: Value of the pairing field in the center of the trap, $\Delta(0)$ (in units of $\hbar\omega$), as a function of the number of particles, N, obtained from HFB (solid line) and LDA (dashed line) calculations [regularization method (b), cutoff $N_C = 100$, coupling constant $g = -1$ in trap units].

where the pairing field grows up to a value of about $\hbar\omega$: when the pairing field becomes comparable with the oscillator level spacing the pairing correlations in a closed shell system can diffuse pairs of atoms towards the higher energy empty shell, resulting in a non-zero pairing field. Globally, we observe that for $N > 5000$ the agreement between HFB and LDA is acceptable, even if the LDA systematically overestimates the value of the pairing field at the center.

Of course, the number of particles needed for the validity of the LDA depends on the strength of the interaction; the true criterion which has to be fulfilled reads $\Delta_{LDA} > \hbar\omega$. This criterion can even be applied locally, as one can see in Fig. 1.2: there the HFB and LDA results are in perfect agreement except in the region of $r \gtrsim 5.5 l_{ho}$, where Δ becomes smaller than $\hbar\omega$.

1.3.3 Results for non-zero temperature

Now we will discuss some results for temperatures different from zero. We are particularly interested in the following question: Within the LDA, the critical temperature T_C is different at each point **r**, i.e., when the temperature increases, the order parameter vanishes at last in the center of the trap, where the local critical temperature is the highest. In contrast to this, within the HFB theory, the gap and the critical temperature are global properties, and naively one would expect that, as long as the temperature is below T_C, the pairing field extends over the whole volume of the system. We will see that even in cases where the LDA works well at zero temperature, it fails at non-zero temperature. On the other hand, also the notion that the gap vanishes globally at $T = T_C$, has to be revised in these cases.

In Figs. 1.5 and 1.6 we show the HFB and LDA pairing fields obtained at different temperatures, again for $g = -1$ (in trap units) and regularization method (b). The chemical potentials chosen are $\mu = 32\hbar\omega$ in Fig. 1.5 and $\mu = 40\hbar\omega$ in Fig. 1.6, corresponding to approximately 1.7×10^4 and 4×10^4 particles, respectively. We

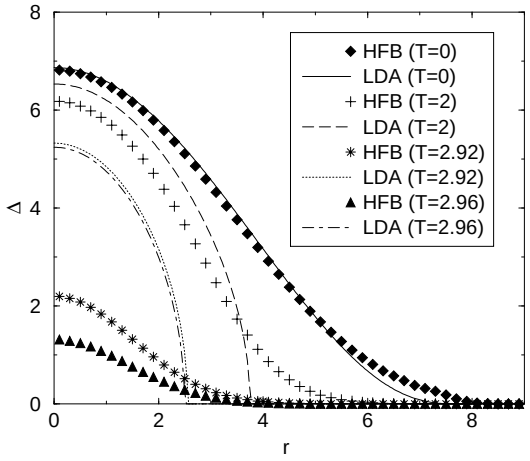

Figure 1.5: Pairing field Δ (in units of $\hbar\omega$) as a function of the distance r (in units of l_{ho}) from the center of the trap, for a chemical potential $\mu = 32\hbar\omega$, corresponding to about 1.7×10^4 atoms in the trap [regularization method (b), cutoff $N_C = 100$, coupling constant $g = -1$ in trap units]. Results obtained within numerical HFB calculations (symbols) are compared with LDA results (lines) for different temperatures T.

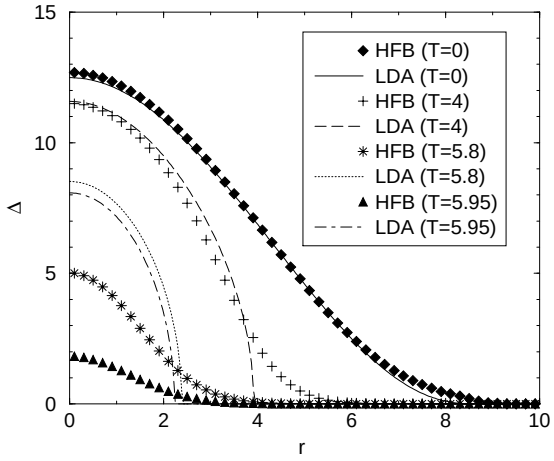

Figure 1.6: Same as Fig. 1.5, but for a chemical potential of $\mu = 40\hbar\omega$, corresponding to $N \approx 4 \times 10^4$ atoms in the trap.

observe that the good agreement obtained at zero temperature is deteriorated at higher temperatures. In Fig. 1.5, already at $T = 2\hbar\omega/k_B$ the LDA reproduces badly not only the tail of the pairing field profile, but also the pairing field in the central region of the trap, in spite of the fact that the pairing field is still large compared with $\hbar\omega$ at this temperature. The LDA description gets worse and worse for higher temperatures and results in an overestimation of the central pairing field and in a too drastic cut of the queue of the profile at large distances. Finally, the LDA method predicts a higher critical temperature than the HFB one. We observed that T_C is equal to 3.89 (in units of $\hbar\omega/k_B$) for LDA and to 2.98 for HFB. In Fig. 1.6, the agreement is somewhat better. Since the critical temperature is higher than in the previous case, the agreement between LDA and HFB is maintained in a wider range of temperatures. Up to $T = 4$ one can see that at least the central region of the trap is well described by LDA. For higher temperatures, we observe the same kind of deterioration of the LDA results shown in Fig. 1.5. Again, the critical temperature is higher in LDA (7.08) than in HFB (5.97).

It is evident that the LDA does not correctly describe the phase transition in both cases. On the other hand, also within the HFB calculations one finds that with increasing temperature the pairing field becomes more and more concentrated in the center of the trap. Such a behavior has been predicted in Ref. [30] using the GL theory, the only assumption being that the critical temperature is large compared with the trapping frequency, $k_B T_C \gg \hbar\omega$. Let us briefly review the main results from this theory and compare them with the results obtained from our HFB calculations (the corresponding numbers are listed in Table 1.1).

In the GL theory the critical temperature T_C is predicted to be lower than the critical temperature $T_C^{(0)}$

obtained from the LDA. The difference can be written as

$$\delta T_C = T_C^{(0)} - T_C = \frac{3\hbar\Omega}{k_B}\sqrt{\frac{7\zeta(3)}{48\pi^2}\Big(1+\frac{\pi}{4k_F(0)|a|}\Big)}\,, \tag{1.34}$$

where ζ denotes the Riemann zeta function ($\zeta(3) = 1.202\ldots$). In the derivation of Eq. (1.34) in Ref. [30] the Hartree potential has been neglected. Here we will include the Hartree potential by using an effective oscillator frequency $\Omega > \omega$. Since near T_C the pairing field is concentrated in the center of the trap, we define Ω by expanding the potential around $r = 0$:

$$\Omega = m\sqrt{\boldsymbol{\nabla}^2[U_0(\mathbf{r}) + W(\mathbf{r}))]_{\mathbf{r}=0}}\,. \tag{1.35}$$

Within the Thomas-Fermi approximation for the density profile the effective oscillator frequency can be written as

$$\Omega = \frac{\omega}{1-\frac{2k_F(0)|a|}{\pi}}\,. \tag{1.36}$$

The estimates for δT_C obtained by inserting the numerical values for $k_F(0)|a|$ given in Table 1.1 into Eqs. (1.34) and (1.36) are very reasonable. This can be seen by comparing them with the δT_C values obtained from the HFB calculations, which are also listed in Table 1.1. If one considers that these numbers can only be a rough estimate, since $k_B T_C$ is not really very large compared with $\hbar\Omega$, the agreement with the HFB results is very satisfying.

Not only the critical temperature, also the shape of the order parameter near the critical temperature can be obtained from the GL theory. It can be shown that for temperatures very close to T_C the pairing field has the form of a Gaussian,

$$\Delta(\mathbf{r}) = \Delta(0)\exp\Big(-\frac{\mathbf{r}^2}{2l_\Delta^2}\Big)\,. \tag{1.37}$$

In contrast to the LDA result, the radius l_Δ of this Gaussian is predicted to stay finite in the limit $T \to T_C$, as it is the case for the solution of the HFB equations. Its value is given by

$$l_\Delta^2 = R_{TF}^2\frac{\hbar\Omega}{k_B T}\sqrt{\frac{7\zeta(3)}{48\pi^2}\,\frac{1}{1+\frac{\pi}{4k_F(0)|a|}}}\,. \tag{1.38}$$

In Ref. [30] the quantity R_{TF} was defined as the Thomas-Fermi radius of the cloud, $R_{TF} = \sqrt{2\mu/(m\omega^2)}$. Generalizing the derivation of Eq. (1.38) to the case of a non-vanishing Hartree field, we see that the corresponding parameter for the pairing field near the center of the trap is given by

$$R_{TF} \to \sqrt{\frac{2[\mu - W(0)]}{m\Omega^2}} = \Big(1-\frac{2k_F(0)|a|}{\pi}\Big)k_F(0)l_{ho}^2\,. \tag{1.39}$$

Table 1.1: Comparison of results (in trap units) obtained from HFB calculations for the two cases $\mu = 32$ and $\mu = 40$ shown in Figs. 1.5 and 1.6 [coupling constant $g = 1$ in trap units, regularization method (b), $N_C = 100$] and the corresponding results obtained from the GL theory.

μ	$k_F(0)\lvert a\rvert$	$T_C^{(0)}$	T_C	δT_C	$\delta T_C^{(GL)}$	l_Δ	$l_\Delta^{(GL)}$
32	0.78	3.89	2.98	0.91	1.12	1.44	1.23
40	0.91	7.08	5.97	1.11	1.29	1.28	0.95

On the other hand, the HFB pairing fields corresponding to the temperatures next to T_C shown in Figs. 1.5 and 1.6 are also perfectly fitted by Gaussians. As shown in Table 1.1, the agreement between the radii obtained from this fit are again in reasonable agreement with the radii obtained from Eqs. (1.38) and (1.39). The deviations are of the order of 30%, which is even better than one could have expected, since the parameter $\hbar\Omega/(k_B T_C)$ is not very small in the present case.

Finally, let us look more closely at the critical behavior near T_C. Again, from the GL theory one can derive that for $T \to T_C$ the value of the pairing field in the center should go to zero like

$$\Delta(0) = \sqrt{\frac{16\pi^2\sqrt{2}}{7\zeta(3)}\, T_C(T_C - T)}\,. \tag{1.40}$$

As shown in Figs. 1.7 and 1.8, this formula is very well satisfied by the HFB results in both cases, $\mu = 32$ and $\mu = 40$ (in trap units). Note that the prefactor in Eq. (1.40) differs from the prefactor in LDA. In LDA one finds for $T \approx T_C^{(0)}$

$$\Delta_{LDA}(0) = \sqrt{\frac{8\pi^2}{7\zeta(3)}\, T_C^{(0)}(T_C^{(0)} - T)}\,. \tag{1.41}$$

The different prefactor, as well as the different critical temperature and the finite radius of the pairing field, are due to the "kinetic" term $\propto \Delta\boldsymbol{\nabla}^2\Delta$ in the GL energy functional, which is absent in the LDA and which is very important for the description of the strongly $\mathbf{r}$ dependent pairing field near the critical temperature.

As a final remark let us mention that the different calculations which we have compared in this paper, are all based on mean-field theory, and therefore do not take into account fluctuations of the order parameter Δ. It is well-known that fluctuations are very important near the phase transition, and in particular in a situation where $k_F|a|$ is not small, as it is the case here, they can lead to a considerable change of the critical temperature. Anyway, what we wanted to point out here, is that the LDA gives the wrong T_C as compared with a theory taking into account the inhomogeneity of the system. From this result we conclude that in order to have a reliable prediction of T_C for the trapped system, it is not sufficient to do a reliable calculation of T_C (even including fluctuations) for a homogeneous gas and then apply the LDA.

1.4 Conclusions

In this paper we have shown a detailed comparison between HFB and LDA calculations at $T = 0$ and at $T \neq 0$ for a low density gas of superfluid fermionic atoms trapped by a spherical harmonic potential. We have used a zero-range interaction for the atoms and we have proposed an improvement of the regularization method adopted to remove the ultraviolet divergence [59]. This improvement is a modification of a procedure proposed for nuclear systems in Ref. [67], where the Thomas-Fermi approximation is used in the calculation of the regular part of the Green's function $G_\mu^{0\,reg}$, Eq. (1.16). The use of the Thomas-Fermi approximation allows to treat systems with a large number of atoms much easier than in the calculations of Ref. [59]. On the other hand, our modification considerably improves the convergence rate of the procedure with respect to the numerical cutoff. By using this regularization method we have observed that the LDA results are in quite good agreement with the corresponding HFB results at zero temperature and for systems with a relatively large number of atoms, where the shell structure effects are washed out. The shell effects, which are important for small systems where the pairing field is smaller than the harmonic level spacing $\hbar\omega$, cannot obviously be reproduced by a LDA calculation.

For non-zero temperatures the agreement between HFB and LDA is deteriorated even in those cases where it was good at $T = 0$. In general, LDA overestimates the value of the pairing field in the center of the trap, cuts

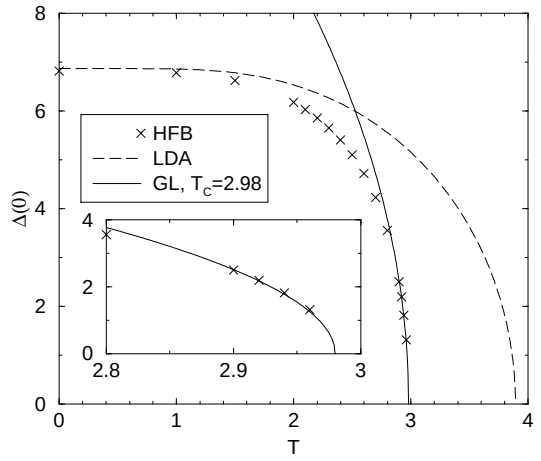

Figure 1.7: Value of the pairing field in the center of the trap, $\Delta(0)$ (in units of $\hbar\omega$), as a function of temperature T (in units of $\hbar\omega/k_B$) for a chemical potential $\mu = 32\hbar\omega$, corresponding to about 1.7×10^4 atoms in the trap [regularization method (b), cutoff $N_C = 100$, coupling constant $g = -1$ in trap units]. Results obtained within numerical HFB calculations (symbols) are compared with the LDA result (dashed line) and with the formula (1.40) obtained from the GL theory (solid line).

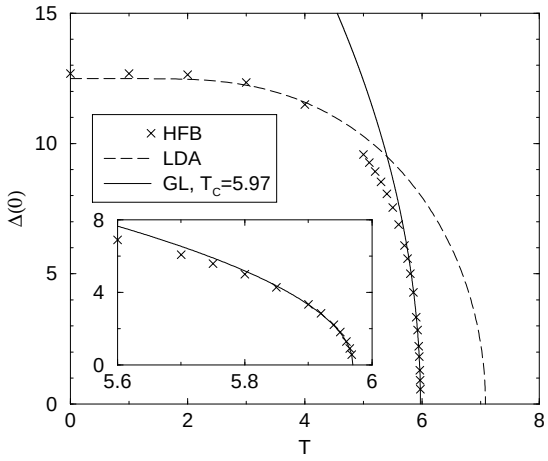

Figure 1.8: Same as Fig. 1.7, but for a chemical potential of $\mu = 40\hbar\omega$, corresponding to $N \approx 4 \times 10^4$ atoms in the trap.

too drastically the tail of the radial profile of the pairing field at large distances, and overestimates the critical temperature with respect to HFB. We have verified that this discrepancy between the HFB and LDA results at T different from zero can be nicely predicted by using the GL theory [30] in cases where the critical temperature is much larger than the harmonic level spacing.

In this article we considered only spherical traps. However, the traps used in experiments are usually cigar-shaped with a low longitudinal and a high transverse trapping frequency, $\omega_z \ll \omega_\perp$. In this case it is possible that the pairing field, even if it is larger than $\hbar\omega_z$, is still smaller than $\hbar\omega_\perp$, and the LDA would probably not work. Therefore in principle one should also perform deformed HFB calculations, but at the moment this seems to be numerically very difficult. On the other hand, as noted above, even in the case where Δ is large compared with both trapping frequencies, the LDA is not adequate at non-zero temperature. Therefore a first step to study non-spherical traps could be to generalize the GL theory of Ref. [30] to the deformed case.

Acknowledgments

The authors wish to thank Elias Khan, Peter Schuck and Nguyen Van Giai for useful discussions. We thank Yvan Castin for supplying us the code for the numerical calculation of the Green's function $G_\mu^{0\,reg}$ which we used to check the TF approximation. M.G. is a recipient of a European Community Marie Curie Fellowship, M.U. acknowledges support by the Alexander von Humboldt foundation.

2 Non-standard pairing in asymmetric trapped Fermi gases

Paolo Castorina, Marcella Grasso, Micaela Oertel, Michael Urban, and Dario Zappalà,
Phys. Rev. A 72, 025601 (2005)

We study an ultracold trapped Fermi gas of atoms in two hyperfine states with unequal populations. In this situation the usual BCS pairing is suppressed and non-standard pairing mechanisms become important. These are treated by solving the Bogoliubov-de Gennes equations, which at the same time correctly take into account the finite size of the trapped system. We find results which can be viewed as generalization of the LOFF phase to finite systems.

In the last years much progress has been made in improving the techniques used to trap and cool dilute gases of bosonic and fermionic atoms [35, 50, 82, 92, 122, 139, 196, 277, 278]. One of the interesting aspects of the properties of ultra-cold gases is that the interatomic interaction can be modified, both in its intensity and in its sign, by changing the applied magnetic field around a Feshbach resonance. Due to the very low densities and temperatures in these systems the details of the interatomic interaction are unimportant and the interaction can be characterized by one single parameter, the s-wave scattering length a. In this article we consider Fermi gases trapped and cooled in two hyperfine states with an attractive interaction, i.e., $a < 0$. We will concentrate on the weakly interacting case ($k_F|a| \ll 1$, where k_F denotes the Fermi momentum). In this region, BCS superfluidity with formation of Cooper pairs is expected below a certain critical temperature. So far, some experimental signals have been found which would indicate the existence of superfluidity in this region [82, 139], but a clear evidence is still missing.

Besides the interaction, also the population of the two hyperfine states can experimentally be controlled. Usually mixtures with equal populations are created, but controlled asymmetric mixtures have also been obtained [276]. Unequal populations of the two hyperfine states can lead to very interesting phenomena. For instance, the BCS pairing mechanism is supposed to become suppressed [131] since the two Fermi momenta associated with the two spin polarizations become different: The formation of zero-momentum Cooper pairs built of two atoms at their respective Fermi surface becomes difficult. Instead, other more exotic pairing phenomena have been suggested for the case of unequal populations, like the Larkin-Ovchinnikov-Fulde-Ferrel (LOFF) phase [87], the Sarma (interior gap) phase [40, 71, 155], or a phase with deformed Fermi surfaces (DFS) [216]. Many of these non-standard pairing mechanisms have already been discussed in other domains of physics where asymmetric two-component fermion systems can be found: Superconductors in a magnetic field [111, 146, 209], neutron-proton pairing in asymmetric nuclear matter [215], color superconductivity in high density QCD [53, 76, 221]. The experimental observation of the LOFF phase in the case of superconductivity is a subject of debate. It seems that quite recently an oscillating superconducting order parameter has been observed in a ferromagnetic thin film [142].

Usually [40, 71, 87, 131, 155, 216] these non-standard pairing types in ultracold Fermi gases are discussed for the case of infinite and homogeneous systems, or for trapped systems in local-density approximation (LDA) which again amounts to treating the system locally as homogeneous. However, as we are going to show, in certain cases the LDA can become a very poor approximation and we therefore want to analyze this problem within a fully microscopic mean field Bogoliubov-de Gennes (BdG) approach [90] taking into account the inhomogeneity and finite size of the trapped system. Recently the solution of the BdG equations has been considered in Ref. [170], where the authors discuss also possibilities for the experimental detection of a spatially modulated pairing gap.

In the present article we study two systems: a small one where shell effects still play a role and a relatively large one, where one could expect the LDA to be a reasonable approximation. As we will show, this is not always the case, although the LDA describes roughly the qualitative features. In addition, we examine

the temperature dependence of the non-standard pairing phase, since this is important in connection with the experimental realization of such a phase.

Let us briefly recall the BdG formalism. We consider a system containing $N = N_+ + N_-$ atoms of mass m trapped by a spherical harmonic potential in two hyperfine states denoted by $+$ and $-$. The many-body Hamiltonian of the system can be written as

$$H = \sum_\sigma \int d^3r \Big(\Psi_\sigma^\dagger(\mathbf{r}) H_0 \Psi_\sigma(\mathbf{r}) + g \Psi_+^\dagger(\mathbf{r}) \Psi_-^\dagger(\mathbf{r}) \Psi_-(\mathbf{r}) \Psi_+(\mathbf{r}) \Big) \,, \tag{2.1}$$

where $H_0 = -\hbar^2\nabla^2/(2m) + m\omega^2 r^2/2$ denotes the harmonic oscillator single-particle Hamiltonian, $\Psi_\sigma(\mathbf{r})$ is the field operator which annihilates a particle at the position $\mathbf{r}$ in the spin state σ ($+$ or $-$), $g = 4\pi\hbar^2 a/m$ is the coupling constant. In mean-field approximation, one can derive the following BdG equations corresponding to the Hamiltonian (2.1):

$$\begin{aligned} u_{\eta\sigma}(\mathbf{r}) E_{\eta\sigma} &= W_\sigma u_{\eta\sigma}(\mathbf{r}) + \Delta(\mathbf{r}) v_{\eta-\sigma}(\mathbf{r}) \,, \\ v_{\eta-\sigma}(\mathbf{r}) E_{\eta\sigma} &= -W_{-\sigma} v_{\eta-\sigma}(\mathbf{r}) + \Delta(\mathbf{r}) u_{\eta\sigma}(\mathbf{r}) \,, \end{aligned} \tag{2.2}$$

where $W_\sigma = H_0 + g\rho_{-\sigma}(\mathbf{r}) - \mu_\sigma$, μ_σ and ρ_σ being the chemical potential and the density, respectively. $\Delta(\mathbf{r})$ denotes the pairing field (gap) and $E_{\eta\sigma}$, $u_{\eta\sigma}$ and $v_{\eta\sigma}$ are the quasiparticle energy and wave functions, respectively, corresponding to the quantum numbers $\eta = n, l, m$ and spin σ. In order to have different populations, the two chemical potentials μ_+ and μ_- must be different. It is convenient to introduce the average chemical potential $\bar{\mu}$ and to write $\mu_\sigma = \bar{\mu} + \sigma\delta\mu/2$ where $\delta\mu$ determines the asymmetry. Eqs. (2.2) reduce to the usual BdG equations in the symmetric case $\mu_+ = \mu_-$. They are solved numerically employing the same regularization method for the pairing field as described in Ref. [119] for the symmetric case.

Eqs. (2.2) are general enough to describe rather complicated types of non-standard pairing. In the case of usual BCS pairing, the dominant matrix elements of the pairing field are the diagonal ones, i.e., each state $|n, l, m, +\rangle$ is paired with its time-reversed counterpart $|n, l, -m, -\rangle$. However, the non-diagonal matrix elements of Δ are also included, which amounts to taking into account also the pairing of states $|n, l, m, +\rangle$ and $|n', l, -m, -\rangle$ with different principal quantum numbers $n' \neq n$. In our present calculation, we still keep the restriction that the Cooper pairs have total angular momentum zero. To release this constraint would mean to allow for a spontaneous breakdown of spherical symmetry, which would be numerically very heavy. The effect of strong non-diagonal matrix elements of Δ in fact corresponds closely to the LOFF phase in the case of a uniform system. There, the states are labeled by their momentum $\mathbf{k}$. In the simplest version of the LOFF phase, the Cooper pairs have total momentum $\mathbf{q}$, i.e., each state $|\mathbf{k}, +\rangle$ is paired with $|-\mathbf{k}+\mathbf{q}, -\rangle$. The corresponding gap is oscillating with wave vector $\mathbf{q}$ and its matrix elements are therefore of the form $\Delta_{\mathbf{k}\mathbf{k}'} = \Delta\delta_{\mathbf{k}-\mathbf{q},\mathbf{k}'}$ (in contrast to the BCS phase, where $\Delta_{\mathbf{k}\mathbf{k}'} = \Delta\delta_{\mathbf{k}\mathbf{k}'}$) [1].

In the discussion of our results all quantities will be given in harmonic oscillator units. We use the same coupling constant as in Ref. [119], i.e., $g = -\hbar^2 l_{ho}/m$, where $l_{ho} = \sqrt{\hbar/(m\omega)}$ denotes the harmonic oscillator length, and we consider two values for the average chemical potential, $\bar{\mu} = 22\ \hbar\omega$ (small system with $N \approx 4900$) and $32\ \hbar\omega$ (large system with $N \approx 17000$).

In Fig. 2.1 we show the values of the pairing gap $\Delta(0)$ at the center of the trap for increasing aymmetry $\delta\mu$ at $T = 0$. Let us first look at the lowest line, corresponding to the small system with $\bar{\mu} = 22\ \hbar\omega$. When both spin states are equally populated ($\delta\mu = 0$), we find $\Delta(0) \approx 2\ \hbar\omega$, i.e., we are no more in the intrashell-pairing

[1] Note, however, that this analogy between the trapped and the homogeneous system is not perfect, since in the trapped system with $\delta\mu \neq 0$ even pairing between states $|n, l, m, +\rangle$ and $|n, l, -m, -\rangle$ includes pairing of states with different wave functions due to the different mean fields felt by atoms with different spin projections.

regime, but shell effects are still important [119]. If we increase $\delta\mu$, the two Fermi surfaces become more and more separated, i.e., if the state $|n,l,m,+\rangle$ lies close to the Fermi level for spin $+$, the state $|n,l,-m,-\rangle$ lies far from the Fermi level for spin $-$, making BCS pairing less and less favorable. As a consequence, at $\delta\mu \approx 1.2$ $\hbar\omega$, corresponding to a particle number asymmetry $\alpha = (N_+ - N_-)/N \approx 0.06$, the pairing disappears (shell closure effect). But then, near $\delta\mu \approx 2\ \hbar\omega$ ($\alpha \approx 0.07$), the states $|n,l,m,+\rangle$ near the Fermi level for spin $+$ approach the states $|n',l,-m,-\rangle$ near the Fermi level for spin $-$ if $n' = n-1$. Therefore, pairing becomes again possible, but now the Cooper pairs are built of two wavefunctions with different numbers of nodes, leading to a gap $\Delta(r)$ which as a function of r has exactly one node.

Let us now turn to the investigation of the larger system, $\bar{\mu} = 32\ \hbar\omega$. Here it seems to be appealing to estimate if and where the LOFF phase could appear by using the LDA, which should be exact in an infinite system. In order to do this, we calculate at each point R the thermodynamic potential Ω of a uniform gas with effective average chemical potential $\bar{\mu}_{\mathit{eff}}(R) = \bar{\mu} - m\omega^2 R^2/2$, assuming a gap of the form $\Delta(\mathbf{r}) = \Delta \exp(i\mathbf{q}\cdot\mathbf{r})$, and minimize Ω with respect to Δ and q. To be more precise, we should have taken a more sophisticated expression for the order parameter, but we stress here that we use the LDA just to have some indications about what kind of behavior one should expect. Let us again look at $\Delta(0)$ as a function of the asymmetry (dashed line in Fig. 2.1). We find that LDA gives the BCS solution $q = 0$ as the most favorable solution up to $\delta\mu = 11.9\ \hbar\omega$. At that asymmetry we find a first-order phase transition (i.e., a discontinuity in $\Delta(0)$) to the LOFF phase with $q \sim l_{ho}^{-1}$ which means that the order parameter oscillates with a wavelength of $\sim 6.2\ l_{ho}$. This behavior is different from the microscopic (BdG) result (solid line in Fig. 2.1), which shows a smooth behavior of $\Delta(0)$. Nevertheless, also in the BdG calculation there is a rapid change of $\Delta(0)$ between $\delta\mu = 10\ \hbar\omega$ ($\alpha \approx 0.25$) and $\delta\mu = 11\ \hbar\omega$ ($\alpha \approx 0.29$), where the system goes from the BCS-type to the LOFF-type phase, as discussed above. The minimum that one observes for the BdG gap at $\delta\mu \approx 10.8\ \hbar\omega$ and the subsequent enhancement are due to shell effects which still persist even in this large system and which cannot be reproduced by the semiclassical LDA calculation.

In Fig. 2.2 we plot the radial profile of the pairing field $\Delta(r)$ for $\delta\mu = 12\ \hbar\omega$, corresponding to $\alpha \approx 0.3$, at $T = 0$. The microscopic (solid line) and the LDA (dashed line) results are shown. Within LDA, in this case, the LOFF phase is more favorable than BCS for all values of r. We observe in Fig. 2.2 that the LDA gap goes abruptly to zero at a radius of $\sim 2\ l_{ho}$, which is smaller than the LDA wavelength of $\sim 6.2\ l_{ho}$. Thus, the region where the gap is non-zero does not even contain one wavelength of the oscillation and therefore the validity of LDA seems to be very questionable. As expected from the symmetric case [119], the LDA fails to describe the tail of the pairing field: The LDA gap goes abruptly to zero while in the microscopic case the gap has a smooth profile. We finally observe that the microscopic order parameter makes an oscillation and that a node is situated at $\approx 3\ l_{ho}$: The modulation of the order parameter and the presence of a node are signals which indicate that the system is in a LOFF-type phase.

Let us consider now the case of a smaller asymmetry, $\delta\mu = 6\ \hbar\omega$, corresponding to $\alpha \approx 0.15$. We show in Fig. 2.3 the radial profiles of the gap $\Delta(r)$ (top) and of the densities (bottom) at $T = 0$. In the upper panel we report the microscopic (BdG) gap (solid line) and the LDA result (dashed line). In this case, according to the LDA, the BCS phase ($q = 0$) would be energetically preferred in the center of the gas (as we have shown in Fig. 2.1) and up to $r = 3.8\ l_{ho}$, while the LOFF phase with $q \sim 0.7\ l_{ho}^{-1}$ would be more favorable in the interval $3.8\ l_{ho} < r < 4.1\ l_{ho}$. For larger values of r, the LDA predicts that the gap should be zero. The wavelength of the oscillation of the order parameter in the LOFF phase ($\sim 8.9\ l_{ho}$) would again be much larger than the region where the gap is non zero. Contrary to the LDA, the microscopic BdG calculation gives a smooth behavior of the order parameter. Near the center, it corresponds rather well to the LDA prediction, indicating that the pairing is more or less of BCS type. Between $r = 4\ l_{ho}$ and $10\ l_{ho}$, the gap is oscillating (see inset in the upper panel of Fig. 2.3), indicating the appearance of the LOFF-type phase. Although within the

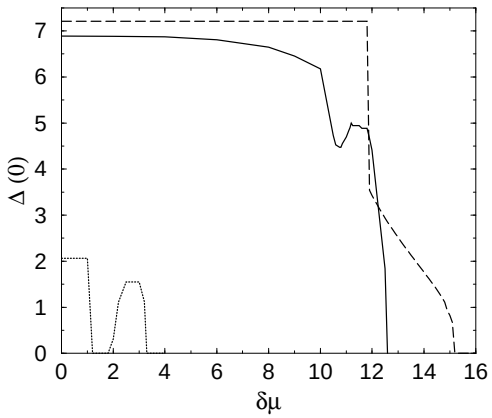

Figure 2.1: Value of the pairing gap at the center of the trap (in units of $\hbar\omega$) as a function of the asymmetry $\delta\mu$ (in units of $\hbar\omega$). The lowest line corresponds to $\bar{\mu} = 22\hbar\omega$. The two upper lines correspond to $\bar{\mu} = 32\hbar\omega$ and show the BdG (solid line) and the LDA result (dashed line).

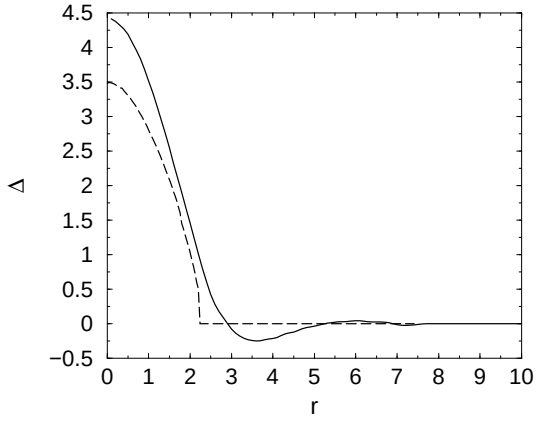

Figure 2.2: Radial profile of the pairing gap $\Delta(r)$ (in units of $\hbar\omega$) for $\delta\mu = 12\ \hbar\omega$. The radial coordinate r is expressed in units of l_{ho}. The microscopic (solid line) and the LDA (dashed line) results are plotted.

BdG calculation there is no sharp transition from one phase to the other, qualitatively it seems that both phases can be present at the same time in different regions of the system.

In the lower panel of Fig. 2.3 the BdG results for the two densities (ρ_+ and ρ_-) are shown. One observes that in the center of the gas the two densities are equal. This is coherent with the fact that in the BCS phase at $T = 0$ the LDA always gives $\rho_+ = \rho_-$ if $\Delta > \delta\mu/2$, as it is the case here.

All the results shown so far refer to $T = 0$. However, in real experiments with trapped atomic gases the temperature is always non-zero. Let us therefore raise the temperature in the case of asymmetry $\delta\mu = 6\ \hbar\omega$ in order to analyze what happens to the gap modulation when the temperature is finite. In Fig. 2.4 we show the order parameter in the radial interval from $4\ l_{ho}$ to $10\ l_{ho}$ (where we observed an oscillation in the case $T = 0$) for four values of temperature, $T = 0$ (solid line), $T = 0.5\ \hbar\omega/k_B$ (dashed line) $T = \hbar\omega/k_B$ (triangles) and $T = 2\ \hbar\omega/k_B$ (circles). One observes that the oscillation has a smaller and smaller amplitude with increasing temperature and that it disappears between $T = \hbar\omega/k_B$ and $T = 2\ \hbar\omega/k_B$. Our interpretation of this result is that the critical temperature of the LOFF-type phase is smaller than the BCS critical temperature. Therefore, the LOFF-type phase disappears at some temperature between $\hbar\omega/k_B$ and $2\ \hbar\omega/k_B$, while the BCS gap in the central region of the gas is still different from zero at $T = 2\ \hbar\omega/k_B$. In this case the LDA results (not shown) are very different from the BdG ones (the gap is much too large), as one could expect from the fact that already in the symmetric case the agreement between LDA and BdG calculations becomes quite poor at finite temperature [119]. Nevertheless, qualitatively the LDA gives again the right indication: Also within LDA the LOFF phase is absent at $T = 2\ \hbar\omega/k_B$. Instead, at that temperature the Sarma phase becomes more favorable in certain regions within the LDA: This phase is characterized by zero momentum Cooper pairs, a gap Δ smaller than $\delta\mu/2$, different densities ρ_+ and ρ_- and typical occupation number distributions as shown in Ref. [155].

To summarize, we have solved the BdG equations for an atomic Fermi gas with different populations of two hyperfine states. It is well-known that an increasing asymmetry of the populations renders BCS pairing difficult, and non-standard pairing mechanisms become possible. In this article we showed that the BdG formalism

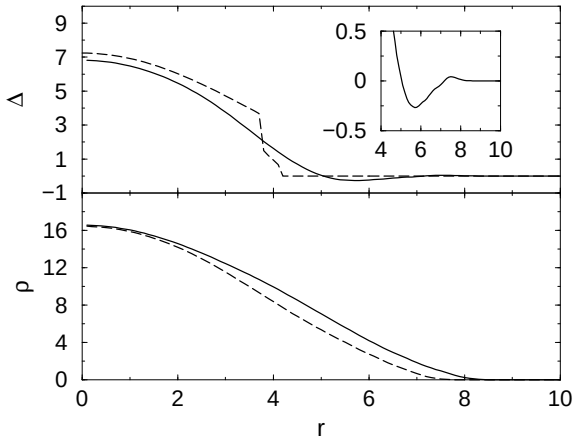

Figure 2.3: Radial profiles of the pairing gap $\Delta(r)$ in units of $\hbar\omega$ (top) and of the densities in units of l_{ho}^{-3} (bottom) for $\delta\mu = 6\ \hbar\omega$ as a function of the radial coordinate r in units of l_{ho}. In the upper panel the solid and dashed lines correspond to the BdG and LDA results, respectively. In the lower panel, the solid and the dashed lines refer to the BdG results for the $+$ and $-$ densities, respectively.

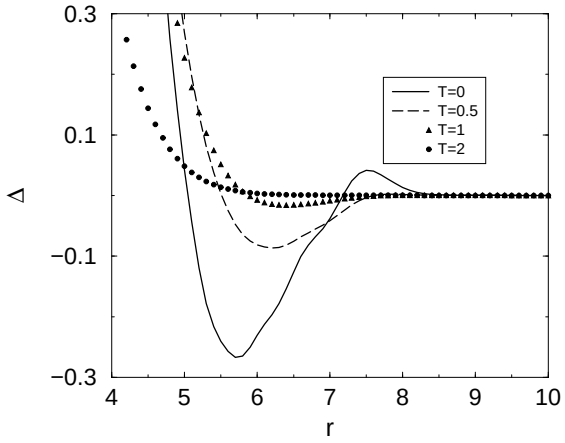

Figure 2.4: Radial profile of the pairing gap $\Delta(r)$ (in units of $\hbar\omega$) for $\delta\mu = 6\ \hbar\omega$. The radial coordinate r is expressed in units of l_{ho}. Results at $T = 0$ (solid line), $T = 0.5\ \hbar\omega/k_B$ (dashed line) $T = \hbar\omega/k_B$ (triangles) and $T = 2\ \hbar\omega/k_B$ (circles) are reported.

automatically includes such non-standard pairing mechanisms through the non-diagonal matrix elements of the gap. For example, in the case of a small system, we found that the usual pairing disappears at a certain asymmetry, but when the asymmetry is strong enough such that the single-particle energies of states with opposite spin and different principal quantum numbers start to match, pairing becomes again possible, but now with an oscillating order parameter. This is very similar to the LOFF phase introduced for the case of a homogeneous system. In the case of a larger system, there is no longer a sharp separation between the BCS pairing and the LOFF-type pairing: As a function of asymmetry, but also as a function of the distance from the center of the trap, the system undergoes smooth transitions from one kind of pairing to the other. This result is qualitatively different from that obtained with LDA calculations, where the transition between the BCS and the LOFF phase is a first order phase transition. We also observe that even a system containing 17000 atoms is still much too small for the LDA to be applicable, since the wavelength of the LOFF oscillations is of the same order of magnitude as the whole system. Finally we looked at the temperature dependence of the LOFF-type phase. We observe that it disappears already at temperatures where the BCS phase is still present. This, of course, can be a problem if one tries to observe the LOFF phase in experiments.

We acknowledge discussions with M. Baldo, F. Cataliotti and A. Sedrakian.

3 Surface effects in color superconducting strange-quark matter

Micaela Oertel and Michael Urban, Phys. Rev. D 77, 074015 (2008)

Surface effects in strange-quark matter play an important role for certain observables which have been proposed in order to identify strange stars, and color superconductivity can strongly modify these effects. We study the surface of color superconducting strange-quark matter by solving the Hartree-Fock-Bogoliubov equations for finite systems ("strangelets") within the MIT bag model, supplemented with a pairing interaction. Due to the bag-model boundary condition, the strange-quark density is suppressed at the surface. This leads to a positive surface charge, concentrated in a layer of ~ 1 fm below the surface, even in the color-flavor locked (CFL) phase. However, since in the CFL phase all quarks are paired, this positive charge is compensated by a negative charge, which turns out to be situated in a layer of a few tens of fm below the surface, and the total charge of CFL strangelets is zero. We also study the surface and curvature contributions to the total energy. Due to the strong pairing, the energy as a function of the mass number is very well reproduced by a liquid-drop type formula with curvature term.

3.1 Introduction

From rather general arguments it is expected that at low temperatures and high densities quark matter is in a color superconducting state [26, 33, 86, 110]. More recently [12, 193] it has been suggested that the diquark pairing gaps for quark matter at densities of several times nuclear matter saturation density could be of the order of ~ 100 MeV. Since this could have important phenomenological consequences in particular for the interior of compact stars, this has triggered much work on color superconductivity in dense quark matter (for reviews, see, e.g., Ref. [8, 66, 133, 191, 197, 203, 211, 222]). These investigations of the QCD phase diagram have revealed a very rich phase structure with many different possible pairing patterns, depending on external conditions such as, for instance, electrical neutrality or quark masses. The largest diquark pairing gaps arise from scalar condensates, leading either to the two-flavor color superconducting (2SC) phase or to the color-flavor-locked (CFL) phase [13, 101, 210, 223]. The latter pairing pattern involves strange (s) quarks, in addition to the two light quark flavors, up (u) and down (d).

If color superconducting quark matter exists in nature, the most likely place to find it is the interior of compact stars because matter is compressed there to densities much higher than nuclear matter saturation density. However, it has been argued that strange-quark matter (SQM) might be absolutely stable [45, 266]. Under this hypothesis, even pure strange stars should exist [6, 127], i.e., stars entirely composed of SQM. Also small lumps of SQM, called "strangelets," might be stable. Because of their low charge to baryon number ratio Z/A, strangelets have been proposed to populate ultra-high energy cosmic rays [164, 206].

In SQM without pairing, the density of strange quarks is supposed to be smaller than that of light quarks because of their higher mass. Consequently, SQM and strangelets are positively charged and the charge neutrality of strange stars has to be achieved via the presence of electrons. At the surface an atmosphere of electrons forms [6, 127] which can potentially be detected [180, 255] via the emission of electron-positron pairs from an extremely strong electric field at the surface.

Recently another possible picture of the surface of a strange star has been proposed [135]: there could be a "crust" composed of strangelets immersed in an electron gas. Similar to an ordinary neutron star, there could be an interface between the crust and the interior in form of the famous "pasta phases." Within this scenario the electric field at the surface would be strongly reduced. Obviously, surface effects for the strangelets play an important role for the description of this scenario. For instance, there is a critical surface tension deciding whether a homogeneous phase or the droplet phase is favored [11]. Another question for which surface effects should be considered is the formation of a strange star in a supernova explosion. Before the explosion the original star contains hadronic matter. During the formation of the star, nucleation of strangelets sets in, leading

then to a conversion of the entire star to SQM. For the nucleation process the properties of small strangelets are important.

Pairing tends to reduce the differences in density of different quark species. For bulk quark matter in the CFL state, requiring color neutrality, all quarks are paired. The densities are thus equal and CFL quark matter is electrically neutral on its own, i.e., without any electrons [192]. This would suggest dramatic changes in the properties of strangelets and SQM inside compact stars. For instance, the electrosphere at the surface of a strange star could completely disappear. But, the presence of the surface can modify this picture since it can lead to a non-zero surface charge which remains even for large objects. For example, the boundary condition of the MIT bag model suppresses the density of the massive strange quarks at the surface, resulting in a positive surface charge [162]. Within this scenario, the total charge of a strangelet, following roughly $Z \approx 0.3A^{2/3}$, is drastically reduced with respect to "normal" strangelets. For strange stars, this requires the presence of electrons [256]. However, pairing has not been treated self-consistently in previous work (see, e.g., Ref. [162]). In this paper we will therefore reinvestigate finite-size strangelets with pairing by considering quark matter in a color superconducting spherical bag, solving the Hartree-Fock-Bogoliubov (HFB) equations. We will show, in particular, that there exist CFL type solutions where all quarks are paired and the total charge of the strangelet strictly vanishes.

The outline of the paper is as follows. In Section 3.2 we will present our model for treating color superconducting quark matter in a finite volume. In Section 3.3 we will show numerical results. In Section 3.3.1 we discuss the possibility of qualitatively different configurations. In Section 3.3.2 we concentrate on the charge-density distributions of the CFL like solutions. In Section 3.3.3 we discuss a liquid-drop like mass formua for the CFL-like solutions and calculate the surface tension. Finally, in Section 3.4 we will summarize our results.

3.2 Model

3.2.1 Lagrangian

Since it is not possible to describe strangelets or SQM with a surface from first principles (QCD), we will use a quark model which allows to describe finite-size objects. For this purpose we will use here the MIT bag model [83]. The idea of this model is that confinement can be simulated by the existence of a "bag" which consists of a "hole" in the non-perturbative QCD vacuum. Inside this "bag", the vacuum is supposed to be perturbative, i.e., inside the bag the interactions of the quarks can be treated perturbatively. To create this "hole" in the non-perturbative QCD vacuum, an energy per volume, B, is necessary. In the present work we will consider a static spherical bag with radius R. On the surface of the bag, the quark field ψ has to satisfy an appropriate boundary condition. In the simplest version of the MIT bag model, the boundary condition reads

$$-i\mathbf{e}_r \cdot \boldsymbol{\gamma}\psi = \psi|_{r=R}\,. \tag{3.1}$$

which ensures that there is no particle flux across the surface. By $r = |\mathbf{r}|$ we denote the radial coordinate, measured from the center of the bag, and $\mathbf{e}_r = \mathbf{r}/r$ is the radial unit vector. The boundary condition (3.1) leads to a suppression of the wave functions of massive particles at the surface. This means that the strange-quark density will a priori be suppressed at the surface with respect to the light quark densities.

The MIT bag model can be expressed in terms of a Lagrangian density as follows [44]:

$$\mathcal{L}_{bag} = [\bar{\psi}(i\gamma^\mu\partial_\mu - m)\psi - B]\theta(R-r) - \frac{1}{2}\bar{\psi}\psi\delta(R-r)\,, \tag{3.2}$$

where m is the matrix of quark masses. Due to the second term, the boundary condition (3.1) follows immediately from the Euler-Lagrange equation for the quark field [44].

In order to include pairing, we will supplement the bag model with a pairing interaction. In principle, perturbative one-gluon exchange generates an attractive paring interaction in certain channels, in particular in the scalar color antitriplet channel. For simplicity, we will use here a four-point pairing interaction acting only in this dominant channel. The corresponding Lagrangian reads (see any of the standard review articles on color superconductivity [8, 66, 133, 191, 197, 203, 211, 222])

$$\mathcal{L}_{pair} = H \sum_{A,A'} (\bar{\psi} i\gamma_5 \tau_A \lambda_{A'} C \bar{\psi}^T)(\psi^T C i\gamma_5 \tau_A \lambda_{A'} \psi)\,, \tag{3.3}$$

where H is a dimensionful coupling constant, C denotes the charge conjugation matrix, and $\tau_A, \lambda_{A'}$ represent $SU(3)$ matrices in flavor and color space, respectively. We follow the convention that capital letters A, A' indicate that we are restricting τ_A and $\lambda_{A'}$ to be antisymmetric, i.e., in terms of the Gell-Mann matrices, $A, A' \in \{2, 5, 7\}$.

In addition to the strong interaction, the quarks will exhibit electromagnetic interactions which, due to their long range, become particularly important for large objects. The corresponding Lagrangian reads

$$\mathcal{L}_{e.m.} = -\frac{1}{4} F_{\mu\nu} F^{\mu\nu} - e\bar{\psi} Q A_\mu \gamma^\mu \psi, \tag{3.4}$$

where $F_{\mu\nu} = \partial_\mu A_\nu - \partial_\nu A_\mu$ and A_μ denote respectively the electromagnetic field strength tensor and four-potential, and Q is the matrix of quark charges in units of e, $Q_u = 2/3$, $Q_d = Q_s = -1/3$.

It would be in the spirit of the bag model to include also the gluon exchange in a perturbative way, i.e., in the same way as the photon. However, this goes beyond the scope of the present paper and will be postponed to a future study.

3.2.2 Solution in the framework of HFB theory

The model described by $\mathcal{L} = \mathcal{L}_{bag} + \mathcal{L}_{pair} + \mathcal{L}_{e.m.}$ will be treated in the framework of HFB theory. By minimizing the energy in mean field approximation (for more details see Appendix 3.B and Ref. [69] where the "Dirac-Hartree-Bogoliubov" approximation was developped for finite nuclei), one obtains the following HFB equations:

$$\begin{pmatrix} h & \Delta \\ \Delta & -h \end{pmatrix} \begin{pmatrix} U_\alpha(\mathbf{r}) \\ \gamma^0 V_\alpha(\mathbf{r}) \end{pmatrix} = \epsilon_\alpha \begin{pmatrix} U_\alpha(\mathbf{r}) \\ \gamma^0 V_\alpha(\mathbf{r}) \end{pmatrix}. \tag{3.5}$$

The single-particle Hamiltonian

$$h = -i\boldsymbol{\alpha} \cdot \boldsymbol{\nabla} + m\gamma^0 + \Sigma - \mu \tag{3.6}$$

includes besides the free Dirac Hamiltonian the quark self-energy Σ (in our case due to Coulomb interaction) and the matrix of chemical potentials μ which depend on flavor $f \in \{u, d, s\}$ and color $c \in \{r, g, b\}$ (we will denote the three colors by red, green, and blue). Δ denotes the pairing field (gap). The spinors U_α and V_α describe the particle- and hole-like components of the quark fields, respectively [see Eq. (3.38)], where α is a multi-index containing all quantum numbers characterizing a single-particle state (see Appendix 3.A). In writing Eq. (3.5), we implicitly assumed that the pairing field Δ can be chosen real, which is the case for the pairing pattern we consider, and that the self-energy Σ is local, which is the case since we neglect the exchange (Fock) term (see below).

The pairing field Δ and the self-energy Σ depend themselves on the wave functions U and V, such that we have to solve a self-consistency problem. To be specific, the pairing field Δ depends on the diquark condensates

$$s_{AA'}(x) = -\langle \bar{\psi_T}(x) \tau_A \lambda_{A'} \psi(x) \rangle\,, \tag{3.7}$$

where ψ_T denotes the time-reversed conjugate of ψ,

$$\psi_T = \gamma_5 C \bar{\psi}^T \,. \tag{3.8}$$

The diquark condensates can be expressed in terms of the U and V functions as

$$s_{AA'}(r) = -\sum_{\beta,\epsilon_\beta<0} \bar{V}_\beta(\mathbf{r})\tau_A\lambda_{A'}U_\beta(\mathbf{r}) \tag{3.9}$$

(since we are dealing with a static problem, the condensates do not depend on time, and due to spherical symmetry, they depend only on the radial coordinate r). We will limit our investigations here to diagonal condensates, i.e., only condensates with $A = A'$ are non-zero[1]. In uniform infinite matter and for an exact $SU(3)$ flavor symmetry, the CFL phase is characterized by nonzero values $s_{22} = s_{55} = s_{77}$, whereas the 2SC state has only $s_{22} \neq 0$. The relation between the condensates s_{AA} and the pairing field Δ reads

$$\Delta(r) = \sum_{A=2,5,7} \Delta_A(r)\tau_A\lambda_A \,, \tag{3.10}$$

$$\Delta_A(r) = 2\,H s_{AA}(r) \,. \tag{3.11}$$

In practice, the expression (3.9) is divergent and it is necessary to introduce a cutoff in order to obtain a finite result. Since in a finite system the levels are discrete, a sharp cutoff would generate discontinuities as a function of the system's size. We therefore introduce a smooth cutoff function $f(p/\Lambda)$ (see Appendix 3.C for details). Another practical problem arises from antiparticle contributions. However, since the chemical potentials μ_{fc} are large and positive and pairing involves mostly the states near the Fermi surface, we assume that the antiparticle contributions are not important and can be neglected. We checked this approximation (analogous to the "no-sea approximation" in nuclear physics [69]) in infinite matter and found that the effect of antiparticle states can be absorbed in a readjustment of the coupling constant by $\sim 20\,\%$.

For the normal self-energy Σ we employ the Hartree approximation, i.e., we neglect the Coulomb exchange (Fock) term as well as exchange contributions from the magnetic field. We also disregard the contribution of $\mathcal{L}_{pair}$ to the normal self-energy. Hence, the self-energy is simply proportional to the static Coulomb potential

$$\Sigma(r) = eQA_0(r)\gamma^0 \,. \tag{3.12}$$

The Coulomb potential is related to the quark densities by

$$A_0(r) = e\int d^3r' \frac{\rho_{ch}(\mathbf{r}')}{|\mathbf{r}-\mathbf{r}'|} \,, \tag{3.13}$$

where

$$\rho_{ch}(r) = \sum_f Q_f \rho_f(r) \tag{3.14}$$

is the charge density (divided by e), ρ_f being the number density of quarks of flavor f. As it was the case for the diquark condensates, the quark number densities can be expressed in terms of the U and V functions. Denoting by $\tilde{\beta}$ all single-particle quantum numbers except flavor, we can write the number density of quarks of flavor f as

$$\rho_f(r) = \sum_{\tilde{\beta},\epsilon_{f\tilde{\beta}}<0} U^\dagger_{f\tilde{\beta}}(\mathbf{r})U_{f\tilde{\beta}}(\mathbf{r}) \,. \tag{3.15}$$

[1] In uniform infinite matter it can be shown [13] that for the energetically favored solution the arbitrary orientation in color can be chosen in such a way that only the diagonal condensates with $A = A'$ are non-zero.

Let us now summarize the procedure how the HFB equations are solved. We start with an initial guess for the pairing fields $\Delta_A(r)$ and for the Coulomb potential $A_0(r)$. Then we solve the eigenvalue problem (3.5) in order to find the U and V functions. From these functions the diquark condensates $s_{AA}(r)$ and the quark densities $\rho_f(r)$ are computed according to Eqs. (3.9) and (3.15), which are then used to update the pairing fields Δ_A and the Coulomb field A_0 according to Eqs. (3.11) and (3.13). These steps are iterated until convergence (i.e., self-consistency) is reached.

The crucial difference to the BCS formalism in homogeneous infinite matter is that in our case the wave functions adapt themselves to the pairing field and to the Coulomb potential, whereas in the case of homogeneous infinite matter the wave functions always stay plane waves, and the U and V factors are just coefficients multiplying them.

3.2.3 Determination of chemical potentials and bag radius

In Section 3.2.2 we described how the HFB equations are solved for given values of the chemical potentials μ_{fc} and of the bag radius R. However, in reality, only one quantity is given, namely the baryon number A. Even the fractions of different quark flavors cannot be fixed, unless one allows for β unstable strangelets. Let us now describe how we determine the chemical potentials μ_{fc} and the bag radius R for given baryon number A.

The first step consists in fixing the quark numbers, N_{fc}, for each flavor f and color c, and to adjust the chemical potentials μ_{fc} in order to obtain these quark numbers. Before we address the question how the nine quark numbers N_{fc} are determined, let us discuss the issue of the bag radius R. Until now, the radius was imposed from outside, but in reality the system will choose its radius such that it minimizes its total energy for given quark numbers N_{fc}. Within the bag model, the total energy is given by

$$E = E_q + BV\,, \tag{3.16}$$

where $V = 4\pi R^3/3$ is the volume of the bag. By E_q we denote the energy of the quarks inside the bag, including the interaction energy, which in our case comes from pairing and Coulomb interactions. It can be obtained from the solution of the HFB equations as follows [69]:

$$E_q = \int_{r<R} d^3r \sum_{\beta,\epsilon_\beta<0} \left(U_\beta^\dagger(\mathbf{r})(\epsilon_\beta+\mu)U_\beta(\mathbf{r}) + \frac{1}{2}\left[\bar{U}_\beta(\mathbf{r})\Delta(r)V_\beta(\mathbf{r}) - U_\beta^\dagger(\mathbf{r})eQA_0(r)U_\beta(\mathbf{r})\right]\right)\,. \tag{3.17}$$

Minimizing the total energy E is of course completely equivalent to saying that the quark pressure in the bag is counterbalanced by the bag pressure B, i.e.,

$$\left.\frac{dE_q}{dV}\right|_N = -B\,. \tag{3.18}$$

This equation determines the radius of the strangelet for given bag pressure B, interaction strength H and quark numbers N_{fc}. In practice, however, we find it more convenient to minimize E rather than solve Eq. (3.18).

Let us now turn to the determination of the quark numbers. The nine quark numbers N_{fc} cannot be chosen arbitrarily, but they have to fulfil certain requirements. Imposing the total baryon number A and color neutrality, i.e., equal numbers of quarks for each color, we have to satisfy the constraint

$$\sum_f N_{fc} = A \qquad \text{for all } c\,. \tag{3.19}$$

Of course, these three equations are not sufficient for determining all the nine quark numbers. In order to get unique values for the N_{fc}, it is necessary to impose β stability, as we will describe now.

In an infinite homogeneous system the condition for β equilibrium gives just a relation between the chemical potentials[1]

$$\mu_{dc} = \mu_{sc} = \mu_{uc} + \mu_e \qquad \text{for all } c\,. \tag{3.20}$$

In a small system this is slightly different. First, even if there are electrons (i.e., if the strangelet is charged), they are not localized inside the strangelet, but they form a large cloud like in ordinary atoms and hence their chemical potential μ_e is approximately equal to the electron mass and can be neglected. Without pairing, it has been estimated in Ref. [103] that this may be still the case for strangelets with charge $Z \lesssim 1000$, corresponding roughly to $A \lesssim 10^6$. The second difference to bulk matter comes from the fact that, due to the discrete levels, particle numbers are discontinuous functions of the chemical potentials. The term β equilibrium should now be replaced by β stability, which means that the system does not gain energy by performing a β decay, inverse β decay, or electron capture, i.e., transforming an up into a down or strange quark, or vice versa, accompanied by the corresponding leptons.

To achieve β stability, we therefore compare the energies of adjacent strangelets with the same total quark number per color, differing only in the number of up, down, and strange quarks, respectively, in order to find the configuration with the lowest total energy E. Of course, in the case of large particle numbers, the minimum-energy configuration fulfils approximately the condition (3.20).

3.2.4 Choice of the model parameters

Besides the quark masses, which we take as $m_u = m_d = 0$ and $m_s = 120$ MeV, our model contains three parameters: the bag constant B, the coupling constant of the pairing interaction, H, and the cutoff Λ which is necessary to avoid the divergence of the gap equation (3.9), see below Eq. (3.11). In fact, a change of the cutoff in reasonable limits can to very good approximation be compensated by a change of the coupling constant. We therefore choose rather arbitrarily $\Lambda = 600$ MeV and give instead of the dimensionful coupling constant H the dimensionless combination $H\Lambda^2$. So we are left with two parameters, B and $H\Lambda^2$

We can get an idea of the value of the bag pressure by looking at the stability of bulk quark matter. Non-strange quark matter should be energetically less favored than normal hadronic matter, whereas SQM should be stable if for some baryon number $A > A_c$ strangelets become stable and consequently strange stars can exist. This means that we want the energy per baryon of SQM to be less than 931 MeV, the energy per baryon of the most stable nucleus, ^{57}Fe. On the other hand, the energy per baryon of non-strange quark matter should be larger than the nucleon mass. Without interaction the window for the values of the bag constant is then 148 MeV $< B^{1/4} <$ 157 MeV. These values change as a function of the interaction strength H. To better compare the results, we will readjust for each coupling strength the bag constant in order to get $E/A = 900$ MeV. The corresponding values are listed in Table 3.1, together with other properties of infinite matter. Non-strange quark matter is unstable with these parameter values. Note that for the weakest non-vanishing coupling constant given in Table 3.1, SQM is in the 2SC phase and not in the CFL phase. For the larger coupling constants, the CFL phase is preferred. Note that, due to the mass difference of light and strange quarks, the flavor $SU(3)$ symmetry is not exact and the gap Δ_2 is different from Δ_5 and Δ_7. However, since the CFL phase is electrically neutral, and we have $m_u = m_d = 0$, the isospin $SU(2)$ symmetry in the up- and down-quark sector is exact and therefore $\Delta_5 = \Delta_7$.

[1] Here we assume that neutrinos are not trapped, i.e., they can freely leave the system

Table 3.1: Values of the bag constants for different values of the coupling constant H, resulting in color and electrically neutral SQM with electrons in β equilibrium with an energy per baryon of $E/A = 900$ MeV. The corresponding baryon densities ρ_B, electron densities ρ_e, and pairing gaps in infinite matter are also displayed.

$H\Lambda^2$	$B^{1/4}$ (MeV)	ρ_B (fm^{-3})	ρ_e (fm^{-3})	Δ_2 (MeV)	$\Delta_5 = \Delta_7$ (MeV)
0	152.03	0.329	7.3×10^{-6}	0	0
1.5	152.44	0.339	9.7×10^{-5}	27.7	0
1.75	153.97	0.367	0	35.1	34.5
2	156.26	0.395	0	50.6	49.7
2.25	159.46	0.427	0	67.2	66.0
2.5	163.46	0.463	0	84.6	83.1

Table 3.2: Parameters and properties of the strangelets discussed in Section 3.3.1: B = bag constant, H = coupling constant of the pairing interaction, A = baryon number, Z = charge, N_{fc} = number of quarks of flavor f and color c, E/A = energy per baryon, R = radius of the bag, $\Delta_A(0)$ = value of the gap at $r = 0$.

$B^{1/4}$ (MeV)	$H\Lambda^2$ (MeV)	A	Z	$\begin{pmatrix} N_{ur} & N_{ug} & N_{ub} \\ N_{dr} & N_{dg} & N_{db} \\ N_{sr} & N_{sg} & N_{sb} \end{pmatrix}$	E/A (MeV)	R (fm)	$\Delta_2(0)$ (MeV)	$\Delta_5(0)$ (MeV)	$\Delta_7(0)$ (MeV)
152.03	0	108	24	$\begin{pmatrix} 44 & 44 & 44 \\ 44 & 44 & 44 \\ 20 & 20 & 20 \end{pmatrix}$	932.5	4.36	0	0	0
152.44	1.5	108	24	$\begin{pmatrix} 44 & 44 & 44 \\ 44 & 44 & 44 \\ 20 & 20 & 20 \end{pmatrix}$	930.7	4.31	32.9	0	0
153.97	1.75	108	24	$\begin{pmatrix} 44 & 44 & 44 \\ 44 & 44 & 44 \\ 20 & 20 & 20 \end{pmatrix}$	934.0	4.24	49.5	0	0
153.97	1.75	108	10	$\begin{pmatrix} 38 & 39 & 41 \\ 39 & 38 & 41 \\ 31 & 31 & 26 \end{pmatrix}$	934.8	4.21	41.6	24.9	24.9
153.97	1.75	108	0	$\begin{pmatrix} 38 & 35 & 35 \\ 35 & 38 & 35 \\ 35 & 35 & 38 \end{pmatrix}$	934.8	4.17	33.9	37.0	36.9

3.3 Results

3.3.1 Different types of solutions

We will first discuss the qualitatively different configurations we find. Let us start by discussing a small strangelet ($A = 108$, $Z = 24$) without any pairing interaction ($H\Lambda^2 = 0$). The mass number has been chosen such that the minimum-energy configuration is a closed-shell configuration. The quark numbers and other relevant information are listed in Table 3.2. Due to the finite size of the bag, the energy per baryon ($E/A = 932.5$ MeV, including 1.0 MeV due to Coulomb) is much higher than that of color neutral infinite matter with $\mu_{uc} = \mu_{dc} = \mu_{sc}$[1] ($E/A = 899.5$ MeV). This effect will be discussed in more detail in Section 3.3.3. The density profiles of light and strange quarks are shown in Fig. 3.1.

[1] As discussed below Eq. (3.20), it is more appropriate to compare a small strangelet with this kind of matter rather than electrically neutral matter with electrons in β equilibrium.

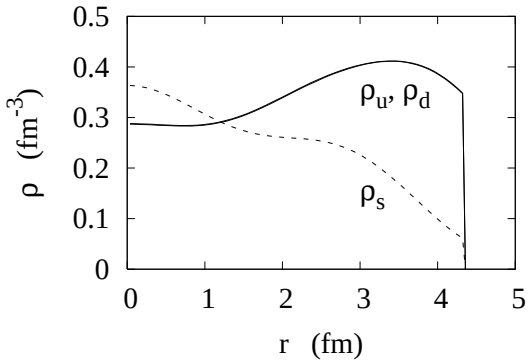

Figure 3.1: Quark number density profiles of the strangelet $A = 108$, $Z = 24$ in the case of vanishing pairing interaction (free quarks in a bag) and $B^{1/4} = 152.03$ MeV.

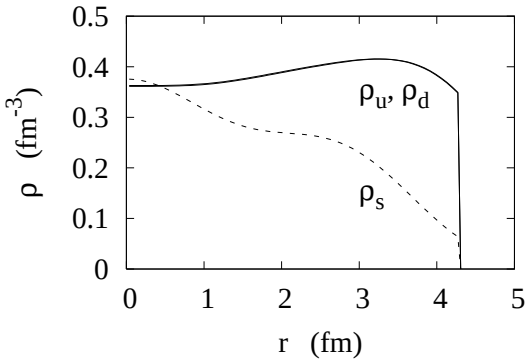

Figure 3.2: Quark number density profiles of the strangelet $A = 108$, $Z = 24$ in the case of $H\Lambda^2 = 1.5$ and $B^{1/4} = 152.44$ MeV.

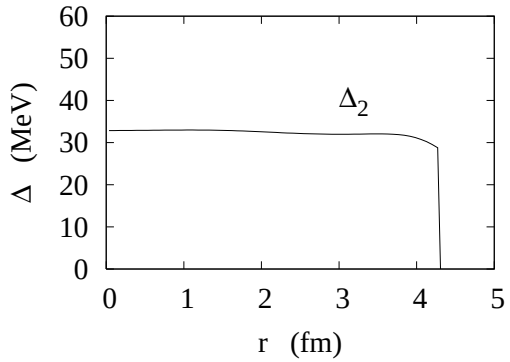

Figure 3.3: Gap $\Delta_2(r)$ of the strangelet $A = 108$, $Z = 24$ in the case of $H\Lambda^2 = 1.5$ and $B^{1/4} = 152.44$ MeV.

As expected, due to the boundary condition, the strange-quark density is strongly suppressed at the surface, contrary to the densities of the light quarks. For comparison we mention that for the same value of the bag constant, the densities in color neutral infinite matter with $\mu_{uc} = \mu_{dc} = \mu_{sc}$ are: $\rho_u = \rho_d = 0.355$ fm^{-3}, $\rho_s = 0.274$ fm^{-3}. We see that not only the strange-quark density, but also the densities of the light quarks are quite different from these values and depend strongly on r because of the existence of discrete levels in the bag. Let us mention that, due to the Coulomb potential, the density profiles of up and down quarks are slightly different, but the difference is too small to be visible in Fig. 3.1.

Now we switch on the pairing interaction. In the case of $H\Lambda^2 = 1.5$, SQM is in the 2SC phase, i.e., only up and down quarks of two colors (red and green in our notation) are paired. This is also true in a finite strangelet. Therefore it is clear that the strange-quark density profile remains the same as without pairing. The oscillations of the densities of the light quarks, however, are much weaker now than in the case without pairing, since pairing washes out the occupation numbers. This can be seen in Fig. 3.2. In this 2SC-like solution, only one of the gaps, Δ_2, is non-zero. Since Δ_2 involves only the wave functions of up and down quarks, which are not suppressed at the surface, it extends up to the surface of the bag, as shown in Fig. 3.3. As a function of r, it is almost constant and quite close to the corresponding value in infinite matter with $\mu_{uc} = \mu_{dc} = \mu_{sc}$, which is $\Delta_2 = 29.2$ MeV.

If we increase the coupling constant to $H\Lambda^2 = 1.75$, we obtain three qualitatively different solutions which

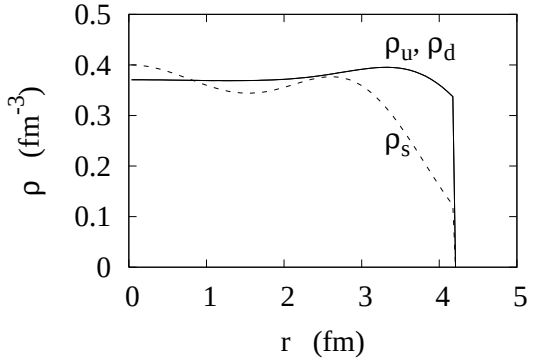

Figure 3.4: Density profiles of the strangelet $A = 108$, $Z = 10$ in the case of $H\Lambda^2 = 1.75$ and $B^{1/4} = 153.97$ MeV.

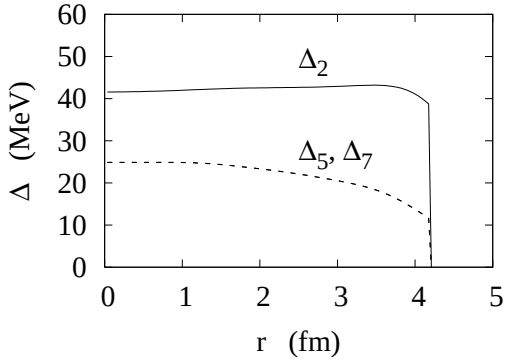

Figure 3.5: Gaps Δ_A as functions of r for the strangelet $A = 108$, $Z = 10$ in the case of $H\Lambda^2 = 1.75$ and $B^{1/4} = 153.97$ MeV.

have comparable energies. The most stable one is still of the 2SC type, although in infinite matter the CFL phase is preferred. In this case, the strangelet still has $Z = 24$ and the density profiles are almost identical to those shown in Fig. 3.2. The main difference is that now the value of the gap is larger.

In the two other solutions, also strange quarks participate in pairing ($\Delta_5 \approx \Delta_7 \neq 0$ – note that Δ_5 and Δ_7 are not exactly equal because the isospin symmetry is broken by the Coulomb interaction). These two solutions have charge $Z = 10$ and $Z = 0$, respectively. Let us first discuss the case $Z = 10$. In this case, there are a couple of up and down quarks which remain unpaired. The wave function of the unpaired level is mainly localized near the surface of the bag, as can be seen in Fig. 3.4, where the density profiles are shown. In the inner part, the densities of up, down, and strange quarks are almost equal, while near the surface, where the strange-quark density is suppressed due to the boundary condition, there is an excess of up and down quarks. This excess is due to the unpaired quarks. The fact that one level of up and down quarks (in the present case the $1g_{9/2}$ level, i.e., the lowest level with $j = 9/2, \kappa = -5$ in the notation of Appendix 3.A) does not participate in pairing means that the occupation number of this level is equal to 1. At the same time, the corresponding level of the strange quarks has an occupation number equal to 0. In a certain sense this situation is analogous to the "breached pairing" phase of infinite matter [155]. The charge Z is equal to the degeneracy $2j + 1$ of the unpaired level. The gaps Δ_A as functions of r corresponding to this solution are displayed in Fig. 3.5.

In the third solution, all quarks are paired. As a consequence, the numbers of up, down, and strange quarks are equal, and the total charge is $Z = 0$. This is analogous to the CFL phase in the infinite system. Since the strange-quark density is suppressed near the surface, but the number of strange quarks is equal to that of up and down quarks, it is clear that the strange-quark density must be larger than the up- and down-quark densities in some other part of the system. This is indeed the case, as can be seen in Fig. 3.6. We also see that the excess of the light-quark densities over the strange-quark density is reduced as compared with the case $Z = 10$ discussed above (cf. Fig. 3.4). We will discuss the charge-density distribution in detail in Section 3.3.2. The gaps, shown in Fig. 3.7, are much closer to the gaps in infinite matter (cf. Table 3.1) than in the case $Z = 10$.

For the larger values of the coupling constant we considered ($H\Lambda^2 = 2, 2.25, 2.5$), it is always the CFL-type solution ($Z = 0$) which has the lowest energy. We do not show any figures because in all these cases the results are analogous to those shown in Figs. 3.6 and 3.7 (just the values of the gaps change, they are close to those given in Table 3.1 for infinite matter).

It should be mentioned that the fully paired solutions with $Z = 0$ are very robust as soon as the coupling

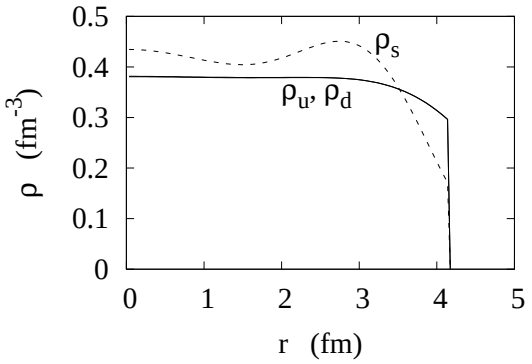

Figure 3.6: Density profiles of the strangelet $A = 108$, $Z = 0$ in the case of $H\Lambda^2 = 1.75$ and $B^{1/4} = 153.97$ MeV.

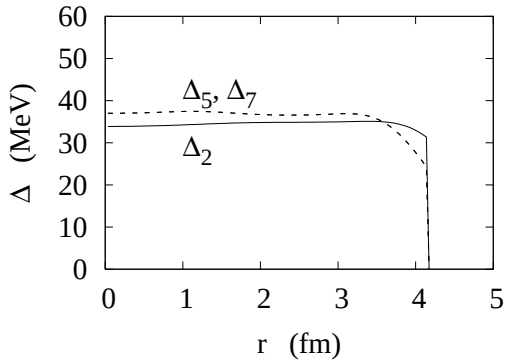

Figure 3.7: Gaps Δ_A as functions of r for the strangelet $A = 108$, $Z = 0$ in the case of $H\Lambda^2 = 1.75$ and $B^{1/4} = 153.97$ MeV.

constant is sufficiently large, i.e., we find this type of solution for arbitrary numbers of quarks[1]. This solution is in contrast to previous findings (see, e.g., Ref. [162]), where it was supposed that the CFL matter should be neutral in the bulk with just a thin positively charged surface layer with an excess of up and down quarks because of the boundary condition. In fact, this idea corresponds roughly to our solution with unpaired up and down quarks near the surface. This solution is, however, very fragile and exists only for certain values of parameters and mass numbers, since it requires the existence of a suitable level of light and strange quarks near the respective Fermi surfaces which can serve as unpaired level.

3.3.2 Charge density distribution

We have seen in Section 3.3.1 that in all cases except the 2SC phase, pairing drastically reduces the total charge Z. Because of surface effects, the local charge density does, however, not vanish, even within the CFL-type solution which has $Z = 0$. Due to the suppression of the strange-quark wave function at the surface, a positively charged surface layer remains with an extension of ~ 1 fm, as has already been pointed out in Ref. [162].

Within the configuration with some unpaired light quarks at the surface, the total charge of the strangelet results from this positive surface charge, the interior of the strangelet has almost zero charge density. The total charge is here reduced compared with a strangelet without pairing, for example the $A = 108$ strangelet has $Z = 10$ within this paired configuration, whereas the corresponding unpaired strangelet has $Z = 24$. A systematic study of the total charge of strangelets in this configuration will not be discussed here since this configuration is rather fragile with respect to the details of the single-particle spectra and thus difficult to realize for many different particle numbers.

Let us therefore concentrate on the CFL-type solution, which exists for arbitrary particle numbers. We consider different mass numbers A from $A = 108$ to $A = 90000$, for one particular value of the coupling constant, $H\Lambda^2 = 2$. In order to reduce the considerable numerical effort, we use for the large strangelets (starting from $A = 15000$) the condition (3.20) with $\mu_e = 0$ (as a consequence, the quark numbers for each flavor and color are not integers) instead of looking for the true energy minimum with respect to β decay. In addition, we do not minimize the energy with respect to the radius, but we simply estimate the volume of the

[1] If the number of quarks is odd, it it impossible to pair all quarks and one or several state(s) should be "blocked" by the unpaired quark(s). At present, we have not included this effect in our calculation, and we restrict ourselves to even quark numbers

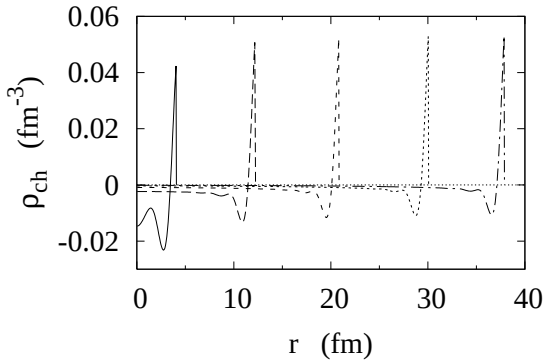

Figure 3.8: Charge density profiles of the fully paired ($H\Lambda^2 = 2$) strangelets A =108, 3000, 15000, 45000, and 90000 (from left to right).

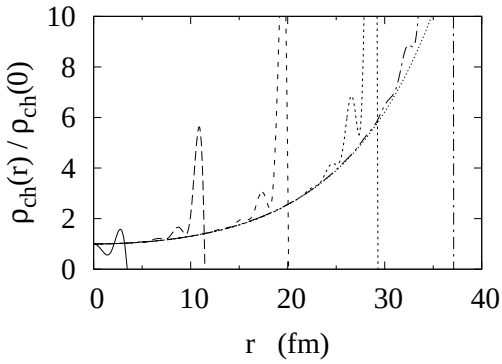

Figure 3.9: Zoom into the part of Fig. 3.8 where the charge density behaves as given by Eq. (3.24). For a better visibility, the charge densities have been divided by their respective values at $r = 0$. The thin dotted curve corresponds to Eq. (3.24) with $\lambda = 7.74$ fm.

bag by dividing the mass number A by the baryon density $\rho_{B\,bulk}$ of infinite matter. These two approximations are very accurate for such large strangelets. Already in the case of $A = 3000$, the quark numbers and the radius are very well reproduced within these approximations: the full minimization results in quark numbers $N_{ur} = N_{dg} = N_{sb} = 1052$, $N_{ug} = N_{dr} = N_{ub} = N_{sr} = N_{db} = N_{sg} = 974$, and a radius $R = 12.23$ fm, while the approximations lead to $N_{ur} = 1051.8$, $N_{dg} = 1051.7$, $N_{sb} = 1051.1$, $N_{ug} = N_{dr} = 973.8$, $N_{ub} = N_{sr} = 974.4$, $N_{db} = N_{sg} = 974.5$, and $R = 12.19$ fm. Our results for the charge densities for A =108, 3000, 15000, 45000, and 90000 are shown in Fig. 3.8.

Since all quarks are paired, we have equal numbers of up, down, and strange quarks such that the total charge of these strangelets is zero. The positive surface charge is mostly compensated by an excess of negative charge concentrated at around 1-3 fm below the surface. We stress that this concentration of negative charge in a thin layer is a consequence of pairing and the effect persists if Coulomb interaction is switched off. In fact, since also the strange quarks are paired, the "missing" strange-quark density at the surface must be compensated by an "overshooting" of the strange-quark density within a distance corresponding to the size of the Cooper pairs, i.e., the coherence length ξ. Due to the strong gap, the coherence length is very small: Using the estimate $\xi \sim 1/(\pi\Delta)$, one finds that it is of the same order as the Fermi wavelength and, strictly speaking, one might therefore question that mean-field results are quantitatively correct [4]. The smallness of ξ explains why the compensation of the negative surface charge is mostly concentrated in such a thin layer at a small distance from the surface.

Below this strongly negatively charged layer, the charge density stays negative but much smaller. Due to Coulomb interaction, which tries to push the charge towards the surface, this negative charge density decreases with increasing distance from the surface, especially for large strangelets. Actually, if Coulomb interaction is switched off, the remaining charge is distributed more or less homogeneously over the whole volume.

The behaviour of the charge density far away from the surface in the presence of Coulomb interaction can easily be interpreted in terms of Debye screening (similar considerations can be found in Ref. [236] for the case of hadron-quark mixed phases): We know that in a uniform medium with Debye screening the Laplace

equation for the Coulomb potential is replaced by

$$\left(\boldsymbol{\nabla}^2 - \frac{1}{\lambda^2}\right) A_0 = 0\,, \tag{3.21}$$

where λ is the screening length, which can be obtained from the limit $\Pi^{00}(q^0 = 0, \mathbf{q} \to 0)$, where $\Pi^{\mu\nu}(q)$ is the polarization tensor in the uniform system. This is equivalent to the expression [236]

$$\frac{1}{\lambda^2} = 4\pi e^2 \sum_{fc} Q_f \frac{\partial \rho_{ch}}{\partial \mu_{fc}}\,. \tag{3.22}$$

Computing numerically this derivative within our model for the case of bulk CFL matter with $B = 156.26$ MeV and $H\Lambda^2 = 2$, we obtain $\lambda = 7.74$ fm.

Taking the Laplacian of Eq. (3.21), we see that the charge density obeys the analogous equation

$$\left(\boldsymbol{\nabla}^2 - \frac{1}{\lambda^2}\right) \rho_{ch} = 0\,. \tag{3.23}$$

In the case of half-infinite matter with a surface at $z = 0$, the solution of this equation shows that the charge density goes to zero as $\rho_{ch} \propto \exp(z/\lambda)$ if one goes away from the surface ($z \to -\infty$). In the case of a sphere, the corresponding solution reads

$$\rho_{ch} \propto \frac{\sinh(r/\lambda)}{r/\lambda}\,. \tag{3.24}$$

Far away from the surface, the charge densities which we obtain are very well described by Eq. (3.24). To show this, we display in Fig. 3.9 the same charge densities as in Fig. 3.8, but divided by their value at $r = 0$. Far away from the surface, all curves follow exactly Eq. (3.24) with the value $\lambda = 7.74$ fm calculated for bulk CFL matter. Near the surface, i.e., at distances which are of the order of a couple of Fermi wavelengths, there are strong deviations from this behavior due to Friedel-type oscillations [102]. This is because Eq. (3.21) is not exact, but it is only valid in a uniform medium and in the long-wavelength limit.

It is interesting to notice that the value of the Debye screeing length we obtain is in reasonable agreement with the photon Debye mass calculated from perturbative QCD, which reads, for the CFL phase, $m_{D,\gamma\gamma}^2 = 1/\lambda^2 = 4\frac{21-8\ln 2}{54} e^2 N_f \mu^2/(6\pi^2)$ [213] ($m_{D,\gamma\gamma}$ denotes the Debye mass without gluon-photon mixing, see below). For typical values of the chemical potential this gives $\lambda \sim 10$ fm.

In principle, in color superconducting phases, the photon can mix with one of the gluons. In the CFL phase, in bulk matter, one linear combination of photon and gluon stays massless. This means that at large distances $d \gg \xi$, the Debye screening for the "rotated" photon [10, 154] does not work, since the Cooper pairs are neutral with respect to the rotated charge $\tilde{Q}$. Within the simple model we use for the moment, there are no gluons, such that the mixing cannot be studied. It could be taken into account, as mentioned at the end of Section 3.2, by including the gluons in the same way as the photon, i.e., on the Hartree level. We expect that if we included the gluons in this way, we would find an even faster decrease of the charge if we go away from the surface, since in addition to the electromagnetic force we would have the color forces, which try to push the color charges to the surface, and in the CFL phase color neutrality goes hand in hand with electrical neutrality. Therefore, this is not in contradiction with the fact that the rotated photon is massless, but it is just a consequence of the fact that the combination of photon and gluon which is orthogonal to the rotated photon is massive (in fact, it is even heavier than the other gluons [154]). This means that in a large object, like a strange star, all the negative charge will be concentrated within a layer of a thickness of at most a few tens of fm below the surface. However, before drawing any firm conclusion, one should study this problem in more detail. This will be left for future work.

Table 3.3: Fitted liquid-drop parameters for the CFL-type neutral strangelets ($Z = 0$). The surface tension σ corresponding to the fitted value of a_S is also given.

$B^{1/4}$ (MeV)	$H\Lambda^2$ (MeV)	a_S (MeV)	a_C (MeV)	σ (MeV/fm^2)
156.26	2	107	289	11.9
159.46	2.25	109	297	12.8
163.46	2.5	112	306	13.9

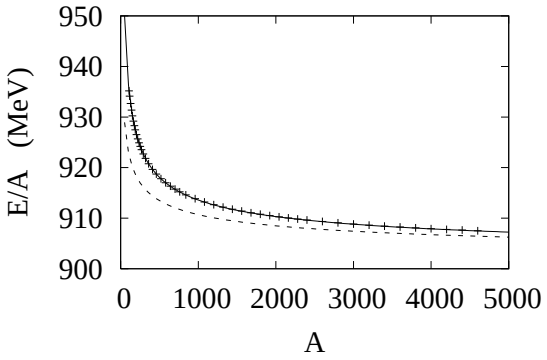

Figure 3.10: Energy per baryon as a function of baryon number for $H\Lambda^2 = 2$ and $B^{1/4} = 156.26$ MeV. The exact results are indicated by the crosses, the fitted liquid-drop formula by the solid line. The dashed line corresponds to the liquid-drop formula without the curvature term.

3.3.3 Liquid-drop type expansion

The advantage of the present approach is that finite size effects are correctly implemented. For large numbers of particles, this becomes, however, rather cumbersome and asymptotic expansions such as a liquid-drop type approach can be very useful. We will discuss here the determination of the parameters, such as the surface tension, of a liquid-drop type formula for the energy per baryon as a function of the baryon number A, including a surface and a curvature term,

$$\frac{E}{A} = \left(\frac{E}{A}\right)_{bulk} + \frac{a_S}{A^{1/3}} + \frac{a_C}{A^{2/3}}\,, \tag{3.25}$$

from our results. As in Section 3.3.2, we will restrict our discussion to the CFL-type solutions with $Z = 0$, such that we do not need to include a Coulomb term $\propto Z/A^{1/3}$.

As explained after Eq. (3.20), $(E/A)_{bulk}$ should be the energy per baryon of infinite matter with $\mu_e = 0$ rather than that of β stable infinite matter. However, since we consider only the CFL-type solution, this distinction is irrelevant. Hence, for our chosen parameter sets, we have $(E/A)_{bulk} = 900$ MeV. Since for the neutral strangelets the Coulomb interaction has only a negligible effect on the total energies (for example, in the case of the strangelets considered in Section 3.3.2, the Coulomb interaction changes the total energy per baryon by less than 5 keV) it will be neglected here in order to reduce the numerical effort. The result of the fitted coefficients a_S and a_C for the different parameter sets are listed in Table 3.3. As an example, in order to show the accuracy of the asymptotic expansion, we display in Fig. 3.10 some results for the energy per baryon together with the liquid-drop formula, Eq. (3.25). The dashed line corresponds to the liquid-drop formula without the curvature term ($a_C = 0$). From this figure it becomes clear that the liquid-drop formula with curvature term works extremely well, much better than in the case without pairing [114]. The reason is that shell effects are completely washed out because, contrary to the situation in ordinary nuclei, the pairing gap is much larger than the spacing between neighboring shells. Another interesting observation is that the

curvature term is very important, even for rather large mass numbers A.

The coefficient a_S is closely related to a very interesting quantity, namely the surface tension. As explained in Ref. [181], the surface tension is obtained as

$$\sigma = \frac{E_S}{4\pi R_0^2}\,, \tag{3.26}$$

where

$$E_S = E - A\left(\frac{E}{A}\right)_{bulk} \tag{3.27}$$

is the energy excess due to the surface and R_0 is an effective radius defined by

$$A = \rho_{B\,bulk}\,\frac{4\pi R_0^3}{3}\,, \tag{3.28}$$

which is actually very close to R for not too small strangelets. On the one hand, using the liquid-drop formula (3.25) for E in Eq. (3.26), one would obtain a surface tension which depends on A because of the curvature term. Therefore it is clear that one has to use Eq. (3.26) in the limit $A \to \infty$, where the curvature term vanishes, i.e.,

$$\sigma = \frac{a_S \rho_{B\,bulk}^{2/3}}{(36\pi)^{1/3}}\,. \tag{3.29}$$

The corresponding numbers are given in the last column of Table 3.3. They are of the same order of magnitude as the estimate $\sigma \sim (70\text{ MeV})^3 = 8.8\,\text{MeV/fm}^2$ for SQM without color superconductivity [103]. On the other hand, the fact that the curvature term is very strong implies that the knowledge of the surface tension alone might not be sufficient in order to determine, e.g., the possibility of mixed phases, the size of droplets, etc.

Before we conclude, let us comment on the physical meaning of the surface tension we obtain. In the MIT bag model, it is supposed that the energy needed to create a bag with volume V is simply given by BV. In principle one could imagine that there is an explicit dependence of the bag energy on, e.g., the surface or the curvature of the bag boundary. In Ref. [103], this contribution to the surface tension was called "intrinsic surface tension", σ_I, and it was argued that it should be small. What we calculate here is the "dynamical surface tension", σ_D, which has its origin in the change of the level density of the quarks inside the bag as a function of the bag geometry.

3.4 Summary

In this paper we have investigated finite lumps of color superconducting SQM. To that end we have treated the MIT bag model, supplemented with a pairing interaction, in the framework of HFB theory. This allows us to correctly include finite size effects for pairing, too. The calculation is numerically rather involved, since in addition to solving self-consistently the HFB equations, we have to determine the bag radius and the fractions of the different quark species by minimizing the total energy of the system.

As expected from previous MIT bag-model studies, we find a suppression of the strange-quark densities at the surface, resulting in a positive surface charge. Our main result is that, in spite of this surface charge, the total charge of the CFL type solution is zero due to pairing, as in bulk matter. Most of the positive surface charge is compensated in a negatively charged layer situated at about 1-3 fm below the surface. The origin of this concentration of the negative charge is pairing: Since all quarks are paired, the positive surface charge must be compensated on a length scale corresponding to the coherence length. The remaining negative charge, which is necessary to compensate all of the positive surface charge, is situated below this layer. With increasing

distance from the surface, the charge density decreases on a length scale of ~ 8 fm, corresponding to the Debye screening length. This number will probably be strongly decreased if the gluons are included in a perturbative way similar to the photon. In any case, in the biggest part of a large object, such as a strange star, one finds vanishing charge density if one goes more than a few tens of fm away from the surface. It remains to be investigated in which way our results change the traditional picture of the surface of a strange star and the detectability of smaller strangelets in current experiments such as AMS-02 or LSSS [163].

We have also compared our results for the energy per baryon of finite strangelets with a liquid-drop like formula. We obtain a surface tension of the order of 12-14 MeV, in reasonable agreement with previous studies where color superconductivity was not considered, and a strong curvature term which is crucial to reproduce the correct energies up to baryon numbers of several thousands. An interesting result is that, in the presence of color superconductivity, the liquid-drop formula describes very accurately the total energies even for $A \lesssim 100$, at least for strangelets with even baryon number. The reason is that, since the gap Δ is much larger than the spacing between the energy levels, shell effects are strongly suppressed.

Acknowledgments

We thank Michael Buballa for useful discussions and for the critical reading of the first version of this manuscript.

Appendix

3.A Spinors in a spherical cavity

In this appendix we recall basic properties of free Dirac spinors in a spherical cavity (see, e.g., Ref. [44]). They can be written as

$$\psi_{fj\kappa mn}(\mathbf{r}) = \begin{pmatrix} g_{fj\kappa n}(r)\mathcal{Y}^m_{jl}(\Omega) \\ i\, f_{fj\kappa n}(r)\mathcal{Y}^m_{jl'}(\Omega) \end{pmatrix} , \tag{3.30}$$

where $\mathcal{Y}$ are spinor spherical harmonics [258]. We have the following relations between the angular momentum quantum numbers

$$\begin{aligned} \kappa = j + \frac{1}{2} \quad &\rightarrow \quad l = j + \frac{1}{2}, \quad l' = j - \frac{1}{2} \\ \kappa = -(j + \frac{1}{2}) \quad &\rightarrow \quad l = j - \frac{1}{2}, \quad l' = j + \frac{1}{2} . \end{aligned} \tag{3.31}$$

For the solutions of the free Dirac equation, the functions f and g are given as follows in terms of the spherical Bessel functions ($\xi_{fj\kappa n} = \sqrt{p^2_{fj\kappa n} + m_f^2}$)

$$\begin{aligned} g_{fj\kappa n}(r) =& C_{fj\kappa n}\, j_l(p_{fj\kappa n} r) \\ f_{fj\kappa n}(r) =& C_{fj\kappa n} \mathrm{sgn}(\kappa n) \sqrt{\frac{\xi_{fj\kappa n} - m_f}{\xi_{fj\kappa n} + m_f}}\, j_{l'}(p_{fj\kappa n} r) , \end{aligned} \tag{3.32}$$

where the $C_{fj\kappa n}$ are normalisation coefficients which can be determined from the normalization

$$\int_0^R dr r^2 \int d\Omega \psi^\dagger(\mathbf{r})\psi(\mathbf{r}) = 1 . \tag{3.33}$$

The momenta $p_{fj\kappa n}$ are obtained from the boundary condition. The boundary condition of the MIT bag model, Eq. (3.1), translates into the following equation

$$f_{fj\kappa n}(R) = -g_{fj\kappa n}(R) , \tag{3.34}$$

or, explicitly,

$$j_l(p_{fj\kappa n}R) = \mathrm{sgn}(\kappa n)\sqrt{\frac{\xi_{fj\kappa n}-m_f}{\xi_{fj\kappa n}+m_f}}\, j_{l'}(p_{fj\kappa n}R)\,, \tag{3.35}$$

where we number by $n > 0$ the positive-energy (particle) states and by $n < 0$ the negative-energy (antiparticle) states. In practice, we will keep only the states with positive eigenvalues and neglect the antiparticle contributions. The latter can approximately be absorbed into a redefintion of the coupling constant.

3.B HFB equations

In this appendix we will give some more details about the HFB equations. Their derivation is analogous to the derivation of the Dirac-Hartree-Bogoliubov equations in finite nuclei, which is given in Ref. [69].

The HFB equations are derived from the Lagrangian by minimizing the energy in the mean field approximation, i.e., linearizing the interaction under the assumption of nonzero expectation values for the condensates $s_{AA'}(x)$, Eq. (3.7). Due to the inhomogeneities of a finite system, the Green's functions become nondiagonal in momentum. In the stationary case, it is convenient to work in $\mathbf{r}$ space for the spatial coordinates but to perform the Fourier transformation for the time variable. Then the Green's functions,

$$S(x,y) = -i\langle T(\Psi(x)\bar{\Psi}(y))\rangle\,, \tag{3.36}$$

with

$$\Psi(x) = \begin{pmatrix}\psi(x)\\ \psi_T(x)\end{pmatrix} \tag{3.37}$$

take the following general form in Nambu-Gorkov space:

$$\begin{aligned} S(\mathbf{r},\mathbf{r}';\omega) &= \begin{pmatrix} G(\mathbf{r},\mathbf{r}';\omega) & F(\mathbf{r},\mathbf{r}';\omega)\\ \tilde{F}(\mathbf{r},\mathbf{r}';\omega) & \tilde{G}(\mathbf{r},\mathbf{r}';\omega)\end{pmatrix}\\ &= \sum_{\alpha(\epsilon_\alpha>0)}\begin{pmatrix}U_\alpha(\mathbf{r})\\ V_\alpha(\mathbf{r})\end{pmatrix}\frac{1}{\omega-\epsilon_\alpha+i\eta}(\bar{U}_\alpha(\mathbf{r}'),\bar{V}_\alpha(\mathbf{r}')) + \sum_{\beta(\epsilon_\beta<0)}\begin{pmatrix}U_\beta(\mathbf{r})\\ V_\beta(\mathbf{r})\end{pmatrix}\frac{1}{\omega+\epsilon_\beta-i\eta}(\bar{U}_\beta(\mathbf{r}'),\bar{V}_\beta(\mathbf{r}'))\,, \end{aligned} \tag{3.38}$$

where $G, \tilde{G}$ and $F, \tilde{F}$ are normal and anomalous Green's functions, respectively. The spinors $U_{\alpha,\beta}$ and $V_{\alpha,\beta}$ correspond to the particle- and hole-like components, respectively.

The energy in mean-field approximation can now be written as [69]

$$E_q = \int d^3x\left(i\,\mathrm{Tr}[(i\boldsymbol{\gamma}\cdot\boldsymbol{\nabla}-m)G(x,x^+)] - \frac{i}{2}\int d^4y\,\mathrm{Tr}[\Sigma(x,y)G(y,x^+)-\Delta(x,y)\tilde{F}(y,x^+)]\right)\,, \tag{3.39}$$

where the derivative in the first term acts only on x and not on x^+, and x^+ means the four vector $(x^0+t,\mathbf{x})$ in the limit $t\to 0^+$. In our case, the normal and anomalous self-energies Σ and Δ are local and time-independent: $\Sigma(x,y) = eQA_0(\mathbf{x})\gamma^0\delta(x-y)$ and $\Delta(x,y) = \Delta(\mathbf{x})\delta(x-y)$, and Eq. (3.39) can be reduced to Eq. (3.17).

As mentioned in Section 3.2.2, the expectation values (like condensates, densities, etc.) which are needed for calculating self-consistently the self-energy Σ and the pairing field Δ can be expressed in terms of the U and V functions. To that end, it is sufficient to express them in terms of the Green's functions, e.g.

$$s_{AA'} = -\langle\bar{\psi}_T(x)\tau_A\lambda_{A'}\psi(x)\rangle = i\,\mathrm{Tr}\,F(x,x^+)\tau_A\lambda_A\,, \tag{3.40}$$

which leads to Eq. (3.9).

By minimizing the total energy with respect to the U and V functions, one obtains the HFB equations, [see Eq. (3.5)]:

$$\mathcal{H}W_\alpha = \epsilon_\alpha W_\alpha \,, \tag{3.41}$$

with $W_\alpha = (U_\alpha, V_\alpha)^T$ and $\mathcal{H}$ being the matrix on the left-hand side of Eq. (3.5).

For homogeneous infinite systems the matrix elements of $\mathcal{H}$ are diagonal in momentum space and solutions to the HFB equations are known for many cases. For finite systems, in general, these equations are solved numerically by diagonalizing the matrix $\mathcal{H}$ in some conveniently chosen basis. Here, we are working in the basis which diagonalizes the Dirac hamiltonian (i.e., h_{fc} without the Coulomb potential), see Appendix 3.A, and the eigenvectors $U_\alpha(\mathbf{r})$ and $V_\alpha(\mathbf{r})$ are developped within this basis.

The matrix elements of the pairing fields $\Delta_A(r)$ and of the Coulomb field $A_0(r)$ are computed in the usual way. For illustration, we give here the explicit expression for the matrix elements of $\Delta_2(r)$, which connects up and down quarks, in the basis described in Appendix 3.A:

$$\begin{aligned}(\Delta_2)_{j\kappa nn'} &= \int_{r<R} d^3r\, \psi^\dagger_{uj\kappa mn}(\mathbf{r})\Delta_2(r)\psi_{dj\kappa mn'}(\mathbf{r}) \\ &= \int_0^R dr\, r^2 \Delta_2(r)(g_{uj\kappa n}(r)g_{dj\kappa n'}(r) + f_{uj\kappa n}(r)f_{dj\kappa n'}(r))\,. \end{aligned} \tag{3.42}$$

Note that, due to spherical symmetry, all matrices are diagonal in j and κ and proportional to the unit matrix with respect to m.

In spite of the spherical symmetry, the matrix to be diagonalized is still huge, limiting the baryon number which can be calculated with reasonable computational effort. It is therefore important to reduce the size of the actual matrix to be diagonalized. By means of an orthogonal transformation

$$\tilde{\mathcal{H}} = S\mathcal{H}S^T, \quad \tilde{W} = SW, \quad SS^T = 1 \tag{3.43}$$

in color, flavor, and Nambu-Gorkov space, the matrix can actually be block-diagonalized (see, e.g., Ref. [9]) containing seven blocks. Six of them, $\tilde{\mathcal{H}}_{B,\ldots G}$, are 2×2 matrices in Nambu-Gorkov space, describing mutual pairing of two particles, such as, e.g., red down quarks (dr) with green up quarks (ug):

$$\tilde{\mathcal{H}}_B = \begin{pmatrix} h_{ug} & \Delta_2 \\ \Delta_2 & -h_{dr} \end{pmatrix}, \tag{3.44}$$

where h_{fc} is the single particle Hamiltonian for flavor f and color c. The second and third 2×2 blocks are

$$\tilde{\mathcal{H}}_C = \begin{pmatrix} h_{ub} & \Delta_5 \\ \Delta_5 & -h_{sr} \end{pmatrix}, \quad \tilde{\mathcal{H}}_D = \begin{pmatrix} h_{db} & \Delta_7 \\ \Delta_7 & -h_{sg} \end{pmatrix}. \tag{3.45}$$

Since we have in addition the pairwise relations $\tilde{\mathcal{H}}_{E,F,G} = -\tilde{\mathcal{H}}_{B,C,D}$, only three of the six 2×2 blocks have to be diagonalized in practice. The seventh block, $\tilde{\mathcal{H}}_A$, is 6×6 in Nambu-Gorkov space and describes pairing between red up, green down and blue strange quarks

$$\tilde{\mathcal{H}}_A = \begin{pmatrix} h_{ur} & 0 & 0 & 0 & \Delta_2 & \Delta_5 \\ 0 & h_{dg} & 0 & \Delta_2 & 0 & \Delta_7 \\ 0 & 0 & h_{sb} & \Delta_5 & \Delta_7 & 0 \\ 0 & \Delta_2 & \Delta_5 & -h_{ur} & 0 & 0 \\ \Delta_2 & 0 & \Delta_7 & 0 & -h_{dg} & 0 \\ \Delta_5 & \Delta_7 & 0 & 0 & 0 & -h_{sb} \end{pmatrix}. \tag{3.46}$$

3.C Cutoff for the gap equation

As mentioned in Section 3.2.2, the divergent gap equation is regularized with the help of a smooth cutoff function

$$f(p/\Lambda) = \frac{1}{1 + c_1 \exp(c_2 a(p/\Lambda - 1))}\,, \tag{3.47}$$

where $c_1 = \sqrt{2} - 1$, $c_2 = 1/(4 - 2\sqrt{2})$, and $a = 22.58$ have been chosen such that $f^2(p/\Lambda)$ approximates the cutoff function $g(p/\Lambda)$ used in Ref. [270], but our function has the advantage to fall off more rapidly at very high momenta, which allows us to truncate the basis at a lower energy.

This function is used as a form factor multiplying each of the four legs of the four-point vertex. In practice, this means that the form factor is used in two places: First, when calculating $s_{AA}(r)$, and second, when calculating the matrix elements of $\Delta_A(r)$ in the basis of the spinors defined in Appendix 3.A. It should be noted that the diagonalization of the HFB matrix does not directly provide us with the eigenfunctions $U_\alpha(\mathbf{r})$ and $V_\alpha(\mathbf{r})$, but with their respective expansion coefficients in the basis of the spinors defined in Appendix 3.A. When calculating $s_{AA}(r)$ according to Eq. (3.9), the coefficients have to be multiplied with the corresponding basis functions, and in this step the factor $f(p_{fj\kappa n}/\Lambda)$ is attached to each basis function. Second, when calculating the matrix elements of the gap Δ_A, we again attach a factor $f(p_{fj\kappa n}/\Lambda)$ to each basis function.

4 BEC-BCS crossover and the liquid-gas phase transition in hot and dense nuclear matter

Meng Jin, Michael Urban, and Peter Schuck, Phys. Rev. C 82, 024911 (2010)

The effect of nucleon-nucleon correlations in symmetric nuclear matter at finite temperature is studied beyond BCS theory. Starting from a Hartree-Fock description of nuclear matter with the Gogny effective interaction, we add correlations corresponding to the formation of preformed pairs and scattering states above the superfluid critical temperature within the in-medium T-matrix approach, which is analogous to the Nozières-Schmitt-Rink theory. We calculate the critical temperature for a BEC superfluid of deuterons, of a BCS superfluid of nucleons, and in the crossover between these limits. The effect of the correlations on thermodynamic properties (equation of state, energy, entropy) and the liquid-gas phase transition is discussed. Our results show that nucleon-nucleon correlations beyond BCS play an important role for the properties of nuclear matter, especially in the low-density region.

4.1 Introduction

Pairing and nucleon-nucleon correlations are important properties of interacting nuclear systems. For example, in the weak-coupling limit, i.e., at high density, the nucleons form Cooper pairs, and below a certain critical temperature T_c the system is in a superfluid phase as described by the Bardeen-Cooper-Schrieffer (BCS) theory. In the strong-coupling limit, i.e., at low density, neutrons and protons form deuteron bound states which will condense if the temperature is below the critical temperature for the corresponding Bose-Einstein condensation (BEC). It was theoretically predicted [174] and recently confirmed by experiments with ultracold atomic Fermi gases [196, 278] that there is a smooth crossover between the BCS and BEC limits. Qualitatively, especially at zero temperature, these features can be studied within the BCS (mean field) approximation [29]. Quantitatively, however, the critical temperature obtained in this way is too high because the BCS theory does not include the existence of non-condensed pairs at finite temperature. In order to go beyond mean field, one has to consider pair correlations already above the critical temperature, as in the Nozières-Schmitt-Rink (NSR) theory [174]. Especially in the low density region, where the coupling between nucleons is strong, such correlations modify the mean-field results to a large extent.

At present, there are several groups who have studied nuclear matter within the NSR approach. Pioneering work has been done by the Rostock group [212, 231]. There are also extensions where the correlations are considered in a more self-consistent way, like in the self-consistent Green's function method [202, 226]. A generalization to temperatures below the superfluid transition temperature was discussed by Bożek [54]. In the case of ultracold Fermi gases, where the results can be compared with very precise measurements, theories for the BEC-BCS crossover based on the NSR approach [184] have been very successful [188].

It is well known that there exists a liquid-gas phase transition in nuclear matter. Experimental information can be obtained from multifragmentation (see, e.g., [48, 84, 97, 98, 158, 159]). The critical temperature deduced from these experiments depends on the mass of the nuclei and can be as low as 6.7 MeV [97, 98] in the case of small systems. For infinite nuclear matter, theoretical predictions give much higher values for the critical temperature between 14 and 18 MeV [48, 84] (see Ref. [246] for a recent theoretical study). Below that temperature, nuclear matter is unstable in a certain range of low densities. Within mean-field theory, we know that the BCS-BEC crossover is completely covered by the instability region of the liquid-gas phase transition. Nevertheless, the investigation of low-density nuclear matter is of interest for applications where regions of low density appear in the framework of the local-density approximation. Contrary to the nuclear matter case, the whole crossover can be studied in the case of ultracold atomic Fermi gases [196, 278], because the pair correlations stabilize the gas [174] such that the system does not collapse into its solid ground state but it

remains in its metastable gas state. By analogy, one expects that pair correlations will stabilize low-density nuclear matter and thus reduce the liquid-gas coexistence region. One of our subjects of investigation will be how strong this effect of nucleon-nucleon correlations on the liquid gas phase transition is quantitatively.

Furthermore, in this paper we will calculate the equation of state of hot and dense symmetric nuclear matter, taking into account the contribution of the mean field together with the nucleon-nucleon correlations. For the mean field we will use the Gogny interaction because it is known to give a good description of the single-particle and thermodynamic properties of nuclear matter, including saturation at the right density, the liquid-gas phase transition, etc. For the part beyond the mean field, we use the T-matrix (or ladder approximation) which contains the information on two-particle correlations. This also allows us to extract the critical temperature for pair condensation smoothly interpolating between the BEC and BCS regimes.

The paper is organized as follows. In Sec. 4.2, we will give a summary of the formalism. The numerical results are provided in Sec. 4.3. The last section is devoted to the summary and discussions.

4.2 Formalism

Before explicitly including two-particle correlations, we calculate the single-particle Green's function within the Hartree-Fock (HF) approximation. In order to get a reasonable description of the single-particle energies, we use the density-dependent D1 Gogny effective interaction to describe the mean field. This force gives nuclear binding at the right saturation point and many other properties of nuclear matter and of finite nuclei [91]. It has the form

$$V(r) = \sum_{m=1}^{2} (W_m + B_m P_\sigma - H_m P_\tau - M_m P_\sigma P_\tau) e^{-r^2/\mu_m^2} + t_0(1 + x_0 P_\sigma)\rho^\alpha \delta(r), \tag{4.1}$$

where the P_σ and P_τ are, respectively, the spin and isospin exchange operators. The spin-orbit coupling term is neglected here, since we consider only the properties of infinite nuclear matter. For the parameters we use the values given in Ref. [91] [1]. For details of the HF description of nuclear matter at finite temperature with the Gogny force, see Refs. [130, 228, 259]. The HF mean field Σ_{HF} contains the direct, the exchange, and the rearrangement contributions. Because of the finite range of the Gogny force, the exchange contribution is momentum dependent, and the single-particle Green's function takes the form

$$G_{HF}(p, \omega) = \frac{1}{\omega - \xi_p + i0}\,, \tag{4.2}$$

where ξ_p is the quasiparticle energy defined by

$$\xi_p = \frac{p^2}{2m} - \Sigma_{HF}(p) - \mu\,, \tag{4.3}$$

where μ denotes the chemical potential. In order to facilitate the numerical calculation of the correlation effects, we use the effective-mass approximation for the Gogny mean field, i.e., we write [130]

$$\xi_p = \frac{p^2}{2m^*} - \mu^*\,. \tag{4.4}$$

[1] We prefer the D1 parametrization to the D1S one [41] because it allows us to compare our HF results with those of Ref. [259] and it gives a better compressibility of symmetric nuclear matter [165]. Anyway, since the effective mass m^* in D1 and D1S is almost the same, the results do not change qualitatively if we use D1S instead of D1.

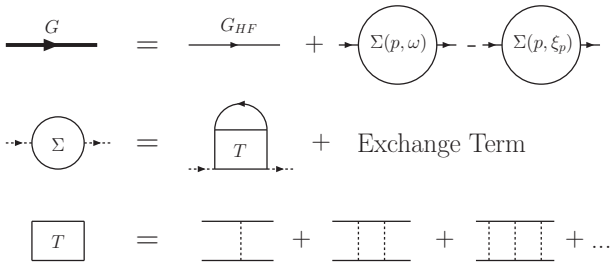

Figure 4.1: The Feynman diagrams for the Green's function (top), for the self-energy (middle), and for the T-matrix in ladder approximation (bottom).

There are different ways to define the effective nucleon mass m^*. In principle, m^* is momentum dependent [259]. Here we use the effective mass defined by expanding Eq. (4.3) around $p = 0$ (we checked that for the final results it makes almost no difference if we expand around zero or around the Fermi momentum), i.e.,

$$\frac{1}{m^*} = \frac{1}{m} + 2\,\frac{d\Sigma_{HF}(p)}{dp^2}\bigg|_{p=0}\,, \tag{4.5}$$

$$\mu^* = \mu - \Sigma_{HF}(0)\,. \tag{4.6}$$

However, the effective-mass approximation will only be used for the calculation of the correlation effects, while the mean-field contributions will be computed with the full momentum dependence of $\Sigma_{HF}(p)$.

In principle, we are looking for the full single-particle Green's function G including correlations. The Dyson equation can be written as

$$G^{-1}(p,\omega) = G^{-1}_{HF}(p,\omega) - \tilde{\Sigma}(p,\omega)\,, \tag{4.7}$$

where $\tilde{\Sigma}$ is the correlation contribution to the single-particle self-energy. Since the Gogny force is a density-dependent effective interaction, which is designed to give good results already at the HF level, we suppose that the Gogny mean field accounts already for most of the correlation effects. We therefore demand that the correlations do not shift the quasiparticle energies ξ_p, i.e., $\tilde{\Sigma}(p,\xi_p) = 0$, and that the role of the correlations is just to reduce the strength of the quasiparticle pole and to distribute the remaining strength in the continuum of the spectral function. Hence, we define $\tilde{\Sigma}$ to be the self-energy subtracted at ξ_p:

$$\tilde{\Sigma}(p,\omega) = \Sigma(p,\omega) - \mathrm{Re}\,\Sigma(p,\xi_p)\,. \tag{4.8}$$

In order to describe pair correlations, we calculate the self-energy Σ within the T-matrix or ladder approximation, as shown in the lower part of Fig. 4.1. This is a frequently used lowest-order correction [174, 184, 212, 231], implying, however, that vertex corrections as well as screening of the interaction due to the medium effects are neglected.

Since our aim is not a completely self-consistent description of the spectral function as in the self-consistent Green's function method [202, 226], we make the assumption that the correlations can be treated as a small correction to the Gogny HF self-energy. This allows us to use the HF Green's function G_{HF} in the calculation of the T matrix and of the self-energy Σ. Then, for consistency, one should also keep only the first-order term of Eq. (4.7), i.e.,

$$G(p,\omega) = G_{HF}(p,\omega) + G^2_{HF}(p,\omega)\tilde{\Sigma}(p,\omega)\,. \tag{4.9}$$

A diagrammatic representation is given in the upper part of Fig. 4.1

That the self-energy in T-matrix approximation should only be treated in first-order perturbation theory may also have a more formal reason. The T-matrix approximation corresponds to particle-particle random-phase approximation (pp-RPA) [201]. It can be shown that the ground-state energy calculated from the single-particle Green's function with self-energy in first order and in T-matrix approximation yields exactly the pp-RPA ground-state energy [51, 52]. At least this holds true for the self-energy without subtraction procedure. Therefore our formalism is closely related to that of Ref. [136], where the pp-RPA formalism is used, except that we apply the subtraction prescription while the authors of Ref. [136] are obliged to reduce the correlation contribution by introducing a cutoff and to change the parameters of the Gogny force in order maintain the right saturation point of nuclear matter.

Note that our approximations are analogous to NSR theory [174], except that in NSR theory free Green's functions instead of HF ones are used and consequently no subtraction is made in the self-energy. In the case of nuclear matter, however, we cannot expect to obtain a good description of the full self-energy from such a simple model for the T matrix. This is why we use the Gogny mean field and the subtraction method described above, while the subtracted self-energy serves only to provide the energy dependence corresponding to the pair correlations in the channels we want to study.

In order to get a simple expression for the T matrix, we use the separable Yamaguchi potential [269],

$$V_\alpha(k,k') = -\lambda_\alpha v(k) v(k') \tag{4.10}$$

where k and k' are the incoming and outgoing relative momenta in the center-of-mass frame, and the form factor is given by

$$v(k) = \frac{1}{k^2+\beta^2}. \tag{4.11}$$

As in Ref. [231], we consider only S-wave scattering ($\alpha = {}^1S_0, {}^3S_1$) and neglect the coupling between the ${}^3S_1$ and ${}^3D_1$ channels (which comes from the tensor force). With the parameters $\beta = 1.4488$ fm^{-1}, $\lambda_{{}^1S_0} = 2994$ MeV fm^{-1} and $\lambda_{{}^3S_1} = 4264$ MeV fm^{-1} [231], the low-energy nucleon-nucleon phase shifts and the vacuum binding energy of the deuteron ($E_b^0 = -2.225$ MeV) are very well reproduced, see results for $n = 0$ in Figs. 4.2 and 4.3, so that it is unlikely that the coupling between the ${}^3D_1$ and ${}^3S_1$ channels would strongly modify our results. With the separable interaction, the resummation of the ladder diagrams shown in the lower part of Fig. 4.1 reduces to a simple geometrical series, and the T matrix can be written as

$$T_\alpha(k,k',K,\omega) = \frac{V_\alpha(k,k')}{1 - J_\alpha(K,\omega)}\,, \tag{4.12}$$

where $\mathbf{k}$ and $\mathbf{k}'$ are the incoming and outgoing momenta in the center of mass frame, $\mathbf{K}$ is the total momentum, and

$$J_\alpha(K,\omega) = \int \frac{d^3k}{(2\pi)^3} V_\alpha(k,k)\, \frac{1 - f(\xi_{\mathbf{K}/2+\mathbf{k}}) - f(\xi_{\mathbf{K}/2-\mathbf{k}})}{\omega - \xi_{\mathbf{K}/2+\mathbf{k}} - \xi_{\mathbf{K}/2-\mathbf{k}} + i0}\,. \tag{4.13}$$

The function $f(\xi) = 1/(e^{\xi/T}+1)$ is the Fermi function, T being the temperature. Within the effective mass approximation, Eq. (4.4), the denominator of Eq. (4.13) does not depend on the angle between $\mathbf{k}$ and $\mathbf{K}$, and the angular integral can be done analytically. The main contribution to the integral over the relative momentum comes from low momenta due to the form factor of the Yamaguchi interaction ($k \lesssim \beta$).

In the ${}^3S_1$ channel, it can happen that $J_{{}^3S_1}(K,\omega_b) = 1$ at some energy ω_b below the threshold energy

$$\omega_0(K) = \frac{K^2}{4m^*} - 2\mu^*\,. \tag{4.14}$$

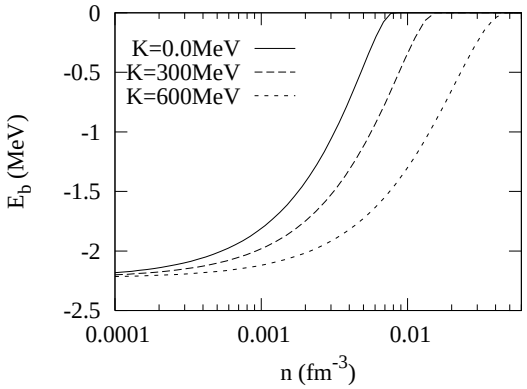

Figure 4.2: The deuteron binding energy in nuclear matter from the Yamaguchi potential and including the effect of the Gogny mean field, as a function of the density for different values of the deuteron momentum K. The temperature is $T = 10$ MeV.

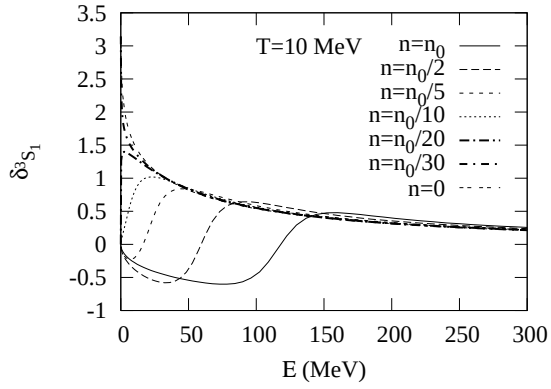

Figure 4.3: In-medium scattering phase shift in the ${}^3S_1$ channel for $K = 0$ as a function of $E = k^2/m^*$ for different densities and $T = 10$ MeV.

This means that there is a bound state (the deuteron) with binding energy $E_b(K) = \omega_b(K) - \omega_0(K)$. As an example, the deuteron binding energies for different values of the deuteron momentum K are displayed in Fig. 4.2. As one can see, the binding gets weaker with increasing density, and eventually the deuteron gets unbound at the so-called Mott density. Since the Pauli blocking effect gets weaker with higher deuteron momentum K, there exists for any density a Mott momentum K_{Mott} above which the deuteron stays bound.

The in-medium nucleon-nucleon phase shifts δ_α can easily be obtained from $1/(1 - J_\alpha) = e^{i\delta_\alpha}/|1 - J_\alpha|$. As an example, we show in Fig. 4.3 the phase shift in the ${}^3S_1$ channel for $K = 0$ at different densities, as function of the energy $E = \omega + 2\mu^* = k^2/m^*$. We see that at higher densities, e.g., at $n \geq n_0/5$ ($n_0 = 0.17$ fm^{-3} being the saturation density of nuclear matter), the phase shift is negative in the low-energy region and then becomes positive as the energy increases. The energy where the phase shift crosses zero is $\omega = 0$, i.e., $E = 2\mu^*$. At lower densities, when μ^* is negative, the phase shift is positive at low energy. At some very low density, the value of the phase shift at $E = 0$ changes from 0 to π. This happens precisely at the density below which the deuteron is bound.

In terms of the T matrix, we can write the self-energy Σ depicted in the middle of Fig. 4.1 within the Matsubara formalism as

$$\Sigma(p, i\omega_n) = \tfrac{3}{2} \sum_{\alpha = {}^3S_1, {}^1S_0} T \sum_{n'} \int \frac{d^3p'}{(2\pi)^3} G_{HF}(p', i\omega_{n'}) T_\alpha(k, k, K, i\omega_n + i\omega_{n'}) \,, \tag{4.15}$$

where ω_n and $\omega_{n'}$ are Fermionic Matsubara frequencies [$\omega_n = (2n+1)\pi T$], $\mathbf{k} = (\mathbf{p} - \mathbf{p}')/2$, and $\mathbf{K} = \mathbf{p} + \mathbf{p}'$. The factor $3/2$ is the product of a factor $1/4$ from the averaging over spin and isospin in symmetric nuclear matter, of a factor 2 from the sum of direct and exchange contributions, and of a factor $(2S + 1)(2T + 1) = 3$ for $\alpha =^3 S_1$ and ${}^1S_0$ from the sum over spin and isospin in the loop. Using standard techniques [106], the self-energy can be analytically continued to real energies, which is necessary for the calculation of the subtraction term $\Sigma(p, \xi_p)$ in Eq. (4.8).

Inserting the self-energy into Eq. (4.9), we calculate the density from

$$n(T,\mu) = -4T\sum_n \int \frac{d^3k}{(2\pi)^3} G(k, i\omega_n)\,. \tag{4.16}$$

The factor 4 comes from the sum over spin and isospin. It is clear that the first term of Eq. (4.9) just gives the Hartree-Fock density, and the second term gives the correction beyond the mean field approximation. After a lengthy derivation (see Appendix), one finds the following formulas initially given in Refs. [212, 231]:

$$n = n_{HF} + n_{corr} = n_{HF} + n_{bound} + n_{scatt}\,. \tag{4.17}$$

The bound-state contribution reads

$$n_{bound} = 6\int_{K>K_{Mott}} \frac{d^3K}{(2\pi)^3} g(\omega_b(K))\,, \tag{4.18}$$

where $g(\omega) = 1/(e^{\omega/T}-1)$ is the Bose function. This term gives the nucleon density corresponding to a Bose gas of deuterons. The scattering-state contribution reads

$$n_{scatt} = -6\int_{K>K_{Mott}} \frac{d^3K}{(2\pi)^3} g(\omega_0(K)) - 6\sum_{\alpha={}^3S_1,\,{}^1S_0} \int \frac{d^3K}{(2\pi)^3} \int_{\omega_0(K)}^{\infty} \frac{d\omega}{\pi} \left(\frac{d}{d\omega} g(\omega)\right) \left(\delta_\alpha - \tfrac{1}{2}\sin 2\delta_\alpha\right). \tag{4.19}$$

In Ref. [212], these equations were derived in a different way using the optical theorem, analogously to the derivation of a similar formula for the electron-hole system in Ref. [273].

Note that in spite of the double pole of the derivative of the Bose function at $\omega = 0$, the integrand in Eq. (4.19) has no pole. This is because δ_α crosses zero at $\omega = 0$. This simple zero is raised to a double one due to the difference of the two terms in the second integral in Eq. (4.19) [1].

Once we have calculated the density, we can calculate the pressure. To that end, we integrate the thermodynamic relation $n = (dP/d\mu)_T$ over μ, i.e.,

$$P(T,\mu) = \int_{-\infty}^{\mu} n(T,\mu')d\mu'. \tag{4.20}$$

Then we calculate the free-energy density F/V, the entropy density S/V, and the energy density E/V from the thermodynamic relations

$$F = -PV + \mu n V\,, \quad S = -\left.\frac{\partial F}{\partial T}\right|_n\,, \quad \text{and} \quad E = F + TS\,. \tag{4.21}$$

4.3 Numerical results

4.3.1 Density and the superfluid critical temperature

We calculate the total density by numerically integrating Eqs. (4.18) and (4.19). The results for the densities at different temperatures as functions of the chemical potential[2] are shown in Fig. 4.4. Comparing the results

[1] Note also that the statement in Ref. [231], saying that Eq. (4.19) reduces to the NSR formula for the density after integration by parts if the term $\propto \sin 2\delta_\alpha$ is omitted, is incorrect. In fact, the NSR formula involves a derivative $d\delta/d\mu$ instead of $d\delta/d\omega$ and therefore does not have a pole in the integrand even if that term is omitted. The term $\propto \sin 2\delta_\alpha$ cannot be identified with the contribution of the subtraction of $\Sigma(p,\xi_p)$ in Eq. (4.8).

[2] Strictly speaking, n is not a function of μ since it is not single-valued, as will be discussed later. In practice, we generate the curves in Figs. 4.4-4.12 by making a loop over the HF density and not over μ.

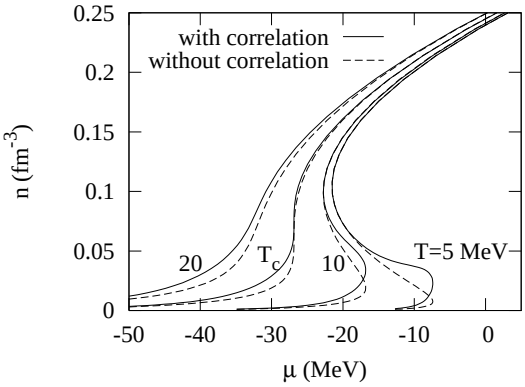

Figure 4.4: The densities at $T = 20$, 15.9, 10, and 5 MeV (from left to right) as functions of the chemical potential within Gogny HF (dashes) and with correlations (solid line). $T_c^{liq\text{-}gas} = 15.9$ MeV is the critical temperature for the liquid-gas phase transition.

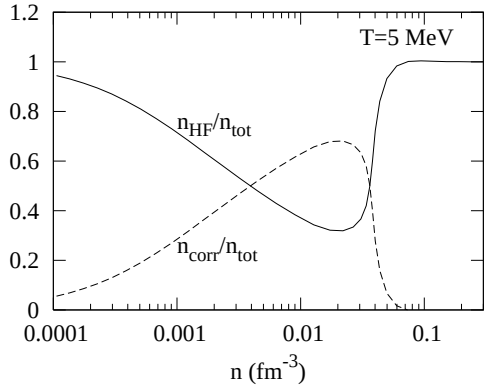

Figure 4.5: HF and correlation contributions to the total density $n_{tot} = n_{HF} + n_{corr}$ for $T = 5$ MeV.

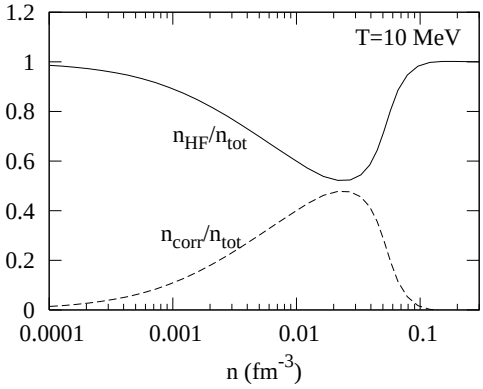

Figure 4.6: Same as Fig. 4.5, but for $T = 10$ MeV.

with correlations (solid lines) with the Gogny HF results (dashed lines), one can see that, for a given chemical potential, the correlations increase the densities. In the high-density region, we notice that the results with and without correlations converge to the same value, i.e., the correlations fade away at high density, as this can be expected. For example, at $T = 5$ MeV, the two results coincide starting from $n = 0.07$ fm^{-3}. This is a consequence of the Mott mechanism, which has been discussed at length in Ref. [212]. As mentioned above, the critical number density where the bound state (at $K = 0$) disappears is called Mott density. When we change the temperature from 5 MeV to 10, 15.9, and 20 MeV, the Mott density changes from 0.07 fm^{-3} to 0.12, 0.18, and 0.22 fm^{-3}. This means that the mean field approximation is valid in the high density region. Below this region, the contribution of the nucleon-nucleon correlations is important.

From this figure we also can see that when the temperature is less than some critical value ($T_c^{liq\text{-}gas} = 15.9$ MeV), the number density has three values corresponding to one definite value of chemical potential. This is a typical feature of the liquid-gas phase transition in nuclear matter. We will discuss this phenomenon in detail in the next subsection.

To see how large the correlation contribution to the density is, we show the composition of the system at different temperatures in Figs. 4.5 and 4.6. Since the density ratios are shown as functions of the density and not of the chemical potential, there are unique solutions even for temperatures below $T_c^{liq\text{-}gas}$. In Fig. 4.5 one can see that at $T = 5$ MeV the correlation contribution to the total density is important at low density ($n < n_0/4$). At

$n = 0.02$ fm^{-3}, the correlated part is even larger than the HF part. This means that most of the nucleons are in correlated pairs in this density region. With increasing temperature, e.g., at $T = 10$ MeV as shown in Fig. 4.6, the ratio of the correlated density to the total density decreases, but the density region with sizeable nucleon correlations is enlarged. Here we do not separate the correlation contribution into bound and scattering state contributions, since individually they are not very meaningful, as discussed in Ref. [212]. For instance, if the temperature is much higher than the deuteron binding energy, the first term of the scattering-state contribution (4.19) cancels almost exactly the bound-state contribution (4.18).

In the above calculation, when the temperature is below some critical value, we get a divergence in the T matrix. This pole corresponds to the formation of Cooper pairs at high density and to Bose-Einstein condensation of deuterons at low density. Below this critical temperature T_c, the equations for the density of the system are not applicable any more. In the superfluid phase, one would have to include the nucleon pairing gap explicitly in the single-particle Green's function (which then becomes a 2×2 matrix in Nambu-Gorkov space [106]), which is beyond the scope of this paper. However, we can determine the critical temperature of the superfluid transition as the temperature where the T matrix develops a pole at zero total momentum ($K = 0$) and at zero energy ($\omega = 0$). This is the well-known Thouless criterion [239] for the onset of superfluidity, coinciding with the BCS gap equation when the gap Δ goes to zero:

$$1 - J_\alpha(K = 0, \omega = 0; T = T_c) = 0. \tag{4.22}$$

From this equation we get the critical temperature as a function of the effective chemical potential. Using the relation between the effective chemical potential and the number density, we obtain the superfluid region beyond the BCS (mean field) result as shown in Fig. 4.7. Qualitatively, this result is similar to the one in [231] except that we have a lower critical temperature for the superfluid phase transition. The maximum T_c in [231] is 7.2 MeV at $n = 0.12$ fm^{-3}, while we have $T_c = 4.5$ MeV at $n = 0.05$ fm^{-3}. The difference stems from the Gogny mean field, in particular from the effective mass, which was neglected in Ref. [231]. One realizes that a T_c of 4.5 MeV is still very high, leading to a maximal gap of about 7 MeV, about three times as much as the maximum value of the neutron-neutron gap in the spin singlet channel. The reason clearly stems from the slightly stronger attraction in the proton-neutron isoscalar channel. However, in finite nuclei barely any enhancement of pairing in the $S = 1, T = 0$ channel can be detected. Probably important screening is at work in that channel. In nuclear matter, this has been investigated in Ref. [68]. The addition of screening effects is, however, beyond the scope of this paper.

As mentioned above, T_c as a function of μ coincides with the BCS result. As a function of the density, the difference between the results $T_c(n)$ with and without correlations comes only from the different relations for n as a function of μ. Since the correlation contribution to the density vanishes in the high density region, the phase boundary coincides with the BCS curve (long dashed line, which is obtained with n_{HF} only). At very low density and temperature, the main contribution to the density comes from the deuteron bound state, as can be seen from Eqs. (4.17) and (4.18). Close to the Bose critical temperature, the Bose distribution function in Eq. (4.18)) starts to diverge and, therefore, dominates the whole expression for the density. Therefore the superfluid critical temperature at low density coincides with the critical temperature for Bose-Einstein condensation of a deuteron gas, which is given by

$$T_c^{BEC} = \frac{\pi}{m} \left(\frac{n}{6\zeta(3/2)} \right)^{2/3}, \tag{4.23}$$

(with $\zeta(3/2) = 2.612\ldots$) and is shown as the short-dashed line in Fig. 4.7.

A surprising behavior of our result is that in the density region between 0.04 fm^{-3} and 0.05 fm^{-3}, Eq. (4.22) for the critical temperature has three solutions for one given density. This behavior is not easy to understand

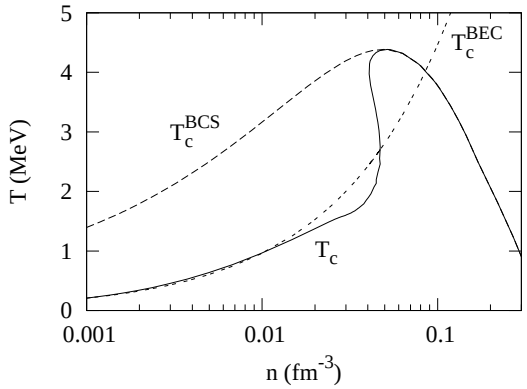

Figure 4.7: Superfluid critical temperature as a function of the (total) density. The solid line is the full calculation, while the long dashes correspond to the BCS result. The short dashes show the critical temperature of Bose-Einstein condensation of a deuteron gas.

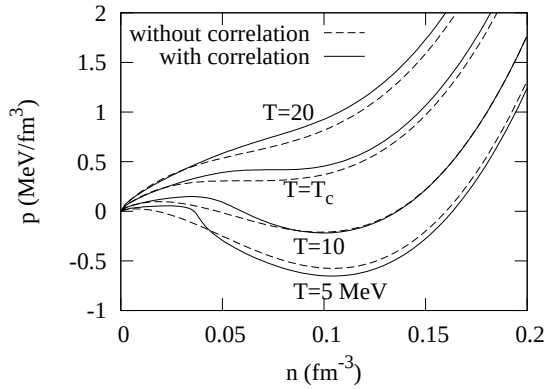

Figure 4.8: The pressure as a function of density at different temperatures. Solid lines: with correlations; dashed lines: mean-field results.

from physical intuition. It seems to be related to the effective mass, since it is absent in Ref. [231]. Anyway, as we will show in the next subsection, this density region lies inside the unstable region of the liquid-gas phase transition.

4.3.2 Pressure and liquid-gas transition

As it was shown in Fig. 4.4, there is a region of densities where the chemical potential decreases with increasing density. This is a typical feature of a liquid-gas phase transition. In order to determine the boundary of this first-order phase transition, we need the pressure. In principle, one can get the pressure as a function of temperature and chemical potential, $P(T,\mu)$, from the number density $n(T,\mu)$ by integration over the chemical potential μ, cf. Eq. (4.20). However, since there is a first-order phase transition, n is not a single-valued function of μ any more. We therefore transform the integral over μ into an integral over n_{HF}:

$$P(T,n_{HF}) = \int_0^{n_{HF}(T,\mu)} n(T,n'_{HF})\,\left.\frac{\partial\mu}{\partial n'_{HF}}\right|_T dn'_{HF}\,. \tag{4.24}$$

Since μ is a single-valued function of n_{HF} (see dashed line in Fig. 4.4), this integral is well defined. In this way we obtain the pressure as a function of n_{HF}, but neither n_{HF} nor P are single-valued functions of μ.

If we plot the pressure as a function of the total density n instead of n_{HF}, we get the results shown in Fig. 4.8. Unfortunately, we cannot calculate the pressure for $T < 4.5$ MeV, at least not at densities above 0.05 fm^{-3}, because our method to calculate the pressure at a given density n necessitates the calculation of all densities $n' < n$, i.e., including the density at $n = 0.05$ fm^{-3} where T_c is maximum. For comparison, we also give the results for the pressure within the mean-field approximation (dashed lines in Fig. 4.8). As it can be seen, the main effect of the nucleon-nucleon correlations is to increase the pressure at very low densities. However, in the case $T = 5$ MeV shown in Fig. 4.8, the pressure at higher densities is lower than the HF result.

Using the pressure, one can determine the coexistence region of the liquid and gas phases of nuclear matter

from the following conditions:

$$P(T, n_1) = P(T, n_2) \quad \text{and} \quad \mu(T, n_1) = \mu(T, n_2). \tag{4.25}$$

The result is shown in Fig. 4.9 as the thin solid line. At the same time, we can determine the spinodal curve from the zeros of $\partial P/\partial n$ (or, equivalently, of $\partial \mu/\partial n$), which is shown as the thick solid line in Fig. 4.9. In the region under the spinodal curve, the system cannot exist in a homogeneous phase. In the region between the thin solid line and the spinodal curve, the gas phase (left-hand part) or the liquid phase (right-hand part) can exist as a metastable state. For comparison, the corresponding mean-field results are presented in Fig. 4.9 as the dashed lines, which coincide with Fig. 6 of Ref. [259].

Comparing the results with and without correlations, one can see that the correlations decrease the phase-transition temperature in the low-density region and reduce the unstable region of the liquid-gas phase transition considerably. As mentioned in the introduction, this is an expected result. In the high density region, the effect of the correlations is almost negligible.

We can determine the critical temperature of the liquid-gas transition, i.e., the maximum temperature of the coexistence and the spinodal curves, from

$$\left.\frac{\partial P}{\partial n}\right|_{T_c^{\textit{liq-gas}}} = \left.\frac{\partial^2 P}{\partial n^2}\right|_{T_c^{\textit{liq-gas}}} = 0, \tag{4.26}$$

see Fig. 4.8. In this way, we obtain $T_c^{\textit{liq-gas}} = 15.9$ MeV, which coincides with the mean-field result [228, 259]. The fact that $T_c^{\textit{liq-gas}}$ remains unchanged is an artifact of our present approach to treat the correlation effects only at a perturbative level, as explained in Sec. 4.2. As shown in Ref. [205], the inclusion of deuteron (and heavier) clusters should reduce the liquid-gas critical temperature. We would have to do the calculation more self-consistently in order to get a lower critical temperature than the mean-field result.

In Fig. 4.10, the results of Fig. 4.7 for the superfluid critical temperature T_c (lower solid line) and Fig. 4.9 for the liquid-gas coexistence region (upper solid line) and the spinodal instability region (dashed line) have been combined in a single phase diagram. As explained above, we unfortunately cannot calculate the liquid-gas coexistence curve for $T < 4.5$ MeV, but extrapolating the solid curve to lower temperatures and remembering that at $T = 0$ the liquid phase gets stable at saturation density, it is clear that the coexistence curve will cross the superfluid T_c curve at $n \sim n_0$, i.e., as one would expect, homogeneous nuclear matter with pairing is stable above this density. From the results of Ref. [230] one can presume that the liquid-gas coexistence region will be slightly reduced below the superfluid critical temperature, but this effect should be almost negligible in the case of symmetric nuclear matter considered here [230, 234]. At low densities, superfluid matter is never stable, because the superfluid T_c curve stays always below the coexistence curve.

The spinodal curve (dashed line) can be calculated until it reaches the superfluid region. From this we see that superfluid nuclear matter is metastable below $n \sim 0.045$ fm^{-3} and above $n \sim 0.1$ fm^{-3}. Note that on the low-density side, the density region where the gas phase is metastable is strongly increased by the correlations, especially when we approach the superfluid transition temperature. This confirms our expectation mentioned in the introduction that the correlations have a stabilizing effect. However, the BEC-BCS crossover lies still in the unstable region of the liquid-gas phase transition.

4.3.3 Energy and entropy

The energy and the entropy can be obtained from the pressure with the help of the thermodynamic relations (4.21). Results for the energy per nucleon, E/A, and for the entropy per nucleon, S/A, for different temperatures are shown in Figs. 4.11 and 4.12. The corresponding mean-field results (dashed lines) are also shown

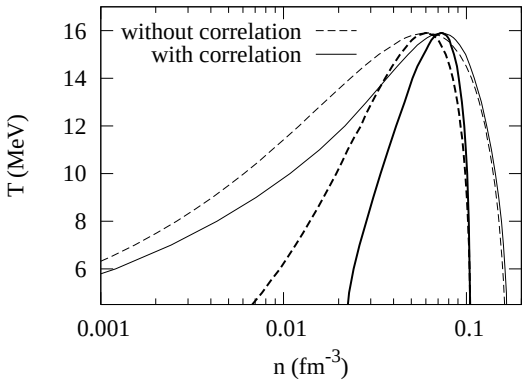

Figure 4.9: The liquid-gas phase diagram as function of density and temperature (for $T \geq 4.5$ MeV). The thin lines are the boundary of the coexistence region, while the thick lines are the boundary of the spinodal region. Solid lines: with correlations; dashed lines: mean field results.

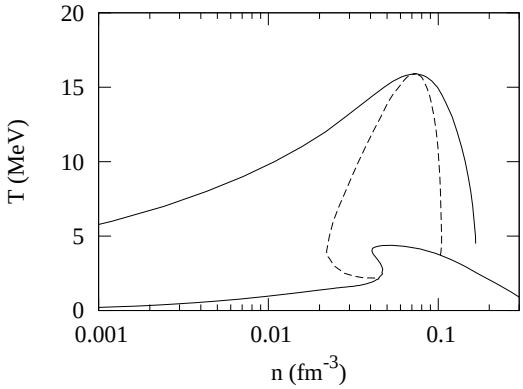

Figure 4.10: Phase diagram combining the boundary of the superfluid phase (lower curve), the liquid-gas coexistence region (upper curve), and the spinodal line (dashed curve). The reason why the spinodal and coexistence curves end at T_c and 4.5 MeV, respectively, is not physical but it simply means that our model does not allow us to compute them at lower temperatures (see text).

for comparison. The results shown in Fig. 4.11 indicate that, for fixed temperature, the correlations shift the minimum of the energy per nucleon to slightly higher densities. Fortunately the change is very small, because otherwise we would have to readjust the parameters of the Gogny force, which gives the right saturation density and energy at zero temperature without correlations.

In the low-density region, where the deuterons and the nucleon-nucleon scattering states dominate, the energy per nucleon is lower than that the HF result. When the density is high, the correlation effect goes to zero and the energy per nucleon gets close to the mean-field result.

When the density approaches zero, both results go to the classical value of an ideal gas of nucleons,

$$\lim_{n\to 0} E/A = \tfrac{3}{2}T. \tag{4.27}$$

This is not surprising, since even the lowest temperature considered here, $T = 5$ MeV, is still much higher than the deuteron binding energy so that almost all deuterons will be dissociated. However, the result (4.27) is also found at temperatures much lower than the deuteron binding energy. This is because, at finite temperature, the deuterons are always dissolved in the low-density limit. This is a consequence of the mass-action law and can easily be understood as follows: At low density, the chemical potential of the nucleons, μ, gets strongly negative, $\mu \ll -T$. The chemical potential of the deuterons is 2μ, which is even more negative. So the nucleon density $\propto e^{\mu/T}$ is much larger than the deuteron density $\propto e^{2\mu/T}$. Only at zero temperature, where the system remains a deuteron BEC at arbitrarily low densities, the energy per nucleon approaches -1.12 MeV (half the deuteron binding energy) in the limit $n \to 0$ [29].

The results for the entropy (cf. Fig. 4.12) have been calculated from Eq. (4.21) and show that, for fixed temperature, the entropy per nucleon decreases with increasing density. In the zero-density limit, the entropy per nucleon increases logarithmically, in agreement with the result for a classical ideal nucleon gas. As is clear from the discussion above, the correlations do not change this asymptotic behavior. At slightly larger values of the density, the correlations tend to increase the entropy.

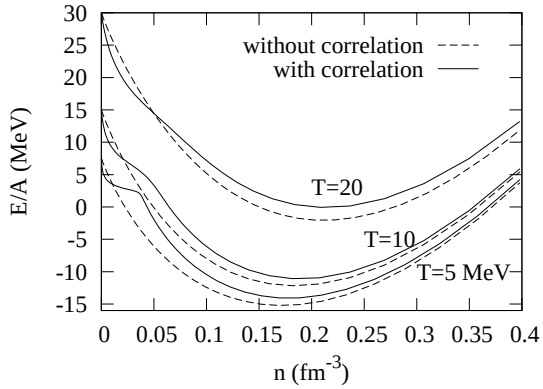

Figure 4.11: Energy per nucleon as a function of density for different temperatures. Solid lines: with correlations; dashed lines: mean field results.

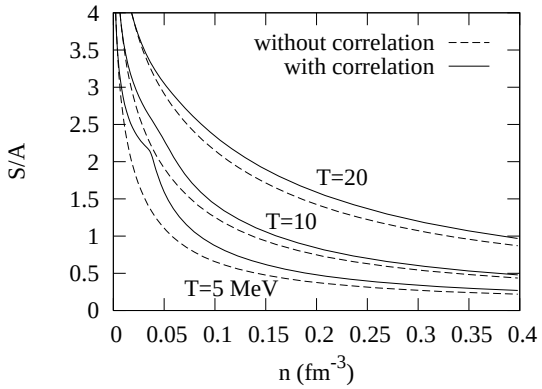

Figure 4.12: Entropy per nucleon as a function of density for different temperatures. Solid lines: with correlations; dashed lines: mean field results.

4.4 Summary

In this paper, we discussed the effect of pair correlations beyond the mean-field approximation in symmetric nuclear matter above the superfluid critical temperature. We include the effects of non-condensed pairs (deuterons) as well as the contribution of scattering states. For the mean field, we use the Gogny effective interaction in order to get the right saturation properties of nuclear matter.

Starting from the single-particle Green's function within the Gogny HF approximation, we include the correlations in a perturbative way by considering in addition to the HF Green's function the diagram with one self-energy insertion, the self-energy being calculated in ladder approximation. This approximation scheme is analogous to the well-known NSR approach. However, in order to avoid double counting of the quasiparticle energy shift which is already accounted for by the Gogny mean field, we have to subtract the self-energy at the quasiparticle energy. This leads finally to the same formula for the density in terms of the in-medium scattering phase shifts as given in Ref. [231]. We use a separable Yamaguchi potential in order to get an analytical formula for the in-medium T matrix and the phase shifts.

Evaluating numerically these formulas for the density, we discussed the different density contributions in hot and dense nuclear matter and found that the nucleon-nucleon correlations are important in the low-temperature and low-density region ($n < n_0$). The correlation effect on the superfluid critical temperature was discussed. The result interpolates between the critical temperature for Bose-Einstein condensation at low density and the BCS critical temperature at high density. We found that the maximum of the superfluid critical temperature decreases from 7.2 MeV (the value given in Ref. [231]) to 4.5 MeV when the effective mass m^* due to the Gogny mean field is taken into account.

Then we studied the liquid-gas phase transition in hot and dense nuclear matter with the help of the pressure calculated from the density. Especially at low density, we found that the boundaries of the coexistence and spinodal regions of the phase transition are shifted by the pair correlations. As we expected, the stable and metastable regions of the gas phase are strongly enlarged. In particular near the superfluid transition temperature, the gas phase stays metastable up to much higher densities if the correlations are taken into account. However, the correlations are not strong enough to suppress the liquid-gas transition. This could have been anticipated from the fact that the liquid-gas critical temperature is much higher than the superfluid one [230, 234]. Because of our perturbative treatment of the correlations, the critical temperature of the liquid-gas transition

remains the same as within the mean field approximation.

Finally, we calculated the energy and entropy of nuclear matter from thermodynamic relations. The nucleon-nucleon correlations decrease the energy per nucleon in the low density region but increase it at high density. For the entropy, the correlations always give a positive contribution.

As mentioned before, our result for the critical temperature of liquid-gas phase transition is not affected by the pair correlations because they are treated only perturbatively. One should improve this by taking the correlations into account self-consistently. Then the correlations will have some effect on the HF field and the critical temperature will change. The saturation point of nuclear matter, given correctly by the Gogny interaction within the HF approximation, may be changed, necessitating a readjustment of the parameters of the Gogny force.

Our equation of state is only valid for temperatures and densities above the superfluid critical temperature. In order to get a result which is valid in the whole temperature and density plane, one should introduce the pairing gap Δ into the single-particle Green's functions. Some work in this direction has been done for nuclear matter [54], and quite elaborate theories have been developed for the BEC-BCS crossover in ultracold atomic Fermi gases [184]. We leave this for future study. Another important extension of the present work would be to consider the case of asymmetric nuclear matter and neutron matter, since these are of great importance for the study of neutron stars and their formation.

Acknowledgments

We thank G. Röpke and J. Margueron for discussions and helpful remarks. M.J. acknowledges financial support from Université Paris-Sud 11 and from CNRS during his postdoctoral stays at Institut de Physique Nucléaire d'Orsay, where most of this work has been done. This work was supported in part by NSFC (grants 10805023 and 10975060) and by ANR (project NEXEN).

Appendix: Derivation of the density formulas

In this Appendix we give a more transparent derivation of the density formulas (4.17), (4.18), and (4.19), which were initially derived in Refs. [212, 273]. For better readability, we will not write out the sum over $\alpha = {}^3S_1$, ${}^1S_0$ and suppress the index α in this appendix.

Let us recall the spectral representation of the T matrix,

$$T(k,k',K,\omega) = V(k,k') - \int \frac{d\omega'}{\pi} \frac{\mathrm{Im}\, T(k,k',K,\omega')}{\omega - \omega' + i0}\,, \tag{4.28}$$

where ω can be real or complex. Analogous dispersion relations exist for the self-energy $\Sigma(p,\omega)$ and for the two-particle propagator $J(K,\omega)$ defined in Eq. (4.13). Using Eq. (4.28), one can evaluate the frequency sum in Eq. (4.15), and one obtains the well-known expression for the imaginary part of the self-energy:

$$\mathrm{Im}\,\Sigma(p,\omega) = \frac{3}{2}\int \frac{d^3p'}{(2\pi)^3}\,\mathrm{Im}\, T(k,k,K,\omega+\xi_{p'})\,[f(\xi_{p'}) + g(\omega+\xi_{p'})]\,. \tag{4.29}$$

where $\mathbf{k}$ and $\mathbf{K}$ are the relative and total momenta as defined below Eq. (4.15).

The correlation correction to the density is given by

$$n_{corr} = -4T\sum_n \int \frac{d^3p}{(2\pi)^3}\frac{\Sigma(p,i\omega_n) - \mathrm{Re}\,\Sigma(p,\xi_p)}{(i\omega_n - \xi_p)^2}\,. \tag{4.30}$$

If we use the spectral representation of Σ, the frequency sum can be evaluated with the result

$$n_{corr} = -4 \int \frac{d^3p}{(2\pi)^3} \mathcal{P} \int \frac{d\omega}{\pi} \operatorname{Im} \Sigma(p,\omega) \frac{f(\omega) - f(\xi_p)}{(\omega - \xi_p)^2} \,, \tag{4.31}$$

where $\mathcal{P}$ denotes the principal value. Inserting Eq. (4.29) into this expression, one obtains with the help of the relation $f(\xi_p) f(\xi_{p'}) = g(\xi_p + \xi_{p'})[1 - f(\xi_p) - f(\xi_{p'})]$ and after some transformations

$$n_{corr} = -6 \int \frac{d^3p\, d^3p'}{(2\pi)^6} \mathcal{P} \int \frac{d\omega}{\pi} \operatorname{Im} T(k,k,K,\omega) \, (1 - f(\xi_p) - f(\xi_{p'})) \frac{g(\omega) - g(\xi_p + \xi_{p'})}{(\omega - \xi_p - \xi_{p'})^2} \,. \tag{4.32}$$

The next step is to introduce the new variable $\omega' = \xi_p + \xi_{p'}$ and to replace the integral over p' by an integral over ω'. Then, using the imaginary parts of Eqs. (4.12) and (4.13), one can show that the resulting expression for n_{corr} can be rewritten as

$$n_{corr} = 6 \int \frac{d^3K}{(2\pi)^3} \mathcal{P} \int \frac{d\omega\, d\omega'}{\pi^2} \operatorname{Im} \frac{1}{1 - J(K,\omega)} \, \operatorname{Im} J(K,\omega') \, \frac{g(\omega) - g(\omega')}{(\omega - \omega')^2} \,. \tag{4.33}$$

With the help of the dispersion relations for the real parts, this expression can be further reduced to

$$n_{corr} = 6 \int \frac{d^3K}{(2\pi)^3} \int \frac{d\omega}{\pi} g(\omega) \left(\operatorname{Im} \frac{1}{1-J} \frac{d}{d\omega} \operatorname{Re} J - \operatorname{Im} J \frac{d}{d\omega} \operatorname{Re} \frac{1}{1-J} \right) \tag{4.34}$$

(the arguments of $J(K,\omega)$ have been suppressed for brevity). In order to express everything in terms of the in-medium scattering phase shifts $\delta = -\operatorname{Im} \ln(1-J)$, we notice that

$$\frac{d\delta}{d\omega} = \operatorname{Im} \frac{1}{1-J} \frac{d}{d\omega} \operatorname{Re} J + \operatorname{Re} \frac{1}{1-J} \frac{d}{d\omega} \operatorname{Im} J \,, \tag{4.35}$$

$$\operatorname{Im} J \operatorname{Re} \frac{1}{1-J} = \sin\delta \cos\delta = \tfrac{1}{2} \sin 2\delta \,. \tag{4.36}$$

With these relations, Eq. (4.34) can be rewritten as

$$n_{corr} = 6 \int \frac{d^3K}{(2\pi)^3} \int \frac{d\omega}{\pi} g(\omega) \frac{d}{d\omega} \left(\delta - \tfrac{1}{2} \sin 2\delta \right) \,. \tag{4.37}$$

The final step is to integrate by parts over ω and to separate in the resulting integral the contributions of $\omega > \omega_0(K)$ (scattering-state contribution n_{scatt}) and $\omega < \omega_0(K)$ (bound-state contribution n_{bound}). The latter reduces to Eq. (4.18) since the phase shift below threshold is (see also Fig. 7 of Ref. [174])

$$\delta(K, \omega < \omega_0(K)) = \begin{cases} 0, & \text{if } K < K_{Mott}, \\ \pi\theta(\omega - \omega_b(K)), & \text{if } K > K_{Mott}. \end{cases} \tag{4.38}$$

Chapitre III

Gaz de fermions superfluides dans un piège en rotation

Dans le chapitre précédent, nous avons discuté les corrélations d'appariement dans des systèmes fermioniques variés : Gaz d'atomes froids, matière de quarks, matière nucléaire. Dans le reste de ce mémoire, nous nous intéresserons à la conséquence de l'appariement sur les propriétés dynamiques des systèmes : la superfluidité.

Une propriété caractéristique des superfluides est que leur champ de vitesse $\mathbf{v}(\mathbf{r})$ est irrotationnel, $\boldsymbol{\nabla} \times \mathbf{v}(\mathbf{r}) = 0$. Ceci n'est pas le cas pour le champ de vitesse correspondant à une rotation rigide, $\mathbf{v}_{rot} = \boldsymbol{\Omega} \times \mathbf{r}$, où $\boldsymbol{\Omega}$ désigne la vitesse angulaire et $\mathbf{r}$ est mesuré depuis l'axe de rotation. Si néanmoins un système superfluide macroscopique comme l'hélium liquide en-dessous du point λ tourne, c'est parce qu'il y a de nombreux vortex quantiques ayant chacun un cœur (microscopique) dans lequel le système n'est pas superfluide. L'observation des réseaux de vortex dans les gaz de fermions piégés représente certainement la preuve la plus convaincante que la phase superfluide a été réalisée [275]. Cependant, les vortex ne peuvent se former qu'à partir d'une certaine vitesse angulaire critique, Ω_c. Ici, nous nous intéresserons au cas où le système tourne sans vortex.

Rotation lente et moment d'inertie (publication n° 5, p. 64)

Dés les années 1950, des expériences d'excitation coulombienne ont permis de mettre des noyaux en rotation et de mesurer leur spectre de rotation [7]. On a trouvé que le moment d'inertie Θ du noyau était beaucoup plus petit que la valeur Θ_{rigid} que l'on obtiendrait si le noyau était un corps rigide, mais plus élevé que la valeur Θ_{irrot} que l'on obtiendrait si le champ de vitesse dans le noyau était irrotationnel. La réduction du moment d'inertie par rapport à Θ_{rigid} était considérée comme un signe de la superfluidité des noyaux. En 1959, Migdal a donné une interprétation quantitative de ces résultats [169] en utilisant la théorie BCS.

Par analogie avec cet exemple de physique nucléaire, la mesure du moment d'inertie dans des gaz de fermions piégés peut donc servir à distinguer la phase superfluide de la phase normale. Ceci était la motivation principale de notre publication [251] (n° 5 ci-après). Plus récemment, l'expérience a été réalisée dans le groupe d'Innsbruck et la réduction du moment d'inertie a été observée [200].

Pour calculer le moment d'inertie du gaz de fermions piégés, nous nous sommes placés dans le référentiel tournant, ce qui revient à rajouter au hamiltonien le terme $-\Omega L_z$ (supposant une rotation autour de l'axe z ; $\mathbf{L}$ est l'opérateur du moment cinétique). Le moment d'inertie étant défini comme la limite de $\Theta = L_z/\Omega$ pour $\Omega \to 0$, il suffit de se limiter au cas d'une rotation lente, dans lequel on peut traiter ce terme de "cranking" comme une perturbation. Mais même la réponse linéaire est difficile à obtenir, et nous avons donc fait des approximations semiclassiques comme dans un travail précédent de Farine et al. [105] afin de pouvoir traiter de

grands nombres d'atomes. De plus, nous avons remplacé le gap $\Delta(\mathbf{r})$ par un gap moyen, Δ. La nouveauté de notre travail a été l'inclusion de la température, qui est essentielle pour la transition de phase superfluide-normal et pour la comparaison avec l'expérience.

Dans le développement semiclassique, deux types de corrections en puissance de $\hbar$ apparaissent. D'une part, il y a des corrections de l'ordre de $\hbar\omega/E_F$, où ω est la fréquence du piège et E_F est l'énergie de Fermi. Ces corrections peuvent être négligées si le nombre d'atomes est suffisamment élevé, ce qui est la condition habituelle pour la validité de l'approximation de Thomas-Fermi (TF). D'autre part, il y a des corrections de l'ordre de $\hbar\omega/\Delta$. Dans le régime BCS, on a $\Delta \ll E_F$, et le paramètre $\hbar\omega/\Delta$ n'est donc pas nécessairement petit. Nous avons inclus ces corrections à tous les ordres et nous avons montré que le champ de vitesse $\mathbf{v}(\mathbf{r})$ devenait irrotationnel uniquement dans la limite $\Delta \gg \hbar\omega$. Si cette condition n'est pas satisfaite, on retrouve une situation analogue à celle des noyaux, c'est-à-dire dans laquelle $\mathbf{v}(\mathbf{r})$ possède une composante rotationnelle même à température nulle, bien que le système soit superfluide.

Concernant la dépendance en température, nous avons démontré que les résultats pouvaient être compris d'une façon très intuitive dans le cadre du modèle à deux fluides : Le système se comporte comme s'il était un mélange d'une composante superfluide (paires de Cooper) et d'une composante normale (paires brisées par l'excitation thermique). Notamment, dans la limite $\hbar\omega \ll \Delta$, le courant $\mathbf{j}(\mathbf{r})$ peut s'écrire comme $\mathbf{j}(\mathbf{r}) = n_s(\mathbf{r})\mathbf{v}_{irrot}(\mathbf{r}) + n_n(\mathbf{r})\mathbf{v}_{rot}(\mathbf{r})$, où $\mathbf{v}_{irrot}(\mathbf{r})$ est le champ de vitesse irrotationnel et n_s et $n_n = n - n_s$ sont les densités superfluide et normale du modèle à deux fluides : À $T = 0$, on a $n_s = n$ et $n_n = 0$, tandis qu'à $T \geq T_c$, on a $n_s = 0$ et $n_n = n$. Cette décomposition du courant reste valable si l'on prend en compte la dépendance spatiale du gap $\Delta(\mathbf{r})$ [247].

Brisure de paires de Cooper par la rotation (publication n° 6, p. 84)

Dans le paragraphe précédent, nous avons considéré le cas d'une rotation lente. À l'ordre le plus bas en Ω, le fait que le système tourne ne supprime pas l'appariement, et les paires de Cooper ne sont brisées que par des effets de température. Mais en physique nucléaire on sait depuis longtemps que si le noyau tourne trop vite, les corrélations d'appariement sont détruites [100, 123], comme dans un supraconducteur dans un champ magnétique.

La situation dans les noyaux et dans les gaz piégés n'est pas tout à fait comparable. En physique nucléaire, la longueur de cohérence ξ ($\simeq$ extension spatiale des paires de Cooper) est du même ordre de grandeur que le noyau, tandis que dans les gaz de Fermi piégés dans le régime du cross-over BEC-BCS, ξ est normalement beaucoup plus petit que le système. C'est pour cette raison que les vortex, dont le cœur a un rayon de l'ordre de ξ [175], peuvent se former dans les gaz piégés [275].

Néanmoins, il a été suggéré par Stringari et al. [37] qu'en augmentant la vitesse angulaire Ω adiabatiquement, il serait possible de créer un système en rotation rapide sans vortex. Dans ce cas, le système pourrait se séparer en deux phases : une phase superfluide près de l'axe de rotation, qui ne participe pas à la rotation, et une phase normale plus loin de l'axe de rotation, qui tourne comme un corps rigide. Et comme dans le régime du cross-over BEC-BCS les équations d'état des deux phases sont différentes, il se formerait une discontinuité de la densité à l'interface entre les deux phases, située à une distance critique $r_{\perp c}$ de l'axe de rotation, qui pourrait éventuellement être observée dans des expériences. Cette idée était fondée sur la simple comparaison entre l'énergie nécessaire à la brisure des paires quand on passe de la phase superfluide à la phase normale et l'énergie que l'on gagne à cause de la force centrifuge.

Pour mieux comprendre le mécanisme de la brisure des paires au niveau microscopique, nous avons étudié ce problème dans le cadre de la théorie BCS [254] (publication n° 6). Cette fois-ci, nous avons supposé que la condition $\xi \ll R_{TF}$ était satisfaite, où R_{TF} est le rayon du gaz piégé dans l'approximation TF. Sous cette hypothèse, qui est équivalente à la condition $\hbar\omega \ll \Delta$ mentionnée ci-dessus, il suffit de se limiter à l'ordre

dominant du développement en puissances de $\hbar$, correspondant à l'approximation de densité locale (LDA).

Nous avons trouvé que toutes les paires ne se brisent pas en même temps, mais qu'elles sont brisées progressivement à partir d'une certaine distance $r_{\perp 1}$ de l'axe de rotation jusqu'á une autre distance $r_{\perp 2}$, où cette fois toutes les paires sont brisées. Il existe donc une phase intermédiaire entre la phase superfluide et la phase normale, dans laquelle à la fois le courant rotationnel (porté par les paires brisées) et le paramètre d'ordre Δ sont non nuls. Dans cette région entre $r_{\perp 1}$ et $r_{\perp 2}$, la densité d'énergie associée à la phase intermédiaire est inférieure aux densités d'énergie correspondant à la phase superfluide au repos et à la phase normale en rotation [250]. À cause de la présence de la phase intermédiaire, la discontinuité de la densité prédite dans réf. [37] disparaît et la densité varie de manière continue entre la densité de la phase superfluide à $r_{\perp 1}$ et la densité de la phase normale à $r_{\perp 2}$.

5 Slow rotation of a superfluid trapped Fermi gas

Michael Urban and Peter Schuck, Phys. Rev. A 67, 033611 (2003)

The moment of inertia, Θ, is one of the possible observables for the experimental determination whether a trapped Fermi system has reached the BCS transition or not. In this article we investigate in detail the temperature dependence of Θ below the critical temperature T_c. Special care is taken to account for the small size of the system, i.e., for the fact that the trapping frequency $\hbar\omega$ is of the same order of magnitude as the gap Δ. It is shown that the usual transport approach, corresponding to the leading order of an expansion in powers of $\hbar$, is not accurate in this case. It turns out that Θ does not change rapidly if T becomes smaller than T_c, but it rather decreases slowly. Qualitatively this behavior can be explained within the two-fluid model, which again corresponds to the leading order in $\hbar$. Quantitatively we find deviations from the two-fluid model due to the small system size.

5.1 Introduction

Since the first observation of Bose-Einstein condensation of magnetically trapped bosonic atoms [17, 55, 89] it has become clear that ultra-cold trapped atomic gases provide an excellent tool to study quantum effects in systems which are almost visible to the naked eye. For example, quantized vortices in the Bose condensate were created by stirring the Bose condensate with the help of a laser beam [160, 161]. Also the quantum pressure related to the Pauli principle could be observed in gases of trapped fermionic atoms [214, 245], which proves that temperatures well below the degeneracy temperature can be reached.

If it was possible to trap two spin states of a fermionic isotope with attractive interaction, and to cool the system below the critical temperature T_c, one could study the BCS transition to the superfluid phase. Unlike the transition of a Bose gas to the Bose-Einstein condensate, the BCS transition of a Fermi gas almost does not change the density profile of the atomic cloud [131]. However, there are other observables which may allow to distinguish between the normal-fluid and the superfluid phase. In a preceding paper [105] the moment of inertia was proposed, since it is much smaller in the superfluid phase than in the normal-fluid phase (see also Ref. [271]). Another observable changing from one phase to the other are the frequencies of collective modes [31, 64, 271]. For example, the frequency of the so-called "scissors mode", an oscillation of the symmetry axis of the cloud with respect to the symmetry axis of the trap, is closely related to the moment of inertia [105]. In Ref. [168] one more observable for the detection of the BCS transition was proposed, namely the change of the deformation of the cloud during the expansion of the system when the trapping potential is switched off. Very recently it has been reported that the best description of the experimentally observed expansion is provided by superfluid hydrodynamics [177], which might be interpreted as a first indication that the superfluid state of a trapped Fermi system has been realized experimentally.

The moment of inertia of a superfluid gas of trapped fermionic atoms at zero temperature was evaluated for the first time in Ref. [105] in close analogy to the calculation of the moment of inertia of superfluid nuclei [96]. This derivation was very similar to the one given by Migdal more than 40 years ago [169], except that everything was reformulated in phase space in terms of Wigner transforms. In the present article we will generalize the calculation of Ref. [105] to the case of non-zero temperature. In addition, we will give a derivation which further clarifies certain points which in Ref. [105] may have been passed over rather quickly.

In addition to the temperature dependence of the moment of inertia, we will address an interesting question which is relevant already at zero temperature. In nuclear physics it is well known that the moment of inertia of superfluid nuclei is much smaller than the rigid-body value, but still higher than the value corresponding to a purely irrotational motion, and that the currents in rotating nuclei have both rotational and irrotational components [96]. The same behavior is found in trapped Fermi gases at zero temperature [105]. In contrast to this, the ordinary hydrodynamical or transport equations for superfluids at zero temperature, which can be

derived from the $\hbar \to 0$ limit of the time-dependent Hartree-Fock-Bogoliubov (TDHFB) equation [43, 95, 124, 218, 262] allow only for a purely irrotational motion. We will work out this difference and discuss the limits of validity of the hydrodynamical description.

The article is organized as follows: In Sec. 5.2 we give a brief review of the formalism, mainly in order to recall some definitions and to clarify our notation. In Sec. 5.3 we derive the expression for the density matrix of the slowly rotating system within linear-response theory. This is the generalization of the calculation of Ref. [105] to non-zero temperatures. In Sec. 5.4 we again derive the linear response of the density matrix, but now using the leading order of the $\hbar$ expansion of the TDHFB equation. In Sec. 5.5 we show numerical results for the moment of inertia obtained within both formalisms as a function of temperature and interprete the results and their differences. Finally, in Sec. 5.6, we summarize and draw our conclusions.

5.2 Brief review of the formalism

Before considering the rotating superfluid trapped Fermi gas, we will briefly review the equilibrium case. Our intention is to explain our notation and conventions. Detailed discussions of the subject can be found in many articles [59, 105, 131] and textbooks [201].

In this article we assume for simplicity that equal numbers of atoms with two spin projections $\sigma = \uparrow, \downarrow$ are trapped in a spin-independent harmonic potential

$$V_0(\mathbf{r}) = \sum_{i=xyz} \frac{m\omega_{0i}^2}{2} r_i^2 \,. \tag{5.1}$$

If the density of the trapped system is very low, the atom-atom interaction can be approximated by a zero-range interaction with a coupling constant g proportional to the s-wave scattering length. Due to the Pauli principle only atoms with opposite spin projections can interact in this way. Under these assumptions the hamiltonian takes the form

$$H = \int d^3r \Big[\sum_{\sigma=\uparrow,\downarrow} \psi_\sigma^\dagger(\mathbf{r}) \Big(-\frac{\hbar^2 \boldsymbol{\nabla}^2}{2m} + V_0(\mathbf{r}) \Big) \psi_\sigma(\mathbf{r}) - g \psi_\downarrow^\dagger(\mathbf{r}) \psi_\uparrow^\dagger(\mathbf{r}) \psi_\uparrow(\mathbf{r}) \psi_\downarrow(\mathbf{r}) \Big] \,. \tag{5.2}$$

The mean-field potential corresponding to this interaction reads

$$V(\mathbf{r}) = V_0(\mathbf{r}) - g\rho(\mathbf{r},\mathbf{r}) = V_0(\mathbf{r}) - g\rho(\mathbf{r}) \,, \tag{5.3}$$

where we have used the following notation for the non-local density matrix:

$$\rho(\mathbf{r},\mathbf{r}') = \langle \psi_\uparrow^\dagger(\mathbf{r}') \psi_\uparrow(\mathbf{r}) \rangle = \langle \psi_\downarrow^\dagger(\mathbf{r}') \psi_\downarrow(\mathbf{r}) \rangle \,. \tag{5.4}$$

(Note that with this definition the local part of the density matrix, $\rho(\mathbf{r}) \equiv \rho(\mathbf{r},\mathbf{r})$ corresponds to the density per spin state.) In the presence of pairing correlations, the pairing gap is given by the gap equation

$$\Delta(\mathbf{r}) = g\kappa(\mathbf{r},\mathbf{r}) \tag{5.5}$$

where the pairing tensor has been defined as

$$\kappa(\mathbf{r},\mathbf{r}') = \langle \psi_\downarrow(\mathbf{r}') \psi_\uparrow(\mathbf{r}) \rangle \,. \tag{5.6}$$

It will turn out that the self-consistent solution of Eq. (5.5) is divergent as a consequence of the zero-range interaction. In the literature several ways how to regularize this divergence can be found [59, 105, 131, 207], but in fact the technical details of the solution of Eq. (5.5) are not important for our purpose.

In order to write down the Hartree-Fock-Bogoliubov (HFB) equations, which relate the density matrix ρ and the pairing tensor κ to the potential V and the gap Δ, it is useful to expand all quantities in a basis of single-particle wave functions $\varphi_n(\mathbf{r})$, where n represents all quantum numbers except spin, i.e., for an arbitrary operator A:

$$A_{nn'} = \int d^3r\, d^3r'\, \varphi_n^*(\mathbf{r})\varphi_{n'}(\mathbf{r}')A(\mathbf{r},\mathbf{r}')\,. \tag{5.7}$$

Expressing the field operators $\psi_\sigma(\mathbf{r})$ and $\psi_\sigma^\dagger(\mathbf{r})$ in terms of annihilation and creation operators $a_{n\sigma}$ and $a_{n\sigma}^\dagger$, we recover the usual definitions

$$\rho_{nn'} = \langle a_{n'\uparrow}^\dagger a_{n\uparrow}\rangle\,, \tag{5.8}$$

$$\kappa_{nn'} = \langle a_{\bar{n}'\downarrow} a_{n\uparrow}\rangle\,. \tag{5.9}$$

The index $\bar{n}'$ in Eq. (5.9) denotes the time-reversed state characterized by $\varphi_{\bar{n}'}(\mathbf{r}) = \varphi_{n'}^*(\mathbf{r})$. We need also the matrix elements $h_{nn'}$ of the grand-canonical (mean-field) single-particle hamiltonian (i.e., of the single-particle hamiltonian minus the chemical potential μ)

$$h = \frac{\mathbf{p}^2}{2m} + V(\mathbf{r}) - \mu\,, \tag{5.10}$$

and the matrix elements $\Delta_{nn'}$ of the gap Δ. For the more general case that the hamiltonian is not time-reversal invariant, we introduce the notation $\bar{A}_{nn'} = A_{\bar{n}'\bar{n}}$. If the matrices mentioned above are combined as follows:

$$\mathcal{R} = \begin{pmatrix} \rho & -\kappa \\ -\kappa^\dagger & 1-\bar{\rho} \end{pmatrix}, \tag{5.11}$$

$$\mathcal{H} = \begin{pmatrix} h & \Delta \\ \Delta^\dagger & -\bar{h} \end{pmatrix}, \tag{5.12}$$

the HFB equations [201, 257] can be written in the form of a 2×2 matrix equation,

$$[\mathcal{H},\mathcal{R}] = 0\,. \tag{5.13}$$

What is relevant for our purpose is the spectrum of the lowest lying quasiparticles, which for a sufficiently small gap can be obtained within the BCS approximation, which is much simpler than the solution of the full HFB equation (5.13). We choose a basis in which h is diagonal, i.e., $h_{nn'} = h_n\delta_{nn'}$. Then, within the BCS approximation, ρ and κ are diagonal, too, and given by

$$\rho_n = \frac{1}{2} - \frac{h_n}{2E_n}[1-2f(E_n)]\,, \tag{5.14}$$

$$\kappa_n = \frac{\Delta_n}{2E_n}[1-2f(E_n)]\,. \tag{5.15}$$

The quasiparticle energies $E_n = \sqrt{h_n^2+\Delta_n^2}$ and the quasiparticle occupation numbers $f(E_n) = 1/[\exp(E_n/T)+1]$ are determined by the diagonal matrix elements $\Delta_n \equiv \Delta_{nn}$ alone. If we neglect the non-diagonal matrix elements of Δ, which are irrelevant for the excitation spectrum and, apart from that, much smaller than the diagonal ones, we can rewrite Eqs. (5.14) and (5.15) in the compact form

$$\mathcal{R} = \frac{1}{2} - \frac{\mathcal{H}}{2E}[1-2f(E)]\,. \tag{5.16}$$

It is evident that the generalized density matrix $\mathcal{R}$ given by Eq. (5.16) solves the HFB equation (5.13) if h and Δ are assumed to be diagonal.

For the spherical case ($\omega_{0x} = \omega_{0y} = \omega_{0z}$) and moderate numbers of particles ($N \lesssim 10^4$), the self-consistent HFB equation can be solved numerically [59]. However, for the deformed case and large numbers of particles (experimentally numbers of the order $N \approx 10^5 \ldots 10^6$ have been reached), even within the BCS approximation, the self-consistent solution becomes numerically intractable. Therefore it may be indicated to apply semiclassical approximations. Semiclassical methods can become very accurate for large numbers of particles, and in addition they often allow for a very clear interpretation of the results. To that end we will use the Wigner transforms of the density matrix ρ, the pairing tensor κ, the single-particle hamiltonian h, etc. The Wigner transform of a single-particle operator A is defined as

$$A(\mathbf{r},\mathbf{p}) = \int d^3s\, e^{-i\mathbf{p}\cdot\mathbf{s}/\hbar} A\Big(\mathbf{r}+\frac{\mathbf{s}}{2},\mathbf{r}-\frac{\mathbf{s}}{2}\Big)\,. \tag{5.17}$$

The Wigner transform $h(\mathbf{r},\mathbf{p})$ of the single-particle hamiltonian h is particularly simple: It is just the classical hamiltonian. We also recall the useful relations $[A^\dagger](\mathbf{r},\mathbf{p}) = A^*(\mathbf{r},\mathbf{p})$ and $[\bar{A}](\mathbf{r},\mathbf{p}) = A(\mathbf{r},-\mathbf{p})$. One advantage of the Wigner transforms in semiclassical calculations is the product rule for the Wigner transform of the product of two operators A and B [201], directly leading to an $\hbar$ expansion:

$$[AB](\mathbf{r},\mathbf{p}) = A(\mathbf{r},\mathbf{p})\,\exp\Big(\frac{i\hbar\overleftrightarrow{\Lambda}}{2}\Big)\,B(\mathbf{r},\mathbf{p})\,, \tag{5.18}$$

where the symbol $\overleftrightarrow{\Lambda}$ stands for the Poisson bracket

$$\overleftrightarrow{\Lambda} = \sum_{i=xyz}\Big(\frac{\overleftarrow{\partial}}{\partial r_i}\frac{\overrightarrow{\partial}}{\partial p_i} - \frac{\overleftarrow{\partial}}{\partial p_i}\frac{\overrightarrow{\partial}}{\partial r_i}\Big)\,. \tag{5.19}$$

From the definition (5.17) it is clear that the local density can be written as

$$\rho(\mathbf{r}) = \rho(\mathbf{r},\mathbf{r}) = \int \frac{d^3p}{(2\pi\hbar)^3}\,\rho(\mathbf{r},\mathbf{p})\,, \tag{5.20}$$

As a very simple case we consider the Thomas-Fermi ($\hbar \to 0$) limit for the density matrix without pairing correlations (i.e., $\Delta = \kappa = 0$) at zero temperature. Quantum-mechanically the density matrix is in this case just given by the Fermi sea filled up to the Fermi energy μ, i.e., $\rho = \theta(-h)$. To leading order in $\hbar$ the Wigner transform of this expression gives $\rho(\mathbf{r},\mathbf{p}) = \theta[-h(\mathbf{r},\mathbf{p})]$. The corresponding (local) density reads

$$\rho(\mathbf{r}) = \frac{p_F^3(\mathbf{r})}{6\pi^2\hbar^3}\,, \tag{5.21}$$

with the local Fermi momentum

$$p_F(\mathbf{r}) = \sqrt{2m[\mu - V(\mathbf{r})]}\,\theta[\mu - V(\mathbf{r})]\,. \tag{5.22}$$

Eq. (5.21) together with Eq. (5.3) can easily be solved self-consistently [105, 131]. Since the pairing gaps and temperatures considered in this article are very small compared with the Fermi energy, we will use Eq. (5.21) also in the presence of pairing correlations and at non-zero temperatures. (The effect of pairing correlations and temperature on the density profile $\rho(\mathbf{r})$ was investigated in Ref. [131]). Furthermore, in this article we are not

interested in the details of the density profile $\rho(\mathbf{r})$. As shown in Ref. [105], the self-consistent solution for $\rho(\mathbf{r})$ can be described to good accuracy by approximating the self-consistent potential $V(\mathbf{r})$ again by a harmonic potential

$$V(\mathbf{r}) = \sum_{i=xyz} \frac{m\omega_i^2}{2} r_i^2 \,, \tag{5.23}$$

with "effective" frequencies $\omega_i > \omega_{0i}$ (we consider an attractive interaction, i.e., $g > 0$) and an appropriately readjusted chemical potential μ. In the remaining part of this article we will use the approximate potential (5.23).

In order to include the pairing correlations, one can also use the HFB equation (5.13) in the limit $\hbar \to 0$:

$$[\mathcal{H}(\mathbf{r},\mathbf{p}), \mathcal{R}(\mathbf{r},\mathbf{p})] = 0 \,. \tag{5.24}$$

This implies that, to leading order in $\hbar$, at each point $\mathbf{r}$ the solution $\mathcal{R}(\mathbf{r},\mathbf{p})$ as a function of $\mathbf{p}$ is given by the solution for a homogeneous system with the density corresponding to the local density at this point $\mathbf{r}$ [Local-Density Approximation (LDA)]:

$$\mathcal{R}(\mathbf{r},\mathbf{p}) = \frac{1}{2} - \frac{\mathcal{H}(\mathbf{r},\mathbf{p})}{2E(\mathbf{r},\mathbf{p})}\big(1 - 2f[E(\mathbf{r},\mathbf{p})]\big) \,, \tag{5.25}$$

with the definition $E(\mathbf{r},\mathbf{p}) = \sqrt{h^2(\mathbf{r},\mathbf{p}) + \Delta^2(\mathbf{r})}$. In terms of the Wigner transform $\kappa(\mathbf{r},\mathbf{p})$, the gap equation [Eq. (5.5)] can be written as

$$\Delta(\mathbf{r}) = g \int \frac{d^3p}{(2\pi\hbar)^3}\, \kappa(\mathbf{r},\mathbf{p}) \,. \tag{5.26}$$

Inserting the expression for $\kappa(\mathbf{r},\mathbf{p})$ corresponding to Eq. (5.25) into Eq. (5.26), we obtain the following non-linear equation for the gap:

$$\Delta(\mathbf{r}) = g \int \frac{d^3p}{(2\pi\hbar)^3}\, \frac{\Delta(\mathbf{r})}{2E(\mathbf{r},\mathbf{p})}\big(1 - 2f[E(\mathbf{r},\mathbf{p})]\big) \,. \tag{5.27}$$

As mentioned before, this equation is divergent and needs some regularization (see Refs. [105, 131, 207] for details).

Contrary to the Thomas-Fermi approximation for the unpaired density matrix, Eq. (5.21), which is valid if the potential can be regarded as constant on a length scale of the inverse Fermi momentum, the local-density approximation in the paired case is valid only if the potential is also constant on a length scale of the coherence length of the Cooper pairs. This latter condition is often not fulfilled. Therefore, in Refs. [104, 105] an alternative semiclassical method for the calculation of the gap has been proposed, which, however, results in an average gap (more precisely: gap averaged over the Fermi surface) of almost the same magnitude as the average gap obtained within the local density approximation.

5.3 Linear response to a slow rotation

In this section we will describe the formalism used for the calculation of the moment of inertia of a superfluid gas of trapped fermionic atoms. Looking at a system rotating with angular velocity Ω around the z axis, we can calculate the moment of inertia from

$$\Theta = \frac{\langle L_z \rangle}{\Omega} = \frac{2}{\Omega} \int \frac{d^3r\, d^3p}{(2\pi\hbar)^3}\, (r_x p_y - r_y p_x)\, \rho(\mathbf{r},\mathbf{p}) \,, \tag{5.28}$$

where $\rho(\mathbf{r},\mathbf{p})$ is the density matrix of the rotating system. Hence the main problem in calculating the moment of inertia is to calculate $\rho(\mathbf{r},\mathbf{p})$, from which also other interesting quantities like the current density (per spin state)

$$\mathbf{j}(\mathbf{r}) = \int \frac{d^3p}{(2\pi\hbar)^3}\,\frac{\mathbf{p}}{m}\rho(\mathbf{r},\mathbf{p}) \tag{5.29}$$

and the velocity field $\mathbf{v}(\mathbf{r}) = \mathbf{j}(\mathbf{r})/\rho(\mathbf{r})$ can be derived.

The system is put into rotation by rotating the external trapping potential around the z axis (of course, for this purpose the trapping potential must not be axially symmetric). In the rotating frame, however, the system is still in a stationary state. In this frame, the Hamiltonian receives the additional term

$$h_1 = -\bar{h}_1 = -\Omega L_z\,, \tag{5.30}$$

which for sufficiently small Ω can be treated as a perturbation. This perturbation induces a change of the density matrix, ρ_1, and of the pairing tensor, κ_1. The mean field potential is not changed to linear order in Ω, since L_z is a time-odd operator. Linearizing Eq. (5.13), we obtain

$$[\mathcal{H},\mathcal{R}_1] = -[\mathcal{H}_1,\mathcal{R}]\,, \tag{5.31}$$

where $\mathcal{H}$ and $\mathcal{R}$ denote the unperturbed quantities, while $\mathcal{H}_1$ and $\mathcal{R}_1$ refer to the deviations. Assuming that the unperturbed quantities ρ, κ, h, and Δ are diagonal (BCS approximation), we can solve Eq. (5.31) for ρ_1 and κ_1. (This is equivalent to solving the linearized Gorkov equations for the normal and anomalous Green's functions at equal times; see, e.g., Ref. [257].) The solution reads:

$$\rho_{1\,nn'} = F^{\rho h}_{nn'} h_{1\,nn'} + F^{\rho\Delta}_{nn'}\Delta_{1\,nn'}\,, \tag{5.32}$$

$$\kappa_{1\,nn'} = F^{\kappa h}_{nn'} h_{1\,nn'} + F^{\kappa\Delta}_{nn'}\Delta_{1\,nn'}\,, \tag{5.33}$$

where (with the short-hand notation $\rho=\rho_n$, $\rho'=\rho_{n'}$, $h=h_n$, $h'=h_{n'}$, $\kappa=\kappa_n$, $\kappa'=\kappa_{n'}$, etc.)

$$F^{\rho h}_{nn'} = \frac{(\rho-\rho')(h+h') - (\kappa-\kappa')(\Delta+\Delta')}{E^2-E'^2}\,, \tag{5.34}$$

$$F^{\rho\Delta}_{nn'} = \frac{(\rho+\rho'-1)(\Delta+\Delta') + (\kappa+\kappa')(h+h')}{E^2-E'^2}\,, \tag{5.35}$$

$$F^{\kappa h}_{nn'} = \frac{(\rho-\rho')(\Delta-\Delta') + (\kappa-\kappa')(h-h')}{E^2-E'^2}\,, \tag{5.36}$$

$$F^{\kappa\Delta}_{nn'} = \frac{(1-\rho-\rho')(h-h') + (\kappa+\kappa')(\Delta-\Delta')}{E^2-E'^2}\,, \tag{5.37}$$

In practice, Eq. (5.33) is an integral equation, since the change of the gap, Δ_1, on the r.h.s. is related to the change of the pairing tensor, κ_1, by the gap equation. In analogy to Eq. (5.26) the gap equation for the perturbed quantities reads

$$\Delta_1(\mathbf{r}) = g\int \frac{d^3p}{(2\pi\hbar)^3}\,\kappa_1(\mathbf{r},\mathbf{p})\,. \tag{5.38}$$

The solution of this integral equation contains some subtleties. For example, the divergence appearing in Eq. (5.38) as a consequence of the zero-range interaction has to be regularized in the same way as the correponding divergence of the unperturbed gap equation (5.26) (see appendix), and the derivations of Eq. (4.34) in Ref. [105], or the second equation after Eq. (16) in Ref. [169] are not very explicit about this point. However, these problems can be circumvented in the following way [43, 124, 262]: Suppose all single-particle

wave functions are multiplied by the same local phase $\exp[i\phi(\mathbf{r})]$. Then the HFB equation (5.13) can be rewritten in terms of the gauge-transformed matrices

$$\tilde{\mathcal{R}} = e^{i\Phi}\mathcal{R}e^{-i\Phi}\,, \tag{5.39}$$

$$\tilde{\mathcal{H}} = e^{i\Phi}\mathcal{H}e^{-i\Phi}\,, \tag{5.40}$$

where

$$\Phi = \begin{pmatrix} \phi & 0 \\ 0 & -\phi \end{pmatrix} \tag{5.41}$$

We will consider ϕ as small, i.e., of the order of the perturbation. Then, to linear order in the perturbation, the gauge transformed HFB equation reads

$$[\mathcal{H}, \tilde{\mathcal{R}}_1] = -[\tilde{\mathcal{H}}_1, \mathcal{R}]\,, \tag{5.42}$$

where

$$\tilde{\mathcal{R}}_1 = \mathcal{R}_1 + i[\Phi, \mathcal{R}]\,, \tag{5.43}$$

$$\tilde{\mathcal{H}}_1 = \mathcal{H}_1 + i[\Phi, \mathcal{H}]\,. \tag{5.44}$$

In the latter expression one has to take into account that h does not commute with ϕ. Explicitly, for a hamiltonian h of the form (5.10) and a local gap $\Delta(\mathbf{r})$ one obtains

$$\tilde{h}_1 = -\bar{\tilde{h}}_1 = -\Omega L_z - \frac{\hbar}{2m}\big(\mathbf{p}\cdot[\boldsymbol{\nabla}\phi(\mathbf{r})] + [\boldsymbol{\nabla}\phi(\mathbf{r})]\cdot\mathbf{p}\big)\,, \tag{5.45}$$

$$\tilde{\Delta}_1(\mathbf{r}) = \Delta_1(\mathbf{r}) + 2i\phi(\mathbf{r})\Delta(\mathbf{r})\,. \tag{5.46}$$

Together with the gauge-transformed gap equation

$$\tilde{\Delta}_1(\mathbf{r}) = g\int\frac{d^3p}{(2\pi\hbar)^3}\,\tilde{\kappa}_1(\mathbf{r},\mathbf{p})\,, \tag{5.47}$$

Eq. (5.42) is again a system of integral equations which for an arbitrary function $\phi(\mathbf{r})$ is completely equivalent to the original one, Eqs. (5.31) and (5.38). However, since the perturbation $\tilde{h}_1$ is time-odd, the change of the gap, $\tilde{\Delta}_1$, is purely imaginary and therefore can be eliminated by an appropriately chosen function $\phi(\mathbf{r})$. Physically, this choice of $\phi(\mathbf{r})$ corresponds to a transformation into the local rest frame of the Cooper pairs [238]. In this particular gauge the linearized HFB equation reduces to

$$\tilde{\rho}_{1\,nn'} = F^{\rho h}_{nn'}\tilde{h}_{1\,nn'}\,, \tag{5.48}$$

$$\tilde{\kappa}_{1\,nn'} = F^{\kappa h}_{nn'}\tilde{h}_{1\,nn'}\,, \tag{5.49}$$

and instead of Eq. (5.47) we have an equation which determines the phase $\phi(\mathbf{r})$:

$$0 \stackrel{!}{=} g\int\frac{d^3p}{(2\pi\hbar)^3}\,\tilde{\kappa}_1(\mathbf{r},\mathbf{p})\,. \tag{5.50}$$

We now proceed to the evaluation of Eq. (5.48). The unperturbed quantities ρ and κ entering in $F^{\rho h}_{nn'}$ [Eq. (5.34)] can be rewritten in terms of h and κ according to the BCS relations (5.14) and (5.15). In addition, as in Ref. [105], we replace Δ_n by its average value at the Fermi surface, Δ, because $F^{\rho h}$ and all other relevant

quantities are strongly peaked at ε_F. This allows us to write $F^{\rho h}_{nn'}$ as a function of two energies $\xi = h_n$ and $\xi' = h_{n'}$:

$$F^{\rho h}(\xi,\xi') = \frac{[1-f(E)-f(E')](\Delta^2+\xi\xi'-EE')}{2EE'(E+E')} + \frac{[f(E)-f(E')](\Delta^2+\xi\xi'+EE')}{2EE'(E-E')}\,, \tag{5.51}$$

where we have introduced the abbreviations $E=\sqrt{\xi^2+\Delta^2}$ and $E'=\sqrt{\xi'^2+\Delta^2}$. In contrast to Ref. [105], we will not drop the thermal quasiparticle occupation numbers $f(E)$ and $f(E')$. As described in detail in Ref. [105], the Wigner transform of an expression like Eq. (5.48) can be evaluated semiclassically in the following way. First we rewrite Eq. (5.48) as an operator equation:

$$\tilde{\rho}_1 = \int d\xi\, d\xi'\, F^{\rho h}(\xi,\xi')\delta(h-\xi)\tilde{h}_1\delta(h-\xi')\,. \tag{5.52}$$

Then we use the Fourier representation for the δ functions, i.e., $\delta(h-\xi)=\int dt/(2\pi\hbar)\,\exp[i(h-\xi)t/\hbar]$, and obtain

$$\tilde{\rho}_1 = \int \frac{d\bar{\xi}\,d\varepsilon\,dT\,dt}{(2\pi\hbar)^2}\,F^{\rho h}\Big(\bar{\xi}+\frac{\varepsilon}{2},\bar{\xi}-\frac{\varepsilon}{2}\Big)\,e^{-i\bar{\xi}T/\hbar}e^{-i\varepsilon t/\hbar}e^{ihT/2\hbar}\tilde{h}_1(t)e^{ihT/2\hbar}\,, \tag{5.53}$$

where we have introduced the notation

$$\tilde{h}_1(t) = e^{iht/\hbar}\tilde{h}_1 e^{-iht/\hbar}\,. \tag{5.54}$$

To leading order in $\hbar$ the Wigner transform of the product of the three operators in the end of Eq. (5.53) can be expressed as the product of their Wigner transforms [see Eq. (5.19)]. Then the integral over T gives a δ function of the form $\delta[h(\mathbf{r},\mathbf{p})-\bar{\xi}]$ and the integral over $\bar{\xi}$ becomes trivial.

However, for the operator product in $\tilde{h}_1(t)$ [Eq. (5.54)] we will not use the product rule. In this sense we resum certain $\hbar$ corrections to all orders. One can also say that, since the Wigner transform of Eq. (5.54) involves the classical trajectories (see below), the long-time information is preserved. On the other hand, developing the Wigner transform of Eq. (5.54) with the product rule (5.19) into powers of $\hbar$ would lead to the Wigner-Kirkwood $\hbar$ expansion, which is only valid in the short-time limit (see Ref. [201]). The different treatment of the operator products in Eqs. (5.53) and (5.54) is necessary for the following reason: The operator $\tilde{h}_1$ connects states with an energy difference of the order $\hbar\omega$. This is small compared with the Fermi energy, which is the relevant scale for the variable $\bar{\xi}$ [since the result $\tilde{\rho}_1(\mathbf{r},\mathbf{p})$ will be used in integrals over $\mathbf{p}$], but not necessarily small compared with the gap Δ, which is the relevant scale for the variable ε [this point will become clearer when we investigate the function $F^{\rho h}(\bar{\xi}+\varepsilon/2,\bar{\xi}-\varepsilon/2)$ explicitly].

In the case of the effective harmonic oscillator potential (5.23) the Wigner transform of Eq. (5.54) can be calculated exactly. The result reads

$$[\tilde{h}_1(t)](\mathbf{r},\mathbf{p}) = \tilde{h}_1[\mathbf{r}^{cl}(\mathbf{r},\mathbf{p};t),\mathbf{p}^{cl}(\mathbf{r},\mathbf{p};t)]\,, \tag{5.55}$$

where $\mathbf{r}^{cl}(\mathbf{r},\mathbf{p};t)$ and $\mathbf{p}^{cl}(\mathbf{r},\mathbf{p};t)$ are the classical orbits in the potential (5.23) corresponding to the initial conditions $\mathbf{r}^{cl}(\mathbf{r},\mathbf{p};0)=\mathbf{r}$ and $\mathbf{p}^{cl}(\mathbf{r},\mathbf{p};0)=\mathbf{p}$, which are given by

$$r_i^{cl}(\mathbf{r},\mathbf{p};t) = r_i\cos(\omega_i t) + \frac{p_i}{m\omega_i}\sin(\omega_i t)\,, \tag{5.56}$$

$$p_i^{cl}(\mathbf{r},\mathbf{p};t) = p_i\cos(\omega_i t) - m\omega_i r_i\sin(\omega_i t)\,. \tag{5.57}$$

Putting everything together, we obtain

$$\tilde{\rho}_1(\mathbf{r},\mathbf{p}) = \int d\varepsilon\, F^{\rho h}\Big(h(\mathbf{r},\mathbf{p})+\frac{\varepsilon}{2},h(\mathbf{r},\mathbf{p})-\frac{\varepsilon}{2}\Big)\int\frac{dt}{2\pi\hbar}\,e^{-i\varepsilon t/\hbar}\tilde{h}_1[\mathbf{r}^{cl}(\mathbf{r},\mathbf{p};t),\mathbf{p}^{cl}(\mathbf{r},\mathbf{p};t)]\,. \tag{5.58}$$

Now we proceed to the calculation of the response of $\tilde{\rho}_1$ to the external perturbation h_1, neglecting for the moment the reaction of the pairing field to the rotation, i.e., the $\mathbf{p}\cdot\boldsymbol{\nabla}\phi$ terms in Eq. (5.45). In Ref. [105] this contribution was called the "Inglis-Belyaev term" ρ_1^{IB}. In this case the Fourier transform in Eq. (5.58) [with $\tilde{h}_1$ replaced by $h_1 = -\Omega(r_x p_y - r_y p_x)$] can easily be evaluated with the aid of Eqs. (5.56) and (5.57). Inserting the result into Eq. (5.58) and observing that $F(\xi,\xi')$ is symmetric under the exchange of its arguments we obtain [the arguments of $h(\mathbf{r},\mathbf{p})$ will be suppressed for brevity]

$$\begin{aligned}\rho_1^{IB}(\mathbf{r},\mathbf{p}) = &-\frac{\Omega\omega_-}{2}\Big(\frac{r_x p_y}{\omega_y}+\frac{r_y p_x}{\omega_x}\Big)F^{\rho h}\Big(h+\frac{\hbar\omega_+}{2},h-\frac{\hbar\omega_+}{2}\Big)\\ &-\frac{\Omega\omega_+}{2}\Big(\frac{r_x p_y}{\omega_y}-\frac{r_y p_x}{\omega_x}\Big)F^{\rho h}\Big(h+\frac{\hbar\omega_-}{2},h-\frac{\hbar\omega_-}{2}\Big)\,,\end{aligned} \tag{5.59}$$

with the definition

$$\omega_\pm = \omega_y \pm \omega_x\,. \tag{5.60}$$

To simplify the expression (5.59) further we note that the distribution function $\rho(\mathbf{r},\mathbf{p})$ is changed only in the vicinity of the Fermi surface, provided the Fermi energy is large compared with $\hbar\omega_\pm$, Δ, and T. Formally this can be inferred from the fact that $F^{\rho h}(\bar{\xi}+\varepsilon/2,\bar{\xi}-\varepsilon/2)$ as a function of $\bar{\xi}$ is strongly peaked at $\bar{\xi}=0$, which leads us to the approximation

$$F^{\rho h}(\bar{\xi}+\varepsilon/2,\bar{\xi}-\varepsilon/2) \approx \Big[G\Big(\frac{\varepsilon}{2\Delta}\Big)-1\Big]\delta(\bar{\xi})\,, \tag{5.61}$$

with

$$G(x) = 1+\int d\bar{\xi}\,F^{\rho h}(\bar{\xi}+x\Delta,\bar{\xi}-x\Delta)\,. \tag{5.62}$$

At zero temperature the integral in Eq. (5.62) can be evaluated analytically, whereas the terms containing the quasiparticle occupation numbers $f(E)$ and $f(E')$ have to be integrated numerically. After some manipulations the function $G(x)$ can be written as

$$G(x) = \frac{\operatorname{arsinh}(x)}{x\sqrt{1+x^2}} + \frac{\Delta}{x}\int_0^\infty \frac{d\bar{\xi}}{\bar{\xi}}\Big(\frac{f(E_+)}{E_+}-\frac{f(E_-)}{E_-}\Big)\,, \tag{5.63}$$

with $E_\pm = \sqrt{(\bar{\xi}\pm x\Delta)^2+\Delta^2}$. Within the approximation (5.61) the change of the density matrix corresponding to the Inglis-Belyaev term finally takes the compact form

$$\rho_1^{IB}(\mathbf{r},\mathbf{p}) = \Omega\delta[h(\mathbf{r},\mathbf{p})]\Big[r_x p_y\Big(1-\frac{\omega_+G_- + \omega_-G_+}{\omega_+ + \omega_-}\Big) - r_y p_x\Big(1-\frac{\omega_+G_- - \omega_-G_+}{\omega_+ - \omega_-}\Big)\Big]\,, \tag{5.64}$$

with

$$G_\pm = G\Big(\frac{\hbar\omega_\pm}{2\Delta}\Big)\,. \tag{5.65}$$

Now we will consider also the change of the pairing field Δ, i.e., the phase $\phi(\mathbf{r})$. As mentioned before, this phase will be determined by Eq. (5.50), where $\tilde{\kappa}_1(\mathbf{r},\mathbf{p})$ is obtained from the Wigner transform of Eq. (5.49). Again we replace Δ_n and $\Delta_{n'}$ entering in $F^{\kappa h}_{nn'}$ by the average value Δ, which allows us to express $F^{\kappa h}_{nn'}$ as a function of two energies:

$$F^{\kappa h}(\xi,\xi') = -\frac{[1-f(E)-f(E')]\Delta(\xi-\xi')}{2EE'(E+E')} - \frac{[f(E)-f(E')]\Delta(\xi-\xi')}{2EE'(E-E')}\,. \tag{5.66}$$

Then the Wigner transform of Eq. (5.49) can be calculated semiclassically as given by Eq. (5.58) with $\tilde{\rho}_1$ and $F^{\rho h}$ replaced by $\tilde{\kappa}_1$ and $F^{\kappa h}$, respectively. As it was the case for $F^{\rho h}(\bar{\xi}+\varepsilon/2, \bar{\xi}-\varepsilon/2)$, the function $F^{\kappa h}(\bar{\xi}+\varepsilon/2, \bar{\xi}-\varepsilon/2)$ is strongly peaked at $\bar{\xi}=0$, and we approximate it by

$$F^{\kappa h}(\bar{\xi}+\varepsilon/2, \bar{\xi}-\varepsilon/2) \approx -\frac{\varepsilon}{2\Delta} G\Big(\frac{\varepsilon}{2\Delta}\Big)\delta(\bar{\xi})\,, \tag{5.67}$$

with

$$G(x) = -\frac{1}{x}\int d\bar{\xi}\, F^{\kappa h}(\bar{\xi}+x\Delta, \bar{\xi}-x\Delta)\,. \tag{5.68}$$

It turns out that the definitions (5.62) and (5.68) indeed define the same function $G(x)$, which is explicitly given by Eq. (5.63). Inserting the Wigner transform of Eq. (5.49) into Eq. (5.50), we obtain

$$0 = -g\int d\varepsilon\, \frac{\varepsilon}{2\Delta} G\Big(\frac{\varepsilon}{2\Delta}\Big)\int \frac{d^3p}{(2\pi\hbar)^3}\,\delta[h(\mathbf{r},\mathbf{p})]\int \frac{dt}{2\pi\hbar}\, e^{-i\varepsilon t/\hbar}\tilde{h}_1[\mathbf{r}^{cl}(\mathbf{r},\mathbf{p};t), \mathbf{p}^{cl}(\mathbf{r},\mathbf{p};t)]\,. \tag{5.69}$$

To solve this equation for the phase $\phi(\mathbf{r})$ we make the ansatz [105]

$$\phi(\mathbf{r}) = \alpha\frac{m r_x r_y}{\hbar}\,. \tag{5.70}$$

Then the last part of Eq. (5.69) is just the Fourier transform of $\tilde{h}_1 = -\Omega(r_x p_y - r_y p_x) - \alpha(r_x p_y + r_y p_x)$, which is readily evaluated with the aid of Eqs. (5.56) and (5.57). Due to the δ functions the remaining integrals are trivial, and Eq. (5.69) finally becomes

$$0 = \frac{igm^2 p_F(\mathbf{r}) r_x r_y}{8\pi^2\hbar^2\Delta}\left[\Omega\omega_+\omega_-(G_+ + G_-) + \alpha(\omega_+^2 G_+ + \omega_-^2 G_-)\right], \tag{5.71}$$

which has the solution

$$\alpha = -\Omega\frac{\omega_+\omega_-(G_+ + G_-)}{\omega_+^2 G_+ + \omega_-^2 G_-}\,. \tag{5.72}$$

Using this expression we can also calculate the change of the original pairing field, Δ_1: Since the change of the gauge-transformed pairing field [Eq. (5.46)] is zero, the original pairing field is modified according to

$$\Delta_1(\mathbf{r}) = -2i\Delta\phi(\mathbf{r}) = -\frac{2i\Delta\alpha m r_x r_y}{\hbar}. \tag{5.73}$$

Having calculated the phase $\phi(\mathbf{r})$, we can now evaluate Eq. (5.58) with the full $\tilde{h}_1$, i.e., including in addition to the Inglis-Belyaev term [Eq. (5.59)] also the response of the density matrix to the $\mathbf{p}\cdot\boldsymbol{\nabla}\phi$ terms. This second contribution to $\tilde{\rho}_1$, which we will call $\rho_1^{M_1}$, is obtained in the same way as discussed above for the first one, and the result reads

$$\rho_1^{M_1}(\mathbf{r},\mathbf{p}) = \alpha\delta[h(\mathbf{r},\mathbf{p})]\Big[r_x p_y\Big(1 - \frac{\omega_+ G_+ + \omega_- G_-}{\omega_+ + \omega_-}\Big) + r_y p_x\Big(1 - \frac{\omega_+ G_+ - \omega_- G_-}{\omega_+ - \omega_-}\Big)\Big]\,. \tag{5.74}$$

However, we are not interested in the change of the gauge-transformed density matrix, $\tilde{\rho}_1$, but of the original density matrix, ρ_1. According to Eq. (5.43) the relation between ρ_1 and $\tilde{\rho}_1$ is given by

$$\rho_1 = \tilde{\rho}_1 - i[\phi,\rho] = \rho_1^{IB} + \rho_1^{M_1} + \rho_1^{M_2}\,. \tag{5.75}$$

Due to the simple $\mathbf{r}$ dependence of ϕ, the Wigner transform of the commutator $[\phi, \rho]$ is identical to the Poisson bracket of the Wigner transforms of ϕ and ρ, i.e.

$$\rho_1^{M_2}(\mathbf{r},\mathbf{p}) = \hbar\phi(\mathbf{r})\overset{\leftrightarrow}{\Lambda}\rho(\mathbf{r},\mathbf{p}) = \alpha m\Big(r_x\frac{\partial}{\partial p_y} + r_y\frac{\partial}{\partial p_x}\Big)\rho(\mathbf{r},\mathbf{p})\,. \tag{5.76}$$

As we did before, we will assume that Δ and T are much smaller than the Fermi energy. Therefore we can write $\rho(\mathbf{r},\mathbf{p}) \approx \theta[-h(\mathbf{r},\mathbf{p})]$ and we obtain

$$\rho_1^{M_2}(\mathbf{r},\mathbf{p}) = -\alpha(r_x p_y + r_y p_x)\delta[h(\mathbf{r},\mathbf{p})]\,. \tag{5.77}$$

The total effect of the phase ϕ, i.e., of the reaction of the pairing field, on the density matrix, which in Ref. [105] was called the "Migdal term" ρ_1^M, is the sum of the two contributions $\rho_1^{M_1}$ and $\rho_1^{M_2}$:

$$\rho_1^M(\mathbf{r},\mathbf{p}) = -\alpha\delta[h(\mathbf{r},\mathbf{p})]\Big(r_x p_y\frac{\omega_+G_+ + \omega_-G_-}{\omega_+ + \omega_-} + r_y p_x\frac{\omega_+G_+ - \omega_-G_-}{\omega_+ - \omega_-}\Big)\,. \tag{5.78}$$

Together with the Inglis-Belyaev term, Eq. (5.64), and the explicit expression for α, Eq. (5.72), our final result for the change of the density matrix reads

$$\rho_1(\mathbf{r},\mathbf{p}) = \Omega\delta[h(\mathbf{r},\mathbf{p})]\Big(r_x p_y - r_y p_x - \frac{4G_+G_-(\omega_x^2 r_x p_y - \omega_y^2 r_y p_x)}{\omega_+^2 G_+ + \omega_-^2 G_-}\Big)\,. \tag{5.79}$$

Given the change of the density matrix, we can immediately calculate the current density $\mathbf{j}(\mathbf{r})$ [Eq. (5.29)] and the velocity field $\mathbf{v}(\mathbf{r})$:

$$\mathbf{j}(\mathbf{r}) = \rho(\mathbf{r})\mathbf{v}(\mathbf{r}) = \Omega\rho(\mathbf{r})\Big(r_x\mathbf{e}_y - r_y\mathbf{e}_x - \frac{4G_+G_-(\omega_x^2 r_x\mathbf{e}_y - \omega_y^2 r_y\mathbf{e}_x)}{\omega_+^2 G_+ + \omega_-^2 G_-}\Big)\,. \tag{5.80}$$

It is interesting to check explicitly that this current fulfils the continuity equation. In the rotating frame the continuity equation reads

$$\boldsymbol{\nabla}\cdot\mathbf{j}(\mathbf{r}) + \dot{\rho}(\mathbf{r}) - \Omega(\mathbf{e}_z\times\mathbf{r})\cdot\boldsymbol{\nabla}\rho(\mathbf{r}) = 0\,, \tag{5.81}$$

where $\dot{\rho}(\mathbf{r}) = 0$ in our case of a stationary rotation. Taking the divergence of Eq. (5.80), we get from the last term a contribution proportional to $[\boldsymbol{\nabla}\rho(\mathbf{r})]\cdot[\mathbf{e}_z\times\boldsymbol{\nabla}V(\mathbf{r})]$. This is zero, since the gradient of the density in Thomas-Fermi approximation [Eq. (5.21)], $\boldsymbol{\nabla}\rho(\mathbf{r})$, is parallel to $\boldsymbol{\nabla}V(\mathbf{r})$. Thus, the divergence of the current is equal to the divergence of the first two terms in Eq. (5.80), which exactly fulfil Eq. (5.81). Note that the contribution of the Migdal term is crucial in order to satisfy the continuity equation. The easiest way to see this is to consider the limit $\Delta\to\infty$. In this limit we have $G_\pm\to 1$ and $\rho_1^{IB}(\mathbf{r},\mathbf{p})\to 0$, which implies $\mathbf{j}^{IB}(\mathbf{r})\to 0$. Hence, with the Inglis-Belyaev contribution alone, Eq. (5.81) cannot be satisfied.

As observed in Ref. [105], the velocity field $\mathbf{v}(\mathbf{r})$ describes a mixture of rotational motion, corresponding to a velocity field proportional to $\mathbf{e}_z\times\mathbf{r}$, and irrotational motion, corresponding to a velocity field proportional to $\boldsymbol{\nabla}(r_x r_y)$. The ordinary rigid rotation is realized if $G_+ = G_- = 0$. This is the case if the temperature approaches the critical temperature T_c, where the gap vanishes [the temperature dependence of the function $G(x)$ will be discussed in Sec. 5.5], but it can also happen at zero temperature if $\Delta \ll \hbar\omega_\pm$, as discussed in Ref. [105]. Purely irrotational motion, as it is expected in homogeneous superfluids, is reached if $G_+ = G_- = 1$. This is only possible if the temperature is very low and if $\Delta \gg \hbar\omega_\pm$.

For completeness let us also discuss the change of the pairing tensor, $\kappa_1(\mathbf{r},\mathbf{p})$, which can be obtained in a way completely analogous to the calculation of the change of the density matrix, $\rho_1(\mathbf{r},\mathbf{p})$. The result reads

$$\kappa_1(\mathbf{r},\mathbf{p}) = \frac{2i\hbar\Omega}{m\Delta}\,\frac{\omega_+\omega_-G_+G_-}{\omega_+^2G_+ + \omega_-^2G_-}p_x p_y\delta[h(\mathbf{r},\mathbf{p})] - 2i\phi(\mathbf{r})\,\kappa(\mathbf{r},\mathbf{p})\,. \tag{5.82}$$

Since the last term is of the order $\hbar^{-1}$ [see Eq. (5.70)], it has been argued that a semiclassical description is possible only in the particular gauge where $\Delta + \Delta_1$ is real and where this term vanishes [124, 262].

5.4 Superfluid rotation in transport theory

The transport or hydrodynamical equations for superfluid systems can be derived by taking the $\hbar \to 0$ limit of the time-dependent Hartree-Fock-Bogoliubov (TDHFB) equation [201, 257, 262]

$$i\hbar\dot{\mathcal{R}} = [\mathcal{H}, \mathcal{R}]\,, \tag{5.83}$$

i.e., by replacing the Wigner transforms of the commutators in Eq. (5.83) by Poisson brackets of the Wigner transforms [43, 95, 124, 218, 262]. Due to the transformation into the rotating frame, we are dealing with a static problem, where the TDHFB equation (5.83) reduces to the HFB equation (5.13). Again we make use of the gauge transformation and retain only terms of linear order in the perturbation. Then, if $\phi(\mathbf{r})$ is chosen such that $\tilde{\Delta}_1$ vanishes [Eq. (5.50)], the leading order in $\hbar$ of Eq. (5.42) becomes

$$i\hbar h \overset{\leftrightarrow}{\Lambda} \tilde{\rho}_1 + 2\Delta\tilde{\kappa}_1 = -i\hbar\tilde{h}_1 \overset{\leftrightarrow}{\Lambda} \rho\,, \tag{5.84}$$

$$i\hbar\Delta \overset{\leftrightarrow}{\Lambda} \tilde{\rho}_1 - 2h\tilde{\kappa}_1 = i\hbar\tilde{h}_1 \overset{\leftrightarrow}{\Lambda} \kappa\,. \tag{5.85}$$

In this equation and in the remaining part of this section, h, ρ, κ, etc. denote the Wigner transforms of the corresponding operators; the arguments $\mathbf{r}$ and $\mathbf{p}$ are suppressed for brevity.

Let us first study the zero-temperature limit, $T = 0$. In this case the unperturbed quantities are given by $\rho = (1 - h/E)/2$ and $\kappa = \Delta/2E$ [see Eq. (5.25) in the limit $T \to 0$], and it is easy to show that $(\tilde{h}_1 \overset{\leftrightarrow}{\Lambda} \rho)h = (\tilde{h} \overset{\leftrightarrow}{\Lambda} \kappa)\Delta$. Thus, for $\Delta \neq 0$, the solution of Eqs. (5.84) and (5.85) reads

$$\tilde{\rho}_1 = 0\,, \tag{5.86}$$

$$\tilde{\kappa}_1 = -\frac{i\hbar}{2\Delta}(\tilde{h}_1 \overset{\leftrightarrow}{\Lambda} \rho)\,. \tag{5.87}$$

As we will see, the relation $\tilde{\rho}_1 = 0$ implies that the velocity field is completely irrotational independent of the magnitude of Δ, which is a well-known property of homogeneous superfluid systems at $T = 0$.

Now we are going to determine the phase ϕ. To that end we insert Eq. (5.87) into Eq. (5.50). If we make again the ansatz (5.70), we obtain the following equation:

$$0 = -\frac{ig\hbar}{2\Delta}\int \frac{d^3p}{(2\pi\hbar)^3}\Big((\Omega + \alpha)r_x\frac{\partial\rho}{\partial r_y} - (\Omega - \alpha)r_y\frac{\partial\rho}{\partial r_x}\Big)\,. \tag{5.88}$$

[Note that in this equation ρ still refers to the Wigner transform of the non-local density matrix, $\rho(\mathbf{r}, \mathbf{p})$.] It is clear that in general this equation does not have a solution for all $\mathbf{r}$, since the ansatz (5.70) is not general enough. But under certain assumptions it turns out that this ansatz is sufficient. Firstly, we assume that the gap $\Delta(\mathbf{r})$ is either replaced by a constant corresponding to its average value at the Fermi surface (as it was done in the previous section), or that $\Delta(\mathbf{r})$ is calculated within the LDA. In these both cases the function $\Delta(\mathbf{r})$ can formally be written as $\Delta[V(\mathbf{r})]$. Using this, we define the following short-hand notation:

$$\frac{d\rho}{dV} = \frac{d\rho}{dh}\,\frac{dh}{dV} + \frac{d\rho}{d\Delta}\,\frac{d\Delta}{dV} = -\frac{\Delta^2}{2E^3} + \frac{h\Delta}{2E^3}\,\frac{d\Delta}{dV}\,, \tag{5.89}$$

which allows us to write $\boldsymbol{\nabla}\rho = (d\rho/dV)\boldsymbol{\nabla}V$. Secondly, as in the previous section, we assume that the potential $V(\mathbf{r})$ is a harmonic oscillator. Then Eq. (5.88) becomes

$$0 = -\frac{ig\hbar m r_x r_y}{2\Delta}\int\frac{d^3p}{(2\pi\hbar)^3}\,\frac{d\rho}{dV}\left[\Omega(\omega_y^2-\omega_x^2)+\alpha(\omega_y^2+\omega_x^2)\right], \tag{5.90}$$

with the solution

$$\alpha = \alpha_0 = -\Omega\frac{\omega_y^2-\omega_x^2}{\omega_y^2+\omega_x^2}. \tag{5.91}$$

Not surprisingly, this result is identical to the $\hbar\to 0$ limit of Eq. (5.72), since for $T=0$ we have $G(0)=1$ and consequently $\lim_{\hbar\to 0} G_\pm = 1$.

As in the previous section, the phase ϕ implies a change of the density matrix, ρ_1, due to the inverse gauge transformation, which to leading order in $\hbar$ reads

$$\rho_1 = \tilde{\rho}_1 + \hbar\phi\overset{\leftrightarrow}{\Lambda}\rho. \tag{5.92}$$

As we have seen, the first term vanishes. Thus, to linear order in the perturbation, Eq. (5.92) can be rewritten in the following, more suggestive way:

$$\rho(\mathbf{r},\mathbf{p}) + \rho_1(\mathbf{r},\mathbf{p}) = \rho[\mathbf{r},\mathbf{p}+\hbar\boldsymbol{\nabla}\phi(\mathbf{r})]. \tag{5.93}$$

From this equation it follows immediately that the velocity field is given by

$$\mathbf{v}(\mathbf{r}) = -\frac{\hbar}{m}\boldsymbol{\nabla}\phi(\mathbf{r}), \tag{5.94}$$

which is completely irrotational. Note that this result does not depend on the form of $\phi(\mathbf{r})$ and the approximations made to calculate $\phi(\mathbf{r})$. It also does not at all depend on the magnitude of Δ, as long as $\Delta\neq 0$. It is rather a direct consequence of the vanishing of $\tilde{\rho}_1$, which in turn follows immediately from the $\hbar\to 0$ limit of the linearized HFB equations for time-odd perturbations and zero temperature. However, as we have seen in the previous section, in a small system where $\hbar\omega$ is of the same order of magnitude as Δ, the velocity field is not irrotational. Our conclusion is that one should be careful when applying transport theory to such systems.

So far we have considered only the zero-temperature limit. In the remaining part of this section we are going to consider also the case $T>0$. In this case it is difficult to solve the coupled Eqs. (5.84) and (5.85). However, if we in analogy to the previous section assume that the the unperturbed gap Δ is constant, we find the following solution for $\tilde{\rho}_1$ and $\tilde{\kappa}_1$:

$$\tilde{\rho}_1 = \Big(\frac{d\rho}{dh} - \frac{\Delta}{h}\frac{d\kappa}{dh}\Big)\tilde{h}_1 = \frac{df(E)}{dE}\tilde{h}_1, \tag{5.95}$$

$$\tilde{\kappa}_1 = -\frac{i\hbar}{2h}\frac{d\kappa}{dh}(\tilde{h}_1\overset{\leftrightarrow}{\Lambda}h). \tag{5.96}$$

If we again make the ansatz (5.70) and insert Eq. (5.96) into Eq. (5.50), we find $\alpha=\alpha_0$ as in the zero-temperature case [see Eq. (5.91)]. This could have been anticipated from the $\hbar\to 0$ limit of Eq. (5.72), which does not depend on the actual value of $G(0)$. Finally we are now going to calculate ρ_1. To that end we insert Eqs. (5.95) and (5.70) with $\alpha=\alpha_0$ into Eq. (5.92), and we obtain

$$\rho_1 = -\Omega\frac{df(E)}{dE}(r_xp_y - r_yp_x) - \alpha_0\Big(\frac{df(E)}{dE} - \frac{d\rho}{dh}\Big)(r_xp_y + r_yp_x). \tag{5.97}$$

Since $df(E)/dE$ and $d\rho/dh$ are both strongly peaked at the Fermi surface, we can make the same approximation as in the previous section, i.e., we replace the strongly peaked functions by δ functions with the appropriate strength. Noting that

$$\lim_{x\to 0} G(x) = 1 + \int d\xi \, \frac{\Delta^2}{\xi} \frac{d}{d\xi} \frac{f(E)}{E} = 1 + \int d\xi \, \frac{df(E)}{dE} \,, \tag{5.98}$$

we can write the result as

$$\rho_1 = \Omega[1 - G(0)]\delta(h)(r_x p_y - r_y p_x) - \alpha_0 G(0)\delta(h)(r_x p_y + r_y p_x) \,, \tag{5.99}$$

which is in perfect agreement with the $\hbar \to 0$ limit of Eqs. (5.64) and (5.78).

5.5 Results and discussion

Using the results for change of the non-local density matrix $\rho_1(\mathbf{r}, \mathbf{p})$ given in the previous sections, we can now calculate the moment of inertia. It should be remembered that an ideal Fermi gas at zero temperature behaves like a rigid body, i.e., the velocity field is given by $\mathbf{v}(\mathbf{r}) = \Omega \mathbf{e}_z \times \mathbf{r}$. Since the critical temperature for the BCS transition is very low, Θ will approach the rigid-body value Θ_{rigid} for $T \to T_c$. Using the Thomas-Fermi density profile (5.21) with the effective harmonic oscillator potential (5.23), we can immediately calculate Θ_{rigid}. The result reads

$$\Theta_{rigid} = \frac{\mu^4(\omega_x^2 + \omega_y^2)}{12\hbar^3 \omega_x^3 \omega_y^3 \omega_z} \,. \tag{5.100}$$

In terms of Θ_{rigid} the moment of inertia of the superfluid system as obtained from $\rho_1(\mathbf{r}, \mathbf{p})$ can be written as

$$\Theta = \Theta_{rigid}\Big(1 - \frac{8\omega_x^2\omega_y^2 G_+ G_-}{(\omega_x^2 + \omega_y^2)(\omega_+^2 G_+ + \omega_-^2 G_-)}\Big) \,. \tag{5.101}$$

In the $\hbar \to 0$ (transport) limit, where $G_\pm \to G(0)$, Eq. (5.101) reduces to

$$\Theta = \Theta_{rigid}\Big[1 - G(0) + G(0)\Big(\frac{\omega_y^2 - \omega_x^2}{\omega_y^2 + \omega_x^2}\Big)^2\Big] \,. \tag{5.102}$$

In fact, this formula can be understood very easily. The moment of inertia corresponding to the purely irrotational velocity field as it is expected for a large superfluid system at zero temperature, $\mathbf{v}(\mathbf{r}) = -\alpha_0 \boldsymbol{\nabla}(r_x r_y)$, is given by

$$\Theta_{irrot} = \Theta_{rigid}\Big(\frac{\omega_y^2 - \omega_x^2}{\omega_y^2 + \omega_x^2}\Big)^2 \,. \tag{5.103}$$

Within the two-fluid model a homogeneous system of density ρ is described as a mixture of a superfluid component of density ρ_s and a normal-fluid component of density ρ_n, with $\rho_s + \rho_n = \rho$. At $T = 0$ one has $\rho_s = \rho$ and $\rho_n = 0$, whereas at $T \geq T_c$ one has $\rho_s = 0$ and $\rho_n = \rho$. If this model was correct also for finite systems, one would expect that the moment of inertia is given by

$$\Theta = \frac{\rho_n}{\rho}\Theta_{rigid} + \frac{\rho_s}{\rho}\Theta_{irrot} \,. \tag{5.104}$$

This would be exactly Eq. (5.102), if we could identify $G(0)$ with ρ_s/ρ. In fact, the microscopic calculation of ρ_s for a homogeneous system gives [106]

$$\rho_s = \rho - \frac{1}{6\pi^2 m\hbar^3} \int_0^\infty dp \, p^4 \Big(- \frac{df(E)}{dE}\Big) \,, \tag{5.105}$$

with $E = \sqrt{(p^2/2m - \mu)^2 + \Delta^2}$. Noting that the integrand is peaked at $p = p_F$ and remembering $\rho = p_F^3/6\pi^2\hbar^3$, we rewrite this as

$$\frac{\rho_s}{\rho} \approx 1 + \int d\xi \, \frac{df(E)}{dE} \,. \tag{5.106}$$

with $\xi = p^2/2m - \mu$. As noted in Sec. 5.4, the r.h.s. of this equation is identical to $\lim_{x\to 0} G(x)$, so that we are left with

$$\frac{\rho_s}{\rho} = G(0) \,. \tag{5.107}$$

The previous paragraph can be summarized in the statement that the transport approach, corresponding to the leading order of the $\hbar$ expansion, reproduces the two-fluid model for homogeneous systems. It does not give any finite-size corrections, as can be seen from the fact that the result does not depend on the trapping frequencies, except for the purely geometrical dependence contained in Θ_{rigid} and Θ_{irrot}. In contrast to this, the method described in Sec. 5.3 is capable to describe the different behavior of the system depending on whether the trapping frequencies (multiplied by $\hbar$) are small or large compared with the gap Δ. This dependence is governed by the $G_\pm$ factors appearing in Eq. (5.101), resulting from the long-time behavior of the operator $\tilde{h}_1(t)$ [see discussion after Eq. (5.54)]. In order to reproduce this behavior within the $\hbar$ expansion, one would have to resum a certain class of corrections proportional to $\hbar\omega_\pm/\Delta$ to all orders, in particular if one wants to cover the whole range of possible parameters from $\hbar\omega_\pm \ll \Delta$ to $\hbar\omega_\pm \gg \Delta$.

Let us now proceed to a quantitative analysis. In order to calculate the moment of inertia Θ as a function of temperature, we need the temperature dependence of the gap Δ. As in Ref. [105], we will assume that it is described by the same universal function relating Δ/Δ_0 to T/T_c in homogeneous matter, where Δ_0 denotes the gap at $T = 0$ and $T_c = 0.567\Delta_0$. This universal function is given by the solution of the non-linear equation [153]

$$-\ln\Big(\frac{\Delta}{\Delta_0}\Big) = \int d\xi \, \frac{f(E)}{E} \,. \tag{5.108}$$

For completeness it is displayed in Fig. 5.1.

For the calculation of the moment of inertia we also need the function $G(\varepsilon/2\Delta)$, which depends on T via the temperature dependence of Δ discussed above, and via the explicit temperature dependence of the function $G(x)$ due to the thermal quasiparticle occupation numbers as given by Eq. (5.63). If only the temperature dependence of Δ was included, $G(\varepsilon/2\Delta)$ as a function of ε would become very strongly peaked at $\varepsilon = 0$ for $T \to T_c$. However, due to the explicit temperature dependence of the function $G(x)$, the peak is suppressed and as a function of ε the function $G(\varepsilon/2\Delta)$ even becomes more and more flat with increasing temperature, as shown in Fig. 5.2.

The decrease of $G(0)$ when T approaches T_c reflects the decrease of the superfluid fraction in the two-fluid model.

Next we have to specify the parameters of the system. As trapping frequency we choose $\hbar\omega_0 = \hbar(\omega_{0x}\omega_{0y}\omega_{0z})^{1/3} = 6.9\,\text{nK}$, corresponding to the trap used in the ^{7}Li experiment of Ref. [55]. Following Ref. [131], we assume that the trap is loaded with 573000 ^{6}Li atoms (i.e., 286500 atoms per spin state). The corresponding effective trapping frequency and chemical potential are given by $\hbar\omega = 8.21\,\text{nK}$ and $\mu = 983\,\text{nK}$ [105].

In the experiments the traps are generally very elongated, i.e. we have a strong deformation $\sigma = \omega_z/\omega_\perp$, where $\omega_\perp = \sqrt{\omega_x\omega_y}$ is the average frequencey in the xy plane. In our examples we choose $\sigma = 1/8$. This results in a rather high value for the average transverse frequency of $\hbar\omega_\perp = \hbar\omega/\sigma^{1/3} = 16.42\,\text{nK}$. In order to rotate the system around the z axis, at least a small deformation in the xy plane is necessary, which we parametrize by $\delta = \omega_x/\omega_y$. (In practice, the rotating deformation of the potential can be generated by a laser beam [160, 161].)

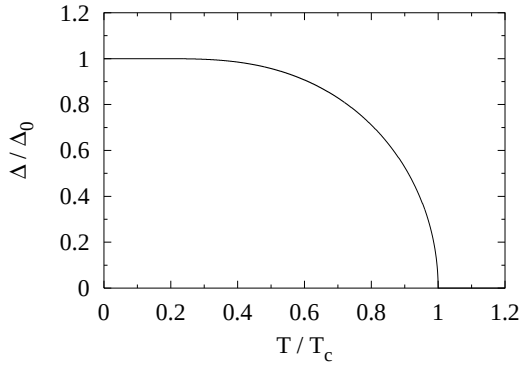

Figure 5.1: Universal function for the temperature dependence of the gap ($T_c = 0.567\Delta_0$).

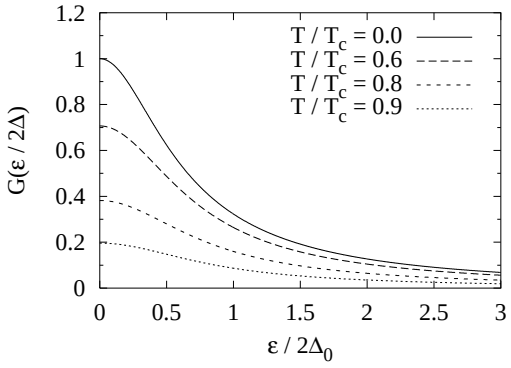

Figure 5.2: Behavior of the function $G(\varepsilon/2\Delta)$ for different temperatures between 0 and T_c.

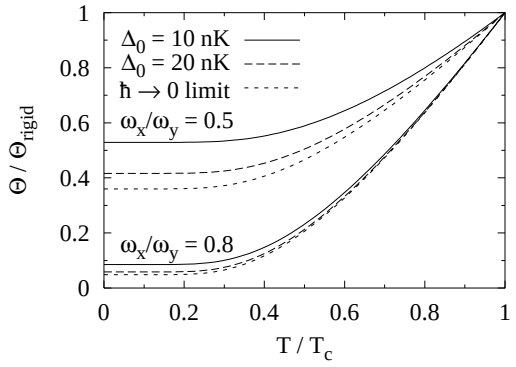

Figure 5.3: Moment of inertia as a function of T/T_c for small ($\omega_x/\omega_y = 0.8$) and large ($\omega_x/\omega_y = 0.5$) deformations in the xy plane and two values of Δ_0 (10 and 20 nK). The short-dashed lines correspond to the $\hbar \to 0$ limit.

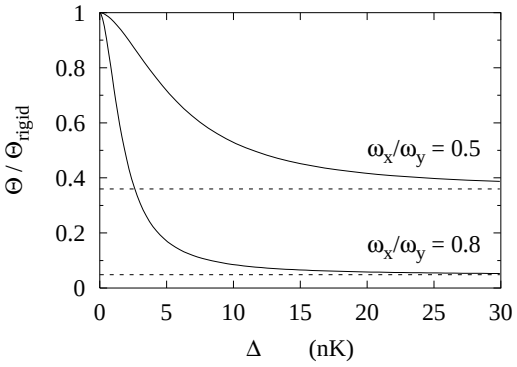

Figure 5.4: Moment of inertia for zero temperature as a function of Δ for small ($\omega_x/\omega_y = 0.8$) and large ($\omega_x/\omega_y = 0.5$) deformations in the xy plane. The dashed lines indicate the corresponding irrotational limits.

The main uncertainty comes from the gap at zero temperature, Δ_0. Note that the coupling constant g does not appear explicitly. The moment of inertia depends on the interaction only via Δ, which can be written as a function of T and Δ_0. The value of the critical temperature $T_c = 0.567\Delta_0$ is still under investigation. In addition, the s-wave scattering length a of the atoms, and consequently g, Δ_0, and T_c, can be tuned in the experiments by a magnetic field due to the presence of Feshbach resonances. Therefore we will treat Δ_0 as a free parameter. As a rough estimate, using the scattering length $a = -2160a_0$ [2], where a_0 is the Bohr radius, one obtains that the gap Δ_0 averaged over the Fermi surface is of the order of magnitude of 15 nK [105], i.e., of the same order of magnitude as the transverse trapping frequency $\omega_\perp$.

In Fig. 5.3 we display the moment of inertia as a function of the temperature for two different deformations δ. The lower curves correspond to a very small deformation, $\delta = 0.8$. In this case the moment of inertia at $T = 0$ is very small. When T approaches T_c, the normal-fluid component becomes more and more important and consequently the moment of inertia increases until it finally reaches the rigid-body value at $T = T_c$. Qualitatively the behavior is similar in the case of a strong deformation in the xy plane (upper curves), except

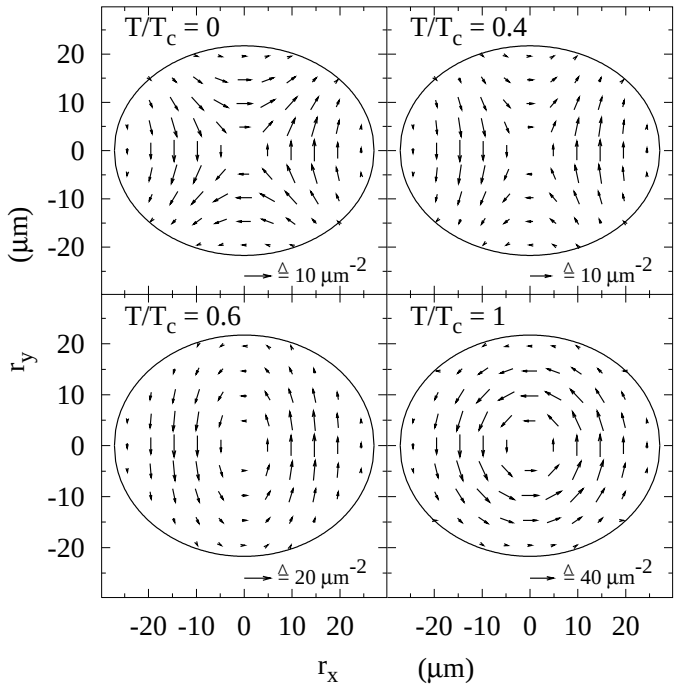

Figure 5.5: Current density divided by the angular velocity of the rotation, $\mathbf{j}/\Omega$, in the xy plane ($r_z = 0$) for $\omega_x/\omega_y = 0.8$, $\Delta_0 = 20\,\mathrm{nK}$, and four different temperatures: $T/T_c = 0$, 0.4, 0.6, and 1.

that in this case the whole curve is shifted upwards, mainly due to the much larger value of Θ_{irrot}. The difference between the three curves shown for each deformation will be discussed below.

In order to illustrate the origin of the temperature dependence of Θ, we show in Fig. 5.5 the current distributions for the case $\delta = 0.8$ for four temperatures between $T = 0$ and $T = T_c$. One can clearly see the continuous transition from the irrotational motion at $T = 0$, resulting in a small angular momentum and therefore a small moment of inertia, to the rigid motion at $T = T_c$.

Now we are going to discuss the differences between the three curves shown in Fig. 5.3 for each deformation. The short-dashed lines correspond to the results obtained within the $\hbar \to 0$ approach, Eq. (5.102). The long-dashed and solid lines were obtained from Eq. (5.101), i.e., they take into account the difference between $G_\pm$ and $G(0)$, resulting from the long-time behavior of the operator $\tilde{h}_1(t)$, Eq. (5.54). From the definition (5.65) it is clear that this difference is less important for large values of Δ, and indeed the long-dashed lines, corresponding to $\Delta_0 = 20\,\mathrm{nK}$, are closer to the $\hbar \to 0$ results than the solid lines, corresponding to $\Delta_0 = 10\,\mathrm{nK}$. More precisely, the criterion for the validity of the $\hbar \to 0$ approach seems to be $\hbar\omega_\perp \ll \Delta_0$ rather than $\hbar\omega_\perp \ll \Delta$, as one might expect. This surprising fact can be understood by looking at Fig. 5.2: Whatever is the actual value of the temperature T [i.e., of $\Delta(T)$], the value of $G(\varepsilon/2\Delta)$ can always be replaced by $G(0)$ if $\varepsilon/2\Delta_0 \ll 1$.

To show more clearly the non-trivial dependence of Θ on Δ, we show in Fig. 5.4 the moment of inertia for zero temperature as a function of Δ for the same deformations as in Fig. 5.3. The irrotational limit, indicated by the dashed lines, is reached for $\Delta \to \infty$. If Δ is much smaller than $\hbar\omega_-$ ($3.67\,\mathrm{nK}$ in the case $\delta = 0.8$ and $11.61\,\mathrm{nK}$ in the case $\delta = 0.5$, respectively), the moment of inertia even approaches the rigid body value, and the $\hbar$ expansion fails completely. For example, in nuclear physics strong deviations from the irrotational value are quite common [96, 169].

Finally let us briefly discuss the question whether the moment of inertia is suitable to detect the superfluidity in experiments. In principle the moment of inertia can be measured directly by measuring the rotational energy

$$E_{rot} = \frac{\Theta}{2}\Omega^2 \,. \tag{5.109}$$

Since the rotation does not change the potential energy (at least not to linear order in Ω), the rotational energy is equal to the difference of the release energies E_{rel} of the rotating system and of the non-rotating system. (The release energy E_{rel} is the total energy of all particles after the trapping potential has been switched off, i.e., the sum of the kinetic energy E_{kin} and of the interaction energy E_{int} of the trapped system.) A disadvantage of the direct measurement of E_{rot} is that it requires two identical systems, one in rotation and one at rest. As a rough estimate we approximate the release energy E_{rel} by the kinetic energy E_{kin} of the particles in the effective harmonic potential (5.23),

$$E_{kin} = 2\int \frac{d^3r\, d^3p}{(2\pi\hbar)^3}\, \frac{\mathbf{p}^2}{2m}\rho(\mathbf{r},\mathbf{p}) = \frac{\mu^4}{8\hbar^3\omega_x\omega_y\omega_z} \,. \tag{5.110}$$

Hence, as a function of the average transverse trapping frequency $\omega_\perp = \sqrt{\omega_x\omega_y}$ and the deformation $\delta = \omega_x/\omega_y$ we obtain

$$\frac{E_{rot}}{E_{kin}} = \frac{1+\delta^2}{3\delta}\frac{\Theta}{\Theta_{rigid}}\Big(\frac{\Omega}{\omega_\perp}\Big)^2 \,. \tag{5.111}$$

Since we used linear response theory, our results are valid only for slow rotations, $\Omega \ll \omega_\perp$. In particular the angular velocity must be small enough in order to avoid the creation of vortices. For an optimistic estimate we choose $\Omega = 0.4\omega_\perp$. Since the difference of Θ between $T = T_c$ and $T = 0$ is most pronounced for small deformation (see Fig. 5.3), we choose $\delta = 0.8$. Using these numbers we find $E_{rot}/E_{kin} \approx 0.1 \times \Theta/\Theta_{rigid}$, i.e., the moment of inertia might indeed be measurable.

5.6 Summary and conclusions

In this article we have discussed the temperature dependence of the moment of inertia of a Fermi gas trapped in a slowly rotating trapping potential. The assumption of a slow rotation allowed us to use linear response theory (RPA), but it is clear that in this way certain interesting effects like the creation of vortices could not be considered, since they depend non-linearly on the angular velocity Ω of the rotation.

In Sec. 5.3 we derived the density matrix of the rotating system using a semiclassical method similar to the one described in Ref. [105], but now taking into account the thermal quasiparticle occupation numbers, which were neglected in Ref. [105] and which give rather important contributions. One important point is that the method takes into account that the energy difference $\hbar\omega_\pm$ of the states connected by the perturbation hamiltonian (i.e., essentially by L_z) is not necessarily negligible in comparison with the gap Δ. This leads to a non-trivial behavior of the density matrix on $\hbar\omega_\pm/\Delta$. These effects can also be regarded as finite-size effects, since $\hbar\omega_\pm$ vanishes in homogeneous systems.

In Sec. 5.4 we presented an alternative method for the calculation of the density matrix, where only the leading order of the $\hbar$ expansion is retained. This is equivalent to the transport or hydrodynamical approach which is often used in the literature [31, 168, 271]. The qualitative difference between the results obtained within the two approaches is that the velocity field obtained in Sec. 5.3 has irrotational and rotational contributions at all temperatures, whereas the transport approach presented in Sec. 5.4 gives a purely irrotational velocity field at zero temperature, as it is the case in homogeneous systems. The dependence on $\hbar\omega_\pm/\Delta$ mentioned above is missed within this approach.

In Sec. 5.5 we used the density matrices obtained in the preceding sections for the calculation of the moment of inertia. The result can qualitatively be understood within the two-fluid model, which describes the superfluid system as a mixture of a superfluid and a normal-fluid component. The density of the normal-fluid component is zero at $T = 0$ and approaches the total density for $T \to T_c$. We have shown that the transport approach exactly reproduces this two-fluid model. Somewhat surprisingly, the condition for the transport approach to be valid turns out to be $\hbar\omega \ll \Delta_0$, where Δ_0 is the value of the gap at $T = 0$. This is less restrictive than the condition $\hbar\omega \ll \Delta$, in particular for temperatures near T_c.

Within the transport approach, the moment of inertia increases smoothly from the irrotational limit at $T = 0$ to the rigid-body value at $T = T_c$. This is a consequence of the increasing density of the normal-fluid component of the two-fluid model. If the condition $\hbar\omega \ll \Delta_0$ is not fulfilled, the behavior is qualitatively similar, but the moment of inertia is always larger than it is within the transport approach, because in this case the rotational contributions to the velocity field are always non-zero due to the finite-size effects mentioned above. In both cases, the smoothly increasing moment of inertia as a function of temperature can be obtained only if the thermal quasiparticle occupation numbers are properly included in the calculation. It is not sufficient to perform a zero-temperature calculation and then replace the gap Δ by the temperature-dependent gap $\Delta(T)$.

Looking at the size of the error made by neglecting the finite-size effects, we conclude that for the trapped fermionic atoms, where $\hbar\omega \lesssim \Delta_0$, the hydrodynamical approach is just at the limit of its applicability. However, we would like to point out that there are other physical situations, where $\hbar\omega > \Delta_0$, and where finite-size corrections are crucial. For example, the moments of inertia of rotating superfluid nuclei ($T = 0$) have at least twice the irrotational value [96]. Also for the description of superconducting metallic grains in a weak magnetic field, corresponding to a perturbation $h_1 = (e/mc)\mathbf{p} \cdot \mathbf{A}(\mathbf{r}) = (e/mc)B_z L_z$ (if $\mathbf{B}$ is parallel to the z axis) and therefore being formally equivalent to a slow rotation, these corrections might be important.

The method used in Sec. 5.3 for the semiclassical solution of the RPA in superfluid systems can also be extended to the dynamical case, i.e., to time-dependent perturbations. In this way collective excitations of the superfluid system, in particular the change of their frequencies compared with the normal-fluid phase, can be described. So far the collective modes in the superfluid phase have been studied either within the hydrodynamical approach [31, 271] or quantum-mechanically for the case of spherical symmetry and moderate numbers of particles [64].

Acknowledgments

We thank M. Farine and X. Viñas for valuable comments and discussions. One of us (M.U.) acknowledges support by the Alexander von Humboldt foundation (Germany) as a Feodor-Lynen fellow.

Appendix

5.A Alternative derivation of the Migdal term

In Sec. 5.3 we derived the change of the pairing field, $\Delta_1(\mathbf{r})$, via a gauge transformation. Here we will present an alternative method, which is more direct, but also somewhat more difficult. We will solve the original integral equation for Δ_1 which one obtains by inserting Eq. (5.33) into Eq. (5.38):

$$\Delta_1(\mathbf{r}) = \Delta_1^{IB}(\mathbf{r}) + \Delta_1^{M}(\mathbf{r}) = g \int \frac{d^3p}{(2\pi\hbar)^3} \left[\kappa_1^{IB}(\mathbf{r},\mathbf{p}) + \kappa_1^{M}(\mathbf{r},\mathbf{p})\right]. \tag{5.112}$$

with

$$\kappa_{1\,nn'}^{IB} = F_{nn'}^{\kappa h} h_{1\,nn'}\,, \tag{5.113}$$

$$\kappa_{1\,nn'}^{M} = F_{nn'}^{\kappa\Delta} \Delta_{1\,nn'}\,. \tag{5.114}$$

The Wigner transforms of these two contributions to κ_1 can be calculated semiclassically as given by Eq. (5.58) with $\tilde{\rho}_1$ replaced by κ_1^{IB} and κ_1^M, respectively, and $F^{\rho h}$ replaced by $F^{\kappa h}$ and $F^{\kappa\Delta}$, respectively.

The first term in Eq. (5.112), Δ_1^{IB}, has already been evaluated in Sec. 5.3 [term proportional to Ω in Eq. (5.71)] with the result

$$\Delta_1^{IB}(\mathbf{r}) = \frac{igm^2 p_F(\mathbf{r}) r_x r_y}{8\pi^2\hbar^2\Delta}\Omega\omega_+\omega_-(G_+ + G_-)\,. \tag{5.115}$$

Now we turn to the evaluation of the second term, Δ_1^M. The explicit expression for $F^{\kappa\Delta}(\xi,\xi')$ reads

$$F^{\kappa\Delta}(\xi,\xi') = \frac{1-2f(E)}{4E} + \frac{1-2f(E')}{4E'} - \frac{[1-f(E)-f(E')](\xi-\xi')^2}{4EE'(E+E')} - \frac{[f(E)-f(E')](\xi-\xi')^2}{4EE'(E-E')}\,, \tag{5.116}$$

which in analogy to $F^{\rho h}(\xi,\xi')$ and $F^{\kappa h}(\xi,\xi')$ can be approximated by

$$F^{\kappa\Delta}\Big(\bar{\xi}+\frac{\varepsilon}{2},\bar{\xi}-\frac{\varepsilon}{2}\Big) \approx \frac{1-2f(\bar{E})}{2\bar{E}} - \Big(\frac{\varepsilon}{2\Delta}\Big)^2 G\Big(\frac{\varepsilon}{2\Delta}\Big)\delta(\bar{\xi})\,, \tag{5.117}$$

with $\bar{E} = \sqrt{\bar{\xi}^2+\Delta^2}$. Using this approximation we get [the arguments of the functions $h(\mathbf{r},\mathbf{p})$ and $E(\mathbf{r},\mathbf{p})$ are omitted for brevity]

$$\Delta_1^M(\mathbf{r}) = g\int\frac{d^3p}{(2\pi\hbar)^3}\Big[\frac{1-2f(E)}{2E}\Delta_1(\mathbf{r}) - \delta(h)\int d\varepsilon\Big(\frac{\varepsilon}{2\Delta}\Big)^2 G\Big(\frac{\varepsilon}{2\Delta}\Big)\int\frac{dt}{2\pi\hbar}\,e^{-i\varepsilon t/\hbar}\Delta_1[\mathbf{r}^{cl}(\mathbf{r},\mathbf{p};t)]\Big]\,. \tag{5.118}$$

At this stage the disadvantage of the present method as compared with the method used in Sec. 5.3 becomes obvious, since we encounter a divergent integral over d^3p, whereas in Sec. 5.3 all expressions were finite. This divergence is the same one which also appears in the gap equation (5.27) for the unperturbed gap in local-density approximation. If we assume that this equation is regularized in some way, we can use it to get rid of the divergence in Eq. (5.118), and we obtain

$$\Delta_1^M(\mathbf{r}) = \Delta_1(\mathbf{r}) + g\int\frac{d^3p}{(2\pi\hbar)^3}\,\delta(h)\int d\varepsilon\Big(\frac{\varepsilon}{2\Delta}\Big)^2 G\Big(\frac{\varepsilon}{2\Delta}\Big)\int\frac{dt}{2\pi\hbar}\,e^{-i\varepsilon t/\hbar}\Delta_1[\mathbf{r}^{cl}(\mathbf{r},\mathbf{p};t)]\,. \tag{5.119}$$

As we will see, the integral equation (5.112) can be solved by the ansatz (5.73). With this ansatz the Fourier transform in Eq. (5.119) can easily be evaluated and we obtain

$$\Delta_1^M(\mathbf{r}) = \Delta_1(\mathbf{r}) + \frac{igm^2 p_F(\mathbf{r}) r_x r_y}{8\pi^2\hbar^2\Delta}\alpha(\omega_+^2 G_+ + \omega_-^2 G_-)\,. \tag{5.120}$$

The coefficient α can now be determined by inserting Eqs. (5.115) and (5.120) into Eq. (5.112). The solution, of course, coincides with Eq. (5.72).

However, we have to admit that the above arguments concerning the divergence in Eq. (5.118) are a little bit hand-waving. For example, Eq. (5.27) (including an appropriate regularization) is valid only in the local-density approximation, and it does not allow for a constant gap Δ, while we have for simplicity assumed that Δ is a constant in order to derive Eq. (5.118). Such inconsistencies do not appear within the formalism presented in Sec. 5.3.

It remains to show that the Migdal term, calculated as the second term of Eq. (5.32), is consistent with the result given in Eq. (5.78). This can be done with the aid of the explicit expression for $F^{\rho\Delta}$, which turns out to be

$$F^{\rho\Delta}(\xi,\xi') = -F^{\kappa h}(\xi,\xi')\,, \tag{5.121}$$

and the Fourier transform of $\Delta_1[\mathbf{r}^{cl}(\mathbf{r},\mathbf{p};t)]$.

6 Pair breaking in rotating Fermi gases

Michael Urban and Peter Schuck, Phys. Rev. A 78, 011601 (2008)

We study the pair-breaking effect of rotation on a cold Fermi gas in the BCS-BEC crossover region. In the framework of BCS theory, which is supposed to be qualitatively correct at zero temperature, we find that in a trap rotating around a symmetry axis, three regions have to be distinguished: (A) a region near the rotational axis where the superfluid stays at rest and where no pairs are broken, (B) a region where the pairs are progressively broken with increasing distance from the rotational axis, resulting in an increasing rotational current, and (C) a normal-fluid region where all pairs are broken and which rotates like a rigid body. Due to region B, density and current do not exhibit any discontinuities.

The surprising properties of superfluids become most evident if one looks at rotating systems. But the rotation does not only reveal the superfluidity, it can also destroy it. To give an example, in nuclear physics, the strong reduction of the nuclear moment of inertia compared to its rigid-body value is a direct consequence of superfluidity due to pairing correlations. But with increasing angular momentum, the pairing correlations are progressively destroyed and the moment of inertia increases to its rigid-body value. This pair-breaking effect of rotation was studied many years ago [100, 123].

In trapped atomic Fermi gases, the picture is somewhat different, since, contrary to the situation in atomic nuclei, the coherence length is much smaller than the system size. It is therefore possible to create quantized vortices or even vortex lattices [275], which allow the system to stay superfluid while rotating.

However, in a recent paper by Bausmerth, Recati, and Stringari [37] it has been argued that it may be possible to put a trapped Fermi gas adiabatically into rotation without creating vortices. In that paper, the destruction of superfluidity by rotation is described in a way which is very different from the nuclear physics case: Instead of decreasing the value of the pairing gap with increasing angular velocity, the authors assume that the system separates into a paired and an unpaired phase, while the properties of the paired phase itself are not affected by the rotation. The authors consider the unitary limit, where the energy densities of the paired and unpaired phases are known from Quantum-Monte-Carlo (QMC) simulations [22, 70]. The phase boundary between the paired and the unpaired phases is determined by energy minimization: Near the rotational axis, the system prefers to stay superfluid, i.e., to stay at rest, since the paired phase has a lower energy density than the unpaired one. But beyond a certain distance from the rotational axis, the centrifugal energy which the system could win if it participated in the rotation becomes equal to the energy which is needed to break the pairs. Hence, the non-rotating superfluid core is surrounded by a rotating normal-fluid phase. At the interface separating the two phases, the density and the current are discontinuous.

This picture is very intuitive, but it is lacking the microscopic understanding of the pair-breaking mechanism. In the present paper we will therefore describe the rotating Fermi gas in the framework of BCS theory. The rotation is most easily described in the rotating frame, where the hamiltonian $\hat{H}$ (minus the chemical potential μ times the particle number $\hat{N}$) is given by

$$\hat{H}-\mu\hat{N}=\int d^3r\Big[\hat{\psi}^\dagger(\mathbf{r})\Big(\frac{\mathbf{p}^2}{2m}+V(\mathbf{r})-\Omega L_z-\mu\Big)\hat{\psi}(\mathbf{r})+g\hat{\psi}^\dagger_\uparrow(\mathbf{r})\hat{\psi}^\dagger_\downarrow(\mathbf{r})\hat{\psi}_\downarrow(\mathbf{r})\hat{\psi}_\uparrow(\mathbf{r})\Big]\,, \tag{6.1}$$

where $\hat{\psi}$ is the Fermion field operator with components for (pseudo-)spin up ($\uparrow$) and down ($\downarrow$), m is the atom mass, $\mathbf{p}=-i\hbar\boldsymbol{\nabla}$ and $\mathbf{L}=\mathbf{r}\times\mathbf{p}$ are momentum and angular momentum, respectively, $V(\mathbf{r})=m(\omega_z^2z^2+\omega_\perp^2r_\perp^2)/2$ is the axially symmetric trap potential and $g<0$ is the coupling constant. The system is supposed to rotate with angular velocity Ω around the symmetry (z) axis of the potential.

If the system is large enough, such that the coherence length is small compared with the oscillator length associated with the trap potential, we can make use of the Thomas-Fermi (TF) or local-density approximation (LDA), which amounts to treating the system at each point $\mathbf{r}$ as uniform with a local chemical potential

$\mu_{loc}(\mathbf{r}) = \mu - V(\mathbf{r})$. Then $\mathbf{p}$ becomes a number instead of an operator, and the "cranking" term ΩL_z can conveniently be written as $\Omega L_z = \mathbf{v}(\mathbf{r}) \cdot \mathbf{p}$, where $\mathbf{v}(\mathbf{r}) = \mathbf{\Omega} \times \mathbf{r}$ is the velocity field corresponding to a rigid rotation. All quantities depend only parametrically on $\mathbf{r}$ via $\mu_{loc}(\mathbf{r})$ and $\mathbf{v}(\mathbf{r})$.

The gap, density, and current can all be derived from the normal and anomalous Matsubara Green's functions $\mathcal{G}$ and $\mathcal{F}^\dagger$ [106]. They have to satisfy the Gorkov equations, which in the presence of the cranking term ΩL_z become

$$(i\hbar\omega_n - \xi + \mathbf{v}\cdot\mathbf{p})\mathcal{G} + \Delta\mathcal{F}^\dagger = \hbar\,, \tag{6.2}$$

$$(i\hbar\omega_n + \xi + \mathbf{v}\cdot\mathbf{p})\mathcal{F}^\dagger + \Delta^*\mathcal{G} = 0\,. \tag{6.3}$$

where we introduced the abbreviation $\xi = \xi(\mathbf{r},\mathbf{p}) = p^2/(2m) - \mu_{loc}(\mathbf{r})$, ω_n denotes a fermionic Matsubara frequency, and $\Delta(\mathbf{r})$ is the gap. Note that we are neglecting the Hartree mean field, but anyway it would not qualitatively change our results in the BCS-BEC crossover regime [185]. Eqs. (6.2) and (6.3) can readily be solved for $\mathcal{G}$ and $\mathcal{F}$. They are formally similar to those describing pairing between particles with unbalanced populations (see, e.g., Ref. [156]), except that here the chemical potentials for the two spins are equal and the asymmetry is between states with opposite momenta ($\mathbf{p}$ and $-\mathbf{p}$).

In the case of a system without superfluid flow (like in our axially symmetric trap, as long as there are no vortices), the gap can be assumed to be real ($\Delta = \Delta^*$). The gap equation is obtained in the usual way by summing $\mathcal{F}$ over ω_n and integrating over $\mathbf{p}$, with the result

$$\Delta = -\frac{4\pi\hbar^2 a}{m}\int\frac{d^3p}{(2\pi\hbar)^3}\Big(\frac{\Delta}{2E}[1 - f(E_+) - f(E_-)] - \frac{m\Delta}{p^2}\Big)\,, \tag{6.4}$$

where we defined the quasiparticle energies $E_\pm = E \pm \mathbf{p}\cdot\mathbf{v}$, with $E = \sqrt{\xi^2 + \Delta^2}$, and $f(E) = 1/(e^{E/(k_BT)} + 1)$ denotes the Fermi function, T being the temperature and k_B the Boltzmann constant. In Eq. (6.4), the divergence of the gap equation due to the contact interaction has been regularized in the usual way by expressing the coupling constant g in terms of the s-wave scattering length a [207].

We are mainly interested in the BCS-BEC crossover regime, where it is known that the BCS description fails at higher temperatures, and in particular the BCS prediction for the critical temperature T_c is much too high. However, at zero temperature, BCS theory gives a reasonable description throughout the crossover. We will therefore restrict ourselves to the zero-temperature case, in which the Fermi function reduces to a step function, $f(E) = \theta(-E)$. Hence, the factor $[1 - f(E_+) - f(E_-)]$ is equal to 1 if both E_+ and E_- are positive and 0 otherwise (at most one of the two energies E_+ and E_- can be negative). In other words, states with $E_\pm < 0$ are excluded from pairing. In order to better understand the role of these states, let us look at the occupation numbers $\rho(\mathbf{r},\mathbf{p})$, which are obtained by summing $\mathcal{G}$ over ω_n:

$$\rho(\mathbf{r},\mathbf{p}) = \frac{1}{2}\Big(1 - \frac{\xi}{E}\Big)[1 - f(E_+)] + \frac{1}{2}\Big(1 + \frac{\xi}{E}\Big)f(E_-)\,. \tag{6.5}$$

For states with both $E_+ > 0$ and $E_- > 0$, this reduces to the usual BCS expression. But if a state with momentum $\mathbf{p}$ has $E_- < 0$, its occupation number is equal to 1. The corresponding time-reversed state with momentum $-\mathbf{p}$ has then $E_+ < 0$ and its occupation number is equal to 0. As we will see below, this gives rise to a normal-fluid (rotational) current.

It is easy to see that the energies $E_\pm$ can only become negative if the velocity v exceeds a critical value such that

$$p'_F v > \Delta\,. \tag{6.6}$$

Here we have introduced the abbreviation $p'_F = \sqrt{2m\mu'_{loc}}$, where $\mu'_{loc} = \mu_{loc} + mv^2/2$ denotes the local chemical potential which includes the effect of the centrifugal force, and p'_F is the corresponding local Fermi

momentum. For a given z coordinate, the condition (6.6) is fulfilled beyond a certain distance $r_{\perp 1}(z)$ from the rotational axis, since the velocity increases as $v = \Omega r_\perp$. At smaller distances, the energies $E_\pm$ are always positive, i.e., the system is in the usual superfluid phase and does not participate in the rotation. Beyond $r_{\perp 1}$, the gap is reduced by the rotation. We will call this region, where a rotational current exists although the gap is non-zero, the partially paired phase. Finally, at a certain distance $r_{\perp 2}$, the gap vanishes and the system enters the normal phase where it rotates like a rigid body.

If the condition (6.6) is fulfilled, i.e., for $r_\perp > r_{\perp 1}$, one can easily see that the energies $E_\pm$ can become negative if the momentum lies between two limits p_- and p_+ which are given by

$$p_\pm^2 = p_F'^2 + m^2 v^2 \pm 2m\sqrt{p_F'^2 v^2 - \Delta^2}\,, \tag{6.7}$$

The integrand of the gap equation (6.4) is only affected by the rotation if p lies between p_- and p_+. Integrating Eq. (6.4) over the angle between $\mathbf{p}$ and $\mathbf{v}$ and dividing both sides of the equation by Δ, we obtain

$$1 = -\frac{a}{\pi\hbar m}\Big[\int_0^\infty dp\Big(\frac{p^2}{E} - 2m\Big) - \int_{p_-}^{p_+} dp\Big(\frac{p^2}{E} - \frac{p}{v}\Big)\Big]\,. \tag{6.8}$$

The first integral is the same as in the gap equation without rotation while the second one is the contribution of the $f(E_\pm)$ terms due to the rotation.

In the weak-coupling limit, when $\Delta \ll \mu_{loc}$, the pair-breaking effects appear already at extremely low angular velocities Ω. In this case it is possible to evaluate the integrals in Eq. (6.8) analytically, and one can show that the critical velocity for which the gap disappears is given by $v_c = (e/2)\Delta_{v=0}/p_F$, where $e = 2.71\ldots$ denotes Euler's number. Hence, for a given z coordinate, the radial coordinates $r_{\perp 1,2}$ separating the fully paired from the partially paired and the partially paired from the unpaired phase, respectively, are the solutions of the equations

$$p_F(r_{\perp 1}, z)\Omega r_{\perp 1} = \Delta_{\Omega=0}(r_{\perp 1}, z)\,, \tag{6.9}$$

$$p_F(r_{\perp 2}, z)\Omega r_{\perp 2} = \frac{e}{2}\Delta_{\Omega=0}(r_{\perp 2}, z)\,. \tag{6.10}$$

In the crossover regime, the situation is more complicated, since the gap Δ may be comparable with μ_{loc}. Therefore the integrals have to be evaluated numerically. In addition, the rotation can now be much faster and the centrifugal force can lead to a sizeable change of the density profile and it is necessary to readjust the global chemical potential μ as a function of Ω in order to keep the total number of particles fixed. The density per spin state, $\rho(\mathbf{r})$, is obtained by integrating the occupation numbers over $\mathbf{p}$. Using Eq. (6.5), one obtains

$$\rho(\mathbf{r}) = \frac{1}{4\pi^2\hbar^3}\Big[\int_0^\infty dp\, p^2\Big(1 - \frac{\xi}{E}\Big) + \int_{p_-}^{p_+} dp\,\xi\Big(\frac{p^2}{E} - \frac{p}{v}\Big)\Big]\,. \tag{6.11}$$

The second term arises from the $f(E_\pm)$ terms and exists only if the condition (6.6) is fulfilled, i.e., beyond $r_{\perp 1}$. Between $r_{\perp 1}$ and $r_{\perp 2}$, the density goes smoothly from its value with pairing to the value without pairing, $\lim_{\Delta\to 0}\rho(\mathbf{r}) = p_F'^3(\mathbf{r})/(6\pi^2\hbar^3)$. Once we have calculated the density, we can obtain the total number of particles by integrating the density over space. This allows us to determine the value of the chemical potential.

An interesting quantity is the current density, which can be obtained by multiplying the occupation numbers with $\mathbf{p}/m$ and integrating over $\mathbf{p}$. From Eq. (6.5) it is clear that for $r_\perp < r_{\perp\,1}$, i.e., close to the rotational axis where the condition (6.6) is not satisfied, the current vanishes as it should in the superfluid phase. Beyond $r_{\perp 1}$, the result can be given in closed form as

$$\mathbf{j} = \frac{(p_F'^2 - \Delta^2/v^2)^{3/2}}{6\pi^2\hbar^3}\mathbf{v}\,. \tag{6.12}$$

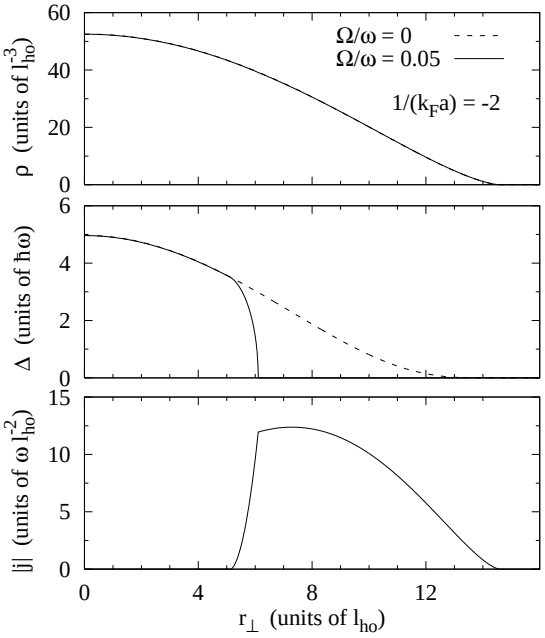

Figure 6.1: From top to bottom: density per spin state ρ, gap Δ, and current $|\mathbf{j}|$ in a rotating Fermi gas ($4 \cdot 10^5$ atoms in an isotropic trap with frequency ω) in the BCS phase as a function of the distance $r_\perp$ from the z axis, for $z = 0$. The solid lines correspond to a gas rotating with angular velocity $\Omega = 0.05\omega$. For comparison, the results for the non-rotating case (ground state) are shown as the dashed lines.

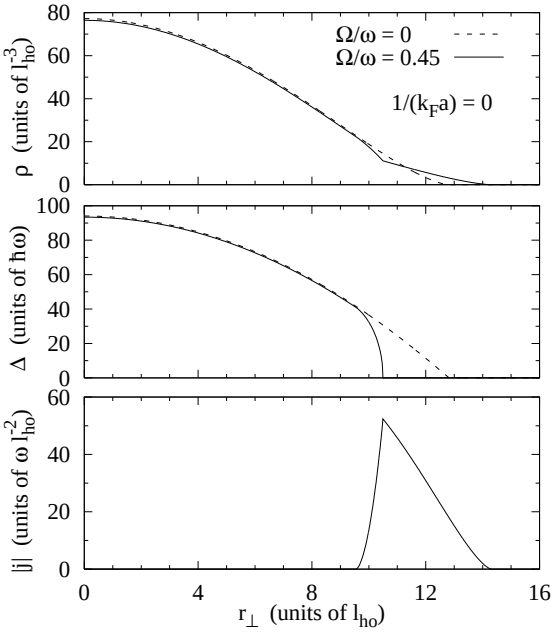

Figure 6.2: Same as Fig. 6.1, but for a unitary Fermi gas rotating with angular velocity $\Omega = 0.45\omega$.

One sees that in the partially paired phase the current increases with decreasing gap and it correctly approaches its rigid-body limit if one approaches the unpaired phase: $\lim_{\Delta \to 0} \mathbf{j}(\mathbf{r}) = \rho(\mathbf{r})\mathbf{v}(\mathbf{r})$.

Let us now discuss some numerical results. We consider a system with $N = 4 \cdot 10^5$ atoms ($2 \cdot 10^5$ atoms per spin state) in two cases: (a) close to the BCS limit, with $1/(k_F a) = -2$ [$k_F = p_F(\mathbf{r} = 0)/\hbar$], and (b) at unitarity, i.e., in the limit $a \to \infty$. We do not consider the BEC side of the cross-over, since as soon as the chemical potential becomes negative, the energies $E_\pm$ are always positive, i.e., the molecules in the BEC phase are never broken by the rotation. For simplicity we choose a spherically symmetric trap ($\omega_z = \omega_\perp$), but this will not qualitatively change our results. In the figures, we will use the harmonic oscillator units set by the trap potential, i.e., $\hbar\omega$ for energies and $l_{ho} = \sqrt{\hbar/(m\omega)}$ for lengths.

Let us first discuss the BCS case. In this case the pairing is so weak that it does not appreciably influence the density (upper panel of Fig. 6.1). It is also very fragile, i.e., the moment of inertia, which can be calculated within linear response theory [105, 247, 251], must be measured at extremely low angular velocity. Already for an angular velocity as small as $\Omega = 0.05\omega$, the gap (second panel of Fig. 6.1) is zero in a large part of the system. Because of the small angular velocity, the centrifugal force has no effect on the density, either. Looking at the gap, one can clearly see the point $r_{\perp 1}(z = 0) = 5.1\, l_{ho}$ where the results for the non-rotating (dashed line) and the rotating (solid line) system start to differ, and the point $r_{\perp 2} = 6.1\, l_{ho}$ where the gap goes

to zero. The three regions are even more evident in the current (lower panel of Fig. 6.1): The current starts to be non-vanishing at $r_{\perp 1}$ and it has a kink at $r_{\perp 2}$ where it reaches the rigid-body value.

More interesting are the results in the cross-over regime, where the gap is strong enough to support a relatively fast rotation. In Fig. 6.2 we display the density, gap and current (from top to bottom) for a system at the unitary limit rotating with $\Omega = 0.45\,\Omega$ (solid lines; for comparison, the density and gap of the corresponding non-rotating system are shown as the dashed lines). In this case, the centrifugal force leads to an oblate deformation of the system: The chemical potential μ and the axial size of the system, which is determined by $z_{max} = \sqrt{2\mu/m}/\omega$, decrease (in the present example, μ decreases from 81.7 to 81.2 $\hbar\omega$), while the radial size, which is determined by $r_{\perp max} = \sqrt{2\mu/[m(\omega^2 - \Omega^2)]}$, increases. The increase of the radial size is visible in the upper panel of Fig. 6.2, where the density is shown as a function of $r_\perp$ for $z = 0$. The depletion of the density in the center is a consequence of the reduced chemical potential. This is also the reason why the gap in the center decreases with the rotation. Due to the strong pairing, the gap has a direct effect on the density. This is the reason for the kink in the density profile at $r_\perp = r_{\perp 2}$. However, we stress that the density stays continuous at $r_{\perp 2}$.

The fact that, in contrast to the results of Bausmerth et al. [37], the density, the gap, and the current remain continuous functions of $r_\perp$ is the main statement of the present paper. In fact, if we followed the arguments given in Ref. [37], we would find a similar discontinuity as they do. The only difference with their result would be the different numerical values of the parameters ξ_S and ξ_N which determine the relationship between the density and the local chemical potential [$\mu_{loc} = \xi_S \hbar^2 (6\pi^2\rho)^{2/3}/(2m)$ or $\mu'_{loc} = \xi_N \hbar^2 (6\pi^2\rho)^{2/3}/(2m)$ in the superfluid and normal phase, respectively]. In BCS theory without mean-field shift, one obtains $\xi_S = 0.59$ and $\xi_N = 1$, whereas the QMC results used in Ref. [37] are $\xi_S = 0.44$ and $\xi_N = 056$. If one excluded the possibility of an intermediate "partially paired" phase, as in Ref. [37], the system would have to split into a fully paired superfluid and a fully unpaired normal-fluid phase, and the density would have a discontinuity across the phase boundary with a ratio $\rho_N/\rho_S = (\xi_S/\xi_N)^{3/5}$, which gives 0.73 with the BCS results and 0.85 with the QMC results for ξ_S and ξ_N. From this we see that, even if BCS theory is not capable to give the right numbers for ξ_S and ξ_N, the ratio is semi-quantitatively correct. Anyway, even if our results for the unitary limit might not be very precise, we believe that they are qualitatively correct and that between the ordinary normal and superfluid phases there will be a region in which some pairs are broken while others stay unbroken. In particular, we checked that in the region between $r_{\perp 1}$ and $r_{\perp 2}$ our energy density is lower than both that of the non-rotating superfluid and the ridigly rotating unpaired gas.

We emphasize that the existence of the intermediate region is not a finite-size effect, but it survives in arbitrarily large systems. For instance, if the trap was a flat potential well instead of a harmonic oscillator, the ratio of the two radii $r_{\perp 2}$ and $r_{\perp 1}$ would become $r_{\perp 2}/r_{\perp 1} = e/2 = 1.36$ according to Eqs. (6.9) and (6.10), independently of the size of the system and of the angular velocity of the rotation. In the harmonic oscillator the intermediate region is smaller since the gap decreases with increasing $r_\perp$ already in the non-rotating case.

This does not mean that finite-size effects do not play any role. For instance, the abrupt decrease of Δ for $r_\perp \to r_{\perp 2}$ is an artefact of the TF approximation, which requires that all spatial variations be slow compared with the length scale set by the coherence length. A necessary condition for this is $\Delta \gg \hbar\omega$. In a true quantum calculation, the profiles of Δ, ρ and $|\mathbf{j}|$ would be rounded and no sharp interface between the different phases could be defined. In addition, beyond a certain critical angular velocity Ω_c the gap should completely disappear, even on the rotational axis [272].

An interesting extension of the present work is to study a system which is deformed in the xy plane, i.e., in the plane perpendicular to the rotational axis. This question is very important since it is impossible to put the system into rotation without such a deformation (of course, once the system rotates, the deformation can be switched off and the conservation of angular momentum ensures that the system keeps rotating). In the

deformed case, also the superfluid part of the system has a non-vanishing current, with an irrotational velocity field. Another important question concerns the collective excitations of the rotating system, in particular the radial quadrupole mode whose precession is used in current experiments for measuring the angular momentum of the system [198]. In order to stay in contact with the experiments, temperature effects should be taken into account, too.

Chapitre IV

Modes collectifs

La rotation discutée dans le chapitre précédent représente un mouvement collectif particulièrement simple, car il est stationnaire (dans le référentiel tournant). Dans ce chapitre, nous nous intéresserons aux mouvements collectifs dépendants du temps, et notamment aux petites oscillations autour de l'état d'équilibre que l'on appelle les modes collectifs. L'observation du spectre de ces excitations peut souvent fournir une information intéressante sur les propriétés du système, par exemple, s'il est superfluide ou pas. De plus, la connaissance des excitations collectives peut être importante pour le calcul des quantités thermodynamiques.

Modes collectifs dans la croûte des étoiles à neutrons (publication n° 7, p. 96)

La courbe de refroidissement (température en fonction de l'âge de l'étoile) est une des sources d'information les plus intéressantes parmi les quantités accessibles aux observations sur les étoiles à neutrons. Elle dépend sensiblement de nombreuses propriétés de l'étoile, notamment des propriétés thermodynamiques de la croûte, car c'est seulement la température à la surface de l'étoile que l'on peut observer. La croûte interne consiste en un réseau de clusters (noyaux) qui flottent dans un gaz de neutrons et un gaz d'électrons dégénérés, tous ces ingrédients contribuant à la chaleur spécifique, c_v. À cause du gap d'appariement Δ dans la matière de neutrons, la chaleur spécifique due aux excitations de neutrons est fortement réduite à des températures $k_B T \ll \Delta$. Cependant, la superfluidité donne lieu à un mode de son hydrodynamique (mode de Bogoliubov-Anderson [18]) de sorte que finalement le spectre ne fait pas apparaître de gap. Pour $k_B T \ll \Delta$, la chaleur spécifique du gaz de neutrons est donc dominée par la contribution de ce mode.

Dans la croûte, le gaz de neutrons n'est pas uniforme parce qu'il se trouve dans un réseau de clusters qui, quand la densité augmente, sont d'abord sphériques, puis déformés pour ensuite commencer à se toucher et former des baguettes (phase "rods" ou "spaghetti") et des plaques (phase "slabs" ou "lasagne") etc. [128, 194]. Pour obtenir les modes collectifs dans la croûte, l'approximation des phases aléatoires de quasiparticules ("quasiparticle random-phase approximation", QRPA) a été utilisée avec l'approximation de Wigner-Seitz (WS) [109, 138, 208]. Dans ces calculs microscopiques, on ne regarde qu'une sphère isolée (la cellule WS [173]) autour du cluster. Mis à part le fait que la cellule élémentaire du réseau cristallin ne soit pas sphérique, on néglige par cette approximation la propagation de l'onde d'une cellule à l'autre ainsi que le couplage entre les cellules qui en résulte. Par conséquent, on ne peut pas décrire des modes dont la longueur d'onde dépasse la taille de la cellule WS. L'objectif de notre travail publié dans réf. [94] (publication n° 7 ci-après) était de considérer des modes d'une longueur d'onde plus grande, parce que ce sont eux qui sont excités à basse température. Afin de pouvoir aller au-delà de l'approximation WS, nous avons résolu les équations de l'hydrodynamique superfluide dans cette géométrie non-uniforme mais périodique, au lieu de faire un calcul microscopique QRPA. De plus, nous nous sommes limités au cas le plus simple qui est la géométrie de la phase lasagne. Pour le calcul des

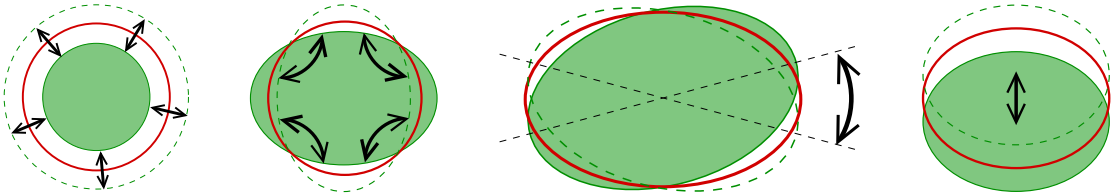

FIGURE IV.1 – Vue schématique des modes collectifs dans un piège. De gauche à droite : (a) mode de respiration, (b) mode quadrupolaire, (c) mode de ciseaux, (d) mode de centre de masse (“sloshing mode”).

quantités qui apparaissent dans les équations hydrodynamiques (potentiels chimiques et pression en fonction des densités de neutrons et protons), nous avons utilisé un modèle de champ moyen relativiste (modèle DDHδ [24, 112]), qui a aussi été utilisé dans [23] pour calculer la géométrie des structures dans la croûte interne.

L’utilisation de l’hydrodynamique superfluide est bien sûr une approximation. Comme discuté dans le chapitre précédent, elle est valable pour $T = 0$ si les variations spatiales du système sont lentes par rapport à la longueur de cohérence ξ. Dans la croûte interne, on est à la limite de validité de cette condition. Mais les calculs QRPA dans l’approximation WS ont montré que l’hydrodynamique donne néanmoins approximativement la bonne fréquence pour les modes [138].

La périodicité de la géométrie nous permet d’introduire un vecteur d’onde de Bloch $\mathbf{q}$ bien que les solutions des équations hydrodynamiques ne soient pas des ondes planes. C’est ce qui se fait en physique des solides pour les fonctions d’onde des électrons dans un cristal. Les solutions pour les modes collectifs s’écrivent donc comme le produit d’une fonction périodique et d’une onde plane. Le spectre d’excitation comporte des modes “acoustiques” (dont la fréquence ω tend vers zéro quand $q \to 0$) et des modes “optiques” (ω reste fini quand $q \to 0$). La fréquence dépend également de la direction entre $\mathbf{q}$ et l’orientation des plaques.

Nous avons calculé la chaleur spécifique de la phase lasagne correspondant aux spectres ainsi obtenus. À des températures de l’ordre de 10^9 K, cette contribution à c_v est beaucoup plus importante que celle des neutrons (qui est exponentiellement supprimée à cause du gap Δ) et du même ordre de grandeur que celle des électrons.

Modes collectifs dans des gaz de fermions superfluides

Dans les gaz d’atomes piégés, les modes collectifs ne sont pas des ondes planes mais ressemblent plus aux modes collectifs des noyaux. Dans un piège déformé en forme de cigare, possédant une symétrie axiale (fréquences du piège $\omega_z \ll \omega_x = \omega_y$), il y a, par exemple, les modes de respiration, qui consistent en une compression du système dans la direction z (mode de respiration axial) ou dans les directions x et y (mode de respiration radial, cf. fig. IV.1a) et le mode quadrupolaire radial, qui consiste en une déformation elliptique du système dans le plan transversal (xy) sans compression (fig. IV.1b). Si le potentiel n’a pas de symétrie axiale ($\omega_x \neq \omega_y$), on peut exciter le “mode de ciseaux”, dans lequel le gaz, qui a maintenant une section elliptique, n’est pas aligné avec le potentiel (fig. IV.1c). Enfin, un dernier exemple très important est l’oscillation du centre de masse (cf. fig. IV.1d), parce qu’elle permet la détermination très précise de la fréquence du potentiel du piège (sa fréquence n’est pas changée par l’interaction entre les atomes [56, 141]).

Comme le mode de respiration comporte une compression du système, sa fréquence dépend de la compressibilité du gaz. Les expériences faites sur ce mode à très basse température (régime hydrodynamique superfluide) ont permis de vérifier avec une très bonne précision l’équation d’état du gaz de fermions dans le cross-over BEC-BCS [14, 15, 34, 139, 140]. Une observation intéressante est que lorsque l’on s’éloigne de la résonance de Feshbach vers le régime BCS, on arrive à un point où le mode est fortement amorti et sa fréquence

dévie de la prédiction hydrodynamique [140].

Le mode quadrupolaire ne comporte pas de compression et sa fréquence dans le régime hydrodynamique est indépendante de l'interaction ; elle vaut $\sqrt{2}\omega_r$ (où $\omega_r = \omega_x = \omega_y$). L'intérêt de ce mode est que sa fréquence est très différente dans le régime hydrodynamique et dans la phase normale dans le régime sans collisions. Dans ce dernier cas, l'oscillation dans l'espace des coordonnées est accompagnée d'une oscillation de la sphère de Fermi, ce qui augmente la fréquence de ce mode à une valeur près de $2\omega_r$ (la valeur précise dépend de l'interaction). Ce changement de la fréquence à la transition de la phase superfluide vers la phase normale dans le régime sans collisions a été observé expérimentalement [16].

Cependant, l'observation d'un comportement hydrodynamique ne prouve pas que le système soit superfluide. Si la longueur de diffusion a est grande, comme dans le régime du cross-over BEC-BCS, le système peut être hydrodynamique dans la phase normale au-dessus de T_c à cause des nombreuses collisions entre les atomes. Dans ce cas là, le régime sans collisions est atteint à des températures plus élevées : Même si les collisions ne sont plus supprimées par le blocage de Pauli à haute température, le gaz peut atteindre le régime sans collisions parce qu'il se dilate de plus en plus et les collisions deviennent donc de plus en plus rares. Cette "transition" du régime hydrodynamique collisionnel au régime sans collisions a été observée expérimentalement en étudiant le comportement des fréquences et de l'amortissement des modes quadrupolaire et ciseaux [199, 267].

Calcul QRPA pour les gaz de fermions superfluides piégés (publication n° 8, p. 109)

Dans la phase superfluide, pour $T = 0$ et pour une longueur de cohérence ξ suffisamment petite (dans un piège harmonique et sphérique cette dernière condition s'écrit $\xi \ll R_{TF}$ ou $\Delta \gg \hbar\omega_i$, cf. chapitre III, p. 62) les modes collectifs et autres processus suffisamment lents[1] peuvent être décrits par l'hydrodynamique superfluide.

Si l'on considère la phase BCS, la température critique T_c est très basse de sorte que $T_c \ll T_F$ (où $T_F = E_F/k_B$ est la "température de Fermi"). Pour $T \gtrsim T_c$ le gaz est donc dans la phase normale, mais il est toujours fortement dégénéré et les collisions entre les atomes sont supprimées par le blocage de Pauli. Dans ce régime (presque) sans collisions, le système ne retourne pas (ou pas assez vite) à l'équilibre local et les excitations comportent en général non seulement des oscillations de la densité, mais aussi de la forme de la sphère de Fermi locale. Si le nombre de particules est suffisamment grand pour que l'approximation TF soit valable (comme mentionné dans le chapitre III, p. 62, c'est une condition beaucoup moins restrictive que celle pour la validité de l'hydrodynamique superfluide), la dynamique dans ce régime peut être décrite par l'équation de Vlasov sans terme de collision.

La théorie pour ces deux cas limites est donc relativement simple. Mais dans les expériences, on a toujours une température $T > 0$ et la condition $\xi \ll R_{TF}$ n'est probablement pas toujours satisfaite non plus. Dans la publication n° 8 [118], nous avons étudié les effets de température ($0 < T < T_c$) et de taille finie ($\Delta \sim \hbar\omega_i$) sur le mode monopolaire et le mode quadrupolaire dans un piège harmonique et sphérique avec la QRPA. C'est une méthode complètement quantique qui correspond aux équations BdG (HFB) dépendant du temps dans la limite des petites amplitudes. Elle est souvent utilisée en physique nucléaire pour calculer les excitations des noyaux avec appariement.

Pour les deux modes, nous avons trouvé que la QRPA reproduisait précisément les prédictions des théories semiclassiques (hydrodynamique ou Vlasov, respectivement) dans les deux limites $T = 0$ et $T > T_c$, si la

[1] En principe, il y a une deuxième condition qui concerne la fréquence ω du mode d'excitation considéré : $\hbar\omega \ll \Delta$. En effet, si la fréquence de l'excitation est trop élevée, on ne peut pas négliger les effets de brisure de paires. Mais comme les fréquences des modes collectifs dans un piège harmonique sont de l'ordre de grandeur des fréquences du piège ω_i, les deux conditions $\xi \ll R_{TF}$ et $\hbar\omega \ll \Delta$ sont souvent équivalentes.

condition $\Delta \gg \hbar\omega_{trap}$ était satisfaite. Après ce test, nous avons étudié ce qui ce passait à des températures intermédiaires. Nos résultats pour $T \approx T_c/2$ montrent que les modes collectifs sont fortement amortis. L'origine de cet amortissement est le couplage entre le mode collectif et des excitations à deux quasiparticules (amortissement de Landau), l'amortissement dû aux collisions n'étant pas contenu dans l'approximation QRPA. Dans le cas du mode quadrupolaire, on a également montré que deux modes (au lieu d'un seul) apparaissaient, tous deux amortis, l'un près de la fréquence hydrodynamique, l'autre près de la fréquence sans collisions.

Afin d'étudier ce qui se passe si la condition $\Delta \gg \hbar\omega_i$ n'est pas satisfaite, nous avons diminué la constante de couplage, ce qui réduit la valeur de Δ. Dans le cas du mode quadrupolaire, on voit que dans ce cas, à $T = 0$, la fréquence du mode hydrodynamique est considérablement abaissée et le mode est amorti, et qu'en même temps, le mode à la fréquence sans collisions apparaît.

Tous ces résultats ont été obtenus pour un piège sphérique, parce que les calculs QRPA deviennent techniquement très lourds si l'on ne peut pas exploiter cette symétrie. Mais qualitativement, on peut dire que les effets de taille finie que nous avons étudiés devraient être particulièrement importants dans le cas des pièges déformés (en forme de cigare, comme dans la plupart des expériences), dans lesquels la fréquence radiale, beaucoup plus élevée que la fréquence axiale, peut facilement être comparable à Δ. Ces effets peuvent éventuellement être la cause de la défaillance de l'hydrodynamique observée dans le mode de respiration radial [140].

Description semiclassique des modes collectifs dans la phase superfluide à des températures finies (publication n° 9, p. 123)

Les méthodes BdG et QRPA sont numériquement assez lourds et on ne peut les appliquer que dans des cas où le nombre d'atomes ne dépasse pas quelques dizaines de milliers dans un piège sphérique. Par contre, des méthodes semiclassiques comme l'hydrodynamique superfluide ou l'équation de Vlasov deviennent de plus en plus précises lorsque le nombre d'atomes augmente, et elles permettent des calculs pour des géométries réalistes. Le problème est que l'hydrodynamique superfluide et l'équation de Vlasov ne peuvent être utilisées qu'à $T = 0$ et à $T > T_c$, respectivement.

Notre idée a donc été de développer un formalisme semiclassique pour les températures intermédiaires, $0 < T < T_c$ [252, 253]. En partant des équations BdG dépendant du temps et en utilisant le développement de Wigner-Kirkwood (développement en puissances de $\hbar$), nous avons dérivé des équations de transport [252]. Ces équations correspondent aux équations de transport de Betbeder-Matibet et Nozières pour des supraconducteurs propres [43]. Dans ce formalisme, la description de la dynamique du système est basée sur une équation de type Vlasov pour la fonction de distribution de quasiparticules, décrivant le mouvement de la composante normale, couplée à une équation hydrodynamique pour la phase ϕ du paramètre d'ordre, décrivant le mouvement de la composante superfluide. Pour étudier les modes collectifs, on peut linéariser ces équations. Un résumé des étapes principales des dérivations est donné dans réf. [248] (publication n° 9).

Ces équations de transport ne peuvent être résolues analytiquement que dans le cas d'une onde plane dans un gaz uniforme [252]. Il fallait donc développer une méthode numérique pour résoudre ces équations dans le cas général. L'idée a été d'adapter la méthode des particules tests, utilisée depuis longtemps pour résoudre l'équation de Vlasov en physique nucléaire [42, 121], au cas de l'équation pour la fonction de distribution de quasiparticules.

La première application de la méthode numérique a été le mode quadrupolaire dans un piège sphérique. Les résultats sont en bon accord avec les résultats obtenus par la QRPA : À basse température, on trouve le mode hydrodynamique, dont l'amortissement augmente fortement avec la température. Ensuite, au fur et à mesure que l'on s'approche de la température critique T_c, un deuxième mode apparaît correspondant au mode quadrupolaire dans la phase normale. Enfin, au-dessus de T_c, seul ce deuxième mode survit.

Dans une autre publication [249], cette méthode m'a permis de fournir, pour la première fois, une explication concernant l'amortissement et le saut de la fréquence du mode quadrupolaire en fonction de $1/k_F a$ observés expérimentalement [16].

Modes collectifs dans la phase normale (publication n° 10, p. 142)

Il a déjà été mentionné que près d'une résonance de Feshbach le gaz de fermions n'est pas dans le régime sans collisions à des températures $T \gtrsim T_c$ mais se comporte de manière hydrodynamique dans la phase normale. Dans ce cas là, on peut utiliser l'hydrodynamique à deux fluides [237] pour les températures en-dessous de T_c. Cependant, comme les expériences [199, 267] ont pu le montrer, au delà d'une certaine température le gaz est toujours dans le régime sans collisions. Entre les régimes hydrodynamiques et sans collisions les modes sont fortement amortis et leurs fréquences montrent une forte dépendance en température.

Dans réf. [199], cette transition du régime hydrodynamique collisionnel au régime sans collisions a été décrite dans le cadre de l'équation de Boltzmann. La section efficace pour le calcul de la probabilité des collisions dans le gaz a été calculée avec une matrice T dans l'approximation d'échelle (cf. p. 49, fig. 4.1 en bas). Cette section efficace dans le milieu augmente fortement quand on s'approche de T_c. Dans réf. [80], nous avons étendu ce modèle en incorporant le champ moyen obtenu comme la partie réelle de la self-énergie correspondante (cf. fig. 4.1 au milieu), ce qui change considérablement le profil de densité du gaz. Par ailleurs, la présence du champ moyen nous a permis d'expliquer le décalage du mode quadrupolaire dans la phase sans collision dans le régime $1/k_F a < -1$ observé dans l'expérience [16]. Cependant, le champ moyen n'a pas d'effet important sur les fréquences et taux d'amortissement des modes quadrupolaire, ciseaux, et de respiration du gaz près de la limite unitaire en fonction de la température. L'accord entre théorie et expérience [199] reste mauvais, notamment si l'on utilise la section efficace dans le milieu (obtenue avec la matrice T) au lieu de la section efficace libre.

Les résultats mentionnés ci-dessus n'ont pas été obtenus par une solution exacte de l'équation de Boltzmann, mais par une méthode où l'on ne regarde que des moments d'ordre deux de la fonction de distribution dans l'espace des phases. Cette approximation implique que les fréquences et taux d'amortissement des modes ne dépendent que d'un seul temps de relaxation τ.

Afin de nous affranchir de cette approximation, nous avons développé un code numérique pour résoudre l'équation de Boltzmann avec la méthode des particules tests. Ceci est l'objet de la publication n° 10 [151]. Dans un premier temps, nous nous sommes limités au mode quadrupolaire dans une géométrie sphérique et nous avons utilisé la section efficace libre pour calculer les probabilités de collision. Le résultat surprenant était que la méthode des moments surestimait systématiquement et de façon significative l'effet des collisions. Dans la méthode des moments, le gaz est donc "trop hydrodynamique" et, par conséquent, la transition du régime hydrodynamique collisionnel vers le régime sans collisions est décalée vers une température trop élevée.

Ce résultat a été consolidé par une extension de la méthode des moments dans laquelle nous avons pris en compte des moments jusqu'à l'ordre quatre. La fréquence et le taux d'amortissement du mode quadrupolaire ainsi obtenus sont en bon accord avec les résultats des simulations numériques. La raison pour la défaillance de la méthode des moments d'ordre deux est probablement qu'elle ne tient pas compte de la dépendance spatiale du temps de rélaxation τ, bien que le taux de collision soit beaucoup plus élevé au centre du piège qu'à la surface du gaz.

Dans une publication plus récente [81], nous avons appliqué la méthode des moments d'ordre quatre aux conditions réalistes (géométrie allongée, grand nombre d'atomes, section efficace dans le milieu). L'accord entre les résultats théoriques et les données de réf. [199] s'est beaucoup amélioré avec l'inclusion des moments d'ordre quatre.

7 Collective excitations in the neutron star inner crust

Luc Di Gallo, Micaela Oertel, and Michael Urban, Phys. Rev. C 84, 045801 (2011)

We study the spectrum of collective excitations in the inhomogeneous phases in the neutron star inner crust within a superfluid hydrodynamics approach. Our aim is to describe the whole range of wavelengths, from the long-wavelength limit which can be described by macroscopic approaches and which is crucial for the low-energy part of the spectrum, to wavelengths of the order of the dimensions of the Wigner-Seitz cells, corresponding to the modes usually described in microscopic calculations. As an application, we will discuss the contribution of these collective modes to the specific heat of the "lasagna" phase in comparison with other known contributions.

7.1 Introduction

Neutron stars are fascinating objects, containing matter under extreme conditions of temperature, density and magnetic field. In order to study these celestial bodies, theoretical modeling has to be confronted with observations. A prominent observable is the thermal evolution of isolated neutron stars. Properties of the crust thereby influence the cooling process mainly during the first 50-100 years, when the crust stays hotter than the core which cools down very efficiently via neutrino emission (see e.g. [268]). Heat transport in the crust is the key ingredient to explain the afterburst relaxation in X-ray transients, too [57, 224]. Concerning the models for the thermal relaxation of the crust, the most important microscopic ingredients are thermal conductivity and heat capacity, and to less extent neutrino emissivities. Here, as a first application, we will concentrate on the heat capacity. More details about the evaluation of the heat capacity and a discussion of the usually considered contributions can be found in [115]. In what follows, we will concentrate on the particularly interesting case of the neutron star inner crust.

The core of neutron stars is composed most probably of homogeneous neutron rich matter, whereas the crust contains different inhomogeneous structures. The inner crust is thereby characterized by the transition from a lattice of atomic nuclei in the outer crust to homogeneous matter in the core. Ravenhall et al. [194] and Hashimoto et al. [128] predicted that this transition passes via more and more deformed nuclei. Starting from an almost spherical shape, they could form rods or slabs immersed in a neutron gas at the different densities. These "spaghetti" and "lasagna" phases are commonly called the nuclear "pasta". At higher densities, even closer to the core, other phases such as neutron-gas bubbles inside the dense matter ("swiss cheese" phase) etc. are expected. The formation of the different structures strongly depends on the relative strength of the nuclear surface energy, Coulomb energy and bulk energy, such that it depends on the nuclear interaction. This prediction has been confirmed within different models for the nuclear interaction, see, e.g., [23, 179, 187, 264]. These evaluations have been performed at zero temperature. It is clear that at some critical temperature the pasta structures will disappear due to thermal excitations. However, this melting temperature is of the order of several MeV (see e.g. [25, 263]).

Another point is that in neutron stars older than several minutes, matter becomes superfluid. A first evidence for superfluidity in neutron stars has been discussed already in 1969 [39], shortly after the discovery of the first pulsars, in connection with the observation of "glitches". Since then much effort has been devoted to the question of superfluidity and superconductivity in neutron star matter, for the inner crust as well as for the homogeneous core, see for example [187]. There is no consensus on the exact value of the energy gaps Δ in the inner crust [113, 157], but the common agreement is that they are of the order of 1 MeV [79]. A pairing gap much larger than the temperature strongly suppresses the contribution of individual neutrons to the specific heat which is thus very much dependent on the pairing strength [109, 115]. For moderate and strong pairing, the main contributions to the heat capacity considered so far in the crust are thus electrons and lattice vibrations

as well as collective excitations of nuclei. However, the superfluid character of neutron star matter induces collective excitations of the neutron gas, not considered before, which can give an important contribution to the heat capacity in certain regions, see [5, 85, 186].

The aim of the present paper is to study these collective excitations in the inner crust employing a superfluid hydrodynamics approach. Naturally, there is a vast literature on hydrodynamics for neutron stars in different contexts, including the effects of superfluidity [20, 72–75, 99, 125]. Most of these models are dedicated to the study of macroscopic neutron star properties, whereas our main aim is to study the excitation spectrum of the crust on much smaller length scales. In spirit this is similar to Refs. [85, 186, 217], where hydrodynamic equations are developed to study the superfluid Goldstone boson and (lattice) phonons in the long wavelength limit. However, we are interested in shorter wavelengths at which effects of the inhomogeneous structure will manifest themselves, too. In this sense, our approach is situated in between the long wavelength limit and the completely microscopic calculations (see e.g. [109, 138, 208]) employing the Wigner-Seitz approximation [173]. In the latter case, the wavelengths are limited to the size of the Wigner-Seitz cell, because of the imposed boundary conditions which do not include the coupling between neighboring cells.

The paper is organized as follows. In Sec. 7.2, we describe the superfluid hydrodynamics approach. We summarize the hydrodynamic equations, discuss the boundary conditions and the microscopic input. In Sec. 7.3, we show our first results. For simplicity, we restrict ourselves to one-dimensional inhomogeneities (lasagna phase) in this exploratory study. We discuss the spectrum of the collective modes and their contributions to the specific heat. A summary and perspectives of our work are exposed in Sec. 7.4.

Throughout the article, c, $\hbar$, and k_B denote the speed of light, the reduced Planck constant, and the Boltzmann constant, respectively.

7.2 Model

7.2.1 Superfluid hydrodynamics approach

In this paper, we are interested in temperatures below $\sim 10^9$ K, which is very small compared to the gap energy Δ. Therefore we can use the zero temperature approximation, thus assuming that there are no normal fluids but only superfluids. In this limit, the dynamics of a superfluid system with slow temporal and spatial variations is completely determined by the dynamics of the phase of the order parameter: If the superfluid order parameter is written as $\Delta(\mathbf{r}) = |\Delta(\mathbf{r})|e^{i\phi(\mathbf{r})}$, the superfluid velocity is given by $\mathbf{v}_s = (\hbar/2m)\boldsymbol{\nabla}\phi$ [153], m being the nucleon mass. Actually, as pointed out in Ref. [78], the phase of the order parameter determines the momentum per particle $\mathbf{p} = m\mathbf{v}_s$ and not the fluid velocity $\mathbf{v}$. This distinction is important in the context of "entrainment" in a system containing protons and neutrons, see below.

An important length scale is the superfluid coherence length, $\xi_0 = \hbar v_F/\pi\Delta$ [106], where v_F denotes the Fermi velocity. It varies from several fm up to tens of fm for typical values of the densities, neutron fractions, and gaps in the inner crust. As can be shown by deriving the equations of superfluid hydrodynamics from the microscopic time-dependent Bogoliubov-de Gennes (or Hartree-Fock-Bogoliubov) equations [242, 252], the hydrodynamic approach is valid if the length scale of spatial variations is larger than ξ_0, and frequencies are small compared with $\Delta/\hbar$. As will be discussed later on, for the concrete examples we consider, we are at the limits of validity of the approach. However, considering the tremendous difficulties to perform completely microscopic calculations beyond the Wigner-Seitz approximation, we leave such investigations for the future and consider our approach sufficient for the moment.

In addition, we will neglect the Coulomb interaction of the protons. This represents an enormous simplification, but at the same time it implies that we cannot correctly reproduce the phonons of the Coulomb lattice. In homogeneous matter, too, the Coulomb interaction plays an important role for the collective modes, in par-

ticular the coupling of the proton plasmon mode with the electrons as discussed in [27, 28], but it is beyond the scope of the present paper. Our main focus lies therefore on the dynamics of the neutron gas, which is however coupled to the proton dynamics due to the nuclear interaction.

In principle, the equations of superfluid hydrodynamics can be derived from the underlying microscopic theory, as it was done for the case of ultracold trapped fermionic atoms in [242, 252]. Here, we follow the simpler way to derive them from local conservation laws. Since the fluid velocities and the densities are low enough, we will use a non-relativistic formulation.

The first conservation law is neutron and proton number conservation [1]. This results in two continuity equations, one for neutrons ($a = n$) and one for protons ($a = p$),

$$\partial_t n_a + \boldsymbol{\nabla} \cdot (n_a \mathbf{v}_a) = 0\,, \tag{7.1}$$

where n_a denotes the particle number density of species a.

The second conservation law, the conservation of momentum, results in the Euler equations, which can be written as

$$n_a \left(\partial_t \mathbf{p}_a + \boldsymbol{\nabla} \tilde{\mu}_a\right) = 0\,, \tag{7.2}$$

where $\tilde{\mu}_a$ is the rest-frame chemical potential defined as the conjugate momentum with respect to the particle density n_a in a variational approach [190]. The explicit expression is

$$\tilde{\mu}_a = \mu_a + \mathbf{v}_a \cdot \mathbf{p}_a - \frac{1}{2} m_a v_a^2\,, \tag{7.3}$$

where μ_a is the local chemical potential of species a. Due to the interaction between neutrons and protons, μ_a depends on the densities of both species.

In pure neutron matter, the momentum $\mathbf{p}_n$ is simply given by $\mathbf{p}_n = m_n \mathbf{v}_n$. However, in a system containing neutrons and protons, the two species drag each other due to their interaction. In the theory of superfluids, this effect is known as entrainment [21]. As a consequence, fluid momenta are misaligned with particle velocities. The relationship between the velocity and the momentum can be expressed via the entrainment matrix (also called Andreev-Bashkin or mass-density matrix) [78]:

$$m_a n_a \mathbf{v}_a = \sum_{b=n,p} \rho_{ab} \frac{\mathbf{p}_b}{m_b}\,. \tag{7.4}$$

In practice, at densities which are relevant in the inner crust, the non-diagonal elements of ρ are small [78], i.e.,

$$\rho_{ab} \approx m_a n_a \delta_{ab}\,. \tag{7.5}$$

7.2.2 Microscopic input

As microscopic input, we need the equation of state, i.e., the relation between the densities n_a and the chemical potentials μ_a, and the entrainment matrix ρ. In our concrete numerical examples, we will use the results of the work by Avancini et al. [23] for the equilibrium configurations. They evaluate the structure of the pasta phases for charge neutral matter in β equilibrium using a density dependent relativistic mean-field model, the DDHδ model (originally called DDH$\rho\delta$) [23, 24, 112], for the nuclear interaction. In order to be consistent, we shall calculate the chemical potentials μ_a and the entrainment matrix ρ with the same interaction. For the entrainment

[1] On the time scales of the collective oscillations we want to study, weak interaction processes transforming neutrons and protons into each other can be safely neglected.

matrix, we closely follow Gusakov et al. [126], who generalized the determination of the entrainment matrix for neutron-proton mixtures based on Landau-Fermi liquid theory [49] to relativistic models. The only modification of the expressions in Ref. [126] we have to perform is due to the presence of the isovector-scalar δ meson in the DDHδ model, which modifies the Dirac effective nucleon mass. In particular, the latter is no longer the same for neutrons and protons. Since our hydrodynamic equations are formulated non-relativistically, we consider only the non-relativistic limit of the entrainment matrix ($\rho_{ab} = m_a m_b c^2 Y_{ab}$ in the notation of [126]).

7.2.3 Linearization around stationary equilibrium

In order to proceed we will linearize Eqs. (7.1) and (7.2) around stationary equilibrium. Let us write the different quantities as a sum of their equilibrium value and a perturbation, $X = X_{eq} + \delta X$ (in the case of the velocities and momenta we will write the perturbation simply as $\mathbf{v}_a$ and $\mathbf{p}_a$, respectively, since the equilibrium values of these quantities are zero). The equations can be simplified a lot, since all temporal and spatial derivatives of equilibrium quantities vanish (except at phase boundaries, which will be treated in the next subsection). Eqs. (7.1) and (7.4) then reduce to

$$\partial_t \delta n_a = -\sum_{b=n,p} \frac{\rho_{ab,eq}}{m_a m_b} \boldsymbol{\nabla} \cdot \mathbf{p}_b \,, \tag{7.6}$$

and Eqs. (7.2) and (7.3) become

$$\partial_t \mathbf{p}_a = -\boldsymbol{\nabla} \delta\mu_a \,. \tag{7.7}$$

We will now express the variation of the densities in Eq. (7.6) in terms of the variation of the chemical potentials,

$$\delta n_a = \sum_{b=n,p} J_{ab} \delta\mu_b \,, \tag{7.8}$$

where

$$J_{ab} = \left(\frac{\partial n_a}{\partial \mu_b}\right)_{eq} . \tag{7.9}$$

Inserting the resulting equation into the divergence of Eq. (7.7) one obtains the following system of two coupled wave equations for $\delta\mu_n$ and $\delta\mu_p$:

$$\sum_{b=n,p} (KJ)_{ab} \, \partial_t^2 \delta\mu_b = \nabla^2 \delta\mu_a \,, \tag{7.10}$$

where K is the inverse of the matrix

$$(K^{-1})_{ab} = \frac{\rho_{ab,eq}}{m_a m_b} \,. \tag{7.11}$$

The coupling arises from the non-diagonal elements of the matrices J and K due to the neutron-proton interaction. Let us now make the ansatz that the perturbations have the form of a plane wave, $\delta\mu_a(\mathbf{r}, t) = U_a e^{-i\omega t + i\mathbf{k}\cdot\mathbf{r}}$. Eq. (7.10) can then be written as a 2×2 eigenvalue problem

$$\sum_{b=n,p} (KJ)_{ab} U_b = \frac{1}{u^2} U_a \,, \tag{7.12}$$

with $u = \omega/k$ denoting the sound velocity. The two eigenvalues give two sound velocities which we will label $u^{\pm}$. Note that the corresponding eigenvectors, $U_a^{\pm}$, do not describe pure proton or neutron waves, but combinations of both. We denote by $+$ and $-$ the modes where neutrons and protons oscillate in phase and out of phase, respectively.

In the special case of pure neutron matter, there is only one mode, which can be obtained from the above equations by setting $n_p = 0$. Its sound velocity is given by

$$u^2 = \Big(\frac{n_n}{m_n}\frac{\partial \mu_n}{\partial n_n}\Big)_{eq} . \tag{7.13}$$

7.2.4 Boundary conditions

In our model, we consider the inhomogeneous phases in the inner crust as mixed phases where a neutron gas (phase 1) coexists with a dense phase (phase 2) containing neutrons and protons. However, in order not to have to write everything separately for phase 1 and phase 2, we will write all equations, unless otherwise stated, for the general case that neutrons and protons are present in both phases. The equations relevant for phase 1 can easily be obtained by considering the special case $n_{p1} = 0$. The fact that both phases coexist implies that in equilibrium the chemical potentials and pressures are equal in both phases: $\mu_{a1} = \mu_{a2}$ and $P_1 = P_2$. The description of the interface between the two phases requires a microscopic formalism and is beyond the scope of this work.

In our model, we assume that the hydrodynamic equations are valid in both the gas and the dense phase, but since they do not say anything about the behavior at the interface, they have to be supplemented by appropriate boundary conditions. The first boundary condition arises from the obvious requirement that contact has to be maintained at all times at the interface [241]. Therefore, the displacement normal to the interface has to be continuous and equal for all components ($a = n, p$) at all times. Hence, the velocities normal to the interface must satisfy:

$$v_{\perp n1}(\mathbf{r}) = v_{\perp p1}(\mathbf{r}) = v_{\perp n2}(\mathbf{r}) = v_{\perp p2}(\mathbf{r}) . \tag{7.14}$$

The second boundary condition arises from the requirement that the pressure P on both sides of the interface must be equal [143]:

$$P_1(\mathbf{r}) = P_2(\mathbf{r}) . \tag{7.15}$$

If we linearize this condition, it can be written as

$$\sum_{a=n,p} n_{a1}(\mathbf{r})\delta\mu_{a1}(\mathbf{r}) = \sum_{a=n,p} n_{a2}(\mathbf{r})\delta\mu_{a2}(\mathbf{r}) , \tag{7.16}$$

where the index eq after n_{a1} and n_{a2} has been dropped for brevity.

Before applying our model to the neutron-star inner crust, let us see whether these boundary conditions give reasonable results for collective modes in isolated nuclei. For simplicity, we will consider a nucleus with equal numbers of neutrons and protons ($N = Z = A/2$). Within the hydrodynamic model, the nucleus is a homogeneous sphere with a sharp surface at $r = R$. The proton and neutron densities inside the nucleus are $n_n = n_p = n_0/2$, where $n_0 = 0.153$ fm^{-3} is the saturation density within the DDHδ model. As a first example, we consider the isoscalar monopole mode, where neutrons and protons oscillate together in radial direction. The solution of the wave equation inside the nucleus is $\delta\mu_n = \delta\mu_p \propto j_0(\omega r/u^+)$, where j_l is a spherical Bessel function and $u^+ = 0.169\,c$ is the sound velocity for the in-phase oscillation of neutrons and protons. Since protons and neutrons move together, the first boundary condition (7.14) is automatically satisfied, while the second one, Eq. (7.16), requires $\delta\mu(r = R) = 0$. Consequently, the energy of the monopole mode is $\hbar\omega = \pi\hbar u^+/R \approx 90$ MeV$/A^{1/3}$.

Another interesting simple case is the isovector giant-dipole resonance (GDR), where neutrons and protons oscillate against each other in z direction. In this case, our approach is identical to the Steinwedel-Jensen model of the GDR [232]. Again, the solution of the wave equation is straight-forward and gives $\delta\mu_n = -\delta\mu_p \propto$

Figure 7.1: Diagram representing the slab structure.

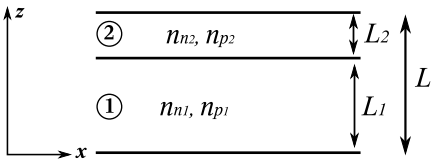

$j_1(\omega r/u^-)\cos\theta$, where θ is the angle between $\mathbf{r}$ and the z axis, and $u^- = 0.233\,c$ is the sound velocity for the out-of-phase oscillation of neutrons and protons. In this case, the second condition (7.16) is automatically fulfilled, but now the first one, Eq. (7.14), becomes relevant. Using the Euler equation (7.7), one can show that the radial component of the velocity field is proportional to $v_{rn} = -v_{rp} \propto \partial\delta\mu/\partial r \propto j_1'(\omega r/u^-)\cos\theta$, so that Eq. (7.14) gives $\hbar\omega = 2.08\hbar u^-/R \approx 82\ \mathrm{MeV}/A^{1/3}$.

These results for the isoscalar monopole and the isovector GDR are quite reasonable, at least for heavy nuclei, although their energies are much higher than the pairing gap Δ, such that superfluid hydrodynamics should strictly speaking not be applicable. The reason is that for these particular resonances (contrary to, e.g., the quadrupole mode [201]) the Fermi-surface distortion does not play any role, so that hydrodynamics works even in the normal phase without pairing. We conclude that, at least in some cases, the limits of validity of the hydrodynamic approach may be interpreted very generously.

7.2.5 Collective modes in a periodic slab structure

Because of their electric charge, the droplets (or rods, or slabs) of the dense phase arrange in a regular periodic lattice in order to minimize the Coulomb energy. Charge neutrality on a macroscopic scale is guaranteed by the presence of an almost uniform, strongly degenerate electron gas. The size and form of the structures is determined by the interplay of Coulomb energy (favoring small structures) and surface energy (favoring large structures). Since both the Coulomb and the surface energy are neglected in our approach, the determination of the size and form of the structures in equilibrium is beyond the scope of our work. Instead, we will consider the equilibrium geometry as input and calculate the collective oscillations in this geometry. For simplicity, we will restrict ourselves to the simplest geometry which is a structure of periodically alternating slabs with different proton and neutron densities as illustrated in Fig. 7.1 (lasagna phase). To be specific, we will consider the slabs to be perpendicular to the z axis.

Our aim is to describe the collective modes of this structure. The equilibrium properties of the structure itself, i.e., the densities n_{n1}, n_{p1}, n_{n2} and n_{p2}, and the slab thicknesses L_1 and L_2, are input parameters which we take from Ref. [23]. The excitations are then obtained by solving in each slab the wave equation (7.10) together with the boundary conditions (7.14) and (7.16) at the interfaces between neighboring slabs.

At each phase boundary, the waves will be partially (or totally) reflected. It is therefore not sufficient to make a plane-wave ansatz in each slab, but one has to consider the reflected wave, too. Thus, we can make the following ansatz in each slab:

$$\delta\mu_a(\mathbf{r},t) = \sum_{\sigma=\pm} e^{-i\omega t + i\mathbf{k}_\parallel\cdot\mathbf{r}_\parallel}\left(\alpha^\sigma e^{ik_z^\sigma z} + \beta^\sigma e^{-ik_z^\sigma z}\right) U_a^\sigma\ , \tag{7.17}$$

where $U_a^\pm$ denote the normalized eigenvectors of Eq. (7.12), $\mathbf{k}_\parallel = (k_x, k_y, 0)$ and $\mathbf{r}_\parallel = (x, y, 0)$ are the components of $\mathbf{k}$ and $\mathbf{r}$ parallel to the slab, and the $k_z^\pm$ have to satisfy

$$k_z^{\pm\,2} = \frac{\omega^2}{u^{\pm\,2}} - k_\parallel^2\,. \tag{7.18}$$

Note that $k_z^\pm$ can be real or imaginary. The velocities $\mathbf{v}_a$ can be expressed in terms of the coefficients $\alpha^\pm$ and $\beta^\pm$, too. By using the Euler equation (7.7), one finds that for a plane wave with wave vector $\mathbf{k}$ the velocity field is given by

$$\mathbf{v}_a = \frac{\mathbf{k}}{n_a \omega} \sum_b (K^{-1})_{ab} \delta\mu_b \,. \tag{7.19}$$

If we define

$$V_a^\pm = \frac{1}{n_a} \sum_b (K^{-1})_{ab} U_b^\pm \,, \tag{7.20}$$

the superposition of plane waves according to Eq. (7.17) gives

$$v_{za} = \sum_{\sigma=\pm} \frac{k_z^\sigma}{\omega} e^{-i\omega t + i\mathbf{k}_\parallel \cdot \mathbf{r}_\parallel} \left(\alpha^\sigma e^{ik_z^\sigma z} - \beta^\sigma e^{-ik_z^\sigma z} \right) V_a^\sigma \tag{7.21}$$

and a similar relation for $\mathbf{v}_\parallel$.

The next step is to determine the coefficients $\alpha^\pm$ and $\beta^\pm$ by matching the solutions in neighboring slabs according to the boundary conditions. If we use indices 1, 2, 3 in order to indicate the quantities in three consecutive slabs, we have perturbations $\delta\mu_{a1}$ valid for $0 < z < L_1$, $\delta\mu_{a2}$ for $L_1 < z < L \equiv L_1 + L_2$, and $\delta\mu_{a3}$ for $L < z < L + L_1$ with four unknown amplitudes, $\alpha^\pm$ and $\beta^\pm$, in each slab. Note that due to the periodicity the equilibrium properties of slab 3 are equal to those of slab 1, but the coefficients $\alpha^\pm$ and $\beta^\pm$ are in general different in slabs 1 and 3.

Written explicitly, the boundary conditions are

$$\begin{aligned} v_{zp2}(z = L_1) &= v_{zn2}(z = L_1) \,, \\ v_{zn1}(z = L_1) &= v_{zn2}(z = L_1) \,, \\ v_{zp1}(z = L_1) &= v_{zn2}(z = L_1) \,, \\ \sum_{a=n,p} n_{a1} \delta\mu_{a1}(z = L_1) &= \sum_{a=n,p} n_{a2} \delta\mu_{a2}(z = L_1) \,, \end{aligned} \tag{7.22}$$

and four analogous equations relating quantities of slabs 2 and 3 at $z = L$.

It is evident that, in order to satisfy the conditions for all $\mathbf{r}_\parallel$, the components $\mathbf{k}_\parallel$ must be equal in all three slabs, i.e.,

$$\mathbf{k}_{\parallel 1} = \mathbf{k}_{\parallel 2} = \mathbf{k}_{\parallel 3} \equiv \mathbf{q}_\parallel \,. \tag{7.23}$$

So far, the boundary conditions give us eight equations for the twelve unknown coefficients $\alpha_1^\pm, \ldots, \beta_3^\pm$. In order to close the system of equations, we have to take into account translational invariance of the system. This can be expressed via the Floquet-Bloch theorem [108]:

$$\delta\mu_a(\mathbf{r} + \mathbf{R}, t) = e^{i\mathbf{q}\cdot\mathbf{R}} \, \delta\mu_a(\mathbf{r}, t) \,, \tag{7.24}$$

where $\mathbf{q}$ is the Bloch momentum and $\mathbf{R} = (R_x, R_y, R_z)$ is a vector such that the system is invariant under a shift $\mathbf{r} \to \mathbf{r} + \mathbf{R}$. In our case, $\mathbf{R}_\parallel$ can be arbitrary, but R_z has to be a multiple of the periodicity L, see Fig. 7.1. With respect to $\mathbf{R}_\parallel$, the condition (7.24) is automatically satisfied due to Eq. (7.23). But in the case $\mathbf{R} = (0, 0, L)$, Eq. (7.24) implies in particular

$$\delta\mu_{a3}(x, y, z = L, t) = e^{iq_z L} \, \delta\mu_{a1}(x, y, z = 0, t) \tag{7.25}$$

and an analogous relation for the velocity. Inserting this into the boundary conditions at the interface between slabs 2 and 3 at $z = L$, we obtain

$$\begin{aligned} v_{zp2}(z = L) &= v_{zn2}(z = L)\,, \\ e^{iq_z L}\, v_{zn1}(z = 0) &= v_{zn2}(z = L)\,, \\ e^{iq_z L}\, v_{zp1}(z = 0) &= v_{zn2}(z = L)\,, \\ e^{iq_z L} \sum_{a=n,p} n_{a1}\delta\mu_{a1}(z = 0) &= \sum_{a=n,p} n_{a2}\delta\mu_{a2}(z = L)\,, \end{aligned} \tag{7.26}$$

i.e., we have now a system of eight equations, Eqs. (7.22) and (7.26), for eight coefficients $\alpha_1^{\pm}, \ldots, \beta_2^{\pm}$.

This system of equations has a non-trivial solution if the determinant of the corresponding 8×8 matrix vanishes. For a given choice of $q_{\|}$ and q_z (q_z may be limited to the first Brillouin zone, i.e., $-\pi/L < q_z < \pi/L$), this gives us an equation for ω with an infinite number of discrete solutions.

Note that, as mentioned before, in the case we will actually consider, the proton density vanishes in slab 1 (and 3). In this case, the proton velocity is not defined in that slab and we have only two coefficients α_1 and β_1 instead of four coefficients $\alpha_1^{\pm}$ and $\beta_1^{\pm}$, since in pure neutron matter there is only one eigenmode instead of two. The number of equations is also reduced by two, since the third equation of Eqs. (7.22) and the third equation of Eqs. (7.26) can be removed. We are therefore left with a 6×6 instead of 8×8 problem. In this case, it is interesting to notice that there are two different types of modes: Modes propagating through all slabs, whose energies depend on q_z, and modes of the dense slabs (slab 2) only, whose energies are independent of q_z. The latter are modes where protons and neutrons oscillate against each other such that at the boundaries ($z = L_1$ and $z = L$) v_{zn}, v_{zp}, and δP vanish simultaneously (analogous to the isovector GDR in an isolated nucleus, discussed at the end of the previous subsection).

When looking for the solutions for ω, one has to be careful to retain only physical solutions. It is easy to see that if one of the three wave numbers k_{z1}, k_{z2}^{+}, or k_{z2}^{-} vanishes, i.e., if $\omega/q_{\|}$ equals one of the three sound velocities u_1, u_2^{+}, or u_2^{-}, the system of equations is solved by choosing the corresponding coefficients as $\alpha = -\beta$ and setting all the other coefficients equal to zero. However, this solution implies $\delta\mu = 0$ and therefore does not correspond to a physical excitation.

7.3 Results for the lasagna phase

7.3.1 Excitation spectrum

Let us now investigate the resulting excitation spectrum for a specific example. As mentioned before, the values for the equilibrium quantities will be taken from the work by Avancini et al. [23], who have studied the structure of pasta phases in a relativistic mean field model. Our geometry corresponds to the lasagna phase, appearing close to the transition to uniform matter in the core, which has been found in Ref. [23] in the case of zero temperature and β-equilibrium for baryon number densities $0.077\ \text{fm}^{-3} \lesssim n_B \lesssim 0.084\ \text{fm}^{-3}$, in good agreement with the results by Oyamatsu [179]. For our example we have chosen an intermediate density, $n_B = 0.08\ \text{fm}^{-3}$. The corresponding properties of the two phases 1 and 2 are listed in Table 7.1.

With the actual numbers for the densities and the dimensions of the structure, the coherence length for a gap of 1 MeV is of the same order of magnitude as the size of the layers, i.e. the scale for spatial variations. That means that our superfluid hydrodynamics approach touches its limit of validity for this example. Strictly speaking, we should also limit ourselves to energies which are small compared to Δ. However, there are many cases where the hydrodynamic approach works reasonably well although its initial assumptions are not

		slab 1	slab 2	total
L	(fm)	9.40	7.38	16.78
n_n	(fm^{-3})	0.0701	0.0885	0.0782
n_p	(fm^{-3})	0	0.0041	0.0018
$n_B = n_n + n_p$	(fm^{-3})	0.0701	0.0926	0.0800
$Y_p = n_p/n_B$		0	0.0447	0.0227
u or u^+	(c)	0.0641	0.0354	
u^-	(c)		0.1369	

Table 7.1: Properties of the lasagna phase within the model by Avancini et al. [23] studied in our example. The average densities of the total system are given by $n_n = (L_1/L)n_{n1} + (L_2/L)n_{n2}$ etc. Baryon density and proton fraction are defined as $n_B = n_n + n_p$ and $Y_p = n_p/n_n$, respectively.

fulfilled. Examples are the dipole and monopole resonances in ordinary nuclei mentioned in the preceding section, or the "supergiant resonances" in spherical Wigner-Seitz cells used to model the neutron-star inner crust, whose excitation energies agree well with an estimate obtained from the sound velocity of the hydrodynamic Bogoliubov-Anderson mode [138].

After this remark of caution, let us discuss the solutions for the energies ω shown in Fig. 7.2 as functions of $q \equiv |\boldsymbol{q}|$ for three different angles θ between $\mathbf{q}$ and the z axis (i.e., $q_z = q\cos\theta$ and $q_{||} = q\sin\theta$). The left panel shows the dispersion relation for waves propagating in z-direction, i.e. perpendicular to the interfaces between the different slabs. One observes an acoustic branch with an approximately linear dispersion law

$$\omega = u_s q \tag{7.27}$$

at low energies, and several optical branches with a finite energy for $q = 0$, analogously to phonons branches in a crystal.

Note that within the Wigner-Seitz approximation, which is usually employed in microscopic calculations [109, 138, 208], we would only obtain a discrete spectrum corresponding to our spectrum in the case $q = 0$. The reason is that in this approximation the coupling between cells is neglected, and thus each cell has the same excitation spectrum. The degeneracy of the modes in each cell is lifted by the coupling between cells, which gives rise to a momentum dependent spectrum as obtained in our approach.

The slope of the acoustic branch, i.e., the speed of sound, coincides (see dashed line in Fig. 7.2) with the usual thermodynamic expression for the sound velocity

$$u_s^2 = \frac{1}{m}\frac{\partial P}{\partial n_B}\Big|_{Y_p}, \tag{7.28}$$

where n_B is the average baryon density of the inhomogeneous phase. To evaluate this derivative, we squeeze or expand our unit cell of length L by a small amount $\delta L = \delta L_1 + \delta L_2$. From the requirement $\delta P_1 = \delta P_2 = \delta P$ we can determine δL_1 and δL_2 and thus δP. The final result can be written in a compact form as

$$\frac{L}{n_B u_s^2} = \frac{L_1}{n_{B1} u_{s1}^2} + \frac{L_2}{n_{B2} u_{s2}^2}, \tag{7.29}$$

where we have defined for each phase $i = 1, 2$

$$u_{si}^2 = \frac{1}{m}\frac{\partial P_i}{\partial n_{Bi}}\Big|_{Y_{pi}}. \tag{7.30}$$

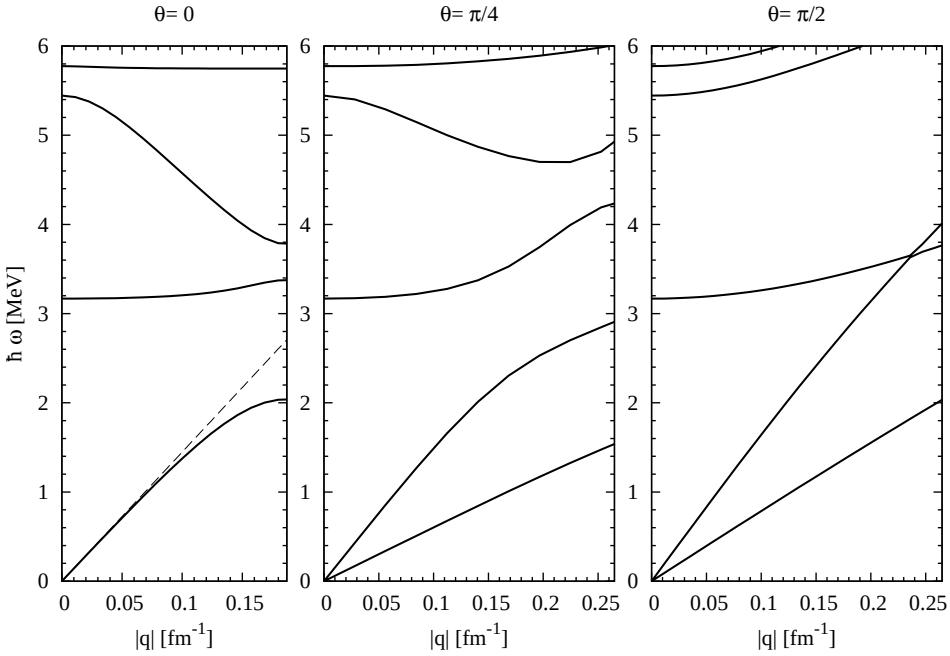

Figure 7.2: Dispersion relation of the modes propagating along the z-axis ($\theta = 0$, left), at an angle of $45°$ ($\theta = \pi/4$, center), and in the plane parallel to the slabs ($\theta = \pi/2$, right). The dashed line in the left panel corresponds to the approximation Eq. (7.27).

Note that u_{s1} is identical to the sound velocity u_1 [cf. Eq. (7.13)], whereas u_{s2} is different from the two sound velocities $u_2^{\pm}$.

This linear branch corresponds roughly to the long wavelength limit discussed in Ref. [85, 186] although, of course, the numerical value of the sound speed is not the same because we neglect elastic effects of the proton lattice due to Coulomb interaction. At higher wave vectors q, there are deviations from the linear behavior related to the inhomogeneous structure. At these energies the long wavelength limit is no longer valid.

The central and right panels of Fig. 7.2 show the excitation spectrum for different values of the angle, $\theta = \pi/4$ and $\pi/2$, respectively. One observes that the slope of the acoustic branch discussed before changes: in the present example, u_s increases from $0.072\,c$ in the case $\theta = 0$ to $0.085\,c$ in the case $\theta = \pi/2$. The reason is that the wave, which is perfectly longitudinal ($\mathbf{v} \parallel \mathbf{q}$) in the case $\theta = 0$, becomes more complicated in the case $\theta \neq 0$ and the nucleons oscillate now in both longitudinal and transverse directions. But the most important consequence of non-zero angle θ is the appearance of a second acoustic branch, whose slope is strongly angle dependent. In fact, if one writes the energy of this new branch as

$$\omega = u_s' q_{\parallel} = u_s' q \sin\theta\,, \tag{7.31}$$

the "two-dimensional sound velocity" u_s' defined by this equation depends only weakly on q_z and $q_{\parallel}$: in the present example, u_s' varies between $0.04\,c$ for $q_z \ll q_{\parallel}$ and $0.046\,c$ for $q_{\parallel} \ll q_z$. A detailed analysis of the solutions for the coefficients α and β corresponding to this branch shows that in this mode, the protons and neutrons oscillate practically only in the direction parallel to the slabs (i.e., $v_z \approx 0$), and the motion takes essentially place in the dense phase.

7.3.2 Application to specific heat

We are interested here in the contribution of the above discussed excitation modes to the specific heat. The specific heat, the heat capacity for constant volume per unit volume, is defined as

$$c_v(T) = \frac{\partial \epsilon}{\partial T}\Big|_n , \tag{7.32}$$

where ϵ denotes the energy density. The contribution of the collective modes can be calculated as follows:

$$\epsilon(T) = \int_{-\pi/L}^{\pi/L} \frac{dq_z}{2\pi} \int \frac{d^2 q_\parallel}{(2\pi)^2} \sum_i \hbar\omega_i(\mathbf{q}) \frac{1}{e^{\hbar\omega_i(\mathbf{q})/k_B T} - 1} . \tag{7.33}$$

Note that we suppose here that the energies $\omega_i(\mathbf{q})$ depend only very weakly on temperature such that it is justified to neglect their temperature dependence. This should be a good approximation as long as the temperature stays well below the value of the energy gap and we therefore have no significant contribution from a normal fluid. Another type of temperature dependence could arise from a change in the structure of the pasta phases. At the temperatures considered here, however, we do not expect a significant effect either since the structure starts to be modified considerably only at higher temperatures [25, 263].

In Fig. 7.3 we show the different contributions to the specific heat in the density range where the model by Avancini et al. [23] predicts the lasagna phase, for a typical temperature of 10^9 K. Besides the contribution of the collective modes (solid line), we display for comparison the contribution of the electrons (dashed line), which are considered as a practically uniform ultra-relativistic ($\mu_e \gg m_e c^2$) ideal Fermi gas with number density $n_e = n_p$. At low temperature, the electron gas is strongly degenerate and its contribution to the specific heat reads

$$c_v^{el.} = \frac{k_B^2 \mu_e^2 T}{(\hbar c)^3} . \tag{7.34}$$

The importance of the collective modes becomes clear if one considers the contribution of the gapped neutron quasiparticles (dotted curve), taken from Ref. [109]: In the absence of collective modes, an excitation of the neutron gas requires the breaking of Cooper pairs, which is suppressed by a factor of the order of $e^{-\Delta/k_B T}$. Even in the case of weak pairing, at the present temperature, this contribution is suppressed by approximately one order of magnitude with respect to the contribution of the collective modes.

In Fig. 7.4, we show the temperature dependence of the specific heat corresponding to the intermediate-density case discussed in Sec. 7.3.1 (solid line). For comparison, we again display the specific heat due to the electrons (dashed line). Due to its linear temperature dependence, Eq. (7.34), the electron contribution is always dominant at low temperature, but at higher temperature, the contribution of the collective modes is comparable or even larger than the electron contribution.

At the low temperatures considered here, which are well below the energy of the first optical branch, the contribution of the collective modes to the specific heat is completely dominated by the two linear branches discussed in the preceding subsection. As is well known [145], the specific heat due to an acoustic branch with a linear dispersion relation, Eq. (7.27), reads

$$c_v = \frac{2\pi^2 k_B^4 T^3}{15 \hbar^3 u_s^3} \equiv b T^3 . \tag{7.35}$$

In the present case, however, we have seen that there is in addition a "two-dimensional" branch which propagates only parallel to the slabs and whose dispersion relation is approximately given by Eq. (7.31). The

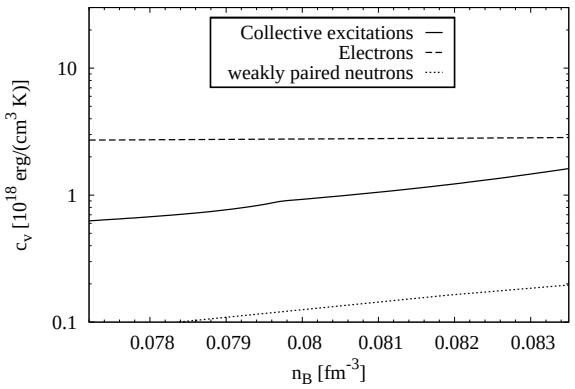

Figure 7.3: Different contributions to the specific heat in the density range where one expects to find the lasagna phase, for $T = 10^9$ K. Solid: collective modes, dashed: electrons, dotted: neutron quasiparticles (from Ref. [109]). Concerning the conversion between astrophysical and nuclear units, note that 10^9 K $= 86.17 k_B^{-1}$ keV and 10^{18} erg K^{-1} cm^{-3} $= 7.246 \times 10^{-6} k_B$ fm^{-3}.

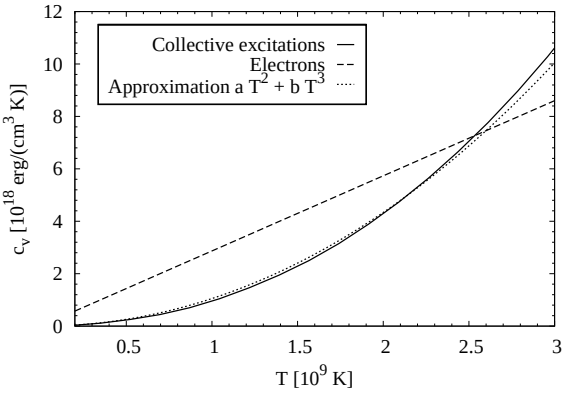

Figure 7.4: Temperature dependence of the contribution of the collective modes (solid line) and of the electrons (dashes) to the specific heat for the the example studied in the preceding subsection (see Table 7.1). The approximate formula , $aT^2 + bT^3$, see Eqs. (7.35) and (7.36), is shown as a dotted line.

contribution of such a mode to the specific heat is readily shown to be

$$c_v = \frac{3\zeta(3) k_B^3 T^2}{\pi \hbar^2 u_s'^2 L} \equiv aT^2 \,, \tag{7.36}$$

where ζ is the Riemann zeta function [$\zeta(3) = 1.202\ldots$]. Due to its quadratic temperature dependence, this is the next dominant contribution at low temperatures after the electrons. The result of the simple formula $aT^2 + bT^3$, where a and b have been calculated with the average values $u_s = 0.078\,c$ and $u_s' = 0.042\,c$, is shown as the dotted line in Fig. 7.4. Up to the temperatures considered here, it fits reasonably well the full calculation.

7.4 Summary

In this paper, we have presented a formalism of superfluid hydrodynamics to treat density-wave propagation in inhomogeneous pasta-like nuclear structures which appear in the inner crust of neutron stars. To account for the periodicity of the structure, we incorporate the Floquet-Bloch boundary conditions. The idea is somewhere in between the approaches of Refs. [85, 186], considering only the long-wavelength limit, averaging over the microscopic details of the structure, and microscopic calculations of the crust within the Wigner-Seitz approximation [138, 208], valid for wavelengths smaller than the radius of the Wigner-Seitz cell. Concerning the microscopic input for the nuclear equation of state and the geometry of the structure, we followed the work by Avancini et al. [23].

Within this approach, we have calculated the excitation spectrum of a periodic structure of parallel slabs, the lasagna phase. We have shown that the structure can indeed induce non-negligible effects on the excitation spectrum. In particular, we found that the sound velocity of the usual acoustic mode depends on the direction

of the propagation, and, more surprisingly, that there is a second acoustic mode whose dispersion relation is almost independent of q_z. In addition, we found different optical branches, similar to the phonon spectrum of ordinary crystals.

We have calculated the specific heat corresponding to this excitation spectrum and found that its contribution is much more important than that of individual neutrons, which is strongly suppressed due to the superfluid gap Δ. At temperatures relevant for neutron stars, the main contributions to the specific heat come from the electrons and from the acoustic collective modes. The latter cannot be obtained within the Wigner-Seitz approximation. Due to the curious sound mode whose energy is independent of q_z, the specific heat due to the collective modes goes like T^2 instead of T^3. [With the same arguments, one would predict that in a rod structure (spaghetti phase), the specific heat should be linear in T.] However, it is not clear whether this feature survives when the Coulomb interaction, which has been neglected here, will be taken into account.

Of course, in order to treat the complex geometry, we were obliged to make a couple of approximations. Contrary to the microscopic approaches based on the Quasiparticle-Random-Phase-Approximation (QRPA) [138, 208], we rely on the assumption that the modes can be described hydrodynamically, which implies in particular that the local neutron and proton Fermi surfaces stay spherical at all times. This assumption is justified if all spatial variations are slow compared to the superfluid coherence length and the temporal variations are slow compared to the superfluid gap. Both assumptions are not very well fulfilled. However, we have cited examples where hydrodynamics gives reasonable answers even beyond these very restrictive limits, and we believe that the results are at least qualitatively correct. The most serious limitation of the present work is probably that the Coulomb interaction has been neglected. The Coulomb interaction between the protons results in an additional coupling between neighboring cells, which can have important consequences for the excitation spectrum. In the approaches of Refs. [85, 186], it was accounted for by including the elasticity of the Coulomb lattice. In our more microscopic approach, the Coulomb potential would have to be included from the beginning into the proton chemical potential $\mu_p(\mathbf{r}, t)$ in the Euler equation (7.2). This is a difficult task which will be left for future studies.

It has to be stressed that the contribution of the collective modes studied here is potentially more important than other contributions, notably the contribution from individual neutrons. Therefore it is interesting to pursue their investigation and to include the additional contribution to the specific heat in studies of neutron star thermal evolution.

Acknowledgments

We are indebted to C. Da Providencia for providing us with the data for densities and geometries of the different pasta phases in the model of Ref. [23] as well as to M. Fortin for providing us with the data of Ref. [109]. We thank S. Chiacchiera, D. Peña, and M. Fortin for discussions. This work was supported by ANR (project NEXEN), and by CompStar, a research networking programme of the European Science Foundation.

8 Temperature dependence and finite-size effects in collective modes of superfluid trapped Fermi gases

M. Grasso, E. Khan, and M. Urban, Phys. Rev. A 72, 043617 (2005)

We discuss collective monopole and quadrupole excitations of a collisionless gas of trapped fermionic atoms in the superfluid BCS phase, comparing the fully microscopic Bogoliubov-de Gennes and quasiparticle random-phase approximation method with widely used semiclassical methods. In particular, the microscopic treatment allows us to address the questions of temperature dependence and non-trivial dependence on the trap parameters, which cannot be answered within the semiclassical approach. The main result concerning the temperature dependence is a strong Landau damping at intermediate temperature, which disappears in the limits of zero and critical temperature. However, even at zero temperature, considerable deviations from superfluid hydrodynamics are found if the trap frequency is of the same order of magnitude as the pairing gap.

8.1 Introduction

Dilute gases of alkaline fermionic and bosonic atoms are superfluid at very low temperature: Bose-Einstein condensates have been obtained in the case of bosonic atoms [17, 55, 89], while condensation of molecules (made out of two atoms) has been observed in the case of fermionic atoms [277]. For fermionic atoms in the weakly interacting regime ($k_F|a| \ll 1$, where k_F is the Fermi momentum and a the s-wave scattering length) BCS superfluidity is expected in the case of attractive interatomic interaction ($a < 0$).

A striking experimental evidence for BCS superfluidity is still missing, even though various signals which would be coherent with a superfluid behavior have been observed in some experiments: the anisotropic expansion of the gas after releasing it from the trap [177], the measurement of the gap [82], the measurement of the frequencies and damping rates of the breathing modes [34, 139].

However, the gap has been actually measured only in the strongly interacting regime and no experimental values exist for the weakly interacting case. The anisotropic expansion on the one hand and the frequencies of the breathing modes on the other hand can be predicted within a hydrodynamic approach for a superfluid gas [31, 168, 233]. In both cases the experimental observations agree very well with the hydrodynamic predictions, and this could actually be considered as an evidence for superfluidity. However, the predictions for a superfluid gas are the same as those for a normal gas in the presence of collisions. It is true that at the very low temperatures achieved in these experiments Pauli principle is expected to inhibit collisions. However, the experimental measurements have been performed during the expansion of the gas after releasing it from the trap. In such a situation momentum space deformations are possible and collisions can survive even at very low temperatures. So far, it has not been possible to completely control this problem from an experimental point of view and, for this reason, no firm conclusions about superfluidity can actually be drawn.

Another limitation is related to the hydrodynamic approach: hydrodynamics can be safely applied only within the limits of validity of semiclassical approaches, $\Delta \gg \hbar\Omega$, where Δ is the pairing gap and Ω is the trapping frequency. Effects from the finite size and inhomogeneity, governed by the finite trap frequency Ω, are neglected. Moreover, the hydrodynamic formalism has been developed so far only for the case of zero temperature ($T = 0$).

In this article we deal with the excitation spectra in the normal and superfluid phases of a dilute Fermi gas and we analyze how these spectra are affected by superfluidity, both in hydrodynamic and microscopic descriptions. In order to study excitations similar to those observed experimentally (the breathing modes) we focused our attention on the monopole and quadrupole modes. However, while the breathing modes have been observed for a cigar-shaped gas (and the radial and axial frequencies have been measured), we restrict our

analysis to a spherical gas for the sake of numerical tractability. Moreover, while the experiments of Refs. [139] and [34] have been done for strongly interacting gases, we treat a weakly interacting system.

We analyze the excitation spectra within a finite-temperature mean-field approach which provides a microscopic treatment for the system. The Bogoliubov-de Gennes (BdG) equations [90] are solved for the ground state and the excitations are treated within the quasiparticle random-phase approximation (QRPA) [18]. This approach has already been developed for atomic Fermi gases in Ref. [64], where the spin-dipole and the quadrupole modes have been analyzed. On the other hand, the monopole modes have already been studied and compared to a schematic model in Ref. [61].

In the present work we want to study systematically the effects related to the temperature and to the trap frequency of the system. In particular, we compare our results with the corresponding hydrodynamic ones in order to check the validity of the semiclassical approach. In addition to the strength distributions related to the excitation spectra, we also present the transition densities which can give important information on nature of the collective modes.

The article is organized as follows. In Sec. 8.2 we briefly sketch the quantum mechanical and semiclassical formalisms to describe collective modes in the superfluid phase and in the normal phase in the collisionless limit. In Sec. 8.3 results for the monopole and quadrupole excitations are shown: the dependence on the temperature and on the frequency of the trap are studied. In Sec. 8.4 we draw our conclusions.

8.2 Quantum mechanical and semiclassical formalism

In this section we will briefly review the theoretical description of collective modes in trapped Fermi gases. As already mentioned in the introduction, one has to distinguish between quantum mechanical ("microscopic") and semiclassical approaches. The fully quantum mechanical calculation consists in solving the QRPA equations, which are the small-amplitude limit of the time-dependent BdG equations. At present such calculations are available only for systems containing up to $\sim 10^4$ atoms in the case of a spherically symmetric trap. These conditions are quite far from the experimental ones, corresponding to particle numbers of $\sim 10^5 - 10^6$ particles in a cigar-shaped trap. Up to now, the "realistic" conditions can only be treated within semiclassical approaches. The simplest semiclassical approach is the hydrodynamic theory. This theory is valid in the superfluid phase at zero temperature, since the pairing correlations keep the Fermi surface spherical during the collective motion of the system. However, hydrodynamics fails at non-zero temperature, unless the local equilibrium can be ensured by collisions. Since we are interested in the weakly interacting regime, the collision rate $1/\tau$ is very small compared to the frequency of the trap. In this "collisionless" regime, the Fermi surface becomes locally deformed during the collective oscillation. This cannot be described by hydrodynamics, but requires a description in the framework of the Vlasov equation. The latter is valid in the normal phase, i.e., above the critical temperature T_c. In the intermediate temperature range $0 < T < T_c$, a semiclassical theory is still missing.

8.2.1 Quantum mechanical formalism (QRPA)

The QRPA method has already been applied to trapped Fermi gases in the weakly [64] as well as in the strongly interacting regime [178] and here we will only give a short summary.

We consider a gas of atoms with mass m in a spherical harmonic trap with frequency Ω, assuming that the atoms equally occupy two hyperfine states $\sigma = \uparrow, \downarrow$. Because of the low temperature and density of the gas, the interaction between the atoms can be chosen as a zero-range interaction and parametrized by the s-wave atom-atom scattering length a. In order to simplify the notation, we will express all quantities in harmonic oscillator (HO) units, i.e., frequencies in units of Ω, energies in units of $\hbar\Omega$, temperatures in units of $\hbar\Omega/k_B$,

and lengths in units of the oscillator length $l_{HO} = \sqrt{\hbar/(m\Omega)}$. Furthermore, instead of the scattering length we will use the coupling constant $g = 4\pi a/l_{HO}$ as parameter of the interaction strength.

As mentioned above, the QRPA describes small-amplitude oscillations around the equilibrium state within the BdG formalism. Therefore, the first step consists in solving the BdG equations [90]

$$\begin{aligned}[H_0 + W(r)]u_{nlm}(\mathbf{r}) + \Delta(r)v_{nlm}(\mathbf{r}) &= E_{nl}u_{nlm}(\mathbf{r})\,,\\ \Delta(r)u_{nlm}(\mathbf{r}) - [H_0 + W(r)]v_{nlm}(\mathbf{r}) &= E_{nl}v_{nlm}(\mathbf{r})\end{aligned} \tag{8.1}$$

for the static case. In this way we obtain a set of quasiparticle energies E_{nl} and wave-functions u_{nlm} and v_{nlm}. In Eq. (8.1), H_0 denotes the hamiltonian of the non-interacting HO minus the chemical potential μ,

$$H_0 = \frac{1}{2}(-\boldsymbol{\nabla}^2 + r^2) - \mu\,, \tag{8.2}$$

while the interaction is accounted for in a self-consistent way through the Hartree potential W and the pairing field Δ. Due to spherical symmetry, the wave functions can be written as

$$u_{nlm}(\mathbf{r}) = u_{nl}(r)Y_{lm}(\theta,\phi)\,, \tag{8.3}$$

$$v_{nlm}(\mathbf{r}) = v_{nl}(r)Y_{lm}(\theta,\phi)\,. \tag{8.4}$$

The quantum numbers l and m are the angular momentum and its projection, while n numbers different states having the same l and m. In practice, the diagonalization of Eq. (8.1) is done in a truncated harmonic oscillator basis, containing the eigenfunctions of the trapping potential up to a certain HO energy $E_C = N_C + \frac{3}{2}$, i.e.,

$$2(n-1) + l \leq N_C\,. \tag{8.5}$$

The self-consistency relates W and Δ to the wave functions u and v. The mean field W is just proportional to the density, i.e.,

$$W(\mathbf{r}) = g\sum_{nl}^{N_C}\frac{2l+1}{4\pi}\{v_{nl}^2(r)[1 - f(E_{nl})] + u_{nl}(r)f(E_{nl})\}\,, \tag{8.6}$$

where

$$f(E) = \frac{1}{e^{E/T}+1} \tag{8.7}$$

denotes the Fermi function. The Hartree field is independent of the cutoff N_C if the latter is taken sufficiently large. The calculation of the pairing field Δ, however, is more complicated. The zero-range interaction leads to a divergence which in the case of uniform systems can be regularized in a standard way by renormalizing the scattering length. This regularization method has been generalized to the case of trapped systems by Bruun et al. [59] and developed further by Bulgac and Yu [67] and two of the authors [119]. As a result, the pairing field can be written as

$$\Delta(\mathbf{r}) = -g_{\mathit{eff}}(r)\sum_{nl}^{N_C}\frac{2l+1}{4\pi}u_{nl}(r)v_{nl}(r)[1 - 2f(E_{nl})]\,, \tag{8.8}$$

with an effective coupling constant g_{eff} which allows to include the contribution from states beyond the cutoff N_C within the Thomas-Fermi approximation (TFA). The explicit expression for g_{eff} reads

$$\frac{1}{g_{\mathit{eff}}(r)} = \frac{1}{g} + \frac{1}{2\pi^2}\Big(\frac{k_F(r)}{2}\ln\frac{k_C(r)+k_F(r)}{k_C(r)-k_F(r)} - k_C(r)\Big)\,, \tag{8.9}$$

where k_F and k_C denote the local Fermi and cutoff momenta, respectively:

$$k_F(r) = \sqrt{2\mu - r^2 - 2W(r)}\,, \tag{8.10}$$

$$k_C(r) = \sqrt{2N_C + 3 - r^2}\,. \tag{8.11}$$

Once the static BdG equations are solved, we can calculate the linear response of the system to a small time-dependent perturbation. Following Ref. [64], we have to compute the QRPA response function Π, which is a 4×4 matrix built out of 16 correlation functions:

$$\Pi(\omega, \mathbf{r}, \mathbf{r}') = \begin{pmatrix} \langle\langle\hat{\rho}_\uparrow\hat{\rho}_\uparrow\rangle\rangle & \langle\langle\hat{\rho}_\uparrow\hat{\rho}_\downarrow\rangle\rangle & \langle\langle\hat{\rho}_\uparrow\hat{\chi}\rangle\rangle & \langle\langle\hat{\rho}_\uparrow\hat{\chi}^\dagger\rangle\rangle \\ \langle\langle\hat{\rho}_\downarrow\hat{\rho}_\uparrow\rangle\rangle & \langle\langle\hat{\rho}_\downarrow\hat{\rho}_\downarrow\rangle\rangle & \langle\langle\hat{\rho}_\downarrow\hat{\chi}\rangle\rangle & \langle\langle\hat{\rho}_\downarrow\hat{\chi}^\dagger\rangle\rangle \\ \langle\langle\hat{\chi}\hat{\rho}_\uparrow\rangle\rangle & \langle\langle\hat{\chi}\hat{\rho}_\downarrow\rangle\rangle & \langle\langle\hat{\chi}\hat{\chi}\rangle\rangle & \langle\langle\hat{\chi}\hat{\chi}^\dagger\rangle\rangle \\ \langle\langle\hat{\chi}^\dagger\hat{\rho}_\uparrow\rangle\rangle & \langle\langle\hat{\chi}^\dagger\hat{\rho}_\downarrow\rangle\rangle & \langle\langle\hat{\chi}^\dagger\hat{\chi}\rangle\rangle & \langle\langle\hat{\chi}^\dagger\hat{\chi}^\dagger\rangle\rangle \end{pmatrix}, \tag{8.12}$$

with the short-hand notation[1]

$$\langle\langle\hat{A}\hat{B}\rangle\rangle = -i\int_0^\infty dt e^{i\omega t}\langle[\hat{A}(t,\mathbf{r}), \hat{B}(0,\mathbf{r}')]\rangle\,, \tag{8.13}$$

where $\langle\rangle$ means the thermal average. The operators of the normal and anomalous densities, $\hat{\rho}$ and $\hat{\chi}$, are defined in terms of the field operators $\hat{\psi}$ and $\hat{\psi}^\dagger$ as follows:

$$\hat{\rho}_\sigma(t,\mathbf{r}) = \hat{\psi}^\dagger_\sigma(t,\mathbf{r})\hat{\psi}_\sigma(t,\mathbf{r})\,, \tag{8.14}$$

$$\hat{\chi}(t,\mathbf{r}) = \hat{\psi}_\downarrow(t,\mathbf{r})\hat{\psi}_\uparrow(t,\mathbf{r})\,. \tag{8.15}$$

In order to obtain Π, we first compute the free or unperturbed response function Π_0, which is defined analogously to Eq. (8.12), but which does not include the effect of interactions between the quasiparticles. Thus Π_0 can be obtained by replacing the field operators $\hat{\psi}$ in Eqs. (8.14) and (8.15) by

$$\hat{\psi}_\sigma(t,\mathbf{r}) = \sum_{nlm}[b_{nlm\sigma}u_{nlm}(\mathbf{r})e^{iE_{nl}t} - \sigma b^\dagger_{nlm-\sigma}v^*_{nlm}(\mathbf{r})e^{-iE_{nl}t}]\,, \tag{8.16}$$

where $\hat{b}$ and $\hat{b}^\dagger$ are annihilation and creation operators of non-interacting quasiparticles. Inserting the resulting expressions into Eq. (8.12) and using the relations $\{b_\alpha, b_\beta\} = \{b^\dagger_\alpha, b^\dagger_\beta\} = 0$, $\{b_\alpha, b^\dagger_\beta\} = \delta_{\alpha\beta}(1 - f(E_\alpha))$, and $\langle b^\dagger_\alpha b_\beta\rangle = f(E_\alpha)\delta_{\alpha\beta}$, we obtain explicit expressions for the 16 functions contained in Π_0 in terms of the u and v functions and the quasiparticle energies obtained from Eq. (8.1).

Due to the spherical symmetry of the trap and the rotational invariance of the interaction, excitations with different angular momenta do not mix. Therefore it is useful to decompose Π_0 into contributions of different angular momenta:

$$\Pi_0(\omega, \mathbf{r}, \mathbf{r}') = \sum_{LM}\Pi_{0L}(\omega, r, r')Y_{LM}(\theta,\phi)Y^*_{LM}(\theta',\phi')\,. \tag{8.17}$$

The QRPA response Π_L for angular momentum L can now be obtained from the quasiparticle response Π_{0L} by solving the Bethe-Salpeter integral equation

$$\Pi_L(\omega, r, r') = \Pi_{0L}(\omega, r, r') + \int_0^\infty dr'' r''^2 \Pi_{0L}(\omega, r, r'')G\Pi_L(\omega, r'', r')\,, \tag{8.18}$$

[1] In the published version of this article, Eq. (8.13) contains an erroneous factor $1/2\pi$.

where G accounts for the residual interaction between the quasiparticles:

$$G = \begin{pmatrix} 0 & g & 0 & 0 \\ g & 0 & 0 & 0 \\ 0 & 0 & 0 & g \\ 0 & 0 & g & 0 \end{pmatrix} . \tag{8.19}$$

When calculating the 16 functions contained in Π_{0L}, one observes that two of them, namely those related to $\langle\langle\hat{\chi}^\dagger\hat{\chi}\rangle\rangle$ and $\langle\langle\hat{\chi}\hat{\chi}^\dagger\rangle\rangle$, are divergent for $N_C \to \infty$. This divergence has the same origin as that of the pairing field. Bruun and Mottelson [64] therefore suggested to use the same pseudopotential method as for the regularization of the pairing field in order to remove the divergence. However, it is not clear how in their prescription, Eq. (7) in Ref. [64], the contribution of states beyond the cutoff N_C can be approximated (as we did in the case of the pairing field by using the TFA), which is crucial for having convergence at reasonable values of the cutoff N_C. We therefore propose a simplified prescription: when calculating Π_{0L}, we have to restrict the sum to states below the cutoff, $2(n-1)+l \leq N_C$. To compensate the resulting cutoff dependence, the interaction in the pairing channel must be replaced by the effective coupling constant given in Eq. (8.9). Thus, we replace G in Eq. (8.18) by $G_{\mathit{eff}}(r'')$, which is defined by

$$G_{\mathit{eff}}(r) = \begin{pmatrix} 0 & g & 0 & 0 \\ g & 0 & 0 & 0 \\ 0 & 0 & 0 & g_{\mathit{eff}}(r) \\ 0 & 0 & g_{\mathit{eff}}(r) & 0 \end{pmatrix} . \tag{8.20}$$

One can show that, in the case of a uniform system, this simplified prescription coincides with the pseudopotential method in the limit of excitations with long wavelengths and low frequencies. We have checked the convergence of the results using this regularization prescription.

Finally, we have to say how physical quantities of interest can be extracted from the correlation function Π. To that end it is useful to look at the spectral representation

$$\sum_{\sigma\sigma'}\langle\langle\hat{\rho}_\sigma\hat{\rho}_{\sigma'}\rangle\rangle = \int d\omega' \frac{S(\omega',\mathbf{r},\mathbf{r}')}{\omega-\omega'+i\varepsilon} , \tag{8.21}$$

with

$$S(\omega,\mathbf{r},\mathbf{r}') = -\frac{1}{\pi}\sum_{\sigma\sigma'}\mathrm{Im}\langle\langle\hat{\rho}_\sigma\hat{\rho}_{\sigma'}\rangle\rangle = (1-e^{-\omega/T})\sum_{ij}\frac{e^{-E_i/T}}{Z}\delta(\omega-E_j+E_i)\sum_{\sigma\sigma'}\langle i|\hat{\rho}_\sigma(\mathbf{r})|j\rangle\langle j|\hat{\rho}_{\sigma'}(\mathbf{r}')|i\rangle , \tag{8.22}$$

where $|i\rangle$ and $|j\rangle$ are eigenstates of the many-body hamiltonian with total energies E_i and E_j, respectively, and $Z = \sum_i \exp(E_i/T)$. In the present QRPA formalism Eq. (8.22) is evaluated using the four upper left elements of the Π response function (8.12), obtained with Eq. (8.18).

In this paper we will consider excitation operators of the form

$$V_1(t,\mathbf{r}) \propto r^2 Y_{LM}(\theta,\phi)e^{-i\omega t} . \tag{8.23}$$

with $L=0$ (monopole excitations) and $L=2$ (quadrupole excitations). The corresponding strength function $S_L(\omega)$, which gives the excitation spectrum, is defined by

$$S_L(\omega) = \int_0^\infty dr r^4 \int_0^\infty dr' r'^4 \sum_{\sigma\sigma'} S_L(\omega,r,r') . \tag{8.24}$$

Another interesting quantity is the transition density $\delta\rho = \rho - \rho_0$, where ρ_0 denotes the density in equilibrium and ρ is the density of the excited system. In the case of zero temperature, where the stationary system is in the ground state $|0\rangle$, the transition density for $\omega = E_j - E_0$ is proportional to

$$\delta\rho(\omega = E_j - E_0, \mathbf{r}) \propto \sum_\sigma \langle j|\hat{\rho}_\sigma(\mathbf{r})|0\rangle \,. \tag{8.25}$$

In this case, the sum over i in Eq. (8.22) reduces to one term ($i = 0$), and therefore the transition density can be obtained from

$$[\delta\rho(\omega = E_j - E_0, \mathbf{r})]^2 \propto \int_{\omega-\delta}^{\omega+\delta} d\omega' S(\omega', \mathbf{r}, \mathbf{r}) \,, \tag{8.26}$$

where δ is supposed to be sufficiently small to avoid that other states than the selected one ($|j\rangle$) contribute.

8.2.2 Superfluid hydrodynamics

At zero temperature, superfluid hydrodynamics provides the equations of motion for the density (per spin state) $\rho(t, \mathbf{r})$ and the irrotational collective velocity field $\mathbf{v}(t, \mathbf{r})$ of the superfluid current (continuity and Euler equations) [88]:

$$\dot{\rho} + \boldsymbol{\nabla} \cdot (\rho \mathbf{v}) = 0 \,, \tag{8.27}$$

$$\dot{\mathbf{v}} = -\boldsymbol{\nabla}\Big(\frac{\mathbf{v}^2}{2} + \frac{V_{ext}}{m} + \frac{\mu_{loc}}{m}\Big) \,. \tag{8.28}$$

These equations can equally be used for fermionic and bosonic systems, only the equation of state, relating the local chemical potential μ_{loc} to the density ρ, must be adapted correspondingly. In the case of weakly interacting fermions, where the density can be regarded as independent of the pairing gap, this equation of state is given by the Thomas-Fermi relation

$$\mu_{loc}(\rho) = \frac{p_F^2}{2m} + g\rho = \frac{\hbar^2(6\pi^2\rho)^{2/3}}{2m} + g\rho \,. \tag{8.29}$$

In the static (equilibrium) case, Eq. (8.28) together with this equation of state gives immediately the usual Thomas-Fermi equation for the density profile $\rho_0(\mathbf{r})$,

$$\mu_{loc}[\rho_0(\mathbf{r})] + V_0(\mathbf{r}) = \mu \,, \tag{8.30}$$

which is valid in both the normal and the superfluid phase. While the TFA in the normal phase is valid if μ_{loc} is much larger than the discrete level spacing of the trapped system ($\hbar\Omega$ in our case), superfluid hydrodynamics requires in addition that also the pairing gap Δ is large compared with the level spacing, which is much more difficult to satisfy.

Since the superfluid velocity field $\mathbf{v}$ is irrotational, it can be written as a gradient. In order to establish a connection with microscopic quantities, we write it in the form

$$\mathbf{v}(\mathbf{r}) = \frac{\hbar}{m}\boldsymbol{\nabla}\varphi(\mathbf{r}) \,. \tag{8.31}$$

where φ is related to the phase of the pairing field by $\Delta(\mathbf{r}) = |\Delta(\mathbf{r})| \exp[2i\varphi(\mathbf{r})]$.

In this article we are interested in small-amplitude motion. We therefore split the density and the external potential into their equilibrium values and small deviations, $\rho = \rho_0 + \delta\rho$ and $V_{ext} = V_0 + V_1$, and expand

Eqs. (8.27) and (8.28) up to linear order in the deviations. In addition, as we did in the preceding subsection, we will specialize to the case of a spherically symmetric harmonic trap and use the corresponding HO units ($\hbar = m = \Omega = 1$), i.e., $V_0 = r^2/2$. We know that for an excitation of the type (8.23) the solution must be of the form

$$\varphi(t, \mathbf{r}) = \varphi(r) Y_{LM}(\theta, \phi) \exp(-i\omega t) \tag{8.32}$$

and analogous for $\delta\rho$. Furthermore, we are interested in the eigenmodes of the system, which persist even if $V_1 = 0$. Then Eqs. (8.27) and (8.28) can be transformed into an eigenvalue equation[1] for the eigenfrequencies ω and the corresponding eigenfunctions $\varphi(r)$,

$$\frac{d\mu_{loc}}{d\rho}\Big|_{\rho_0} \Big(\frac{1}{r^2}(r^2 \rho_0 \varphi')' - \frac{L(L+1)}{r^2} \rho_0 \varphi \Big) = -\omega^2 \varphi \,, \tag{8.33}$$

where f' means df/dr, and an equation for the transition density,

$$\delta\rho = -i\omega \Big(\frac{d\mu_{loc}}{d\rho}\Big|_{\rho_0} \Big)^{-1} \varphi = \frac{-i\omega}{r} \rho_0' \varphi \,. \tag{8.34}$$

The numerical solution of Eq. (8.33) is not difficult. However, in the present article we are only interested in the lowest monopole ($L = 0$) and quadrupole ($L = 2$) modes. For these two modes, the velocity field $\mathbf{v}$ is practically linear in $\mathbf{r}$, and we can thus obtain a very accurate analytic approximation to the numerical solution. Let us start with the quadrupole mode ($L = 2$). We insert the ansatz $\varphi \approx a r^2$ into Eq. (8.33), multiply the equation by $\rho_0(r)$ and integrate over d^3r. By this integration the small deviations of the quadratic ansatz from the exact solution of Eq. (8.33) are averaged out and one thus obtains a very precise prediction for the frequency. After a lengthy calculation we reproduce the well-known result

$$\omega_{L=2} = \sqrt{2} \,, \tag{8.35}$$

which is independent of the interaction.

In a similar way we can find an approximation for the eigenfrequency of the lowest monopole mode ($L = 0$). In this case the function φ has the form $\varphi(r) \approx a - br^2$. Inserting this ansatz into Eq. (8.33), taking the derivative with respect to r in order to get rid of the constant a, multiplying by r and proceeding in the same way as in the case of the quadrupole mode, we finally obtain

$$\omega_{L=0} = 2\sqrt{1 + \frac{3E_{int}}{8E_{pot}}} \,, \tag{8.36}$$

where E_{int} and E_{pot} are the interaction and potential energies,

$$E_{int} = \int d^3r g \rho_0^2(\mathbf{r}) \,, \quad E_{pot} = \int d^3r r^2 \rho_0(\mathbf{r}) \,. \tag{8.37}$$

Contrary to the quadrupole frequency, the monopole frequency depends on the interaction. Since E_{int} is negative, the frequency $\omega_{L=0}$ is slightly lower than twice the trap frequency, 2Ω. Finally, the ratio of the constants a and b, which is needed in order to compute the transition density $\delta\rho$, can be determined from the condition that the integral over $\delta\rho$ must vanish, since the total number of particles stays constant.

[1] In the published version of this article, the last term on the lhs. of Eq. (8.33) is missing a factor ρ_0/r^2.

8.2.3 Vlasov description

Let us now consider a normal Fermi gas just above T_c. In the weakly interacting limit, T_c is very small as compared with the Fermi energy, i.e., except for the fact that the system is not superfluid, we can neglect temperature effects. We will also assume that the effect of collisions can be neglected. Under this condition the system cannot come to local equilibrium during the collective motion. In order to describe this effect, we will use the Wigner function $f(t, \mathbf{r}, \mathbf{p})$. In equilibrium and within the TFA, this function simply describes a Fermi sphere:

$$f_0(\mathbf{r}, \mathbf{p}) = \Theta(p_F(\mathbf{r}) - p)\,. \tag{8.38}$$

Out of equilibrium, if the particles do not undergo enough collisions to restore the isotropic momentum distribution, the local Fermi surface will assume a more complicated shape. The equation of motion for the Wigner function is the Vlasov equation

$$\dot{f} = (\boldsymbol{\nabla} V) \cdot (\boldsymbol{\nabla}_p f) - \frac{\mathbf{p}}{m} \cdot (\boldsymbol{\nabla}_r f)\,, \tag{8.39}$$

where $V(t, \mathbf{r}) = V_{ext}(t, \mathbf{r}) + g\rho(t, \mathbf{r})$ is the total (external+mean-field) potential and $\boldsymbol{\nabla}_r$ and $\boldsymbol{\nabla}_p$ are acting in coordinate and momentum space, respectively.

Contrary to the hydrodynamic equations in the superfluid phase, it is very difficult to solve the Vlasov equation directly. We are therefore again looking for approximate solutions for the special case of small-amplitude monopole and quadrupole oscillations in a spherical harmonic trap. We will employ the "generalized scaling ansatz" [201], which has been used with great success to describe giant resonances in atomic nuclei and which has also been applied to trapped atomic Fermi gases [168]. In this approach, the possible deformations of the local Fermi surface are restricted to quadrupolar shape. Introducing a small displacement field $\boldsymbol{\xi}(t, \mathbf{r})$, one can write

$$f(t, \mathbf{r}, \mathbf{p}) = f_0(\mathbf{r}', \mathbf{p}')\,, \tag{8.40}$$

with

$$\mathbf{r}' = \mathbf{r} - \boldsymbol{\xi}(t, \mathbf{r})\,, \tag{8.41}$$

$$\mathbf{p}' = \mathbf{p} - m\dot{\boldsymbol{\xi}}(t, \mathbf{r}) + \boldsymbol{\nabla}_r[\mathbf{p} \cdot \boldsymbol{\xi}(t, \mathbf{r})]\,. \tag{8.42}$$

The velocity field is then simply given by $\mathbf{v} = \dot{\boldsymbol{\xi}}$, and the last term in Eq. (8.42) describes the deformation of the Fermi sphere. For the form of the velocity field we make the same ansatz as before, i.e.,

$$\boldsymbol{\xi}(t, \mathbf{r}) = a\boldsymbol{\nabla} r^2 Y_{LM}(\theta, \phi) e^{-i\omega t}\,, \tag{8.43}$$

with $L = 0$ (monopole mode) or $L = 2$ (quadrupole mode). In analogy to the procedure in the preceding subsection, we linearize the Vlasov equation (8.39) with respect to $\boldsymbol{\xi}$, multiply by $\mathbf{p} \cdot \boldsymbol{\xi}^*$ and integrate over d^3p and d^3r. Using Eqs. (8.30) we reproduce after a tedious calculation the results originally derived in Ref. [168] [1],

$$\omega_{L=0} = 2\sqrt{1 + \frac{3E_{int}}{8E_{pot}}}\,, \quad \omega_{L=2} = 2\sqrt{1 - \frac{3E_{int}}{4E_{pot}}}\,. \tag{8.44}$$

Note that the monopole mode has the same frequency in the normal phase as in the superfluid phase. This can be understood as follows. If the displacement field is purely radial ($\boldsymbol{\xi} \propto \mathbf{r}$), as it is the case for the monopole mode, one can see from Eq. (8.40) that the Fermi surface stays spherical. Therefore hydrodynamics gives the same frequency as the Vlasov equation. The frequency of the quadrupole mode in the normal phase, however,

[1] In the published version of this article, Eq. (8.44) contains a few typos which have been corrected here.

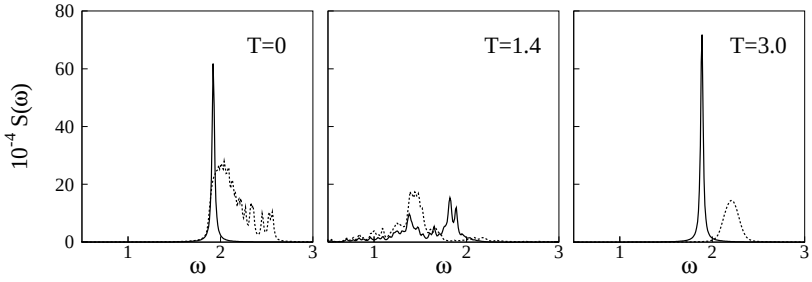

Figure 8.1: Free quasiparticle response (dashed line) and QRPA response (solid line) of the monopole excitation as a function of the frequency ω (in units of the trap frequency Ω), for three different temperatures: $k_B T = 0$, $1.4\,\hbar\Omega$, and $3\,\hbar\Omega$ (from left to right).

is higher than in the superfluid phase by a factor of approximately $\sqrt{2}$. From Eq. (8.40) one can see that in this case the Fermi surface gets a quadrupole deformation perpendicular to the deformation of the density profile in coordinate space. This deformation costs energy and therefore increases the frequency of the mode as compared to hydrodynamics.

8.3 Results

In this section we will compare QRPA and semiclassical results for monopole and quadrupole oscillations in a spherical trap. We are mainly interested in the limits of validity of superfluid hydrodynamics, since this theory is widely used in order to analyze experimental results. For instance, a recent experiment of the Innsbruck group showed that the axial breathing mode in a cigar-shaped trap follows the hydrodynamic behavior throughout the BCS-BEC crossover, while the radial breathing mode deviates considerably from the hydrodynamic predictions [34], especially on the BCS side of the crossover region. This contrasts a similar experiment at Duke University [139], of course with different trap parameters, where the frequency of the radial breathing mode was in reasonable agreement with hydrodynamics. In both experiments the systems were still very strongly interacting even on the BCS side of the crossover (in the Innsbruck experiment, the strongest deviations happened when $k_F|a|$ was of the order of 2), such that our weak-coupling theory (valid for $k_F|a| \ll 1$) cannot directly be compared to these experiments. Nevertheless, it is clear that the limits of validity of hydrodynamics should be clarified.

It is known that hydrodynamics works at zero temperature and if the level spacing $\hbar\Omega$ is much smaller than the gap Δ, but both conditions are generally not fulfilled in the experiments. Since experiments cannot be done at zero temperature, it is interesting to see what kind of temperature effects can arise below the critical temperature T_c. The second condition is also very strong, especially if the trap is strongly deformed and the transverse trap frequency is large, and it is therefore important to know up to which ratio $\hbar\Omega/\Delta$ hydrodynamics can be trusted.

8.3.1 Temperature dependence

In this subsection we will study how the properties of collective modes change in the small temperature range from zero to the critical temperature T_c. For this investigation we are using the parameter set $\mu = 32\,\hbar\Omega$ and $g = -0.965$ (in HO units). With these parameters, the number of particles is approximately 17000 and the gap in the center of the trap at zero temperature is approximately $6\,\hbar\Omega$; one can therefore expect that at least at zero temperature hydrodynamics should work very well.

In Figs. 8.1 and 8.2 we show the monopole and quadrupole response functions, respectively, for three

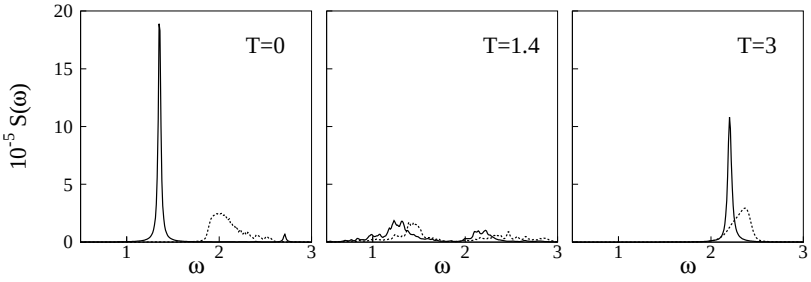

Figure 8.2: Free quasiparticle response (dashed line) and QRPA response (solid line) of the quadrupole excitation as a function of the frequency ω (in units of the trap frequency Ω) for three different temperatures: $k_BT = 0$, $1.4\,\hbar\Omega$, and $3\,\hbar\Omega$ (from left to right).

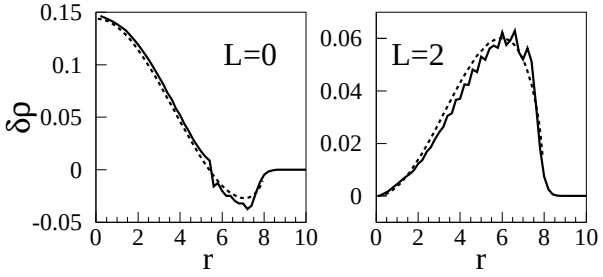

Figure 8.3: Transition densities for the collective monopole (left panel) and quadrupole (right panel) modes as a function of r (in units of the oscillator length l_{HO}), at $T = 0$. Solid and dashed lines represent the QRPA and the semiclassical results, respectively.

different values of the temperature. The figures on the left show the response at zero temperature. The solid lines correspond to the QRPA results while the dashed lines represent the free quasiparticle response. In principle, the response function consists of a very large number of discrete levels. For the purpose of graphical presentation, these delta functions must be smeared out, and we therefore introduce a small imaginary part of $\epsilon = 0.015\,\Omega$ in the denominators of the correlation functions [see Eq. (8.22)]. For T=0, the QRPA quadrupole response shows one single collective peak whose frequency is very close to that predicted by hydrodynamics (see Table 8.1). The QRPA response is completely different from the free quasiparticle response, which has a broad and almost continuous distribution of strength between $\sim 1.8\,\Omega$ and $\sim 2.7\,\Omega$. As has been realized before [64, 178], the threshold of the two-quasiparticle strength is related to the energy of the lowest-lying quasiparticles which are located near the surface of the atomic cloud.

In the case of the monopole mode the good agreement between QRPA and hydrodynamics (Table 8.1) is even more surprising than in the case of the quadrupole mode, since the frequency of the monopole mode is so high that it lies in the two-quasiparticle continuum (see dashed line in Fig. 8.1) and one would therefore expect a certain amount of Landau damping.

Apart from the study of the frequencies of the collective modes, the comparison between hydrodynamics and QRPA can be extended also to the analysis of the character of such modes. We display in Fig. 8.3 the transition densities of the two collective modes, which, since the density profile is known, can be related to the velocity field [see Eq. (8.34)]. The normalization of the QRPA transition density is obtained from the integral of the corresponding peak in the strength function, while that of the semiclassical transition density has been adjusted to the QRPA one. We see that the simple formulas from Sec. 8.2.2 are in good agreement with the QRPA transition densities. However, the QRPA transition densities exhibit small Friedel-like oscillations, especially near the surface where the gap is small and the local Fermi surface is therefore relatively sharp.

Let us now consider an intermediate temperature between 0 and T_c. For the present set of parameters the critical temperature is $T_c \approx 2.8\,\hbar\Omega/k_B$; we therefore choose $T = 1.4\,\hbar\Omega/k_B \approx T_c/2$. As can be seen in

Table 8.1: Frequencies (in units of the trap frequency Ω) of monopole ($L = 0$) and quadrupole ($L = 2$) modes for $\mu = 32\ \hbar\Omega$ and $g = -0.965$ (in HO units) at zero temperature and above T_c. The QRPA results for $T > T_c$ were obtained with $T = 3\ \hbar\Omega/k_B$.

	$T = 0$		$T > T_c$	
	QRPA	hydro.	(Q)RPA	Vlasov
$L = 0$	1.9	1.88	1.9	1.88
$L = 2$	1.4	$\sqrt{2}$	2.2	2.22

the middle of Figs. 8.1 and 8.2, due to the presence of thermally excited quasiparticles the free quasiparticle response starts now already at $\omega = 0$. As a consequence, both the collective monopole and quadrupole modes become strongly fragmented and damped. Qualitatively, this strong Landau damping at temperatures between zero and T_c could be related to the damping mechanism which is responsible for the experimentally observed damping of breathing modes on the BCS side of the BEC-BCS crossover [34, 139]. Interesting is also the double-peak structure which can be seen in the quadrupole response, as if there were two damped modes, one corresponding to the hydrodynamic mode and another one corresponding to the quadrupole mode in the collisionless normal phase (see below). This can be interpreted in the sense of the two-fluid model [148, 149], which states that between $T = 0$ and $T = T_c$ the system effectively behaves as if it consisted of a mixture of normal and superfluid components.

Now we increase the temperature further to $T = 3\,\hbar\Omega/k_B$, which lies slightly above T_c, i.e., the system reaches the normal phase, but still the temperature is very low compared with the Fermi energy. In the normal phase, the BdG equations become identical to the usual Hartree-Fock equations, and the QRPA becomes equal to the usual RPA. In the case of the monopole mode (right panel of Fig. 8.1), the QRPA response is almost identical to that at zero temperature (left panel of Fig. 8.1), although the free quasiparticle response is quite different. Again there is one collective mode having the same frequency as at $T = 0$. This is not very surprising. As mentioned in the preceding section, the Vlasov equation predicts the same frequency as superfluid hydrodynamics, since in the case of the monopole mode there is no deformation of the local Fermi surface. This is different in the case of the quadrupole mode (right panel of Fig. 8.2). Also here a collective mode reappears, but it is situated at a different frequency than at zero temperature. The higher frequency in the normal phase compared with the superfluid phase is due to the Fermi surface deformation and is well described by the Vlasov equation (cf. Table 8.1).

8.3.2 Dependence on the size of the system

Let us now investigate the importance of the discrete level spacing at zero temperature. In the case without superfluidity, the semiclassical $\hbar \to 0$ limit (TFA in equilibrium and the Vlasov equation in the dynamical case) is known to work very well if the number of particles is sufficiently large. The reason is very simple: The only dimensionless parameter on which corrections can depend is $\hbar\Omega/\mu$, which becomes very small for large numbers of particles. In the current experiments involving $\sim 10^5 - 10^6$ atoms this type of corrections is completely negligible. For our study we choose, as in the preceding subsection, a chemical potential of $\mu = 32\,\hbar\Omega$. This is large enough to make these corrections small, and the numerical calculations are still tractable. The corresponding numbers of atoms lie between ~ 14000 and ~ 17000 depending on the chosen values of the coupling constant g due to the Hartree field (see Table 8.2).

In the case of superfluidity, however, another dimensionless parameter becomes important, which is $\hbar\Omega/\Delta$. Since in the BCS phase $\Delta \ll \mu$, this parameter is not necessarily small even if the number of particles is very large. In order to study the validity of hydrodynamics as a function of $\hbar\Omega/\Delta$, we change Δ by varying the coupling constant g between -0.636 and -0.965 (in HO units). As a measure for Δ we take its value at the

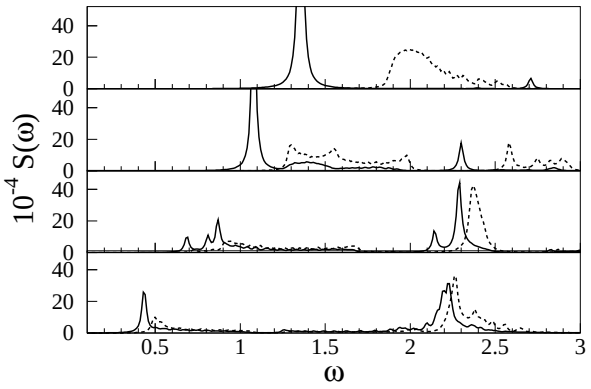

Figure 8.4: Unperturbed response (dashed line) and QRPA response (solid line) of the quadrupole excitation as a function of the frequency ω (in units of the trap frequency Ω) for $T = 0$ and $\mu = 32\,\hbar\Omega$ and four different values of the coupling constant: $g = -0.965$, $g = -0.8$, $g = -0.7$, and $g = -0.636$ (in HO units; from top to bottom).

center of the trap, $\Delta(0)$. The values of $\Delta(0)$ corresponding to the different coupling constants are listed in Table 8.2.

We are now going to analyze the finite-size effects on the quadrupole response function by using the different values of the coupling constant listed in Table 8.2. Note that, since we are using HO units, changing the coupling constant $g \propto a/l_{HO}$ is equivalent to changing the oscillator length l_{HO} and thus the radius of the cloud $R = \sqrt{2\mu/\hbar\Omega}\, l_{HO}$. Anyway, as argued above, the important parameter for finite-size effects is the ratio $\hbar\Omega/\Delta(0)$ and not the cloud size itself.

For the strongest coupling, $g = -0.965$ (in HO units), the central value of the gap, $\Delta(0)$, is large compared with $\hbar\Omega$, and hydrodynamics works almost perfectly at zero temperature, as we have already seen in the preceding subsection. Fig. 8.4 shows, from top to bottom, the evolution of the quadrupole response at $T = 0$ for decreasing coupling constant g, i.e., for increasing importance of the discrete level spacing. Besides the QRPA response (solid lines), we also show the free quasiparticle response (dashed lines). For $g = -0.8$ (in HO units), the gap at the center is still larger than $\hbar\Omega$ by a factor of three, but now we find considerable deviations of the QRPA response from the hydrodynamic result. Since the free quasiparticle response is now shifted to lower frequencies, the hydrodynamic mode becomes fragmented, which experimentally would show up as damping effect, and its frequency ($\omega \approx 1.1\,\Omega$) lies below the hydrodynamic prediction ($\sqrt{2}\,\Omega$). For $g = -0.7$ and $g = -0.636$ (in HO units), the central value of the gap is comparable to $\hbar\Omega$ and it is clear that hydrodynamics must fail. Indeed, the QRPA response becomes more and more similar to the free quasiparticle response which in the case of weak pairing looks very different from the strong-pairing case. The double-peak structure is a consequence of the two types of transitions which are allowed by the selection rules of the harmonic oscillator, i.e., transitions inside an oscillator shell ($\delta N = 0$, where N denotes the number of oscillator quanta) and transitions with $\delta N = 2$. As the interaction decreases, the strength of the $\delta N = 0$ transitions becomes less important while the $\delta N = 2$ transitions become stronger. This can be understood from the fact that in the limit

Table 8.2: Chosen values of the coupling constant g (first column; in HO units) and corresponding results for the number of particles, N (second column), and for the gap at the center of the trap, $\Delta(0)$ (third column; in units of $\hbar\Omega$). The remaining parameters were fixed to $\mu = 32\,\hbar\Omega$ and $T = 0$.

g	N	$\Delta(0)$
-0.965	16500	6.0
-0.8	15000	2.9
-0.7	14300	1.4
-0.636	13900	0.7

of a noninteracting harmonic oscillator without pairing ($g \to 0$) the $\delta N = 0$ transitions are forbidden by Pauli principle and only the $\delta N = 2$ transitions survive. In this limit the response has a single peak at $\omega = 2\Omega$, in exact agreement with the prediction from the Vlasov equation. In the semiclassical language, one can say that in this case the pairing is too weak to restore the spherical shape of the Fermi sphere during the oscillation, and therefore one finds the normal collisionless frequency instead of the hydrodynamical one.

8.4 Summary and conclusions

In this article we have studied the properties of collective monopole and quadrupole modes in superfluid Fermi gases in the BCS phase ($k_F|a| \ll 1$, $a < 0$) in a spherical harmonic trap. Having briefly recalled the quantum mechanical and semiclassical formalisms (QRPA, hydrodynamics, Vlasov equation), we presented numerical results and compared the different formalisms. Our main interest was focused on two types of effects: temperature and finite-size effects. Both cannot be treated within the semiclassical approaches available in the present literature, and they can therefore only be studied in the framework of the fully microscopic QRPA formalism.

In the case of a sufficiently large system (large meaning $\Delta \gg \hbar\Omega$), superfluid hydrodynamics can be used to describe the properties of collective modes at zero temperature. Our results confirm earlier findings [64] which show that already for parameters which lead to $\Delta(0) = 6\hbar\Omega$ the extremely simple theory of superfluid hydrodynamics is in almost perfect agreement with the numerically heavy QRPA method. This is not only true for the frequencies, but also for the transition densities, i.e., the velocity fields associated with the collective modes. However, experiments can never be done at zero temperature. The critical temperature T_c being extremely low, it is clear that already at very low temperatures between 0 and T_c the properties of the collective modes must undergo dramatic changes. This is evident if the hydrodynamic frequency ($T = 0$) is different from that in the collisionless normal phase ($T = T_c$), like in the case of the quadrupole mode. In the case of the monopole mode we also find a strong temperature dependence, although its frequency at $T = 0$ is the same as at $T = T_c$. In the intermediate temperature range between 0 and T_c the collective modes exhibit strong Landau damping. When the critical temperature is reached, the damping disappears and the collective modes can be very well described by the semiclassical Vlasov equation within the generalized scaling approximation.

It is interesting to compare these temperature effects with those found previously in the case of the twist mode [120], which is an excitation where the upper hemisphere rotates against the lower one. Near T_c, the behavior is rather similar: At $T = T_c$ the twist mode is a collective mode which can be described by the generalized scaling approximation to the Vlasov equation and whose frequency is slightly higher than the trap frequency. If the temperature is lowered, the twist mode becomes strongly damped, like the quadrupole and monopole modes. However, an important qualitative difference appears near zero temperature. Since the velocity field of the twist mode cannot be written as a gradient, the twist mode disappears completely at zero temperature, whereas the quadrupole and monopole modes have an irrotational velocity field and they reappear at zero temperature as hydrodynamic modes. In the case of the twist mode, the disappearance of the $1/\omega$ weighted integrated strength could be well described within a rather simple two-fluid model [120, 247]. It remains to be studied if a generalization of the two-fluid model to the dynamical case can also explain the damping of the quadrupole and monopole modes and the two-peak structure in the quadrupole response function at temperatures between 0 and T_c.

In addition to temperature effects, we studied how the properties of the quadrupole mode change at zero temperature when the condition for the validity of the hydrodynamic approach, $\Delta \gg \hbar\Omega$, is no longer satisfied. For parameters leading to $\Delta(0) \approx 3\hbar\Omega$ the QRPA already shows considerable deviations from the hydrodynamic theory. In the case of the quadrupole mode, the frequency for these parameters is found to be lower by 20% than the hydrodynamic prediction, and a certain fragmentation of the excitation spectrum (i.e., damping of the collective mode) can be observed. If $\Delta(0) \approx \hbar\Omega$, the hydrodynamic mode has more or less disappeared.

At the same time, a fragmented strength appears in the excitation spectrum near the frequency of the collective quadrupole mode in the normal collisionless phase.

These results should be kept in mind when frequencies of collective modes measured in experiments with strongly deformed traps are compared with the hydrodynamic predictions. Due to the strong deformation, the radial trap frequency Ω_r is often much higher than the axial one, Ω_z. Even in the case of strong pairing, the gap might be of the order of, say, $3\,\hbar\Omega_z$, and considerable deviations from hydrodynamics are possible.

9 Coupling of hydrodynamics and quasiparticle motion in collective modes of superfluid trapped Fermi gases

Michael Urban, Phys. Rev. A 75, 053607 (2007)

At finite temperature, the hydrodynamic collective modes of superfluid trapped Fermi gases are coupled to the motion of the normal component, which in the BCS limit behaves like a collisionless normal Fermi gas. The coupling between the superfluid and the normal components is treated in the framework of a semiclassical transport theory for the quasiparticle-distribution function, combined with a hydrodynamic equation for the collective motion of the superfluid component. We develop a numerical test-particle method for solving these equations in the linear response regime. As a first application we study the temperature dependence of the collective quadrupole mode of a Fermi gas in a spherical trap. The coupling between the superfluid collective motion and the quasiparticles leads to a rather strong damping of the hydrodynamic mode already at very low temperatures. At higher temperatures the spectrum has a two-peak structure, the second peak corresponding to the quadrupole mode in the normal phase.

9.1 Introduction

Most of the current experiments involving trapped atomic Fermi gases focus on the BEC-BCS crossover. By changing the magnetic field around a Feshbach resonance, the scattering length a of the atoms can be varied from small positive values through very large values near the resonance to small negative values. For $a > 0$, $k_F a \ll 1$ (where k_F denotes the Fermi momentum) the system can be considered as a Bose-Einstein condensate (BEC) of diatomic molecules. The crossover region, $k_F|a| \gtrsim 1$, is not yet very well understood from a theoretical point of view. Finally, on the other side of the resonance, when $a < 0$, $k_F|a| \ll 1$, the system should be in the BCS phase if the temperature is sufficiently low. However, the BCS critical temperature T_c is extremely low, and very soon the magnetic field reaches the point where T_c becomes smaller than the actual temperature T, and the system undergoes the phase transition to the normal (non-superfluid) phase.

One possibility to study the crossover experimentally is to measure the properties of certain collective oscillations. For example, the radial and axial breathing modes of a cigar-shaped trapped Fermi gas have been measured over the whole crossover region [14, 15, 34, 139, 140]. In these experiments one can observe how the frequencies and damping rates of the modes change from what one expects for a BEC to what one expects for a collisionless normal Fermi gas. Assuming that, except in the collisionless normal phase, hydrodynamics is valid, the measured frequencies can give some information on the equation of state in the crossover region.

However, this schematic picture is not completely accurate. Since the system is in a trap, there is no sharp transition from the superfluid to the normal phase. This can be seen as follows: The BCS critical temperature T_c depends on the atom density ρ, and the density depends on the position $\mathbf{r}$. In the center of the trap, the density $\rho(\mathbf{r})$ and hence the local critical temperature $T_c(\mathbf{r})$ are higher than in the outer part of the trap. As a consequence, for a given temperature, the outer part gets already normal at a magnetic field where the inner part is still superfluid. To be more precise, a system in the BCS phase at finite temperature behaves effectively like a mixture of superfluid and normal components with densities ρ_s and ρ_n, respectively, which become $\rho_s = \rho$, $\rho_n = 0$ in the limit $T = 0$ and $\rho_s = 0$, $\rho_n = \rho$ in the limit $T \geq T_c$. As a consequence, if $0 < T < T_c(\mathbf{r} = 0)$, the superfluid inner part of the trap behaves like a mixture of normal and superfluid components, while only the outer part with $T_c(\mathbf{r}) < T$ is completely normal [247].

If the collision rate was high enough, also the normal component of the gas would behave hydrodynamically. Such a system could be described by Landau's two-fluid hydrodynamics which has been applied to collective modes in trapped superfluid gases at finite temperature [237]. However, although in the recent experiments the transition to the normal phase seemed to occur at a value of $k_F|a| \approx 2$ [14, 15, 34] (i.e., the BCS

phase has not really been reached), the system behaved already like a collisionless normal Fermi gas. Hence it seems to be clear that the normal component cannot be treated in terms of hydrodynamics, but a description in terms of a Vlasov equation is required.

We note that there are other approaches to the description of the collective modes at finite temperature. In particular, let us mention the quasiparticle random phase approximation (QRPA) [61, 64, 118], which can be seen as the linearized form of the time-dependent Bogoliubov-de Gennes (BdG) equations. However, for practical reasons this method is limited to systems with spherical symmetry and numbers of particles up to a few times 10^4. Another disadvantage of this method is that it does not allow to include a collision term.

For the case of clean superconductors, a semiclassical transport theory taking the coupling between normal and superconducting components into account has been developed by Betbeder-Matibet and Nozières [43]. Transport theories of this type have also been used for describing the dynamics of superfluid ^{3}He [218, 262]. In a preceding paper [252, 253], we derived the semiclassical transport equations for the case of trapped atomic Fermi gases and applied them to the quadrupole mode of a gas in a spherical trap. We found that the presence of the normal component leads to a strong damping of the hydrodynamic collective mode. The same mechanism might explain the strong damping observed experimentally near the transition to the collisionless behavior [14, 15, 34]. However, in Ref. [252, 253] we had to replace the gap $\Delta(\mathbf{r})$ by a constant in order to find an analytical solution of the transport equations. Due to this simplification, which cannot really be justified, the damping of the hydrodynamic mode at a given temperature was much weaker than that obtained in QRPA calculations [118].

In the present paper we will work out a numerical method which allows us to treat the realistic $\mathbf{r}$-dependence of the gap. In addition, the method is very versatile and allows to treat much more general cases than can be solved analytically in the constant-gap approximation. The basic idea is to replace the continuous phase-space distribution function of the quasiparticles by a sum of a finite number of delta functions in phase space, called "test particles." In the normal phase, the test-particle method is routinely used for solving the Vlasov equation, e.g. for simulating heavy-ion collisions in nuclear physics [42]. It has also been applied to the simulation of the dynamics of normal trapped atomic Fermi gases with collision term [243, 244] and of Bose-Fermi mixtures [166]. However, to our knowledge, the test-particle method has not yet been used in the context of superfluid systems, and in fact the numerical difficulties are quite different from those encountered in the usual applications.

The article is organized as follows. In Sec. 9.2, we give a brief summary of the transport equations for the BCS phase and their linearization in the case of small deviations from equilibrium. We also give arguments why some terms which appear in the equations can be neglected. In Sec. 9.3 we introduce the test-particle method for the case of small oscillations around equilibrium. We describe in detail a number of tricky points we encountered during the implementation of the method, in particular the calculation of the test-particle trajectories, the generation of the test-particle distribution in phase space, and the initialization after a delta-like perturbation. In Sec. 9.4 we present the first results obtained with the help of this method, again for the quadrupole mode in a spherical system. Finally, in Sec. 9.5, we summarize and draw our conclusions.

9.2 Transport equations for the BCS phase

9.2.1 Summary of the kinetic equations

In this subsection we will give a brief summary of the kinetic equation approach developed by Betbeder-Matibet and Nozières [43] for the case of clean superconductors and adapted to the case of trapped atomic Fermi gases in Ref. [252, 253]. In this paper we will only give the final equations. For details of the derivations, see Ref. [252, 253].

We consider a dilute gas of fermionic atoms of mass m in two equally populated hyperfine states $\uparrow$ and $\downarrow$, trapped by an external potential V_{ext} and interacting via an attractive short-range interaction which leads to a scattering length $a < 0$. The corresponding classical mean-field hamiltonian (minus the chemical potential μ) reads

$$h(\mathbf{r}, \mathbf{p}) = \frac{\mathbf{p}^2}{2m} + V(\mathbf{r}) - \mu \,, \tag{9.1}$$

where V denotes the sum of the external and the Hartree potential,

$$V(\mathbf{r}) = V_{ext}(\mathbf{r}) + V_{Hartree}(\mathbf{r}) = V_{ext}(\mathbf{r}) + g\rho(\mathbf{r}) \,. \tag{9.2}$$

In the latter equation, $g = 4\pi\hbar^2 a/m$ denotes the coupling constant and ρ is the density per spin state. The Vlasov equation (without collision term) for the phase-space distribution function $\varrho(\mathbf{r}, \mathbf{p})$ in the normal phase can be written in the compact form

$$\dot{\varrho} = \{h, \varrho\} \,, \tag{9.3}$$

where $\{\cdot, \cdot\}$ denotes the Poisson bracket. One way to derive this equation is to perform a Wigner-Kirkwood expansion up to order $\hbar$ of the time-dependent Hartree-Fock equation [42, 201].

In the superfluid phase the derivation of an analogous transport equation is much more complicated due to the presence of the complex order parameter (gap) $\Delta(\mathbf{r})$ whose phase describes the collective motion of the Cooper pairs. In addition to the density matrix ϱ, there exists now an anomalous density matrix (pairing tensor) κ. The gap Δ and the anomalous density are related by the gap equation

$$\Delta(\mathbf{r}) = -g \int \frac{d^3p}{(2\pi\hbar)^3} \Big(\kappa(\mathbf{r}, \mathbf{p}) - \frac{\Delta(\mathbf{r})}{p^2/m} \Big) \,. \tag{9.4}$$

The time-dependence of ϱ and κ is governed by the time-dependent Hartree-Fock-Bogoliubov or BdG equations. As in the normal phase, the semiclassical transport theory can be derived from these equations by performing a Wigner-Kirkwood expansion up to order $\hbar$. However, it turns out that it is necessary to introduce a gauge transformation with a phase $\phi(\mathbf{r})$ that makes the order parameter Δ real. This corresponds to a transformation into the local rest frame of the Cooper pairs, which are moving with the collective velocity $\mathbf{v}_{coll}(\mathbf{r}) = -(\hbar/m)\boldsymbol{\nabla}\phi(\mathbf{r})$. The effect of this transformation is to change the gap Δ, the single-particle hamiltonian h, the normal and anomalous density matrices ϱ and κ according to

$$\tilde{\Delta}(\mathbf{r}) = \Delta(\mathbf{r}) e^{2i\phi(\mathbf{r})} \equiv |\Delta(\mathbf{r})| \,, \tag{9.5}$$

$$\tilde{h}(\mathbf{r}, \mathbf{p}) = h[\mathbf{r}, \mathbf{p} - \hbar\boldsymbol{\nabla}\phi(\mathbf{r})] - \hbar\dot{\phi}(\mathbf{r}) \,, \tag{9.6}$$

$$\tilde{\varrho}(\mathbf{r}, \mathbf{p}) = \varrho[\mathbf{r}, \mathbf{p} - \hbar\boldsymbol{\nabla}\phi(\mathbf{r})] \,, \tag{9.7}$$

$$\tilde{\kappa}(\mathbf{r}, \mathbf{p}) = \kappa(\mathbf{r}, \mathbf{p}) e^{2i\phi(\mathbf{r})} \,. \tag{9.8}$$

Roughly speaking, the phase ϕ determines the dynamics of the superfluid component of the system, while the dynamics of the normal component, consisting of thermally excited quasiparticles, has to be described separately. The distribution of these quasiparticles, denoted by $\nu(\mathbf{r}, \mathbf{p})$, obeys the following equation of motion:

$$\dot{\nu} = \{E, \nu\} \,. \tag{9.9}$$

This equation looks formally very similar to the Vlasov equation (9.3), except that the hamiltonian h is replaced by the quasiparticle energie E, which is defined as

$$E = \sqrt{\tilde{h}_{ev}^2 + \tilde{\Delta}^2} + \tilde{h}_{od} \,. \tag{9.10}$$

Throughout this article, the indices "ev" and "od" denote the time-even and time-odd parts of a phase-space function, i.e., the parts which are even and odd in $\mathbf{p}$, respectively. The quasiparticle-distribution function ν is related to the normal and anomalous density matrices in the new gauge, $\tilde{\varrho}$ and $\tilde{\kappa}$, by

$$\tilde{\varrho} = \frac{1}{2} - \frac{\tilde{h}_{ev}}{2E_{ev}}(1 - 2\nu_{ev}) + \nu_{od}\,, \tag{9.11}$$

$$\mathrm{Re}\,\tilde{\kappa} = \frac{\tilde{\Delta}}{2E_{ev}}(1 - 2\nu_{ev})\,. \tag{9.12}$$

The Vlasov-like equation (9.9) has to be complemented with an equation of motion for the phase ϕ. It turns out that ϕ has to be determined from the continuity equation

$$\dot{\rho}(\mathbf{r}) + \boldsymbol{\nabla}\cdot\mathbf{j}(\mathbf{r}) = 0\,, \tag{9.13}$$

where the density ρ and the current $\mathbf{j}$ are given by

$$\rho(\mathbf{r}) = \int \frac{d^3p}{(2\pi\hbar)^3}\tilde{\varrho}(\mathbf{r},\mathbf{p})\,, \tag{9.14}$$

$$\mathbf{j}(\mathbf{r}) = \int \frac{d^3p}{(2\pi\hbar)^3}\frac{\mathbf{p}}{m}\,\tilde{\varrho}(\mathbf{r},\mathbf{p}) - \frac{\hbar}{m}\rho(\mathbf{r})\boldsymbol{\nabla}\phi(\mathbf{r})\,. \tag{9.15}$$

9.2.2 Linearization around equilibrium

Let us now assume that the external potential V_{ext} can be written as

$$V_{ext} = V_{0ext} + V_{1ext}\,, \tag{9.16}$$

where V_{0ext} is time-independent and V_{1ext} is a small perturbation. The equilibrium quantities (corresponding to the potential V_{0ext}) will be marked by an index "0". In particular, since in equilibrium the gap can be chosen to be real, we have

$$\phi_0 = 0\,, \quad \tilde{h}_0 = h_0\,, \quad \tilde{\Delta}_0 = \Delta_0\,. \tag{9.17}$$

The quasiparticle distribution function in equilibrium is given by

$$\nu_0(\mathbf{r},\mathbf{p}) = f[E_0(\mathbf{r},\mathbf{p})]\,, \tag{9.18}$$

where $f(E)$ denotes the Fermi function,

$$f(E) = \frac{1}{e^{E/(k_BT)}+1}\,. \tag{9.19}$$

Our aim is to calculate the small deviations from equilibrium induced by the perturbation V_{1ext}, which will be marked by an index "1". To that end we linearize the transport equation (9.9) for the quasiparticle-distribution function,

$$\dot{\nu}_1 - \{E_0,\nu_1\} = f'(E_0)\{E_1,E_0\}\,, \tag{9.20}$$

where $f'(E_0) = df/dE_0$. The deviation of the quasiparticle energy, E_1, which appears on the r.h.s., depends itself on ν_1 through the deviation of the Hartree field, $g\rho_1$, and the deviation of the gap, $\tilde{\Delta}_1$. Expressing ρ_1 and

$\tilde{\Delta}_1$ in terms of ν_1, we can write Eq. (9.20) as

$$\dot{\nu}_1 - \{E_0, \nu_1\} = -\frac{f'(E_0)}{m}\Big(- \mathbf{p}\cdot\boldsymbol{\nabla}\frac{V_{1ext} + g\rho_{1\nu} - \hbar\dot{\phi}_1}{1+gA} + \frac{\Delta_0}{E_0^2}\mathbf{p}\cdot\boldsymbol{\nabla}\frac{\Delta_0(V_{1ext} + g\rho_{1\nu} - \hbar\dot{\phi}_1)}{1+gA} + \frac{h_0}{E_0^2}\mathbf{p}\cdot\boldsymbol{\nabla}\frac{\Delta_0\Delta_{1\nu}}{gA} + \frac{\hbar}{m}\frac{h_0}{E_0}(\mathbf{p}\cdot\boldsymbol{\nabla})^2\phi_1 - \hbar\frac{h_0}{E_0}(\boldsymbol{\nabla}V_0)\cdot\boldsymbol{\nabla}\phi_1 - \hbar\frac{\Delta_0}{E_0}(\boldsymbol{\nabla}\Delta_0)\cdot\boldsymbol{\nabla}\phi_1\Big)\,. \quad (9.21)$$

where $\rho_{1\nu}$ and $\Delta_{1\nu}$ are the quasiparticle contributions to ρ_1 and $\tilde{\Delta}_1$,

$$\rho_{1\nu}(\mathbf{r}) = \int \frac{d^3p}{(2\pi\hbar)^3}\frac{h_0(\mathbf{r},\mathbf{p})}{E_0(\mathbf{r},\mathbf{p})}\nu_1(\mathbf{r},\mathbf{p})\,, \quad (9.22)$$

$$\Delta_{1\nu}(\mathbf{r}) = g\int \frac{d^3p}{(2\pi\hbar)^3}\frac{\Delta_0(\mathbf{r})}{E_0(\mathbf{r},\mathbf{p})}\nu_1(\mathbf{r},\mathbf{p})\,, \quad (9.23)$$

while $A(\mathbf{r})$ is a function which depends only on equilibrium quantities. The explicit expression for the function $A(\mathbf{r})$ reads

$$A(\mathbf{r}) = \frac{mp_F(\mathbf{r})}{2\pi^2\hbar^3}[1-\varphi(\mathbf{r})]\,, \quad (9.24)$$

where the local Fermi momentum $p_F(\mathbf{r})$ is defined as usual by $p_F^2(\mathbf{r})/(2m) = \epsilon_F(\mathbf{r}) = \mu - V_0(\mathbf{r})$, and the temperature dependence of $A(\mathbf{r})$ is governed by the function

$$\varphi(\mathbf{r}) = -\int d\xi \frac{\xi^2}{E_\xi^2}f'(E_\xi)\,, \quad (9.25)$$

with $E_\xi = \sqrt{\xi^2 + \Delta_0^2(\mathbf{r})}$. In the two limiting cases $T = 0$ and $T \geq T_c(\mathbf{r})$, the function $\varphi(\mathbf{r})$ takes the values 0 and 1, respectively. As a consequence, $A(\mathbf{r}) = 0$ if $T \geq T_c(\mathbf{r})$.

In order to determine the phase ϕ_1, we also linearize the continuity equation (9.13):

$$\dot{\rho}_1(\mathbf{r}) + \boldsymbol{\nabla}\cdot\mathbf{j}_1(\mathbf{r}) = 0\,. \quad (9.26)$$

Again, we express all quantities in terms of equilibrium quantities and the unknown quantities ν_1 and ϕ_1. According to Eq. (9.15), the current $\mathbf{j}_1$ can be decomposed into quasiparticle and superfluid contributions,

$$\mathbf{j}_1(\mathbf{r}) = \mathbf{j}_{1\nu}(\mathbf{r}) - \frac{\hbar}{m}\rho_0(\mathbf{r})\boldsymbol{\nabla}\phi_1(\mathbf{r}) = 0\,, \quad (9.27)$$

where the quasiparticle contribution is given by

$$\mathbf{j}_{1\nu}(\mathbf{r}) = \int \frac{d^3p}{(2\pi\hbar)^3}\frac{\mathbf{p}}{m}\nu_1(\mathbf{r},\mathbf{p}) \quad (9.28)$$

(note that only the time-odd part of ν_1 contributes to the integral, and $\nu_{1od} = \tilde{\varrho}_{1od}$). The time derivative $\dot{\nu}_1$ which appears when one writes down the explicit expression for $\dot{\rho}_1$ can be eliminated with the help of Eq. (9.21). As a result, the l.h.s. of the continuity equation becomes

$$\dot{\rho}_1 + \boldsymbol{\nabla}\cdot\mathbf{j}_1 = \frac{A}{1+gA}\Big[\hbar\ddot{\phi}_1 - \dot{V}_{1ext} - \Big(\frac{2\pi^2\hbar^3}{mp_F} + g\Big)\frac{\hbar}{m}\boldsymbol{\nabla}\cdot(\rho_0\boldsymbol{\nabla}\phi_1) + g\boldsymbol{\nabla}\cdot\mathbf{j}_{1\nu} + \frac{\Delta_0}{A}\boldsymbol{\nabla}\cdot\int\frac{d^3p}{(2\pi\hbar)^3}\frac{\Delta_0}{E_0^2}\frac{\mathbf{p}}{m}\nu_1\Big]\,. \quad (9.29)$$

As noted in Ref. [252, 253], the continuity equation is trivially satisfied in the normal phase ($T \geq T_c$). This becomes evident if its l.h.s. is written in the form (9.29), since in the normal phase we have $\Delta_0 = 0$ and $A = 0$.

9.2.3 Identification of important and unimportant terms

Eq. (9.21) is still very complicated. In order to simplify the problem, let us look more closely at the different terms in order to see if some of them are less important than others. The basic assumption being that Δ, k_BT_c, and k_BT are much smaller than ϵ_F, the distribution function is sharply peaked near the Fermi surface. Under this condition it is useful to express the distribution function ν in terms of the variables $\mathbf{r}$, ξ, and $\hat{\mathbf{p}}$ instead of $\mathbf{r}$ and $\mathbf{p}$, where

$$\xi = h_0(\mathbf{p},\mathbf{r}) \approx v_F(\mathbf{r})[|\mathbf{p}| - p_F(\mathbf{r})]\,, \quad \hat{\mathbf{p}} = \frac{\mathbf{p}}{|\mathbf{p}|}\,, \tag{9.30}$$

and $v_F(\mathbf{r}) = p_F(\mathbf{r})/m$. In terms of these variables, ν is sharply peaked near $\xi = 0$, and the relevant values of ξ are of the same order of magnitude as Δ, k_BT_c, and k_BT.

If ν_1 is written as a function of the new variables, the Poisson bracket on the l.h.s. of Eq. (9.21) becomes

$$\{E_0,\nu_1\} = \frac{\Delta_0}{E_0} v_F\hat{\mathbf{p}}\cdot(\boldsymbol{\nabla}\Delta_0)\frac{\partial\nu_1}{\partial\xi} + \frac{\xi}{E_0}\frac{1}{p_F}(\boldsymbol{\nabla}V_0)\cdot\frac{\partial\nu_1}{\partial\hat{\mathbf{p}}} - \frac{\xi}{E_0}v_F\hat{\mathbf{p}}\cdot\boldsymbol{\nabla}\nu_1 + \frac{\Delta_0}{E_0}\frac{1}{p_F}(\boldsymbol{\nabla}\Delta_0)\cdot\frac{\partial\nu_1}{\partial\hat{\mathbf{p}}}\,, \tag{9.31}$$

with the short-hand notation

$$\frac{\partial\nu_1}{\partial\hat{\mathbf{p}}} = \frac{\partial\nu_1}{\partial\vartheta_p}\frac{\partial\hat{\mathbf{p}}}{\partial\vartheta_p} + \frac{1}{\sin^2\vartheta_p}\frac{\partial\nu_1}{\partial\varphi_p}\frac{\partial\hat{\mathbf{p}}}{\partial\varphi_p} \tag{9.32}$$

where ϑ_p and φ_p denote the angles characterizing the unit vector $\hat{\mathbf{p}} = (\sin\vartheta_p\cos\varphi_p, \sin\vartheta_p\sin\varphi_p, \cos\vartheta_p)$.

In addition to the assumption $\Delta \ll \epsilon_F$, our semiclassical theory requires that all quantities vary slowly in space, i.e., on a length scale L which should be larger than the coherence length $\hbar v_F/(\pi\Delta)$ [106]. Then, using $\Delta_0 \sim E_0 \sim \xi \sim \Delta$, $\boldsymbol{\nabla} \sim 1/L$, $\partial/\partial\xi \sim 1/\Delta$, and $\partial/\partial\hat{\mathbf{p}} \sim 1$, all terms in Eq. (9.31) can be estimated to be of the order of magnitude $(v_F/L)\nu_1$, except the last one, which is of the order $(v_F/L)(\Delta/\epsilon_F)\nu_1$. Hence, the last term of Eq. (9.31) is negligible.

Let us now distinguish different kinds of contributions to ν_1, depending on whether they are even or odd functions in ξ and $\hat{\mathbf{p}}$:

ν_{1oe}: the part of ν_1 which is odd in ξ and even in $\hat{\mathbf{p}}$ describes, roughly speaking, a change of the Fermi momentum, i.e., fluctuations of the density, and contributes to $\rho_{1\nu}$,

$$\rho_{1\nu} \approx \frac{mp_F}{2\pi^2\hbar^3}\int\frac{d\Omega_p}{4\pi}\int d\xi\frac{\xi}{E}\nu_{1oe}\,, \tag{9.33}$$

with $d\Omega_p = \sin\vartheta_p d\vartheta_p d\varphi_p$, while its contribution to $\Delta_{1\nu}$ is suppressed by one power of Δ/ϵ_F and can be neglected.

ν_{1eo}: the part of ν_1 which is even in ξ and odd in $\hat{\mathbf{p}}$ describes a shift of the Fermi sphere and therefore contributes to the current $\mathbf{j}_{1\nu}$,

$$\mathbf{j}_{1\nu} \approx \frac{p_F^2}{2\pi^2\hbar^3}\int\frac{d\Omega_p}{4\pi}\hat{\mathbf{p}}\int d\xi\,\nu_{1eo}\,, \tag{9.34}$$

and also to the other integral in the continuity equation (9.29).

ν_{1ee}: the part of ν_1 which is even in ξ and in $\hat{\mathbf{p}}$ describes, roughly speaking, a local temperature fluctuation and leads to a non-vanishing value of $\tilde{\Delta}_1$ (via $\Delta_{1\nu}$),

$$\tilde{\Delta}_1 \approx -\frac{1}{1-\varphi}\int\frac{d\Omega_p}{4\pi}\int d\xi\frac{\Delta_0}{E}\nu_{1ee}\,, \tag{9.35}$$

while its contribution to $\rho_{1\nu}$ is suppressed by one power of Δ/ϵ_F and can be neglected.

ν_{1oo}: the part of ν_1 which is odd in ξ and odd in $\hat{\mathbf{p}}$ gives only a negligible contribution to the current $\mathbf{j}_{1\nu}$ (suppressed by one power of Δ/ϵ_F).

If one neglects the last term in Eq. (9.31), the Poisson bracket in Eq. (9.21) leads only to a coupling between ν_{1eo} and ν_{1oe} and between ν_{1oo} and ν_{1ee}. To be more specific, ν_{1ee} and ν_{1oo} do not contribute to the dynamics of ν_{1oe} and ν_{1eo}. Since we are interested in density oscillations and currents, which are determined by ν_{1oe} and ν_{1eo}, we might wonder if we could disregard completely ν_{1ee} and ν_{1oo}. To that end we have to check that also on the r.h.s. of Eq. (9.21) there is no term which couples the undesired quantities ν_{1ee} and ν_{1oo} to ν_{1oe} or ν_{1eo}. Actually, on the r.h.s. of Eq. (9.21) there is no term containing ν_{1oo} and only one term containing ν_{1ee}, namely the third one,

$$-\frac{f'(E_0)}{m}\frac{h_0}{E_0^2}\mathbf{p}\cdot\boldsymbol{\nabla}\frac{\Delta_0\Delta_{1\nu}}{gA} \approx v_F f'(E_0)\frac{\xi}{E_0^2}\hat{\mathbf{p}}\cdot\boldsymbol{\nabla}(\Delta_0\tilde{\Delta}_1)\,. \tag{9.36}$$

This term clearly contributes to $\dot{\nu}_{1oo}$, but at least to leading order in Δ/ϵ_F it does not contribute to $\dot{\nu}_{1eo}$ or $\dot{\nu}_{1oe}$. In the continuity equation (9.29), ν_{1ee} and ν_{1oo} do not appear, i.e., the undesired quantities ν_{1ee} and ν_{1oo} do not contribute to the dynamics of ϕ_1, either. We are therefore allowed to disregard them.

Now, since we are not interested any more in ν_{1ee} and ν_{1oo}, we can remove all the terms on the r.h.s. of Eq. (9.21) which contribute only to the dynamics of these uninteresting quantities. As mentioned above, this is the case for the third term, Eq. (9.36), which contributes only to $\dot{\nu}_{1oo}$. The last term on the r.h.s. of Eq. (9.21),

$$\frac{f'(E_0)}{m}\hbar\frac{\Delta_0}{E_0}(\boldsymbol{\nabla}\Delta_0)\cdot\boldsymbol{\nabla}\phi_1 \tag{9.37}$$

can be omitted, too, since it contributes only to $\dot{\nu}_{1ee}$. In conclusion, we are left with a simplified version of Eq. (9.21), which reads

$$\dot{\nu}_1 - \{E_0,\nu_1\} = -\frac{f'(E_0)}{m}\Big(-\mathbf{p}\cdot\boldsymbol{\nabla}\frac{V_{1ext}+g\rho_{1\nu}-\hbar\dot{\phi}_1}{1+gA} + \frac{\Delta_0}{E_0^2}\mathbf{p}\cdot\boldsymbol{\nabla}\frac{\Delta_0(V_{1ext}+g\rho_{1\nu}-\hbar\dot{\phi}_1)}{1+gA} + \frac{\hbar}{m}\frac{h_0}{E_0}(\mathbf{p}\cdot\boldsymbol{\nabla})^2\phi_1 - \hbar\frac{h_0}{E_0}(\boldsymbol{\nabla}V_0)\cdot\boldsymbol{\nabla}\phi_1\Big)\,. \tag{9.38}$$

9.3 Test-particle method

9.3.1 Description of the method

The aim of the present work is to solve the Vlasov-like equation (9.9) for the quasiparticle-distribution function ν together with the continuity equation (9.13) for the phase of the order parameter with the help of the test-particle method, in analogy to the test-particle method which is used to solve the usual Boltzmann equation. The basic idea of this method is to replace the continuous distribution function $\nu(\mathbf{r},\mathbf{p})$ by a sum of delta functions in phase space,

$$\nu(\mathbf{r},\mathbf{p};t) \propto \sum_i \delta[\mathbf{r}-\mathbf{R}_i(t)]\delta[\mathbf{p}-\mathbf{P}_i(t)]\,, \tag{9.39}$$

corresponding to a finite number of test particles, each of which follows the classical equation of motion

$$\dot{\mathbf{R}}_i = \frac{\partial E(\mathbf{R}_i,\mathbf{P}_i;t)}{\partial\mathbf{P}_i}\,, \quad \dot{\mathbf{P}}_i = -\frac{\partial E(\mathbf{R}_i,\mathbf{P}_i;t)}{\partial\mathbf{R}_i}\,, \tag{9.40}$$

as can be seen by inserting Eq. (9.39) into Eq. (9.9). Note that, contrary to the usual test-particle method, our test particles here cannot be identified with real particles but rather with Bogoliubov quasiparticles. In its

general form, the test-particle method can be applied to situations far from equilibrium. However, here we are only interested in the linear-response regime, i.e., in the limit of small deviations from equilibrium. In this case it is possible to formulate the method in such a way that only the classical trajectories corresponding to the unperturbed system appear.

To that end, we make the following ansatz for the deviation of the distribution function from equilibrium:

$$\nu_1(\mathbf{r},\mathbf{p};t) = -y(\mathbf{r},\mathbf{p};t) f'[E_0(\mathbf{r},\mathbf{p})]\,. \tag{9.41}$$

Inserting this into the linearized transport equation (9.38), we obtain the following equation of motion for the function y:

$$\dot{y}(\mathbf{r},\mathbf{p};t) - \{E_0(\mathbf{r},\mathbf{p}), y(\mathbf{r},\mathbf{p};t)\} = F(\mathbf{r},\mathbf{p};t)\,, \tag{9.42}$$

where

$$F(\mathbf{r},\mathbf{p};t) = -\frac{\mathbf{p}}{m}\cdot\boldsymbol{\nabla}\frac{V_{1ext}+g\rho_{1\nu}-\hbar\dot{\phi}_1}{1+gA} + \frac{\Delta_0}{E_0^2}\frac{\mathbf{p}}{m}\cdot\boldsymbol{\nabla}\frac{\Delta_0(V_{1ext}+g\rho_{1\nu}-\hbar\dot{\phi}_1)}{1+gA} + \hbar\frac{h_0}{E_0}\Big(\frac{\mathbf{p}}{m}\cdot\boldsymbol{\nabla}\Big)^2\phi_1 - \frac{\hbar}{m}\frac{h_0}{E_0}(\boldsymbol{\nabla}V_0)\cdot\boldsymbol{\nabla}\phi_1\,. \tag{9.43}$$

Denoting by $\mathbf{R}(\mathbf{r},\mathbf{p};t)$ and $\mathbf{P}(\mathbf{r},\mathbf{p};t)$ the classical trajectories satisfying the equations of motion

$$\dot{\mathbf{R}} = \frac{\partial E_0(\mathbf{R},\mathbf{P})}{\partial\mathbf{P}}\,,\quad \dot{\mathbf{P}} = -\frac{\partial E_0(\mathbf{R},\mathbf{P})}{\partial\mathbf{R}} \tag{9.44}$$

with the initial conditions

$$\mathbf{R}(\mathbf{r},\mathbf{p};0) = \mathbf{r}\,,\quad \mathbf{P}(\mathbf{r},\mathbf{p};0) = \mathbf{p}\,, \tag{9.45}$$

one can easily show that

$$\frac{d}{dt}y[\mathbf{R}(\mathbf{r},\mathbf{p};t),\mathbf{P}(\mathbf{r},\mathbf{p};t);t] = F[\mathbf{R}(\mathbf{r},\mathbf{p};t),\mathbf{P}(\mathbf{r},\mathbf{p};t);t]\,. \tag{9.46}$$

Let us now replace the quasiparticle-distribution function by N_ν delta functions in phase space. Since the order of magnitude of ν_1 is dominated by $-f'(E_0)$, it is clear that these delta functions should be distributed near the Fermi surface. To be more specific, we choose N_ν points $\mathbf{r}_i$, $\mathbf{p}_i$ in phase space which are distributed according to a probability density which is proportional to $-f'(E_0)$, in such a way that for arbitrary but sufficiently smooth phase-space functions $\chi(\mathbf{r},\mathbf{p})$ the integral of $\chi(\mathbf{r},\mathbf{p})$ times the function $f'[E_0(\mathbf{r},\mathbf{p})]$ can be approximated by

$$\int\frac{d^3rd^3p}{(2\pi\hbar)^3}\chi(\mathbf{r},\mathbf{p})f'[E_0(\mathbf{r},\mathbf{p})] \approx -C\sum_{i=1}^{N_\nu}\chi(\mathbf{r}_i,\mathbf{p}_i)\,. \tag{9.47}$$

Note that, if $\mathbf{r}_i$, $\mathbf{p}_i$ are distributed in such a way, the same is true for $\mathbf{R}_i(t) = \mathbf{R}(\mathbf{r}_i,\mathbf{p}_i;t)$, $\mathbf{P}_i(t) = \mathbf{P}(\mathbf{r}_i,\mathbf{p}_i;t)$, since the quasiparticle energy $E_i = E_0[\mathbf{R}_i(t),\mathbf{P}_i(t)]$ is a constant of the motion. In particular, defining $y_i(t) = y[\mathbf{R}_i(t),\mathbf{P}_i(t);t]$ and using Eq. (9.47), we can approximate the integral of an arbitrary function χ times the distribution function ν_1 as

$$\int\frac{d^3rd^3p}{(2\pi\hbar)^3}\chi(\mathbf{r},\mathbf{p})\nu_1(\mathbf{r},\mathbf{p};t) \approx C\sum_{i=1}^{N_\nu}y_i(t)\chi[\mathbf{R}_i(t),\mathbf{P}_i(t)]\,. \tag{9.48}$$

In other words, we have replaced ν_1 by

$$\nu_1(\mathbf{r},\mathbf{p};t) \to C\sum_{i=1}^{N_\nu} y_i(t)\delta[\mathbf{r}-\mathbf{R}_i(t)]\delta[\mathbf{p}-\mathbf{P}_i(t)]\,. \tag{9.49}$$

According to Eq. (9.46), the equation of motion of the coefficients y_i is reduced to

$$\dot{y}_i(t) = F[\mathbf{R}_i(t),\mathbf{P}_i(t);t]\,. \tag{9.50}$$

Above we assumed the function $\chi(\mathbf{r},\mathbf{p})$ to be sufficiently smooth. Of course, this causes some trouble if we want to calculate local quantities like the density or the current. For instance, we obtain

$$\rho_{1\nu}(\mathbf{r}) = C\sum_{i=1}^{N_\nu} y_i(t)\frac{\xi_i(t)}{E_i}\delta[\mathbf{r}-\mathbf{R}_i(t)]\,, \tag{9.51}$$

where $\xi_i(t) = h_0[\mathbf{R}_i(t),\mathbf{P}_i(t)]$. This result makes sense only after the delta functions have been averaged over a volume containing a sufficiently large number of test particles in order to have a reasonable statistics. Supposing that this can be done, and supposing that $V_{ext}(\mathbf{r};t)$ and the phase $\phi_1(\mathbf{r};t)$ are known, we can use the result for $\rho_{1\nu}$ in the explicit expression for F in order to obtain a system of N_ν coupled first-order differential equations of the form (9.50) for the coefficients y_i. This represents a tremendous simplification with respect to the original partial differential equation (9.38) in seven dimensions ($\mathbf{r}$, $\mathbf{p}$, and t).

However, the phase $\phi_1(\mathbf{r},t)$ is not known, but it has to be determined from the continuity equation (9.26). This is, again, very difficult. Hence, instead of solving the continuity equation exactly, we make an ansatz for ϕ_1 and determine the parameters by minimizing the violation of the continuity equation,

$$\int d^3r(\dot{\rho}_1 + \boldsymbol{\nabla}\cdot\mathbf{j}_1)^2 = \min\,, \tag{9.52}$$

the explicit expression for $\dot{\rho}_1 + \boldsymbol{\nabla}\cdot\mathbf{j}_1$ being given by Eq. (9.29). The idea is to expand ϕ_1 on an appropriately chosen set of orthogonal functions ψ_n,

$$\phi_1(\mathbf{r};t) = \sum_{n=1}^{N_\phi} x_n(t)\psi_n(\mathbf{r})\,. \tag{9.53}$$

Inserting this ansatz into Eq. (9.29), we see that the integral in Eq. (9.52) depends on x_n and $\ddot{x}_n$. At a given time, we regard x_n and $\dot{x}_n$ as given (e.g., at the moment when the perturbation is switched on, we know that $x_n = \dot{x}_n = 0$). Hence, in order to have a minimal violation of the continuity equation, we have to minimize Eq. (9.52) with respect to $\ddot{x}_n$ by demanding

$$\frac{d}{d\ddot{x}_n}\int d^3r(\dot{\rho}_1 + \boldsymbol{\nabla}\cdot\mathbf{j}_1)^2 = 0\,. \tag{9.54}$$

At this stage it turns out to be convenient to choose the basis functions ψ_n such that they satisfy the orthogonality relation

$$\int d^3r\Big(\frac{\hbar A}{1+gA}\Big)^2\psi_n(\mathbf{r})\psi_m(\mathbf{r}) = \delta_{nm}\,. \tag{9.55}$$

Then we obtain the following differential equation for the coefficients x_n:

$$\ddot{x}_n(t) = \sum_{m=1}^{N_\phi} a_{nm}x_m(t) + \int d^3r\frac{\hbar A^2\psi_n}{(1+gA)^2}\Big(\dot{V}_{1ext} - g\boldsymbol{\nabla}\cdot\mathbf{j}_{1\nu} - \frac{\Delta_0}{A}\boldsymbol{\nabla}\cdot\int\frac{d^3p}{(2\pi\hbar)^3}\frac{\Delta_0}{E_0^2}\frac{\mathbf{p}}{m}\nu_1\Big)\,, \tag{9.56}$$

where a is a time-independent matrix,

$$a_{nm} = \frac{\hbar^2}{m} \int d^3r \frac{A^2 \psi_n}{(1+gA)^2} \Big(\frac{2\pi^2 \hbar^3}{m p_F} + g \Big) \boldsymbol{\nabla} \cdot (\rho_0 \boldsymbol{\nabla} \psi_m) \,. \tag{9.57}$$

Using Eq. (9.48) and integrating by parts, we can rewrite Eq. (9.56) in a more convenient form as

$$\ddot{x}_n(t) = \sum_{m=1}^{N_\phi} a_{nm} x_m(t) + \sum_{i=1}^{N_\nu} b_{ni}(t) y_i(t) + \dot{v}_n(t) \,, \tag{9.58}$$

where $b(t)$ denotes the matrix

$$b_{ni}(t) = \frac{\hbar C}{m} \mathbf{P}_i(t) \cdot \Big(\boldsymbol{\nabla} \frac{g A^2 \psi_n}{(1+gA)^2} + \frac{\Delta_0}{E_i^2} \boldsymbol{\nabla} \frac{A \Delta_0 \psi_n}{(1+gA)^2} \Big)_{\mathbf{R}_i(t)} \tag{9.59}$$

and the vector v is defined by

$$v_n = \hbar \int d^3r \frac{A^2 \psi_n V_{1ext}}{(1+gA)^2} \,. \tag{9.60}$$

Mainly for formal purposes, we note that also the equation (9.50) for the coefficients y_i can be rewritten in matrix notation as

$$\dot{y}_i(t) = \sum_{n=1}^{N_\phi} [c_{in}(t) \dot{x}_n(t) + d_{in}(t) x_n(t)] + f_i(t) + \sum_{j=1}^{N_\nu} g_{ij}(t) y_j(t) \,, \tag{9.61}$$

where

$$c_{in}(t) = \frac{\hbar}{m} \mathbf{P}_i(t) \cdot \Big(\boldsymbol{\nabla} \frac{\psi_n}{1+gA} - \frac{\Delta_0}{E_i^2} \boldsymbol{\nabla} \frac{\Delta_0 \psi_n}{1+gA} \Big)_{\mathbf{R}_i(t)} \,, \tag{9.62}$$

$$d_{in}(t) = \frac{\hbar}{m} \frac{\xi_i(t)}{E_i} \Big(\frac{(\mathbf{P}_i(t) \cdot \boldsymbol{\nabla})^2 \psi_n}{m} - (\boldsymbol{\nabla} V_0) \cdot \boldsymbol{\nabla} \psi_n \Big)_{\mathbf{R}_i(t)} \,, \tag{9.63}$$

$$f_i(t) = -\frac{\mathbf{P}_i(t)}{m} \cdot \Big(\boldsymbol{\nabla} \frac{V_{1ext}}{1+gA} - \frac{\Delta_0}{E_i^2} \boldsymbol{\nabla} \frac{\Delta_0 V_{1ext}}{1+gA} \Big)_{\mathbf{R}_i(t)} \,, \tag{9.64}$$

and

$$g_{ij}(t) = -gC \frac{\xi_j(t)}{E_j} \frac{\mathbf{P}_i(t)}{m} \cdot \Big(\boldsymbol{\nabla} \frac{\tilde{\delta}[\mathbf{r} - \mathbf{R}_j(t)]}{1+gA} - \frac{\Delta_0}{E_i^2} \boldsymbol{\nabla} \frac{\Delta_0 \tilde{\delta}[\mathbf{r} - \mathbf{R}_j(t)]}{1+gA} \Big)_{\mathbf{R}_i(t)} \,. \tag{9.65}$$

In the latter equation, $\tilde{\delta}$ denotes a kind of "smeared" delta function which accounts for the averaging mentioned below Eq. (9.51).

However, as mentioned above, Eqs. (9.61) and (9.65) will be used for formal purposes only. In practice, it is much faster to calculate $\rho_{1\nu}(\mathbf{r})$ after each time step on a discrete mesh, and to interpolate the stored values when performing the next time step for the coefficients y_i. For the calculation of $\rho_{1\nu}(\mathbf{r})$, we replace the delta function in Eq. (9.51) by a Gaussian having a width d_ρ.

In summary, the coupled system of partial differential equations, namely the transport equation for the distribution function ν_1 and the continuity equation for the phase ϕ_1 [Eqs. (9.38) and (9.26)], has been replaced by a coupled system of ordinary linear differential equations for the coefficients y_i and x_n [Eqs. (9.61) and (9.58)], which can formally be written as

$$\frac{d}{dt} \begin{pmatrix} x(t) \\ \dot{x}(t) \\ y(t) \end{pmatrix} = \begin{pmatrix} 0 & 1 & 0 \\ a & 0 & b(t) \\ d(t) & c(t) & g(t) \end{pmatrix} \begin{pmatrix} x(t) \\ \dot{x}(t) \\ y(t) \end{pmatrix} + \begin{pmatrix} 0 \\ \dot{v}(t) \\ f(t) \end{pmatrix} . \tag{9.66}$$

9.3.2 Trajectories of the test particles

In practice, the solution of the classical equations of motion for the test particles, Eqs. (9.44), faces us with some unusual features which are not present with the usual Newtonian equations of motion. Note that we are not dealing with ordinary particles but with Bogoliubov quasiparticles, which have some surprising properties. For instance, E_i being a constant of the motion and $E_i^2 = \xi_i^2 + \Delta_0^2(\mathbf{r}_i)$, it is evident that the energy ξ_i cannot be conserved if the gap Δ_0 depends on $\mathbf{r}$. In particular, when a test particle with quasiparticle energy E_i reaches the surface where $\Delta_0(\mathbf{r}) = E_i$, it is reflected (Andreev reflection). During this reflection, the momentum $\mathbf{P}_i$ stays almost constant, but the energy ξ_i changes its sign (i.e., a particle is transformed into a hole or vice versa), such that the velocity $\mathbf{v}_i = \partial E_i/\partial \mathbf{P}_i = (\xi_i/E_i)\mathbf{P}_i/m$ is reversed. As a consequence, the quasiparticle is reflected into the direction where it came from, which is very surprising if the incident angle is different from 90°.

In order to find the test-particle trajectories numerically, it does not seem very efficient to start directly from Eqs. (9.44), since a small numerical error in the momentum of the order of $\delta P/P \sim \Delta/\epsilon_F$ would immediately lead to a completely wrong behavior. It is therefore advantageous to make use of the variable ξ_i, whose equation of motion reads

$$\dot{\xi}_i = -\frac{\Delta_0(\mathbf{R}_i)}{E_i}\frac{\mathbf{P}_i}{m}\cdot\boldsymbol{\nabla}\Delta_0(\mathbf{R}_i)\,. \tag{9.67}$$

Solving this equation together with the equations for $\mathbf{R}_i$ and $\mathbf{P}_i$, we can correct $\mathbf{P}_i$ after each time step according to

$$\mathbf{P}_i^{corr.} = \frac{\mathbf{P}_i}{|\mathbf{P}_i|}\sqrt{2m\xi_i + p_F^2(\mathbf{R}_i)}\,. \tag{9.68}$$

In practice, the variable ξ_i also allows us to introduce a very reliable method for determining the step size. Let us denote by ξ_i' the result we obtain after one time step of size δt, and by ξ_i'' the result we obtain after two time steps of size $\delta t/2$ each. Then the quantity $\delta t|\xi' - \xi''|$ is a measure for the numerical error and can be used for adapting the step size δt to the situation. It turns out that the step size has to become very small only during Andreev reflection.

Now let us give some examples for typical test-particle trajectories. For that purpose, let us restrict ourselves to the most simple case which is a spherical harmonic trap,

$$V_{0ext}(\mathbf{r}) = \frac{1}{2}m\Omega^2 r^2\,. \tag{9.69}$$

This potential defines the so-called trap units, i.e., energies are measured in units of $\hbar\Omega$, temperatures in units of $\hbar\Omega/k_B$, lengths in units of $l_{ho} = \sqrt{\hbar/(m\Omega)}$, etc. In this example, due to spherical symmetry, not only the quasiparticle energy E, but also the angular momentum $\mathbf{L} = \mathbf{r}\times\mathbf{p}$ of a test particle is a constant of the motion.

Within the local-density approximation (LDA) [119, 131], the density $\rho_0(r)$ has its maximum at the center of the trap and vanishes approximately (except for very small temperature effects) at the Thomas-Fermi radius $R_{TF} = \sqrt{2\mu/(m\Omega^2)}$. The gap $\Delta_0(r)$ has its maximum at the center of the trap, too, and goes to zero at some critical radius R_c which is temperature dependent and determined by the equation $T = T_c(R_c)$. In order to avoid numerical problems arising from the infinite derivative of $\Delta_0(r)$ at $r = R_c$, we convolute the LDA result for $\Delta_0(r)$ with a Gaussian of width d_Δ. In fact, this is more realistic than the LDA result since the exact solution of the BdG equations also leads to a gap $\Delta_0(r)$ which has an exponential tail [30, 59, 119]. As parameters we choose $\mu = 32\,\hbar\Omega$, $g = -\hbar^2 l_{ho}/m$, and $T = 1.4\,\hbar\Omega/k_B$. The corresponding number of atoms in the trap is approximately 1.7×10^4. For these parameters quantum mechanical (BdG, QRPA) results are available for comparison. The width d_Δ is chosen such as to optimize the agreement with the BdG gap, which for the present parameters is achieved with $d_\Delta = l_{ho}$.

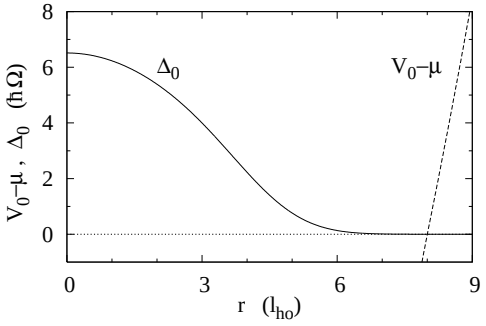

Figure 9.1: Gap $\Delta_0(r)$ (solid line) and potential $V_0(r) - \mu$ (dashed line) for the case of a spherical trap with frequency Ω, chemical potential $\mu = 32\,\hbar\Omega$, coupling constant $g = -\hbar^2 l_{ho}/m$, and temperature $k_B T = 1.4\,\hbar\Omega$. Δ_0 and $V_0 - \mu$ are in units of $\hbar\Omega$, r is in units of the oscillator length l_{ho}. Roughly speaking, these two curves determine the classically allowed region for a quasiparticle with given energy E.

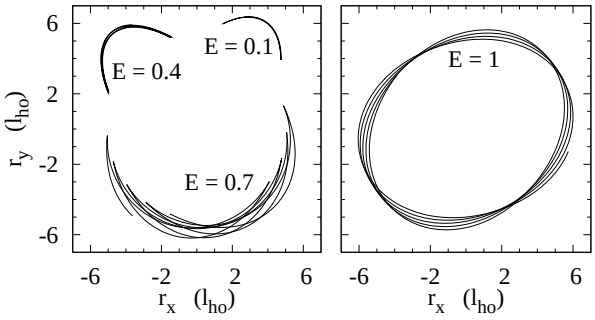

Figure 9.2: Four examples of quasiparticle trajectories in a trap with parameters given below Fig. 9.1. The three trajectories shown in the left panel belong to quasiparticles with $E = 0.1\,\hbar\Omega$, $0.4\,\hbar\Omega$, and $0.7\,\hbar\Omega$, respectively. The trajectory displayed in the right panel belongs to a quasiparticle with $E = \hbar\Omega$.

In Fig. 9.1 we show the corresponding gap $\Delta_0(r)$ as a function of the distance r from the center of the trap. From this figure it is evident that due to the condition $E \geq \Delta_0(r)$, the relevant quasiparticles (having $E \lesssim k_B T = 1.4\,\hbar\Omega$) are excluded from the region $r \lesssim 4 l_{ho}$. In addition to the gap, we display the potential $V_0(r) - \mu$, since the motion of a quasiparticle with given energy E and angular momentum $\mathbf{L}$ is also limited by the condition $\sqrt{E^2 - \Delta_0^2(r)} - \mathbf{L}^2/2mr^2 \geq V_0(r) - \mu$. It has been shown that also within the fully quantum-mechanical BdG theory the lowest-lying quasiparticle states are localized in this region [63]. In our example, the motion of the relevant quasiparticles is restricted to the region $4 \lesssim r/l_{ho} \lesssim 8$.

Most of these quasiparticles will undergo Andreev reflection. Their trajectories are approximately described by an ellipse which is cut at the points where $\Delta_0(r) = E$. If $E \ll \epsilon_F$, the quasiparticle will move hence and forth on the same partial ellipse. Such trajectories with $E = 0.1\,\hbar\Omega$ and $0.4\,\hbar\Omega$ are shown in the left panel of Fig. 9.2. However, if the quasiparticle energy is higher, the change in energy from $\xi \approx E$ to $\xi \approx -E$ (or vice versa) during the Andreev reflection results in a change of momentum which is no more negligible. Then, due to angular momentum conservation, the angle of reflection is slightly different from the angle of incidence, and the whole trajectory is precessing. An example for such a trajectory with $E = 0.7\,\hbar\Omega$ is also shown in the left panel of Fig. 9.2. A completely different picture arises if the initial conditions are such that the quasiparticle does never reach the point where $\Delta(r) = E$. Then the trajectory is just a precessing, slightly deformed ellipse, as shown in the right panel of Fig. 9.2 for the case of a trajectory with $E = \hbar\Omega$. There is a striking analogy between these trajectories and the "glancing" orbits discussed, e.g., in Ref. [58] in the context of a superconducting cylinder which is coated by a normal-metal layer.

9.3.3 Distribution of test particles in phase space

In Sec. 9.3.1 we supposed that one can generate a distribution of points $\mathbf{r}_i$, $\mathbf{p}_i$ in phase space such that Eq. (9.47) is approximately satisfied for sufficiently smooth functions $\chi(\mathbf{r}, \mathbf{p})$. In practice, this distribution is obtained in

two steps. First we generate the coordinates $\mathbf{r}_i$, and in a second step the momenta $\mathbf{p}_i$.

The mean density of test particles at a certain point $\mathbf{r}$ is given by

$$n(\mathbf{r}) = \sum_{i=1}^{N_\nu} \tilde{\delta}(\mathbf{r}_i - \mathbf{r})\,, \tag{9.70}$$

where $\tilde{\delta}$ denotes a smeared delta function in order to account for the averaging. Using Eq. (9.47), we conclude

$$n(\mathbf{r}) = -\frac{1}{C}\int \frac{d^3p}{(2\pi\hbar)^3} f'[E_0(\mathbf{r},\mathbf{p})] \equiv \frac{w(\mathbf{r})}{C}\,. \tag{9.71}$$

The algorithm for the generation of the coordinates $\mathbf{r}_i$ is now very simple. First we look for the maximum w_{max} of the function $w(\mathbf{r})$. Defining $P(\mathbf{r}) = w(\mathbf{r})/w_{max}$, we obtain a function whose values lie between 0 and 1. Then we generate uniformly distributed random points $\mathbf{r}_k$ in a volume which contains the whole system, and retain each point with the probability $P(\mathbf{r}_k)$, until the desired number of points, N_ν, is reached.

The formula (9.71) for the test-particle density $n(\mathbf{r})$ can also be used for the determination of the normalization constant C. Integrating $n(\mathbf{r})$ over space, we must recover the total number of test particles. This implies

$$C = \frac{1}{N_\nu}\int d^3r\, w(\mathbf{r})\,. \tag{9.72}$$

Now we turn to the distribution of the momenta $\mathbf{p}_i$. It is evident that the angular distribution of the momenta is isotropic, i.e., the interesting part of the problem is the distribution of the absolute values, $p_i = |\mathbf{p}_i|$, which is, of course, directly related to the distribution of the energies ξ_i. Let us define the mean number of test particles per energy and volume

$$n(\mathbf{r},\xi) = \sum_{i=1}^{N_\nu} \tilde{\delta}(\mathbf{r}_i - \mathbf{r})\tilde{\delta}(\xi_i - \xi)\,. \tag{9.73}$$

Again, with the help of Eq. (9.47), this becomes

$$n(\mathbf{r},\xi) = -\frac{1}{C}\frac{m p_\xi}{2\pi^2\hbar^3} f'(E_\xi)\,, \tag{9.74}$$

with $p_\xi = \sqrt{2m\xi + p_F^2(\mathbf{r})}$, i.e., for given spatial coordinates $\mathbf{r}$, the probability density for finding a particle at energy ξ is proportional to $-p_\xi f'(E_\xi)$. Such a distribution can be generated in the following way. Starting from random numbers z_k which are uniformly distributed in the interval $(0,1)$, it is straight-forward to show that the energies

$$\xi_k = T\ln\frac{z_k}{1-z_k} \tag{9.75}$$

are distributed according to the probability density $-f'(\xi)$. It is evident that negative energies with $\xi < -\epsilon_F(\mathbf{r})$ have to be removed. Furthermore, it is preferable to cut the distribution at energies which lie too far away from the Fermi surface, e.g., $|\xi| > 15T$ (the probability that this happens is less than 10^{-6}). The momenta p_ξ are thus limited by $p_{max} = \sqrt{30mT + p_F^2(\mathbf{r})}$, and the function defined by $P(\xi) = p_\xi f'(E_\xi)/p_{max} f'(\xi)$ cannot become greater than 1 and can serve as a probability. If we retain each energy ξ_k generated according to Eq. (9.75) with the probability $P(\xi_k)$, the remaining energies are distributed according to the desired distribution.

In order to give an illustration for the resulting distribution of test particles, we show in Fig. 9.3 the radial distribution of $N_\nu = 10^5$ test particles in a trap with the same parameters as in Fig. 9.1. In agreement with

what we discussed in the preceding subsection, we see that the test particles are mainly located in the region $4 \lesssim r/l_{ho} \lesssim 8$, corresponding to the region where the system is mainly normal fluid. Due to the angular average the statistical fluctuations around the ideal distribution, Eq. (9.71), which is represented by the dotted line, are very small. We verified that, apart from the statistical fluctuations, our test-particle distribution stays constant, which is a good numerical test of both the initial test-particle distribution and of the test-particle trajectories.

9.3.4 Initial condition

In the linear response regime, as the name implies, the response to a time-dependent perturbation of the form $V_1(\mathbf{r};t) = \hat{V}_1(\mathbf{r})f(t)$, with an arbitrary time dependence $f(t)$, can be obtained as convolution of $f(t)$ with the response to a delta function in time. It is therefore sufficient to study perturbations of the form

$$V_{1ext}(\mathbf{r};t) = \hat{V}_1(\mathbf{r})\delta(t)\,. \tag{9.76}$$

We thus set the inhomogeneous terms in Eq. (9.66) to $\dot{v}(t) = \hat{v}\dot{\delta}(t)$ and $\dot{f}(t) = \hat{f}\delta(t)$, respectively, $\hat{v}$ and $\hat{f}$ being defined analogously to Eqs. (9.60) and (9.64) but with V_{1ext} replaced by $\hat{V}_1$.

Assuming that the system was in equilibrium before this perturbation, we may ask the question: What are the values of the coefficients y_i and x_n immediately after the perturbation, i.e., at infinitesimally small $t > 0$? This question can be answered exactly, since during the infinitesimal period where the perturbation is active, the matrix in Eq. (9.66) can be regarded as time-independent. Integrating Eq. (9.66) over time from $-t_0$ to t_0, we obtain in the limit $t_0 \to 0$

$$\lim_{t_0\to 0}\begin{pmatrix} x(t_0) \\ \dot{x}(t_0) \\ y(t_0) \end{pmatrix} = \begin{pmatrix} \hat{v} \\ 0 \\ c\hat{v} + \hat{f} \end{pmatrix}. \tag{9.77}$$

Let us now assume that the function $\hat{V}_1$ lies in the space spanned by the functions ψ_n. Then it is evident that the corresponding linear combination is given by the coefficients $\hat{v}_n$, i.e.,

$$\hat{V}_1(\mathbf{r}) = \hbar\sum_{n=1}^{N_\phi} \hat{v}_n\psi_n(\mathbf{r})\,. \tag{9.78}$$

Note that the functions ψ_n do not necessarily have to have this property. For example, we could define a basis of functions satisfying the orthogonality relation (9.55) and maybe even a suitably defined completeness relation if $N_\phi \to \infty$, but which all vanish identically outside the superfluid region, i.e., in the region where $\Delta_0 = 0$ (and $A = 0$). Eq. (9.78) would then be satisfied inside the superfluid region, but not outside. Hence, it is an additional requirement for the choice of the functions ψ_n. Combining Eqs. (9.77) and (9.78), we find

$$\lim_{t_0\to 0}\phi_1(\mathbf{r};t_0) = \frac{1}{\hbar}\hat{V}_1(\mathbf{r})\,. \tag{9.79}$$

Eq. (9.78) also leads to a simplification of the initial value of the coefficients y_i and the quasiparticle-distribution function. Using the explicit expressions for the matrix c and the vector $\hat{f}$ [Eqs. (9.62) and (9.64) with V_{1ext} replaced by $\hat{V}_1$], we obtain from the third line of Eq. (9.77)

$$\lim_{t_0\to 0} y_i(t_0) = \sum_{n=1}^{N_\phi} c_{in}\hat{v}_n + \hat{f}_i = \frac{\mathbf{p}_i}{m}\cdot\Big(\boldsymbol{\nabla}\frac{\hbar\sum_{n=1}^{N_\phi}\hat{v}_n\psi_n - \hat{V}_1}{1+gA} - \frac{\Delta_0}{E_i^2}\boldsymbol{\nabla}\frac{\Delta_0(\hbar\sum_{n=1}^{N_\phi}\hat{v}_n\psi_n - \hat{V}_1)}{1+gA}\Big)_{\mathbf{r}_i}. \tag{9.80}$$

As a consequence, if Eq. (9.78) is satisfied, the initial values of the coefficients y_i vanish, which implies

$$\lim_{t_0 \to 0} \nu_1(\mathbf{r}, \mathbf{p}; t_0) = 0\,. \tag{9.81}$$

In fact, the simple result of this subsection, which is summarized in Eqs. (9.79) and (9.81), could have been anticipated without any calculation. The effect of a perturbation of the form (9.76) is to give a particle at position $\mathbf{r}$ a kick

$$\delta\mathbf{p} = -\int dt \boldsymbol{\nabla} V_{1\,ext}(\mathbf{r}; t) = -\boldsymbol{\nabla}\hat{V}_1(\mathbf{r})\,. \tag{9.82}$$

Since this kick does not depend on the momentum of the particle, the local Fermi sphere is shifted as a whole, there is no change in density and no Fermi surface deformation. Within the present theoretical framework, Cooper pairs are not broken either, they just acquire a center of mass momentum. Thus, the distribution function in the local rest frame stays unchanged ($\nu_1 = 0$), and the collective velocity is given by $\mathbf{v}_{coll} = -(\hbar/m)\boldsymbol{\nabla}\phi_1 = -(1/m)\boldsymbol{\nabla}\hat{V}_1$.

Note, however, that in reality a perturbation which has the form of a short pulse would lead to much more complicated effects (e.g., pair breaking). Since our semiclassical description requires that the time dependence of the perturbation is slow, our formal result for a delta-like excitation becomes physically meaningful only after it has been convoluted with a function $f(t)$ which varies slowly in time. In other words, we can only calculate the low-frequency part of the response function.

9.4 First results

In this section we will discuss first numerical results which have been obtained using the test-particle method. Our intention here is to see whether this method is in principle capable to describe the most important features of collective excitations in superfluid trapped Fermi gases. To that end, we will study the quadrupole excitation of a spherical system, which is excited by

$$\hat{V}_1(\mathbf{r}) = \alpha\, m\Omega(2r_z^2 - r_x^2 - r_y^2) \tag{9.83}$$

(the factor $m\Omega$ has been introduced in order to make the coefficient α dimensionless).

For practical purposes, we will make an additional approximation: We will restrict our ansatz for the phase, Eq. (9.53), to only one or two functions ψ_n. It is clear from rotational symmetry that in the case of a quadrupole excitation of the form (9.83) the most general form the phase can have is

$$\phi_1(\mathbf{r}) = \Phi(r)[2r_z^2 - r_x^2 - r_y^2]\,, \tag{9.84}$$

such that that the functions ψ_n can be written as

$$\psi_n(\mathbf{r}) = \Psi_n(r)[2r_z^2 - r_x^2 - r_y^2]\,. \tag{9.85}$$

It is known from superfluid hydrodynamics that at zero temperature the velocity field is essentially linear in the coordinates, i.e., the function $\Phi(r)$ is almost constant. As a first guess we will assume that this is still true at non-zero temperature, and hence we will take only one single function ($N_\phi = 1$) in the ansatz (9.53) for the phase, $\Psi_1 = const$. The proportionality constant will be determined from the normalization condition (9.55).

Such a restricted ansatz means of course that the continuity equation will not be exactly satisfied in the superfluid region (remember that outside the superfluid region the phase has no effect whatsoever). We will therefore improve this initial ansatz by including a second function ($N_\phi = 2$) which allows to modulate $\Phi(r)$ in the superfluid region.

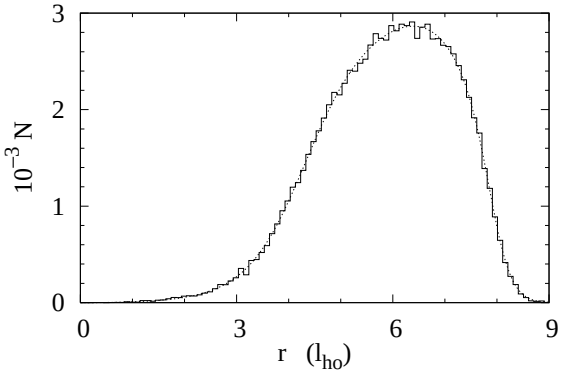

Figure 9.3: Radial distribution of 10^5 test particles in a trap with parameters given below Fig. 9.1, counted in bins of size $\delta r = 0.1\, l_{ho}$. For comparison, the dotted curve represents the ideal distribution according to Eq. (9.71).

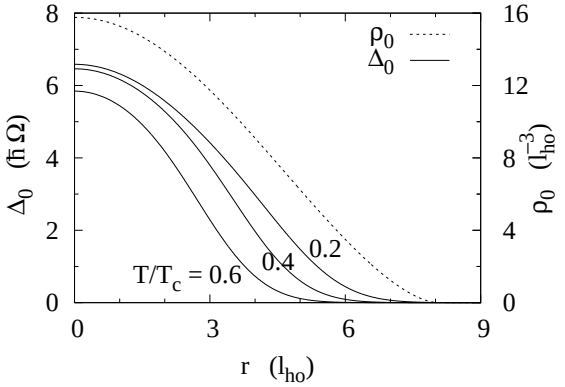

Figure 9.4: Density profile $\rho_0(r)$ (dashed line) and gap $\Delta_0(r)$ (solid lines) in a spherical harmonic trap containing 1.7×10^4 atoms ($\mu = 32\,\hbar\Omega$, interaction strength $g = -\hbar^2 l_{ho}/m$). The gap is displayed for three different temperatures, $T/T_c = 0.2$, 0.4, and 0.6, while the density profile is practically independent of T.

The first idea one might have is to use for $\Psi_n(r)$ polynomials in r^2 and to orthogonalize the resulting functions ψ_n. However, it turns out that this leads to numerical instabilities due to the fast growing of the resulting polynomials outside the superfluid region. Let us explain this effect in some more detail. As seen from the transport equation for the quasiparticle-distribution function, the phase ϕ_1 outside the superfluid region enters directly the dynamics of ν_1. Although the net effect of the phase and of the quasiparticle motion should be independent of the choice of ϕ_1 outside the superfluid region, each of these contributions depends on this choice. If ϕ_1 changes too rapidly, the numerical solution of the equation of motion for the coefficients y_i becomes less accurate and the cancellation of the two effects does not work any more.

We therefore have to look for functions Ψ_n which are linearly independent inside the superfluid region, but which do not grow outside. Here we will choose the functions $\tilde{\Psi}_1(r) = 1$ and $\tilde{\Psi}_2(r) = [1 - \varphi(r)]^2$, where $\varphi(r)$ is the function defined in Eq. (9.25). The function $\tilde{\Psi}_2(r)$ has its maximum in the center of the trap and goes smoothly to zero at the boundary of the superfluid region. From $\tilde{\Psi}_1$ and $\tilde{\Psi}_2$ the functions Ψ_1 and Ψ_2 are determined according to the orthogonality condition (9.55) with the help of the Gram-Schmidt orthogonalization method. As we will see, the results obtained with $N_\phi = 1$ and $N_\phi = 2$ are very similar and we therefore claim that they would not change a lot if we included additional functions.

Let us now present the results. As in the examples shown in the preceding section, we consider a spherical harmonic trap with $\mu = 32\hbar\Omega$, containing approximately 1.7×10^4 atoms. The resulting density profile $\rho_0(r)$ is shown in Fig. 9.4 as the dashed line. The critical temperature within LDA is $T_c = T_c(r = 0) \approx 3.9\,\hbar\Omega/k_B$. As before, the LDA result for the gap $\Delta_0(r)$ is convoluted with a Gaussian having a width $d_\Delta = l_{ho}$. We will study the quadrupole mode for three different temperatures, $T/T_c = 0.2$, 0.4, and 0.6. The equilibrium gap $\Delta_0(r)$ for these three temperatures is also displayed in Fig. 9.4.

After the system is excited, its shape will oscillate. A measure for this quadrupole deformation is the ratio

$$\frac{\langle 2r_z^2 - r_x^2 - r_y^2 \rangle}{\langle r^2 \rangle_0}\,, \tag{9.86}$$

where $\langle r^2 \rangle_0$ denotes the mean square radius in equilibrium, which in the present case has the value $\langle r^2 \rangle_0 \approx 23\, l_{ho}^2$. In the linear response, the quadrupole deformation is of course proportional to the strength of the perturbation, and we therefore divide our results by this strength [denoted α in Eq. (9.83)]. In our simulation we use $N_\nu = 10^5$ test particles, the width of the Gaussians used for smearing $\rho_{1\nu}$ (see Sec. 9.3.1) is set to $d_\rho = l_{ho}$. In Fig. 9.5 we display the time dependence of the quadrupole deformation after the perturbation for the three temperatures mentioned before. The corresponding spectra, obtained by Fourier transformation, are shown in Fig. 9.6. The results for the two cases $N_\phi = 1$ and $N_\phi = 2$ are displayed as dashed and solid curves, respectively. In all cases the two curves are in reasonable agreement, such that we can say that the use of $N_\phi = 2$ independent functions in the ansatz for the phase is sufficient.

We see that the temperature dependence of the spectrum is highly non-trivial. At low temperatures (upper panel of Fig. 9.6), we see essentially the hydrodynamic quadrupole mode, which at zero temperature lies at $\omega = \sqrt{2}\Omega$ [31, 62, 88] and which is now damped as a consequence of its coupling to the normal component. At higher temperatures (middle of Fig. 9.6), a second peak builds up in the spectrum, corresponding to the quadrupole mode in the normal phase, which lies slightly above $\omega = 2\Omega$ [168, 261] (for the present set of parameters, its frequency is $\omega \approx 2.2\,\Omega$ [118]). As the temperature approaches T_c (lower panel of Fig. 9.6), the strength contained in this second peak increases, while the hydrodynamic mode, whose frequency is slightly shifted downwards, disappears. These findings are in good agreement with quantum mechanical QRPA calculations [118].

We note that the damping width of the hydrodynamic mode at low temperature is now comparable with that found within the QRPA and much stronger than that found in our previous work [252, 253], where we replaced the gap $\Delta_0(r)$ by a constant. The reason is in fact very simple: With a constant gap, the fraction ρ_n/ρ_0 of the normal component is independent of r, whereas in the case of an r-dependent gap the normal component in the outer part of the system is already important at very low temperatures [247].

As the temperature T approaches T_c, the quadrupole mode of the normal phase (that at $\omega = 2.2\,\Omega$) becomes undamped, as it is the case within the QRPA. However, even though collisions are strongly suppressed at these low temperatures, it should be kept in mind that the collision term, which is neglected in the present work, is non-zero and its inclusion would lead to a finite lifetime of this oscillation, too.

Finally, let us compare our semiclassical results more quantitatively to quantum mechanical QRPA results. In Fig. 9.7 we show the QRPA result of Ref. [118] for the quadrupole excitation spectrum (dotted line) together with the semiclassical result we obtain with the same parameters (solid line). As one can see, the total normalization and the relative weights of the two peaks are in reasonable agreement. Also the widths of the QRPA peaks are well reproduced by the semiclassical calculation. The main differences are that within the semiclassical calculation the two peaks lie a bit too high and that they are not as well separated as within the QRPA. A comparison of the two curves for $N_\phi = 1$ and $N_\phi = 2$ in the $T/T_c = 0.4$ case shown in the middle of Fig. 9.6, whose parameters are quite close to those of Fig. 9.7, suggests that the latter effect might be partly due to the restricted ansatz for the phase. However, as one can deduce from the irregular structure of the QRPA spectrum, even in a system with 32000 atoms shell effects, i.e., effects which depend on the discrete single-particle spectrum, are still quite pronounced. It is clear that such effects cannot be reproduced within a semiclassical calculation. In this sense the agreement between the two spectra is very satisfactory, in particular since one can assume that the shell effects decrease with increasing number of particles.

9.5 Conclusions

In this paper, we developed a numerical test-particle method for solving the semiclassical transport equations for an ultracold trapped Fermi gas in the BCS phase in the collisionless limit. These transport equations take into account the coupling between the dynamics of the Cooper pairs (superfluid component) and the thermally

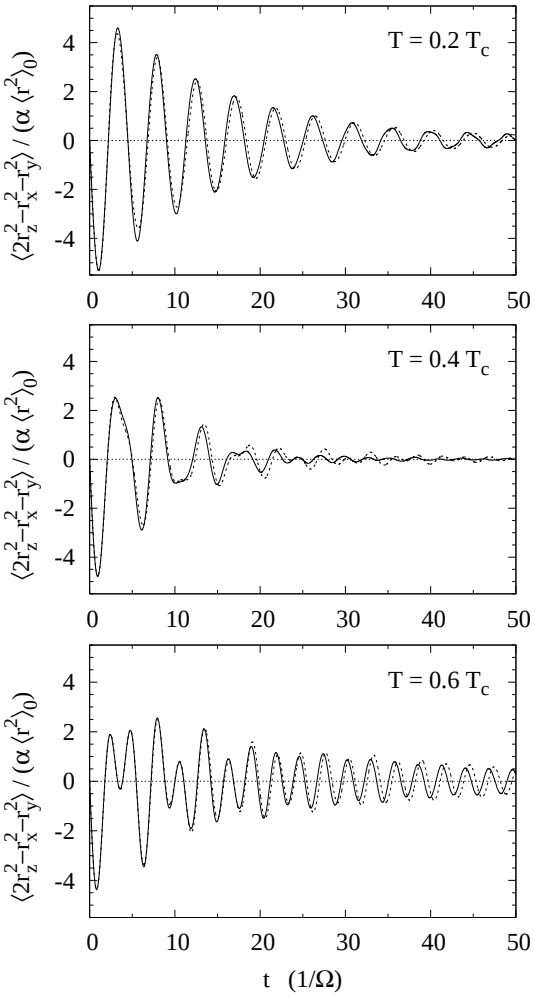

Figure 9.5: Time dependence of the quadrupole deformation after a delta-like perturbation at $t = 0$. The parameters are the same as in Fig. 9.4, the three panels correspond, from top to bottom, to $T/T_c = 0.2$, 0.4, and 0.6. The dashed and solid lines correspond to $N_\phi = 1$ and $N_\phi = 2$, respectively.

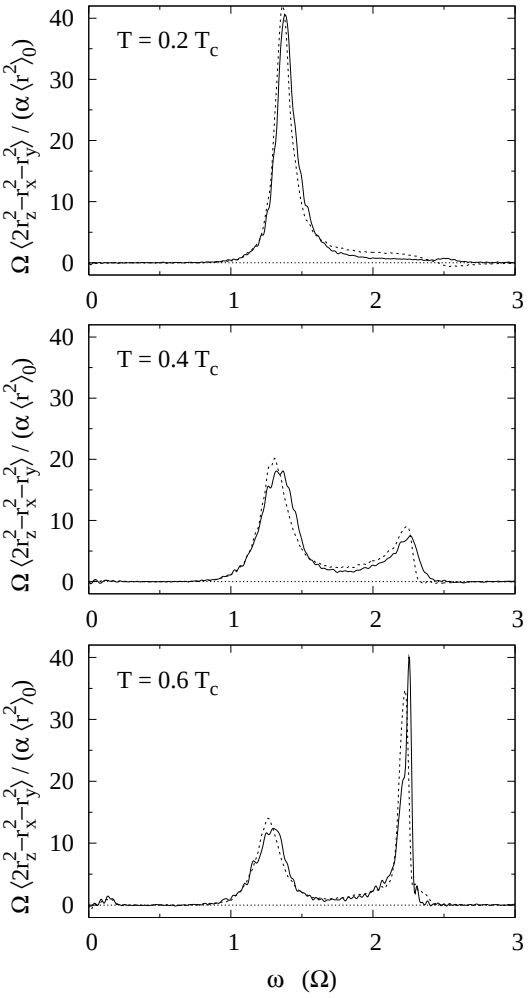

Figure 9.6: Fourier transforms of the quadrupole responses shown in Fig. 9.5.

Figure 9.7: Quantitative comparison between the semiclassical and the QRPA result for the quadrupole excitation spectrum of a system with $\mu = 32\hbar\Omega$, $g = -0.965\,\hbar^2 l_{ho}/m$, $k_B T = 1.4\,\hbar\Omega$. The semiclassical result (solid line) was obtained with $N_\phi = 2$ basis functions for the phase. The QRPA result (dotted line) was taken from Ref. [118].

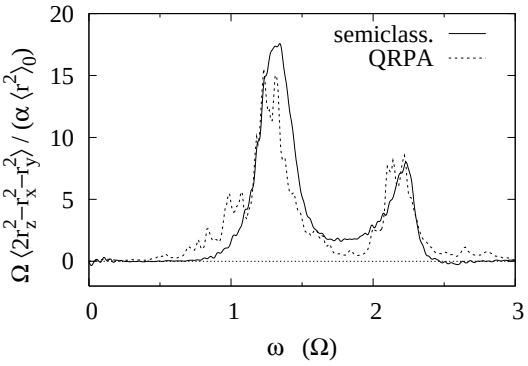

excited Bogoliubov quasiparticles (normal component). We developed the method for the case of small deviations from equilibrium, so that the test-particle trajectories can be calculated in the equilibrium state. Since the test-particles describe Bogoliubov quasiparticles rather than real particles, the trajectories have very unusual properties compared with the trajectories one has to deal with when applying the test-particle method to the normal Vlasov equation. Our test particles can have the character of particles as well as holes, depending on whether their energy ξ is positive or negative, and they can also be transformed from the one into the other if they hit the region where the gap Δ becomes larger than their quasiparticle energy E (Andreev reflection). Another complication as compared with the normal Vlasov equation is that the dynamics of the quasiparticles is coupled to the collective motion of the superfluid component, which is described by the phase ϕ of the order parameter. This phase has to be determined simultaneously with the evolution of the quasiparticle-distribution function by solving the continuity equation. In the present work, we make an ansatz for ϕ with time-dependent coefficients, leading to an approximate solution of the continuity equation.

As a first application, we calculated the response of a gas trapped in a spherical trap to a delta-like perturbation of quadrupole form. After this perturbation, the shape of the gas shows a damped oscillation. At low temperatures, this oscillation is just the hydrodynamic quadrupole mode which is damped by its coupling to the normal component. With increasing temperatures, the extension of the normal component increases, and, as a consequence, the normal component can perform its own quadrupole oscillation. Since the frequency of the quadrupole mode in the normal collisionless Fermi gas is higher than that of the hydrodynamic mode, this leads to a two-peak structure in the response function. As the temperature approaches T_c, the strength of the hydrodynamic mode disappears and only the normal mode survives.

The next step will be to apply the method presented here to more realistic cases, namely to the axial and radial breathing modes of a gas in a cigar-shaped trap containing a larger number of particles. In fact, the deformation and the large particle number do not pose a big problem, which is one of the main advantages of the present method as compared with quantum mechanical QRPA calculations. Another possible application of the method is to study the dynamics of a vortex, where already the equilibrium situation is characterized by a non-vanishing phase of the order parameter.

However, there are still a number of unsolved problems and possible improvements of the method. First of all, the collision term [262] should be included, which is an additional source of damping of the collective oscillations. As mentioned in the introduction, the possibility to include collisions is an important advantage of the present method as compared with the QRPA, where collision effects cannot be taken into account since this would necessitate to include four-quasiparticle excitations. Second, from a fundamental point of view, the fact that the continuity equation is only approximately fulfilled is of course unsatisfactory and one should think about another numerical method for solving the continuity equation. Finally, one might ask the question how the present theory can be extended to the strongly interacting regime. Unfortunately, this question is up to now completely open, since in this regime thermal fluctuations of the order parameter, which are not contained in the BdG equations, play a crucial role (see, e.g., Ref. [184]).

Acknowledgments

The author wishes to thank P. Schuck for numerous fruitful discussions and the critical reading of the manuscript.

10 Numerical solution of the Boltzmann equation for the collective modes of trapped Fermi gases

Thomas Lepers, Dany Davesne, Silvia Chiacchiera, and Michael Urban,
Phys. Rev. A 82, 023609 (2010)

We numerically solve the Boltzmann equation for trapped fermions in the normal phase using the test-particle method. After discussing a couple of tests in order to estimate the reliability of the method, we apply it to the description of collective modes in a spherical harmonic trap. The numerical results are compared with those obtained previously by taking moments of the Boltzmann equation. We find that the general shape of the response function is very similar in both methods, but the relaxation time obtained from the simulation is significantly longer than that predicted by the method of moments. It is shown that the result of the method of moments can be corrected by including fourth-order moments in addition to the usual second-order ones and that this method agrees very well with our numerical simulations.

10.1 Introduction

In experiments on ultracold trapped Fermi gases, there are many situations where the system is out of thermal equilibrium. The first one is of course the trapping and cooling stage, i.e., before the system has reached its equilibrium state which is usually the starting point for the actual experiment. Then, in some experiments the system is excited in order to observe its dynamical behavior. For instance, many experiments studied collective oscillations of the system [14, 16, 34, 139, 140, 172, 199], another example being a recent experiment at MIT where the collision of two atom clouds (both in equilibrium) was studied [274]. Finally, often the system is not imaged directly during the experiment, but only after the trap was switched off and the system has expanded for a certain time, in order to increase its size.

The modeling of such time-dependent processes from the theoretical point of view can be quite complicated. For practical reasons, only semiclassical approaches are suitable for the description of time-dependent phenomena involving typically several 10^5 atoms in a three-dimensional, non-uniform geometry. In some cases, it is possible to use hydrodynamic approaches: Superfluid hydrodynamics describes the expansion [168] and the collective modes [88] of superfluid systems at zero temperature. Hydrodynamics is also applicable in the normal-fluid phase if the mean time between collisions is much shorter than all other time scales of the process under consideration, so that the system can always be considered to be in a local equilibrium [88, 183]. Superfluid and normal hydrodynamics can be combined to two-fluid hydrodynamics in order to describe superfluid systems at finite temperature [237]. However, in many cases hydrodynamic approaches are not sufficient. In all cases where it is important that even locally the distribution $f(\mathbf{r},\mathbf{p},t)$ of the atoms is not an equilibrium one, the Boltzmann equation allows a very general description, provided the system is in the normal phase. If the system is superfluid, a more elaborate theory is necessary which couples the dynamics of the quasiparticle distribution function to the dynamics of the superfluid order parameter [248, 249, 252].

In the past, several authors used the Boltzmann equation for the investigation of collective oscillations in normal-fluid trapped Fermi gases [65, 80, 167, 183, 199, 243, 244]. In most cases, the Boltzmann equation was not solved directly in order to find the distribution function f, but semi-analytical approximate solutions were found by using the scaling ansatz [183] or the method of moments [65, 80, 167, 199]. These methods rely explicitly or implicitly on the assumption that the collision term can be treated in the relaxation-time approximation, with a single relaxation time τ which is independent of the position in the trap. An exception is the work by Toschi et al. [243, 244], where the Boltzmann equation was solved numerically, using a test-particle method very similar to the one we are using here. The test-particle method for the solution of the

Boltzmann equation has been used for many years in nuclear physics for the simulation of heavy-ion collisions [42]. In the context of trapped atoms, it was also used for the simulation of the dynamics of the thermal cloud in a Bose-Einstein condensate [134] and (without collision term) of the normal-fluid component in a superfluid Fermi gas [248, 249].

For the collision term of the Boltzmann equation, it is important to know the cross section which in principle can be modfied by in-medium effects. In the work by Riedl et al. [199], it was shown that by using in the Boltzmann equation instead of the free cross-section the in-medium one, the agreement between theoretical and experimental frequencies and damping rates of different collective modes is deteriorated. The reason is that the in-medium cross section is larger than the free one, so that the relaxation time is dramatically reduced. In our previous work [80], our aim was to include in addition to the in-medium cross section medium effects into the mean-field potential. This mean field resulted in better density profiles and allowed us to understand the shift of the quadrupole frequency in the collisionless regime at very low temperature observed in [16]. However, it did not help to improve the agreement between theory and experiment in the region of higher temperatures, where the properties of the collective modes are completely dominated by collisions.

Hence, one of our motivations for the present work was to check the validity of the relaxation-time approximation which is implicitly made in the method of moments. Here we will restrict ourselves to the case without mean field and with the free cross section. As we will show in Sec. 10.3, the numerical solution of the Boltzmann equation gives indeed a significantly longer relaxation time than the method of moments. As we will show, this discrepancy is due to the restriction of the method of moments to second-order moments in the existing literature [65, 80, 167, 199]. Once fourth-order moments are included, the results of the method of moments and of the numerical solution are in good agreement. However, already in the simplest case of a spherical harmonic trap without mean field, the inclusion of fourth-order moments is a very tedious task, while the numerical method can easily be generalized to more realistic cases.

In addition, there are some other reasons why we felt the necessity for a numerical method. For example, there are damping effects due to the anharmonicity of the trap potential which cannot be described by the method of moments. Another advantage of the numerical method is that it offers the possibility to simulate not only the oscillation of the cloud, but also the subsequent expansion after the trap has been switched off.

In Sec. 10.2 of the present paper, we give a detailed description of the method. In particular, we explain in detail how the collisions are simulated, since our method is somewhat different from that of Ref. [244]. Moreover we discuss some tests we made in order to estimate up to which precision we can trust our simulation. Then, in Sec. 10.3, we come to the main point of our article and calculate the properties of some collective modes for a system in a spherical harmonic trap. While the sloshing and breathing modes are rather trivial, the frequency and damping rate of the quadrupole mode are very sensitive to the collisions. We compare the numerical results with those of the method of moments. Finally, in Sec. 10.4 we summarize and give an outlook to future studies.

Throughout the paper, we will use units with $\hbar = k_B = 1$ ($\hbar$ = reduced Planck constant, k_B = Boltzmann constant). The strength of the interaction is characterized by the dimensionless quantity $k_F a$, where a is the scattering length. Concerning the Fermi momentum k_F and the Fermi energy E_F we follow the usual convention that these quantities are defined by the corresponding ones of an ideal Fermi gas at zero temperature, i.e., $k_F = \sqrt{2mE_F}$, m being the atomic mass, and $E_F = (3N)^{1/3}\omega_0$, where N is the number of atoms and ω_0 the trap frequency. Temperatures will be measured in units of the Fermi temperature $T_F = E_F$ (since $k_B = 1$).

10.2 Description of the numerical method

10.2.1 Test-particle method

We study a two-component ($\sigma = \uparrow, \downarrow$) gas of fermionic atoms of mass m in a potential $V(\mathbf{r}, t)$ with attractive interaction $a < 0$. We assume that the system is in the normal phase and that it can be described semiclassically by phase-space distribution functions $f_\sigma(\mathbf{r}, \mathbf{p}, t)$. In this paper, we will restrict ourselves to the case that the distribution functions of both spin states are equal ($f_\uparrow = f_\downarrow = f$), but the generalization of the method to the cases of different distribution functions, more than two components, or components with different masses is straight-forward.

The time evolution of the distribution function f is governed by the Boltzmann equation [152]

$$\dot{f} + \dot{\mathbf{r}} \cdot \boldsymbol{\nabla}_r f + \dot{\mathbf{p}} \cdot \boldsymbol{\nabla}_p f = -I[f] \,, \tag{10.1}$$

where the left-hand side (lhs) describes the particle propagation, with

$$\dot{\mathbf{r}} = \frac{\mathbf{p}}{m} \quad \text{and} \quad \dot{\mathbf{p}} = -\boldsymbol{\nabla} V \,, \tag{10.2}$$

and $I[f]$ on the right-hand side (rhs) denotes the collision term which will be discussed later. The potential felt by the particles is the trap potential that contains a static part and a time dependent one (used in the following to simulate the excitation of the collective modes) $V(\mathbf{r}, t) = V_T(\mathbf{r}) + V_1(\mathbf{r}, t)$.

The density per spin state is related to the distribution function by

$$\rho(\mathbf{r}, t) = \int \frac{d^3p}{(2\pi)^3} f(\mathbf{r}, \mathbf{p}, t) \,, \tag{10.3}$$

and the number of atoms is given by

$$N = N_\uparrow + N_\downarrow = 2 \int d^3r \rho(\mathbf{r}, t) \,. \tag{10.4}$$

The basic idea of the test-particle method (also called pseudoparticle method) for solving the Boltzmann equation consists in replacing the continuous distribution function by a sum of delta functions,

$$f(\mathbf{r}, \mathbf{p}, t) = \frac{N}{2\tilde{N}} \sum_{i=1}^{\tilde{N}} (2\pi)^3 \delta(\mathbf{p} - \mathbf{p}_i(t)) \delta(\mathbf{r} - \mathbf{r}_i(t)) \,, \tag{10.5}$$

where $\tilde{N}$ is the number of "test particles". This allows one to express the average of an arbitrary single-particle observable $F(\mathbf{r}, \mathbf{p})$ in the simple form

$$\langle F \rangle = \frac{2}{N} \int \frac{d^3r d^3p}{(2\pi)^3} f(\mathbf{r}, \mathbf{p}, t) F(\mathbf{r}, \mathbf{p}) = \frac{1}{\tilde{N}} \sum_{i=1}^{\tilde{N}} F(\mathbf{r}_i, \mathbf{p}_i) \,. \tag{10.6}$$

In order to sample the six-dimensional phase space, it is necessary to choose a sufficiently large number of test particles $\tilde{N}$ (usually $\tilde{N} > N$). Neglecting the collision term $I[f]$ for the moment, it is easy to see that Eq. (10.5) satisfies the Boltzmann equation (Eq. (10.1)) if the positions $\mathbf{r}_i$ and momenta $\mathbf{p}_i$ of each test particle i follow the classical equations of motion, Eq. (10.2).

In practice, the delta functions in Eq. (10.5) can pose some problems. For instance, they do not result in a continuous density $\rho(\mathbf{r})$. Therefore it is often useful to replace them by Gaussians of width w_r and w_p in position and momentum space, respectively:

$$\delta(\mathbf{p}-\mathbf{p}_i)\delta(\mathbf{r}-\mathbf{r}_i) \to g_{w_p}(\mathbf{p}-\mathbf{p}_i)g_{w_r}(\mathbf{r}-\mathbf{r}_i)\,, \tag{10.7}$$

with

$$g_{w_p}(\mathbf{p}) = \frac{e^{-p^2/w_p^2}}{(\sqrt{\pi}w_p)^3} \quad \text{and} \quad g_{w_r}(\mathbf{r}) = \frac{e^{-r^2/w_r^2}}{(\sqrt{\pi}w_r)^3}\,. \tag{10.8}$$

The widths w_r and w_p must be adapted such that they smooth out the fluctuations due to the finite number of test particles, but not the structure of the distribution function f. The statistical fluctuations are of the order of $(2\tilde{N}w_r^3w_p^3/N)^{-1/2}$, i.e., the first condition is equivalent to

$$w_r w_p \gg \left(\frac{N}{2\tilde{N}}\right)^{1/3}\,. \tag{10.9}$$

The second condition implies of course that $w_r \ll R_{TF}$ and $w_p \ll p_F$, where R_{TF} and p_F are the Thomas-Fermi radius and the Fermi momentum, respectively, but this is not always sufficient. At low-temperature, it is crucial to resolve the rapid change of the distribution function around the Fermi surface, i.e.,

$$w_p \ll p_F\frac{T}{T_F} \quad \text{and} \quad w_r \ll R_{TF}\frac{T}{T_F}\,. \tag{10.10}$$

In practice, as the computation time increases as $\tilde{N}^2$, it turns out that the conditions (10.9) and (10.10) cannot simultaneously be satisfied at too low temperatures.

10.2.2 Particle propagation

In the absence of collisions, the numerical task consists only in solving simultaneously the classical equations of motion (10.2) for the $\tilde{N}$ test particles. We do this by using the velocity Verlet algorithm [235], which contrary to the original Verlet algorithm [260] uses the positions $\mathbf{r}_i(t_n)$ and velocities $\mathbf{v}_i(t_n) = \mathbf{p}_i(t_n)/m$ as starting point for the time step from t_n to $t_{n+1} = t_n + \Delta t$. The propagation from t_n to t_{n+1} is done according to

$$\mathbf{v}_i(t_{n+1/2}) = \mathbf{v}_i(t_n) + \mathbf{a}_i(t_n)\Delta t/2 \tag{10.11}$$

$$\mathbf{r}_i(t_{n+1}) = \mathbf{r}_i(t_n) + \mathbf{v}_i(t_{n+1/2})\Delta t \tag{10.12}$$

$$\mathbf{v}_i(t_{n+1}) = \mathbf{v}_i(t_{n+1/2}) + \mathbf{a}_i(t_{n+1})\frac{\Delta t}{2}\,, \tag{10.13}$$

where $\mathbf{a}_i(t) = -\boldsymbol{\nabla}V(\mathbf{r}_i(t),t)/m$ is the acceleration of the i-th test particle. If it is written in this way, it is obvious that the velocity Verlet algorithm is identical to the leap-frog algorithm [189]. Note that the accelerations $\mathbf{a}_i(t_{n+1})$ can be reused in the next time step, so that the algorithm needs only one evaluation of the acceleration per time step, but nevertheless its global error is of the order $\mathcal{O}(\Delta t)^2$. This allows us to obtain a good accuracy for reasonable time steps Δt. A good test of the particle propagation is to check the energy conservation: typically we find $|E_i(t) - E_i(0)|/E_i(0) \simeq 10^{-6}$ for each test particle and for all times considered.

10.2.3 Collision term

The rhs of the Boltzmann equation (10.1) describes the collisions between particles of opposite spin. It thus depends on the scattering cross section $d\sigma/d\Omega$ and reads [152]

$$I[f] = \int \frac{d^3p_1}{(2\pi)^3} \int d\Omega \frac{d\sigma}{d\Omega} |\mathbf{v} - \mathbf{v}_1| [f f_1 (1 - f')(1 - f'_1) - f' f'_1 (1 - f)(1 - f_1)] \,. \tag{10.14}$$

In the first term, $\mathbf{p}$ and $\mathbf{p}_1$ are the incoming momenta, $\mathbf{p}'$ and $\mathbf{p}'_1$ are the outgoing ones, Ω is the solid angle formed by the incoming relative momentum $\mathbf{p} - \mathbf{p}_1$ and the outgoing relative momentum $\mathbf{p}' - \mathbf{p}'_1$, and $f \equiv f(\mathbf{r}, \mathbf{p}, t)$, $f_1 \equiv f(\mathbf{r}, \mathbf{p}_1, t)$, etc. In the second term, the role of incoming and outgoing momenta is exchanged. Momentum and energy conservation implies $\mathbf{p} + \mathbf{p}_1 = \mathbf{p}' + \mathbf{p}'_1$ and $|\mathbf{p} - \mathbf{p}_1| = |\mathbf{p}' - \mathbf{p}'_1|$. Here we consider the case of pure s-wave scattering, in which the cross section is isotropic, i.e., $d\sigma/d\Omega = \sigma/4\pi$. In principle the cross section is modified by medium effects [65, 80], but in the present paper we will only use the free cross-section (i.e., the cross-section for the scattering of two atoms of opposite spin in free space) which is given by [144]

$$\sigma = \frac{4\pi a^2}{1 + (qa)^2} \,, \tag{10.15}$$

where $q = |\mathbf{p} - \mathbf{p}_1|/2 = |\mathbf{p}' - \mathbf{p}'_1|/2$.

In our numerical simulation, the collision term is included by allowing the test particles to collide with each other. The cross section of the test particles, $\tilde{\sigma}$, is related to the cross section of the atoms by $\tilde{\sigma} = \sigma N/2\tilde{N}$ (since $\tilde{N}$ test particles represent $N/2$ atoms of a given spin). Whether a pair i, j of test particles collides in a time step t_n or not is determined as follows: First, we determine if the two particles are at their closest approach in the present time step. Explicitly, if we write $\mathbf{r}_{ij} = \mathbf{r}_i - \mathbf{r}_j$ and $\mathbf{v}_{ij} = \mathbf{v}_i - \mathbf{v}_j$, the closest approach is reached at $t_{min} = t_n - \mathbf{r}_{ij} \cdot \mathbf{v}_{ij}/v_{ij}^2$ and we check if $|t_{min} - t_n| < \Delta t/2$. If yes, we calculate the corresponding minimal distance by $d_{min}^2 = r_{ij}^2 - (\mathbf{r}_{ij} \cdot \mathbf{v}_{ij})^2/v_{ij}^2$ and check if $\pi d_{min}^2 < \tilde{\sigma}$. In this case, the collision is classically allowed. We then propagate both test particles to t_{min}, change the direction of their relative velocity $\mathbf{v}_{ij}$ in a random way (thus conserving the total momentum and the total energy), and propagate them back to the original time t_n. Finally, in order to take into account the Pauli-blocking factors in Eq. (10.14), we calculate the occupation numbers f'_i and f'_j at the new positions and momenta ($f'_i = f(\mathbf{r}'_i, \mathbf{p}'_i)$ etc.) using Eq. (10.5) with Gaussians instead of delta functions, see Eq. (10.7)). With probability $(1 - f'_i)(1 - f'_j)$ the collision is allowed and we keep the new positions and momenta, otherwise the collision is blocked and we keep the old ones.

We checked that the total energy is still well conserved when collisions are switched on: typically we find better than $|\langle E \rangle(t) - \langle E \rangle(0)|/\langle E \rangle(0) \simeq 10^{-5}$ for all times considered.

10.2.4 Initialization

Before the simulation can start, the test-particle positions and momenta have to be initialized. Here we assume that the system is initially in equilibrium.

A suitable equilibrium distribution is given by the distribution function within the Thomas-Fermi or local-density approximation (LDA),

$$f_{eq}(\mathbf{r}, \mathbf{p}) = \frac{1}{e^{\beta(p^2/2m + V_T(\mathbf{r}) - \mu)} + 1} \,, \tag{10.16}$$

since it is a stationary solution of the Boltzmann equation [152]. This distribution has two parameters, namely the inverse temperature $\beta = 1/T$ and the chemical potential μ. The temperature T is an input parameter, whereas the chemical potential μ is determined by demanding that the integral of Eq. (10.16) over $\mathbf{r}$ and $\mathbf{p}$ gives the right number of atoms.

Having determined the chemical potential μ, we randomly generate the test-particle positions and momenta in such a way that the probability to be at position $\mathbf{r}$ and to have momentum $\mathbf{p}$ is proportional to $f_{eq}(\mathbf{r},\mathbf{p})$. In practice, we do this by first generating the positions according to the density profile obtained from Eq. (10.3) with $f = f_{eq}$. Then we generate the momenta according to f_{eq}.

10.2.5 Tests of reliability and accuracy

In this subsection we describe two main tests we made to be sure that our code is reliable. Here, we assume the potential to be static and, as in the rest of the paper, we use a spherical harmonic potential

$$V(\mathbf{r},t) = V_T(\mathbf{r}) = \frac{1}{2}m\omega_0^2 r^2\,. \tag{10.17}$$

This potential defines naturally a time scale $1/\omega_0$, a length scale $l_{ho} = 1/\sqrt{m\omega_0}$, an energy scale ω_0, and so on.

Let us consider the energy distribution of the atoms,

$$\frac{dN}{dE} = 2\int \frac{d^3r\,d^3p}{(2\pi)^3} f(\mathbf{r},\mathbf{p})\delta\Big(\frac{p^2}{2m} + V_T(\mathbf{r}) - E\Big)\,. \tag{10.18}$$

In equilibrium, the distribution should be given by $dN/dE = g(E)/(e^{(E-\mu)/T}+1)$, where $g(E)$ is the density of states (including the degeneracy factor 2). In the present case of a spherical harmonic oscillator, we have $g(E) = E^2/\omega_0^3$. In the absence of collisions, energy conservation automatically implies that the distribution stays constant, but in the presence of collisions this test is a non-trivial check of the Pauli blocking in the simulation. Within the test particle method, dN/dE is obtained by counting the test particles in energy bins.

In Fig. 10.1 we show, for $T/T_F = 0.2$, the initial Fermi distribution (solid line) and the stationary distribution obtained in the numerical simulation after $t = 30/\omega_0$ (filled circles). The agreement between the distribution generated by the simulation and the initial Fermi one is not perfect, but satisfactory. In order to show that this is not a trivial result, let us see what happens if we switch off the Pauli blocking in the simulation of the collision term. In this case, already after a relatively short time $\sim 3/\omega_0$, the distribution in the numerical simulation (empty circles) has converged to a Boltzmann distribution with the same number of atoms and total energy (dashed line). So, the stability of the Fermi distribution in our full simulation shows clearly that Pauli blocking is correctly implemented. The small deviations from the ideal Fermi distribution are a consequence of the fact that with the chosen widths of the Gaussians ($w_r = 1.5 l_{ho}$ and $w_p = 1.5/l_{ho}$), the condition (10.10) is not well satisfied at $T/T_F = 0.2$. When we did the same kind of comparison at higher temperatures, we found that the agreement between the simulation and the Fermi distribution improves: at $T/T_F = 0.4$, it is already perfect.

The test described above is independent of the actual number of collisions. In order to check the latter, let us look at the collision rate

$$\dot{N}_{coll} = \int d^3r \int \frac{d^3p}{(2\pi)^3}\int \frac{d^3p_1}{(2\pi)^3}\int d\Omega \frac{d\sigma}{d\Omega}|\mathbf{v}-\mathbf{v}_1| f f_1 (1-f')(1-f_1')\,. \tag{10.19}$$

In the numerical simulation, this quantity can be obtained as $\dot{N}_{coll} = (N/\tilde{N})\dot{\tilde{N}}_{coll}$, where $\dot{\tilde{N}}_{coll}$ denotes the number of collisions of test particles per unit time.

Although in equilibrium the net effect of collisions is zero, the collision rate in equilibrium is a good test for the simulation because it can be compared with the exact result [Eq. (10.32), see Appendix 10.A]. For

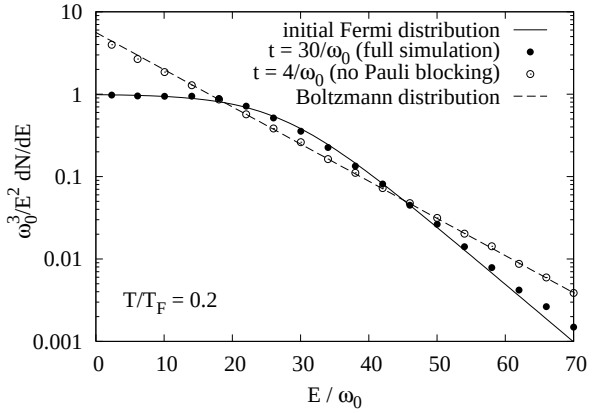

Figure 10.1: Energy distribution of the atoms (divided by the density of states) for $T/T_F = 0.2$ (see text for details). The system consists of $N = 10000$ atoms with a scattering length $a = -0.2537 l_{ho}$ ($1/(k_F a) = -0.5$). The parameters of the simulation are: $\tilde{N} = 50000$, $w_r = 1.5 l_{ho}$, $w_p = 1.5/l_{ho}$, and $\Delta t = 0.02/\omega_0$.

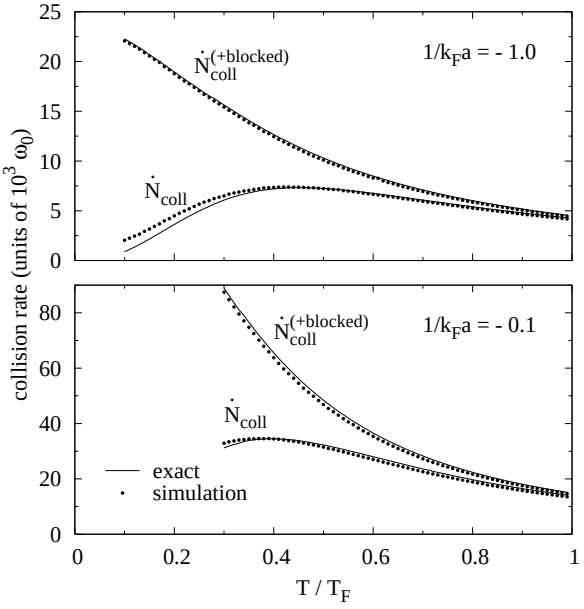

Figure 10.2: Simulated collision rates (filled circles) with and without blocking compared with the corresponding exact results, Eqs. (10.32) and (10.33) (solid lines), for a gas of 10000 atoms with interaction strength $1/k_F a = -1.0$ (top) and -0.1 (bottom).

testing purposes, it is useful to compare also the total rate of allowed and blocked collisions with the exact result [Eq. (10.33)].

In Fig. 10.2, the collision rates (with and without blocking) of the simulation are shown together with the exact results as functions of the temperature for two different values of the scattering length. In the case of relatively weak interaction, $1/k_F a = -1$ (upper panel), we see that the agreement between the simulation and the exact result is excellent for temperatures above $\sim 0.35\, T_F$. Below that temperature, the collision rate in the simulation with Pauli blocking gradually becomes too high since the finite widths of the Gaussians ($w_r = 1.5 l_{ho}$, $w_p = 1.5/l_{ho}$) do not satisfy any more the condition (10.10) and act in the Pauli-blocking factors like an enhanced temperature. In the rest of this paper, we will therefore restrict ourselves to temperatures above $0.2\, T_F$. Near unitarity ($1/k_F a = -0.1$), we consider only temperatures above $0.3\, T_F$ because this is close to the superfluid transition temperature at unitarity [80]. As it can be seen in the lower panel of Fig. 10.2, the agreement between the collision rate obtained in the simulation and the exact one is satisfactory in the temperature range considered. The agreement is not as good as for $1/k_F a = -1$ at high temperature because of the larger cross section which leads to collisions between test particles which are further apart.

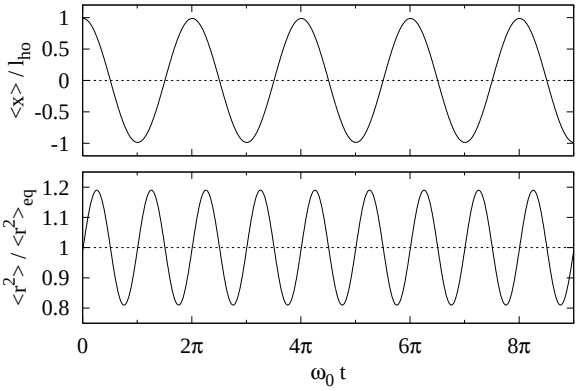

Figure 10.3: Top: simulation of the sloshing mode. The mode was excited at $t = 0$ by displacing all test particles by l_{ho} in the x direction. Bottom: simulation of the breathing mode. The mode was excited by changing at $t = 0$ all test-particle momenta according to $\mathbf{p}_i \rightarrow \mathbf{p}_i + c\mathbf{r}_i$ ($c = 0.2m\omega_0$). Both simulations were done for a system of $N = 5000$ particles at $T = 0.4\,T_F$ and $1/k_F a = -0.3$.

10.3 Simulation of collective modes

10.3.1 Sloshing mode

The sloshing mode is an oscillation of the center of mass of the system. It plays a special role because in a harmonic trap it is undamped and its frequency is equal to that of the trap, independently of the number of atoms, of the temperature, and of the interaction between the atoms (Kohn mode [56, 141]). This is why it is often used for the experimental determination of the trap frequency [14]. Within the test-particle method, this general theorem is satisfied and it is easy to see why:

Let us first neglect collisions. From the equations of motion of the individual test particles in the harmonic potential (10.17),

$$\dot{\mathbf{r}}_i = \mathbf{p}_i/m \quad \text{and} \quad \dot{\mathbf{p}}_i = -m\omega_0^2\mathbf{r}_i \tag{10.20}$$

it is evident that the averages $\langle\mathbf{r}\rangle$ and $\langle\mathbf{p}\rangle$ obey analogous equations of motion,

$$\frac{d}{dt}\langle\mathbf{r}\rangle = \frac{\langle\mathbf{p}\rangle}{m} \quad \text{and} \quad \frac{d}{dt}\langle\mathbf{p}\rangle = -m\omega_0^2\langle\mathbf{r}\rangle\,. \tag{10.21}$$

Let us now consider the effect of a collision of two test particles. Of course, the trajectories of the colliding test particles will not obey any more the original equations of motion (10.20), but the collision has absolutely no effect on the averages: Since the positions do not change during the collision, $\langle\mathbf{r}\rangle$ remains unchanged, and since the total momentum of the two colliding test particles is conserved, the average $\langle\mathbf{p}\rangle$ is not changed either. So, the equations of motion (10.21) for the averages $\langle\mathbf{r}\rangle$ and $\langle\mathbf{p}\rangle$ remain valid in the presence of collisions. Their solution is of course an undamped oscillation of the center of mass $\langle\mathbf{r}\rangle$ with frequency ω_0. This is confirmed by the numerical result shown in the upper panel of Fig. 10.3.

10.3.2 Breathing mode

A couple of experiments studied the damping of the longitudinal and radial breathing modes [14, 34, 139, 140, 199] in elongated traps. In a spherical trap, there is only one breathing mode (monopole mode), corresponding to an oscillation of the mean-square radius $\langle r^2\rangle$ around its equilibrium value $\langle r^2\rangle_{eq}$. In a spherical harmonic trap, this mode is undamped and its frequency $2\omega_0$ is independent of the number of collisions, like in the case of the sloshing mode.

Again, this is easy to see. Consider the average kinetic and potential energies, $\langle E_{kin}\rangle = \langle p^2\rangle/2m$ and $\langle E_{pot}\rangle = m\omega_0^2\langle r^2\rangle/2$. In equilibrium, both are equal (virial theorem). Now let us assume that the system is

compressed or expanded, such that $\langle E_{kin}\rangle \neq \langle E_{pot}\rangle$. Using again the equations of motion (10.20), one obtains

$$\frac{d}{dt}(\langle E_{kin}\rangle - \langle E_{pot}\rangle) = -2\omega_0^2\langle \mathbf{r}\cdot\mathbf{p}\rangle\,, \tag{10.22}$$

$$\frac{d}{dt}\langle \mathbf{r}\cdot\mathbf{p}\rangle = 2(\langle E_{kin}\rangle - \langle E_{pot}\rangle)\,. \tag{10.23}$$

Obviously, these two equations describe an undamped oscillation with frequency $2\omega_0$. Let us now look if they stay valid in the presence of collisions. Since the collisions do not change the positions of the particles and conserve the total kinetic energy, it is clear that $\langle E_{kin}\rangle$ and $\langle E_{pot}\rangle$ are not affected. Now let us write the difference of $\langle \mathbf{r}\cdot\mathbf{p}\rangle$ before and after a collision of two test particles i and j:

$$\langle \mathbf{r}\cdot\mathbf{p}\rangle' - \langle \mathbf{r}\cdot\mathbf{p}\rangle = \frac{1}{\tilde{N}}\mathbf{r}_{ij}\cdot(\mathbf{q}'_{ij} - \mathbf{q}_{ij})\,, \tag{10.24}$$

where $\mathbf{q}_{ij}$ and $\mathbf{q}'_{ij}$ are the relative momenta (e.g., $\mathbf{q}_{ij} = (\mathbf{p}_i - \mathbf{p}_j)/2$) before and after the collision. In the original collision term as written in Eq. (10.14), particles have to be at the same position to collide, i.e., $\mathbf{r}_{ij} = 0$, such that $\langle \mathbf{r}\cdot\mathbf{p}\rangle$ is not changed. In our simulation this is somewhat different, since the test particles can collide at a distance of up to $\sqrt{\tilde{\sigma}/\pi}$. This adds a small noise to $\langle \mathbf{r}\cdot\mathbf{p}\rangle$. In all practical cases, however, this noise is completely negligible. As an example we show in the lower panel of Fig. 10.3 the oscillation of the mean-square radius of the cloud as a function of time. As one can see, it is a perfectly undamped harmonic oscillation with frequency $2\omega_0$.

10.3.3 Excitation of an arbitrary mode

For the theoretical investigation of collective modes, it is convenient to consider a system which is in equilibrium until it is excited by a short pulse at $t = 0$. Formally, this is achieved by adding to the time-independent trap potential a perturbation term of the form

$$V_1(\mathbf{r}, t) = \hat{V}_1(\mathbf{r})\delta(t)\,. \tag{10.25}$$

The reason for this choice, which is of course different from the experimental way of exciting a collective mode, is the following: Provided the perturbation $\hat{V}_1$ is small enough (such that the system reacts linearly to it), the response to a perturbation with arbitrary time dependence, $V_1(\mathbf{r}, t) = \hat{V}_1(\mathbf{r})F(t)$, can easily be obtained by folding the result for the perturbation (10.25) with the function $F(t)$.

By integrating the Boltzmann equation over the (infinitesimal) duration of the pulse, one can show that the effect of the perturbation (10.25) is to change the distribution function as

$$f(\mathbf{r}, \mathbf{p}, 0^+) = f(\mathbf{r}, \mathbf{p} + \boldsymbol{\nabla}\hat{V}_1(\mathbf{r}), 0^-)\,, \tag{10.26}$$

where 0^+ and 0^- denote the limits $t \to 0$ from above and below, respectively. In the numerical simulation, this means that all test particles get a kick at $t = 0$,

$$\mathbf{p}_i(0^+) = \mathbf{p}_i(0^-) - \boldsymbol{\nabla}\hat{V}_1(\mathbf{r}_i(0)) \tag{10.27}$$

whereas their positions are not changed by the perturbation.

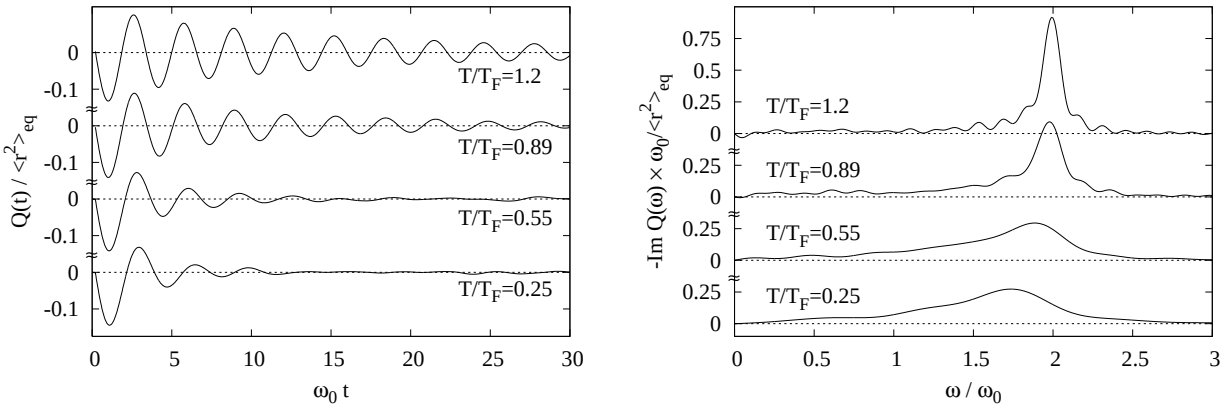

Figure 10.4: Left panel: Quadrupole response to a perturbation of the form (10.28) with $c = 0.2m\omega_0$ for different temperatures. The system has $N = 10000$ atoms and $1/k_F a = -0.5$. Right panel: imaginary part of the corresponding Fourier transforms.

10.3.4 Quadrupole mode

From now on we will study the quadrupole mode as an example for a collective mode with non-trivial properties. We write the perturbation as

$$\hat{V}_1(\mathbf{r}) = \frac{c}{2}(x^2 - y^2)\,, \tag{10.28}$$

corresponding to a kick at $t = 0$ of $p_x(0^+) = p_x(0^-) - cx(0)$ and $p_y(0^+) = p_y(0^-) + cy(0)$. The parameter c determines the amplitude of the perturbation. If c is chosen too small, it is difficult to separate the oscillation of the mode from fluctuations; if it is chosen too large, one is not in the linear-response regime. All the following results were obtained with $c = 0.2m\omega_0$, corresponding to moderate amplitudes. By varying c within reasonable limits, we checked that the amplitude of the resulting oscillation scales linearly with c.

After the excitation of the radial quadrupole mode, we can look at the time evolution of the quadrupole moment $Q = \langle x^2 \rangle - \langle y^2 \rangle$ as a function of time. Results for different temperatures are displayed in Fig. 10.4. Contrary to the sloshing and breathing modes, the quadrupole mode is damped and the system approaches equilibrium ($Q \to 0$) after a certain time. At high temperatures ($T/T_F \gtrsim 1$), the system gets so dilute that it is in the collisionless regime ($\omega_0 \tau_{coll} \gg 1$, τ_{coll} being the mean time between collisions of one atom). In this case, it takes many oscillations before the system returns to equilibrium. For lower temperatures, the mode is damped because of the high collision rate ($\omega_0 \tau_{coll} \sim 1$), but the system is not yet in the hydrodynamic regime ($\omega_0 \tau_{coll} \ll 1$) where the mode would become undamped again.

For the analysis of the results, it is useful to apply a Fourier transform

$$Q(\omega) = \int_0^\infty dt Q(t) e^{i\omega t}\,. \tag{10.29}$$

The so-called response function is the imaginary part of $Q(\omega)$ and can easily be obtained from the numerical results for $Q(t)$ by using a fast Fourier transform (FFT) algorithm [189]. As an example, the Fourier transforms of the results discussed above are shown in the right panel of Fig. 10.4. From the Fourier transform one can clearly see that the spectrum of the mode in the collisionless regime, i.e., at high temperature, has a sharp maximum at $\omega = 2\omega_0$, as it should be in an ideal Fermi gas, whereas at lower temperature the spectrum is broadened and the centroid of the spectrum is shifted to lower frequencies. This can be understood since at lower temperature the system is closer to the hydrodynamic regime, where the frequency should be $\omega = \sqrt{2}\omega_0$.

Of course, one would like to give numbers ω_q and Γ_q corresponding to the frequency and damping rate of the quadrupole mode in order to quantify these effects. The simplest way to obtain such numbers would be to fit the response function $Q(t)$ with a damped oscillation of the form $-Ae^{-\Gamma_q t}\sin\omega_q t$. However, in the case of strong damping, this ansatz fits very badly the numerical results for $Q(t)$. This can be understood by looking at the Fourier transforms: The Fourier transform of this ansatz function is a Lorentzian, which has a line shape quite different from that obtained in our numerical simulation for $T/T_F = 0.25$ or 0.55, cf. right panel of Fig. 10.4. Hence, in order to analyze our numerical results, we need some physically motivated ansatz for the fit.

10.3.5 Comparison with the method of moments

In most of the theoretical work on collective modes in normal-fluid Fermi gases, the Boltzmann equation was not solved numerically, but approximate analytical solutions were found with the help of the method of moments [65, 80, 167, 199]. For a detailed description of the method, see e.g. Ref. [80].

Applying the method of moments to the case of a perturbation of the form (10.25) with $\hat{V}_1$ according to Eq. (10.28), one obtains a theoretical prediction for the response function $\mathrm{Im}\,Q(\omega)$. A brief description of the derivation is given in Appendix 10.B, the final result reads

$$\mathrm{Im}\,Q(\omega) = -c\frac{8\langle E\rangle}{3m^2}\frac{\omega\tau}{(\omega^2-2\omega_0^2)^2+\omega^2\tau^2(\omega^2-4\omega_0^2)^2}\,, \tag{10.30}$$

where $\langle E\rangle = m\omega_0^2\langle r^2\rangle$ is the mean energy per atom in equilibrium, and τ is the relaxation time as defined in Refs. [65, 80], and depends on the cross section (i.e., the interaction strength), and the equilibrium distributions, cf. Eq. (10.44). One can see from Eq. (10.30) that in the collisionless and hydrodynamic limits the quadrupole mode has the frequencies $\omega = 2\omega_0$ and $\omega = \sqrt{2}\omega_0$, respectively. The shape of the response function is completely determined by a single parameter, τ.

By looking for the poles of Eq. (10.30), one can calculate the inverse Fourier transform which gives $Q(t)$. The result has the form

$$Q(t) = -Ae^{-\Gamma_q t}\sin\omega_q t + B(e^{-\Gamma_q t}\cos\omega_q t - e^{-\Gamma_1 t})\,, \tag{10.31}$$

i.e., it is a superposition of a damped oscillation with frequency ω_q and damping Γ_q, and a non-oscillating, exponentially decaying term. The explicit expressions for Γ_1, Γ_q, and ω_q as functions of τ as well as for the amplitudes A and B are given in Appendix 10.C. We will refer to ω_q and Γ_q as the frequency and damping rate of the quadrupole mode. Note that in experiments determining these quantities, the data are usually fitted with a function that is similar to Eq. (10.31) [16].

In Fig. 10.5 we compare the response function obtained from the numerical simulation (solid line) with the result obtained from the method of moments, Eq. (10.30) (dotted line). As one can see, the height of the peak and its general shape are in good agreement, but the position of the maximum is at different frequencies. However, if we try to fit the numerical result with a function of the form of Eq. (10.30), using τ as fitting parameter, we can very well reproduce the numerical response function (long-dashed line). It is remarkable that by adjusting only one parameter, τ, one can simultaneously reproduce the position, the height and the width of the peak, and also the shape far away from the maximum. However, surprisingly, the fitted value of τ is larger by approximately 30% than the one obtained by the method of moments. As a consequence, the frequency ω_q and damping rate Γ_q obtained from the fit of the response function deviate significantly from those predicted by the method of moments. These results are summarized in Table 10.1.

In the existing literature [65, 80, 167, 199], the method of moments was limited to second-order moments, as described in appendix 10.B. However, as we have seen above, this implies that the system is characterized

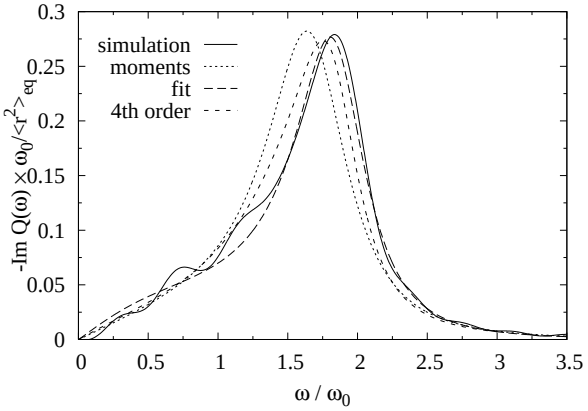

Figure 10.5: Fourier transform of the numerical simulation of the quadrupole response (solid line) compared with Eq. (10.30) where the parameter τ is obtained by the method of moments (dots), or by a fit to the simulation (long dashes). The short dashes represent the response obtained with the extended method of moments including fourth-order moments. The system is a gas of $N = 10000$ particles at $T = 0.4\,T_F$ and $1/k_F a = -0.5$.

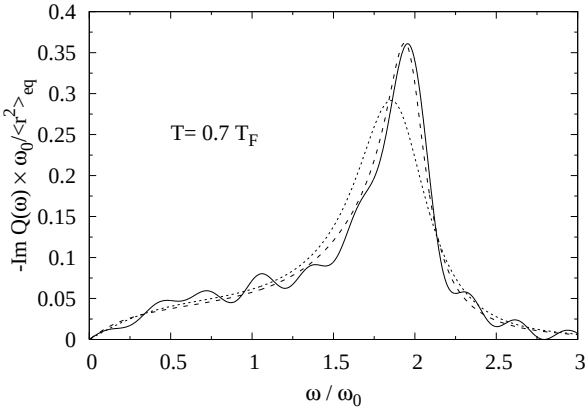

Figure 10.6: Same as Fig. 10.5 for a temperature $T = 0.7\,T_F$. For clarity, the fit of the simulation is not shown. The system is a gas of $N = 10000$ particles at $1/k_F a = -0.5$.

by a single relaxation time τ, whereas in the spirit of a local-density approximation one would expect that in a trapped system the relaxation time should be position-dependent, $\tau = \tau(\mathbf{r})$. For instance, one could imagine that the gas in the center of the trap is more or less hydrodynamic (short relaxation time), whereas far away from the trap center it gets very dilute and hence collisionless (long relaxation time). In the case of the quadrupole mode, this means that the Fermi-surface deformation is stronger at larger radii than in the trap center. It seems therefore natural to include into the ansatz for the perturbed distribution function in addition to the standard term $\propto p_x^2 - p_y^2$ describing the Fermi-surface deformation, a term $\propto r^2(p_x^2 - p_y^2)$. More generally speaking, we should go beyond the standard approximation to include only second-order moments, and include also fourth-order (or perhaps even higher) moments.

The task of extending the method of moments to the next higher order is in principle straight-forward but in practice very tedious: In the case of the quadrupole mode, the number of moments is increased from three to twelve. Some details are given in appendix 10.D. The resulting response function is shown in Fig. 10.5 as the short-dashed line. Surprisingly, its shape is still similar, but now the position of the maximum agrees rather

method	$\omega_0\tau$	ω_q/ω_0	Γ_q/ω_0
moments	0.451	1.676	0.353
simulation	0.587	1.787	0.336

Table 10.1: Relaxation time, frequency, and damping of the quadrupole mode as obtained from the method of moments and fitting the results of the numerical simulation with a function of the form (10.30), corresponding to the dotted and dashed curves in Fig. 10.5.

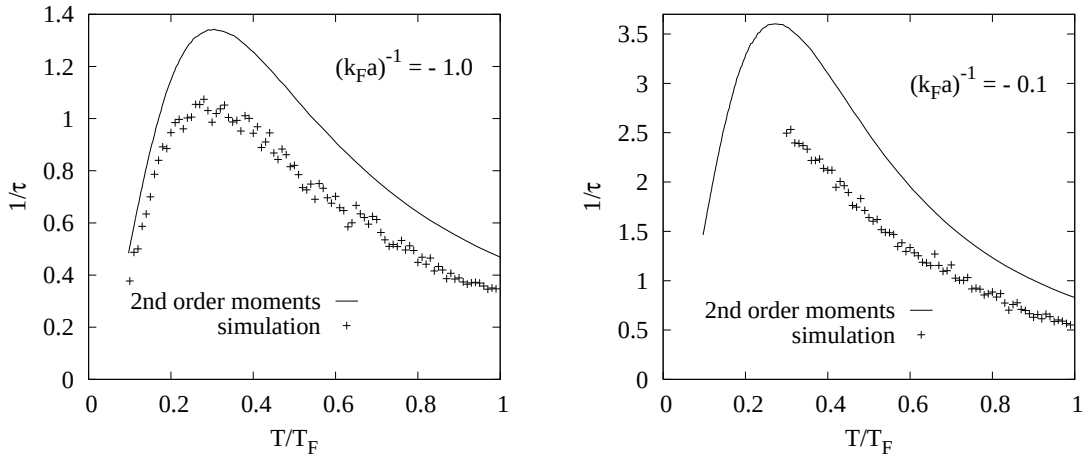

Figure 10.7: Comparison of the inverse relaxation time, $1/\tau$, as obtained from the simulation (crosses) and from the method of moments Eq. (10.44) (solid lines), as a function of temperature. The system consists of $N = 10000$ atoms with $1/k_F a = -1$ (left) and -0.1 (right).

well with the result of the numerical simulation (solid line). The agreement is even better at higher temperature (see Fig. 10.6). This nicely confirms the correctness of our numerical simulation and shows explicitly that the method of moments, if truncated at the lowest order, is insufficient.

By doing calculations for various interaction strengths and temperatures, we found that the relaxation time from the simulation is systematically longer than that from the method of moments (without fourth-order moments), Eq. (10.44). Results for weaker and stronger interactions ($1/k_F a = -1$ and -0.1) are displayed in Fig. 10.7. We see that the general behavior of τ as a function of temperature is the same within the simulation and the method of moments, but quantitatively there is a discrepancy of the order of 30% in the whole range of temperatures where our numerical simulation is very accurate ($T > 0.35\, T_F$, cf. Fig. 10.2 showing the temperature dependence of the collision rate). Note that at lower temperatures, the determination of the Pauli-blocking factors in the simulation of the collisions is not completely accurate, as discussed below Fig. 10.2, such that the collision rate below $0.35\, T_F$ is slightly too high. Nevertheless the inverse relaxation time is too small. From this one can conclude that if we could improve the Pauli blocking in the simulation, the discrepancy between the simulation and the method of moments (without fourth-order moments) would be even worse. The fourth order is thus important for the determination of the relaxation of the system and particularly for the frequency and the damping of collective modes.

10.3.6 Frequency and damping of the quadrupole mode

As we have just seen, the numerical simulation gives systematically a longer relaxation time τ than the method of moments. As the frequency ω_q and damping rate Γ_q of the quadrupole mode are parametrized in terms of τ (see Appendix Sec. 10.C), one can ask the question how strongly this difference in τ will affect the results for ω_q and Γ_q. Since we are mainly interested in the intermediate regime $\omega\tau \sim 1$ between the hydrodynamic and collisionless limits, a difference of 30% in τ can completely change the temperature dependence of ω_q and Γ_q. This is shown in Fig. 10.8, where the crosses are the results obtained from the simulation, whereas the solid lines are the results from the method of moments. One can clearly see that the numerical results stay close to the collisionless limit to much lower temperatures than the results obtained by the method of moments.

To estimate the resulting precision of our numerical result on ω_q and Γ_q, we show in Fig. 10.8 the error

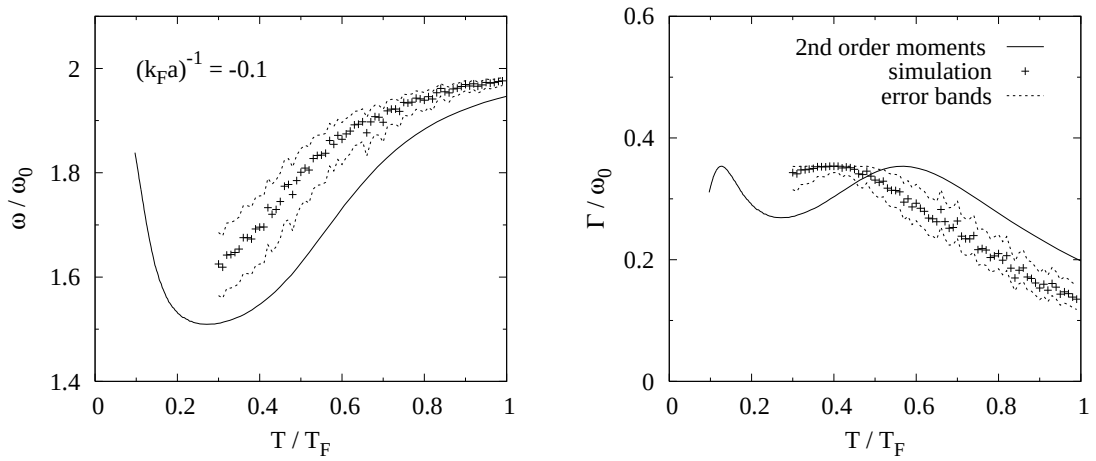

Figure 10.8: Frequency (left) and damping rate (right) of the quadrupole mode as a function of the temperature as obtained from the numerical simulation (crosses) and from the method of moments (solid line). The short-dashed lines indicate the error band of the results from the simulation if we admit that the relaxation time τ of the simulation may be wrong by 15%. The system consists of $N = 10000$ particles close to unitarity ($1/k_F a = -0.1$).

bands (short-dashed lines) which we obtain if we assume that our simulation may give a τ which is wrong by at most 15%. This error includes numerical uncertainties which can be estimated from the scattering of the points in Fig. 10.7 and the systematic deviation of the collision rate shown in Fig. 10.2.

If we include the fourth order moments, a global relaxation time τ does not exist anymore but we could define an effective one by fitting the response function as we did for the simulation. This effective relaxation time agrees very well with the one of the simulation so that both results give very similar frequency and damping. However, from a theoretical point of view, the definition of these quantities should come from the zeroes of the determinant of the matrix A_{ij} defined in Appendix 10.D. Such a discussion is postponed to a forthcoming publication [81, 150].

10.4 Conclusions

In this paper, we presented a test-particle method for solving numerically the Boltzmann equation for trapped Fermi gases. While such methods have been popular in other fields of physics for many years, there have been only a few applications to ultracold atomic gases [134, 243, 244, 248, 249]. Our method is similar to that of Refs. [243, 244] with some differences in the treatment of the collision term. In order to compute the occupation numbers in the Pauli-blocking factors in the collision term, we represent each test particle by a Gaussian in $\mathbf{r}$ and $\mathbf{p}$ space. The minimum value of the width of the Gaussian is dictated by the statistical fluctuations due to the finite number of test particles, limiting the applicability of the method to temperatures above $\sim 0.2\,T_F$.

As a first application of the method we discussed some collective modes. For simplicity, we considered only toy systems consisting of $\sim 10^4$ atoms in a spherical harmonic trap and neglected the mean-field potential and medium modifications of the cross section. As expected, the sloshing and monopole modes are undamped and independent of the collisions. In contrast, the quadrupole mode is very sensitive to collisions. In the hydrodynamic limit, its frequency should approach $\sqrt{2}\omega_0$, while it is $2\omega_0$ in the collisionless limit. In our simulations, we never reach the hydrodynamic regime, but the collisionless regime can be realized at high temperature due to the diluteness of the gas.

Surprisingly, the frequency and damping rate of the quadrupole mode obtained within the numerical simulation are quite different from those obtained within the widely used method of moments including moments up to second order in $\mathbf{r}$ and $\mathbf{p}$. The method of moments predicts a relaxation time τ which is significantly shorter than the one obtained within the simulation. The reason is that the $\mathbf{r}$ dependence of the relaxation time is neglected if only the $p_x^2 - p_y^2$ moment is taken into account for the description of the Fermi-surface deformation. We have shown that if the method of moments is extended to moments up to fourth order in $\mathbf{r}$ and $\mathbf{p}$, e.g., the $r^2(p_x^2 - p_y^2)$ moment, the agreement with the simulation becomes very good.

The focus of the present paper was mainly to explain the test-particle method and to show its usefulness. For instance, the deficiency of the method of moments up to second order would not have been detected without the comparison with the numerical result. In future studies, we plan to apply the method to more realistic cases. In particular, in order to reach the typical numbers of atoms in the experiments, we will have to increase N by a factor of $\sim 10 - 100$. However, this should not pose a big problem: According to Eq. (10.10), if we increase N but keep the ratio T/T_F fixed, the widths w_r and w_p may be chosen larger ($\propto N^{1/6}$). This means that Eq. (10.9) stays satisfied with the same number of test particles, $\tilde{N}$, i.e., with a reduced ratio $\tilde{N}/N$. The computation time will only grow because of the increased collision rate (due to the larger test-particle cross section $\tilde{\sigma} = \sigma N/2\tilde{N}$). Another point is the trap geometry. The traps in the experiments are usually not spherical, but elongated. Concerning the propagation of the test particles, this does not cause any difficulty, but in the calculation of the occupation numbers, it will probably be necessary to replace the width w_r of the Gaussian in $\mathbf{r}$ space by different widths w_x, w_y, and w_z in the three space directions. Another important advantage of the numerical method is that an anharmonicity of the trap potential, which is always present in real experiments, can easily be included.

Finally, the mean field [80] and medium modifications of the cross section [80, 199] should be included. The mean field, which originally depends on the chemical potential μ and the temperature T, can be expressed as a function of the local density and energy density, which are both obtainable in the simulation. However, as shown previously [80], the mean field is not just proportional to the density: this leads to a huge numerical effort which is beyond the scope of this paper. The in-medium cross section is also difficult to be included because it depends on too many variables to be tabulated: $\sigma = \sigma(k = |\mathbf{p} + \mathbf{p}_1|/2, q = |\mathbf{p} - \mathbf{p}_1|; \mu, T)$. One possible solution of this problem is to replace the full k and q dependence of the in-medium cross section by a simple parametrization which results in the same local relaxation time $\tau(\mu, T)$. Work in this direction is already in progress. In Refs. [80, 199], within the method of moments up to second order, the use of the in-medium cross section spoiled the agreement with experimental data because the resulting relaxation times were too short. Since the present work shows that the numerical simulation gives a longer relaxation time than the method of moments, we hope that this problem can be solved.

Further important extensions of the present work are the generalization to polarized Fermi gases and to superfluid systems. These questions, however, require more fundamental theoretical studies before they can be tackled numerically.

Appendix

10.A Collision rate at equilibrium

Replacing the distribution functions in Eq. (10.19) by equilibrium distribution functions f_{eq}, one obtains after some algebra the equilibrium collision rate

$$\dot{N}_{coll,eq} = \frac{1}{4\pi^4} \int d^3r \int_0^\infty dk\, k^2 \int_0^\infty dq\, q^2 \frac{2q}{m} \sigma(q) \left(\frac{\tanh^{-1}(\tanh \frac{X}{2} \tanh \frac{Y}{2})}{Y \sinh X} \right)^2 , \tag{10.32}$$

where $\mathbf{k} = \mathbf{p} + \mathbf{p}_1$, $\mathbf{q} = (\mathbf{p} - \mathbf{p}_1)/2$, $X = \beta(k^2/8m + q^2/2m + V_T - \mu)$ and $Y = \beta kq/2m$. The total rate of allowed and blocked collisions is, in turn, given by Eq. (10.19) but without the factor $(1 - f')(1 - f_1')$ in the integrand, leading to

$$\dot{N}_{coll,eq}^{(+blocked)} = \frac{1}{4\pi^4} \int d^3r \int_0^\infty dk\, k^2 \int_0^\infty dq\, q^2 \frac{2q}{m} \sigma(q)\, \frac{\tanh^{-1}(\tanh\frac{X}{2}\tanh\frac{Y}{2})}{Ye^X \sinh X}\,. \tag{10.33}$$

If the trap potential is spherically symmetric or harmonic, the spatial integrals can be reduced to one-dimensional ones. The remaining three-dimensional integrals are evaluated numerically with a Monte-Carlo algorithm.

10.B Quadrupole response within the method of moments

In the case of a weak perturbation, we can write the deviation of the distribution function from the equilibrium one in the form

$$f - f_{eq} = f_{eq}(1 - f_{eq})\Phi(\mathbf{r}, \mathbf{p}, t)\,. \tag{10.34}$$

Inserting this expression into the Boltzmann equation and keeping only terms linear in the perturbation, one obtains (see Eq. (36) of Ref. [80], for the case without mean field but with an external perturbation):

$$f_{eq}(1 - f_{eq})\Big(\dot{\Phi} + \frac{\mathbf{p}}{m} \cdot \boldsymbol{\nabla}_r \Phi - \boldsymbol{\nabla}_r V_T \cdot \boldsymbol{\nabla}_p \Phi + \beta \frac{\mathbf{p}}{m} \cdot \boldsymbol{\nabla}_r V_1\Big) = -I[\Phi]. \tag{10.35}$$

Here, $I[\Phi]$ is the linearized collision term as defined in Eq. (37) of Ref. [80] (up to a factor $(2\pi)^3$ since here we are using a different normalization of f):

$$I[\Phi] = \int \frac{d^3p_1}{(2\pi)^3} \int d\Omega \frac{d\sigma}{d\Omega} |\mathbf{v} - \mathbf{v_1}| f_{eq} f_{eq\,1} (1 - f'_{eq})(1 - f'_{eq\,1})(\Phi + \Phi_1 - \Phi' - \Phi'_1)\,. \tag{10.36}$$

The perturbation V_1 is given by Eqs. (10.25) and (10.28). The usual approximation consists in making the ansatz

$$\Phi(\mathbf{r}, \mathbf{p}, t) = \sum_{i=1}^{3} c_i(t) \phi_i(\mathbf{r}, \mathbf{p})\,, \tag{10.37}$$

with time-dependent coefficients c_i and $\phi_1 = x^2 - y^2$, $\phi_2 = xp_x - yp_y$, and $\phi_3 = p_x^2 - p_y^2$, i.e., only quadratic moments are considered. Evaluating the moments $\int d^3r d^3p \phi_i(\mathbf{r}, \mathbf{p}) \times$ Eq. (10.35), one obtains a system of equations for the Fourier transformed coefficients:

$$\sum_{j=1}^{3} A_{ij} c_j(\omega) = a_i \tag{10.38}$$

with

$$A_{ij} = \int \frac{d^3r d^3p}{(2\pi)^3} \phi_i \left[f_{eq}(1 - f_{eq}) \left(-i\omega\phi_j + \left\{ \phi_j, \frac{p^2}{2m} + \frac{m\omega_0^2 r^2}{2} \right\} \right) + I[\phi_j] \right] \tag{10.39}$$

and

$$a_i = -\beta \int \frac{d^3r d^3p}{(2\pi)^3} \phi_i f_{eq}(1 - f_{eq}) \frac{\mathbf{p}}{m} \cdot \boldsymbol{\nabla} \hat{V}_1\,, \tag{10.40}$$

where $\{.,.\}$ are the Poisson brackets. Using the virial theorem, we obtain explicitly:

$$-i\omega c_1 - m\omega_0^2 c_2 = 0 \tag{10.41}$$

$$2c_1 - im\omega c_2 - 2m^2\omega_0^2 c_3 = -\beta c\,, \tag{10.42}$$

$$c_2 + \Big(\frac{1}{\tau} - i\omega\Big) m c_3 = 0\,, \tag{10.43}$$

where the relaxation time τ is defined by [80, 199]

$$\frac{1}{\tau} = \frac{3\beta}{m^2 N\langle E_{kin}\rangle}\int \frac{d^3r d^3p}{(2\pi)^3} p_x p_y I[p_x p_y]\,. \tag{10.44}$$

Solving this system of equations, we find

$$c_1(\omega) = \frac{\beta\omega_0^2 c(1-i\omega\tau)}{\omega^2 - 2\omega_0^2 - i\omega\tau(\omega^2 - 4\omega_0^2)}\,. \tag{10.45}$$

and similar expressions for c_2 and c_3. However, only the coefficient c_1 contributes to Q: With Eq. (10.34), and using again the virial theorem, we obtain $Q(t) = \langle x^2 - y^2\rangle = 4T\langle r^2\rangle c_1(t)/3m\omega_0^2$, or explicitly:

$$Q(\omega) = \frac{4\langle r^2\rangle c}{3m}\,\frac{1-i\omega\tau}{\omega^2 - 2\omega_0^2 - i\omega\tau(\omega^2 - 4\omega_0^2)}\,. \tag{10.46}$$

Taking the imaginary part, we obtain Eq. (10.30).

10.C Time dependence of the quadrupole response within the method of moments

In order to compute the Fourier transform of Eq. (10.46), let us start by factorizing the denominator:

$$\omega^2 - 2\omega_0^2 - i\omega\tau(\omega^2 - 4\omega_0^2) = -i\tau(\omega-\omega_1)(\omega-\omega_2)(\omega-\omega_3)\,. \tag{10.47}$$

The expressions for the roots ω_i can be given in closed form. Defining $\tilde\tau = \omega_0\tau$ and

$$\Theta = \Big(1 + 9\tilde\tau^2 + 3\tilde\tau\sqrt{6 - 39\tilde\tau^2 + 192\tilde\tau^4}\Big)^{1/3}\,, \tag{10.48}$$

$$u_\pm = \frac{1}{3\tau}\left(\Theta \pm \frac{1-12\tilde\tau^2}{\Theta}\right)\,, \tag{10.49}$$

we can write the roots ω_i as

$$\omega_1 = -i\Gamma_1\,, \quad \omega_2 = \omega_q - i\Gamma_q\,, \quad \omega_3 = -\omega_q - i\Gamma_q\,, \tag{10.50}$$

with

$$\Gamma_1 = \frac{1}{3\tau} + u_+\,, \quad \Gamma_q = \frac{1}{3\tau} - \frac{u_+}{2}\,, \quad \omega_q = \frac{\sqrt{3}}{2}u_-\,. \tag{10.51}$$

Now it is straight-forward to evaluate the inverse Fourier transform of the response (10.30) using the residue theorem. The result is given by Eq. (10.31) with

$$A = \frac{4c\langle r^2\rangle}{3m\omega_q\tau}\,\frac{\omega_q^2\tau + (\Gamma_1-\Gamma_q)(1-\Gamma_q\tau)}{\omega_q^2 + (\Gamma_q-\Gamma_1)^2}\,, \tag{10.52}$$

$$B = \frac{4c\langle r^2\rangle}{3m\tau}\,\frac{1-\Gamma_1\tau}{\omega_q^2 + (\Gamma_q-\Gamma_1)^2}\,. \tag{10.53}$$

10.D Extension of the method of moments to fourth-order moments

Taking fourth order moments into account, we extend the previous ansatz Eq. (10.37) as follows:

$$\begin{aligned}\Phi =& c_1(x^2-y^2)+c_2(xp_x-yp_y)+c_3(p_x^2-p_y^2)\\ &+c_4r^2(x^2-y^2)+c_5p^2(x^2-y^2)+c_6\mathbf{r}\cdot\mathbf{p}(x^2-y^2)\\ &+c_7r^2(xp_x-yp_y)+c_8p^2(xp_x-yp_y)+c_9\mathbf{r}\cdot\mathbf{p}(xp_x-yp_y)\\ &+c_{10}r^2(p_x^2-p_y^2)+c_{11}p^2(p_x^2-p_y^2)+c_{12}\mathbf{r}\cdot\mathbf{p}(p_x^2-p_y^2)\end{aligned} \tag{10.54}$$

which can be written as $\Phi = \sum_{i=1}^{12} c_i\phi_i$ with, for example, $\phi_1 = (x^2-y^2)$. Following the same steps as explained in Appendix 10.B, we obtain now a system of twelve equations. The matrix A_{ij} can be computed explicitly. Contrary to the second order calculations, the virial theorem can no longer be used to reduce the number of unknown quantities so that the system now depends on $\langle r^2\rangle$, $\langle r^4\rangle$ and $\langle r^6\rangle$. In the matrix elements of the collision term, more parameters appear, generalizing the single parameter τ of the second order method.

After solving the system of equations numerically, we can express the quadrupole moment in terms of the coefficients c_i as :

$$Q(\omega) = \frac{4T}{3}\left[\frac{\langle r^2\rangle}{m\omega_0^2}c_1 + \frac{\langle r^4\rangle}{5}\left(\frac{7c_4}{m\omega_0^2}+3mc_5+mc_9\right)\right]. \tag{10.55}$$

Further details and explicit formulas for the matrix can be found in [81, 150].

Chapitre V

Perspectives

Dans les prochaines années, je pense poursuivre mes travaux dans les deux domaines présentés ici, c'est-à-dire les atomes piégés et les applications de la physique nucléaire aux étoiles à neutrons.

Gaz d'atomes piégés : Dynamique des gaz asymétriques

Mes travaux sur le mouvement collectif dans les gaz d'atomes piégés, décrits dans les chapitres III et IV, ne concernaient que des systèmes avec le même nombre d'atomes des deux états de spin $\uparrow$ et $\downarrow$. Dans les prochaines années, je pense également aborder les systèmes asymétriques, c'est-à-dire avec des densités $n_\uparrow$ et $n_\downarrow$ différentes. Ce projet sera étudié (en partie) en collaboration avec P.-A. Pantel, qui vient de commencer sa thèse à l'IPN de Lyon, et D. Davesne.

Une expérience intéressante dans ce contexte a récemment été réalisée au LKB (ENS Paris) [172]. Dans cette expérience, les modes de respiration axiaux d'un gaz polarisé ont été étudiés. Une première analyse théorique par Recati et al. [195], basée sur une approche de type fonctionelle de densité d'énergie et l'approximation de "scaling," n'a pas encore donné d'explication complète de l'expérience. Cette approche n'est valable que dans la phase normale, donc, à des polarisations très fortes où il ne reste même pas de cœur superfluide au centre du piège (limite de Chandrasekhar-Clogston) [38]. Pour la description des modes collectifs dans le cas où le cœur est superfluide, il existe un travail de Lazarides et al. [147]. Dans ce travail, l'hydrodynamique superfluide est utilisée pour le cœur, tandis que la partie extérieure est décrite par l'équation de Vlasov sans collisions. Cette approche n'est valable qu'à température nulle.

Afin de prendre en compte les effets de température, mon projet est de généraliser la théorie de transport de quasiparticules présentée dans la publication n° 9 [248] au cas asymétrique. Dans le régime d'interaction forte, on ne peut plus utiliser l'expression Hartree pour le champ moyen comme dans la réf. [248]. On pourra déterminer le champ moyen en utilisant la matrice T comme nous l'avons fait dans réf. [80] mais en généralisant au cas asymétrique. Un aspect important qui n'a encore jamais été étudié, même dans le cas non-polarisé, est l'inclusion des collisions entre quasiparticules dans cette théorie de transport. Pour cela, on pourra se fonder sur la littérature concernant un problème similaire dans l'hélium-3 superfluide [262].

Même dans le cas où le système n'est pas superfluide parce que la température est trop élevée, il peut être intéressant de considérer le degré de liberté de spin dans le mouvement collectif. Une expérience intéressante [227] à ce propos a consisté à étudier la collision de deux nuages d'atomes polarisés dans des sens opposées. Il a été montré que, dans un premier temps et selon la température, les nuages se repoussaient ou se traversaient, puis oscillaient. Ceci est un processus loin de l'équilibre que l'on ne peut pas décrire dans le cadre de la réponse linéaire.

Le code numérique pour la solution de l'équation de Boltzmann présenté dans la publication n° 10 [151] est bien adapté pour décrire des situations hors équilibre. Il peut facilement être généralisé pour traiter indépendamment les deux états de spin. Une première simulation par Goulko et al. utilisant un code très similaire [117] a montré que l'équation de Boltzmann est capable de reproduire qualitativement les deux régimes de répulsion et de transmission observés dans l'expérience [227], mais on est encore loin d'avoir expliqué cette expérience quantitativement. La question se pose notamment d'estimer l'effet du champ moyen, négligé dans [117], et qui, puisqu'il est attractif, devrait rendre la répulsion des deux gaz plus difficile.

Une possibilité supplémentaire pour créer une asymétrie, autre que la polarisation de spin, est d'avoir dans le piège des atomes de masse différente. Par exemple, on a ainsi piégé à Innsbruck des atomes de ^{6}Li (dans deux états de spin) et de ^{40}K (polarisé) dans le même piège [229]. Dans un premier temps on pourra se concentrer sur la modélisation du refroidissement du gaz de ^{40}K par le gaz de ^{6}Li, qui est un problème très complexe puisque le gaz de ^{6}Li est généralement dans la phase superfluide dans le régime d'interaction forte. Il sera intéressant également d'étudier les modes collectifs de ce mélange.

Étoiles à neutrons : Appariement et modes collectifs dans la croûte interne

Dans la publication n° 4 [137], nous avons discuté le cross-over BEC-BCS dans la matière nucléaire symétrique dans le cadre de la théorie de Nozières et Schmitt-Rink. Pour l'application aux étoiles à neutrons, il est évidemment nécessaire de généraliser cette étude au cas de la matière riche en neutrons.

J'ai récemment commencé à travailler avec S. Ramanan (actuellement à Chennai, Inde) sur ce sujet. Dans un premier temps, nous considérons la matière de neutrons. Dans ce cas précis, comme il n'existe pas d'état lié neutron-neutron, on reste toujours du côté BCS du crossover BEC-BCS. Cependant, à basse densité on se situe près de la limite unitaire et on s'attend donc à ce que les effets de corrélation sur la température critique soient importants. Pour décrire l'appariement neutron-neutron, nous utilisons une interaction de basse impulsion v_{low-k} [46]. Cette interaction n'est pas séparable, ce qui rend le calcul de la matrice T plus compliqué que dans notre travail sur la matière symétrique (on utilise la technique des vecteurs propres de Weinberg [265]). Pour étudier non seulement la température critique, mais également les propriétés de la matière dans la phase superfluide, il faudra aussi étendre l'étude à des températures en-dessous de T_c, comme cela a été fait pour décrire le cross-over BEC-BCS dans les atomes froids [184].

Dans la matière asymétrique, on pourra regarder l'appariement neutron-neutron, proton-proton, et neutron-proton. Dans notre travail sur la matière symétrique nous avons vu que les corrélations pouvaient avoir un effet sur l'instabilité liquide-gaz. Il sera intéressant d'étudier cela pour la matière asymétrique, notamment dans le contexte de la formation des étoiles à neutrons. Cependant, dans ce contexte, des corrélations de type α (deux neutrons et deux protons) sont probablement aussi très importants. Pour traiter ce problème difficile, on pourra se fonder sur le travail [225] de T. Sogo, qui est actuellement post-doc à l'IPN d'Orsay.

Un autre aspect qui m'intéresse sont les modes collectifs dans la croûte à basse température. L'approche hydrodynamique que nous avons développée dans la publication n° 7 [94] n'est peut-être pas précise au niveau quantitatif (parce que la longueur de cohérence ξ est trop élevée), mais on peut supposer que les résultats sont au moins qualitativement corrects (et pour décrire le refroidissement de l'étoile il n'est probablement pas nécessaire de connaître le spectre d'excitation avec tous ses détails et une très haute précision). Il sera intéressant d'étendre ce travail dans plusieurs directions.

Jusqu'à présent, notre étude s'est limitée à la géométrie de la phase lasagne. L'extension aux autres géométries, comme à la phase spaghetti et à la phase cristalline, sera donc nécessaire pour faire des calculs de la chaleur spécifique dans toute la croûte interne. Pour cela, il faudra résoudre numériquement les équations hydrodynamiques dans la cellule élémentaire du réseau avec des conditions aux bords de Bloch. Une autre grande limitation du modèle actuel est que nous avons négligé l'interaction coulombienne entre les protons.

Cependant, c'est cette interaction qui est responsable des oscillations du réseau (phonons) qui elles-mêmes contribuent pour une part importante à la chaleur spécifique [109]. Il faudra donc inclure l'interaction coulombienne dans l'équation d'accélération (équation d'Euler) des protons. On pourra ainsi décrire en même temps les phonons du réseau, les modes collectifs du gaz et les modes collectifs internes des clusters en tenant compte des couplages entre ces trois types excitations.

Mis á part les deux sujets explicitement décrits ci-dessus, il y a encore beaucoup d'autres questions à étudier, comme par exemple le transport de chaleur dans la croûte ou les propriétés des vortex dans le réseau cristallin. Pour conclure, je dirai que dans l'étude de la croûte interne des étoiles à neutrons, la physique nucléaire et la physique des solides se rencontrent et que c'est ce que je trouve le plus fascinant dans ce sujet. Je suis en effet convaincu qu'un échange entre différentes disciplines, comme c'est le cas des atomes froids et des étoiles à neutrons, est très bénéfique.

Bibliographie

[1] ABO-SHAEER, J. R., RAMAN, C., VOGELS, J. M., AND KETTERLE, W. Observation of Vortex Lattices in Bose-Einstein Condensates. *Science 292* (2001), 476–479.

[2] ABRAHAM, E. R. I., MCALEXANDER, W. I., GERTON, J. M., HULET, R. G., CÔTÉ, R., AND DALGARNO, A. Triplet s-wave resonance in ^{6}Li collisions and scattering lengths of ^{6}Li and ^{7}Li. *Phys. Rev. A 55*, 5 (1997), R3299–R3302.

[3] ABRIKOSOV, A. A. On the Magnetic Properties of Superconductors of the Second Group. *Sov. Phys. JETP 5* (1957), 1174–1182. translation from Zh. Eksp. i Teor. Fiz. 32, 1442 (1957).

[4] ABUKI, H., HATSUDA, T., AND ITAKURA, K. Structural change of Cooper pairs and momentum-dependent gap in color superconductivity. *Phys. Rev. D 65* (2002), 074014, arXiv:hep-ph/0109013.

[5] AGUILERA, D. N., CIRIGLIANO, V., PONS, J. A., REDDY, S., AND SHARMA, R. Superfluid Heat Conduction and the Cooling of Magnetized Neutron Stars. *Phys. Rev. Lett. 102*, 9 (2009), 091101.

[6] ALCOCK, C., FARHI, E., AND OLINTO, A. Strange stars. *Astrophys. J. 310* (1986), 261–272.

[7] ALDER, K., BOHR, A., HUUS, T., MOTTELSON, B., AND WINTHER, A. Study of Nuclear Structure by Electromagnetic Excitation with Accelerated Ions. *Rev. Mod. Phys. 28* (1956), 432–542.

[8] ALFORD, M. G. Color superconducting quark matter. *Ann. Rev. Nucl. Part. Sci. 51* (2001), 131–160, arXiv:hep-ph/0102047.

[9] ALFORD, M. G., BERGES, J., AND RAJAGOPAL, K. Unlocking color and flavor in superconducting strange quark matter. *Nucl. Phys. B 558* (1999), 219–242, arXiv:hep-ph/9903502.

[10] ALFORD, M. G., BERGES, J., AND RAJAGOPAL, K. Magnetic fields within color superconducting neutron star cores. *Nucl. Phys. B 571* (2000), 269–284, arXiv:hep-ph/9910254.

[11] ALFORD, M. G., RAJAGOPAL, K., REDDY, S., AND STEINER, A. W. The stability of strange star crusts and strangelets. *Phys. Rev. D 73* (2006), 114016, arXiv:hep-ph/0604134.

[12] ALFORD, M. G., RAJAGOPAL, K., AND WILCZEK, F. QCD at finite baryon density: Nucleon droplets and color superconductivity. *Phys. Lett. B 422* (1998), 247–256, arXiv:hep-ph/9711395.

[13] ALFORD, M. G., RAJAGOPAL, K., AND WILCZEK, F. Color-flavor locking and chiral symmetry breaking in high density QCD. *Nucl. Phys. B 537* (1999), 443–458, arXiv:hep-ph/9804403.

[14] ALTMEYER, A., RIEDL, S., KOHSTALL, C., WRIGHT, M. J., GEURSEN, R., BARTENSTEIN, M., CHIN, C., HECKER DENSCHLAG, J., AND GRIMM, R. Precision Measurements of Collective Oscillations in the BEC-BCS Crossover. *Phys. Rev. Lett. 98* (2007), 040401, arXiv:cond-mat/0609390.

[15] ALTMEYER, A., RIEDL, S., KOHSTALL, C., WRIGHT, M. J., HECKER DENSCHLAG, J., AND GRIMM, R. Note on "Collective Excitations of a Degenerate Gas at the BEC-BCS Crossover", Phys. Rev. Lett. 92, 203201 (2004). *ArXiv Condensed-matter e-prints* (2006), arXiv:cond-mat/0611285.

[16] ALTMEYER, A., RIEDL, S., WRIGHT, M. J., KOHSTALL, C., HECKER DENSCHLAG, J., AND GRIMM, R. Dynamics of a strongly interacting Fermi gas: The radial quadrupole mode. *Phys. Rev. A 76* (2007), 033610.

[17] ANDERSON, M. H., ENSHER, J. R., MATTHEWS, M. R., WIEMAN, C. E., AND CORNELL, E. A. Observation of Bose-Einstein Condensation in a Dilute Atomic Vapor. *Science 269*, 5221 (1995), 198–201.

[18] ANDERSON, P. W. Random-Phase Approximation in the Theory of Superconductivity. *Phys. Rev. 112*, 6 (1958), 1900–1916.

[19] ANDERSON, P. W., AND ITOH, N. Pulsar Glitches and Restlessness as a Hard Superfluidity Phenomenon. *Nature 256* (1975), 25.

[20] ANDERSSON, N., AND COMER, G. L. On the dynamics of superfluid neutron star cores. *Mon. Not. R. Astron. Soc. 328* (2001), 1129–1143, arXiv:astro-ph/0101193.

[21] ANDREEV, A. F., AND BASHKIN, E. P. Three-velocity hydrodynamics of superfluid solutions. *Sov. Phys. JETP 42* (1975), 164.

[22] ASTRAKHARCHIK, G. E., BORONAT, J., CASULLERAS, J., AND GIORGINI, S. Equation of State of a Fermi Gas in the BEC-BCS Crossover: A Quantum Monte Carlo Study. *Phys. Rev. Lett. 93*, 20 (2004), 200404.

[23] AVANCINI, S. S., BRITO, L., MARINELLI, J. R., MENEZES, D. P., DE MORAES, M. M. W., PROVIDÊNCIA, C., AND SANTOS, A. M. Nuclear "pasta" phase within density dependent hadronic models. *Phys. Rev. C 79*, 3 (2009), 035804.

[24] AVANCINI, S. S., BRITO, L., MENEZES, D. P., AND PROVIDÊNCIA, C. Instabilities in asymmetric nuclear matter. *Phys. Rev. C 70*, 1 (2004), 015203.

[25] AVANCINI, S. S., CHIACCHIERA, S., MENEZES, D. P., AND PROVIDENCIA, C. Warm pasta phase in the Thomas-Fermi approximation. *Phys. Rev. C 82* (2010), 055807.

[26] BAILIN, D., AND LOVE, A. Superfluidity and Superconductivity in Relativistic Fermion Systems. *Phys. Rep. 107* (1984), 325.

[27] BALDO, M., AND DUCOIN, C. Elementary excitations in homogeneous neutron star matter. *Phys. Rev. C 79*, 3 (2009), 035801.

[28] BALDO, M., AND DUCOIN, C. Plasmon excitations in homogeneous neutron star matter. *Phys. Atom. Nucl. 72* (2009), 1188–1196, arXiv:0902.2552.

[29] BALDO, M., LOMBARDO, U., AND SCHUCK, P. Deuteron formation in expanding nuclear matter from a strong coupling BCS approach. *Phys. Rev. C 52* (1995), 975–985.

[30] BARANOV, M. A., AND PETROV, D. S. Critical temperature and Ginzburg-Landau equation for a trapped Fermi gas. *Phys. Rev. A 58*, 2 (1998), R801–R804.

[31] BARANOV, M. A., AND PETROV, D. S. Low-energy collective excitations in a superfluid trapped Fermi gas. *Phys. Rev. A 62*, 4 (2000), 041601.

[32] BARDEEN, J., COOPER, L. N., AND SCHRIEFFER, J. R. Theory of Superconductivity. *Phys. Rev. 108* (1957), 1175–1204.

[33] BARROIS, B. C. Superconducting Quark Matter. *Nucl. Phys. B 129* (1977), 390.

[34] BARTENSTEIN, M., ALTMEYER, A., RIEDL, S., JOCHIM, S., CHIN, C., HECKER DENSCHLAG, J., AND GRIMM, R. Collective Excitations of a Degenerate Gas at the BEC-BCS Crossover. *Phys. Rev. Lett. 92*, 20 (2004), 203201.

[35] BARTENSTEIN, M., ALTMEYER, A., RIEDL, S., JOCHIM, S., CHIN, C., HECKER DENSCHLAG, J., AND GRIMM, R. Crossover from a Molecular Bose-Einstein Condensate to a Degenerate Fermi Gas. *Phys. Rev. Lett. 92*, 12 (2004), 120401.

[36] BAUR, S. K., BASU, S., DE SILVA, T. N., AND MUELLER, E. J. Theory of the normal-superfluid interface in population imbalanced Fermi gases. *Phys. Rev. A 79* (2009), 063628.

[37] BAUSMERTH, I., RECATI, A., AND STRINGARI, S. Destroying Superfluidity by Rotating a Fermi Gas at Unitarity. *Phys. Rev. Lett. 100*, 7 (2008), 070401.

[38] BAUSMERTH, I., RECATI, A., AND STRINGARI, S. Chandrasekhar-Clogston limit and phase separation in Fermi mixtures at unitarity. *Phys. Rev. A 79* (2009), 043622.

[39] BAYM, G., PETHICK, C., AND PINES, D. Superfluidity in Neutron Stars. *Nature 224* (1969), 673–674.

[40] BEDAQUE, P. F., CALDAS, H., AND RUPAK, G. Phase Separation in Asymmetrical Fermion Superfluids. *Phys. Rev. Lett. 91*, 24 (2003), 247002.

[41] BERGER, J. F., GIROD, M., AND GOGNY, D. Time-dependent quantum collective dynamics applied to nuclear fission. *Comp. Phys. Comm. 63*, 1-3 (1991), 365–374.

[42] BERTSCH, G., AND DAS GUPTA, S. A Guide to microscopic models for intermediate-energy heavy ion collisions. *Phys. Rep. 160* (1988), 189–233.

[43] BETBEDER-MATIBET, O., AND NOZIÈRES, P. Transport equations in clean superconductors. *Ann. Phys. (N.Y.) 51*, 3 (1969), 392–417.

[44] BHADURI, R. K. *Models of the Nucleon: From Quarks to Soliton*. Addison-Wesley, Redwood City, 1988.

[45] BODMER, A. R. Collapsed nuclei. *Phys. Rev. D 4* (1971), 1601–1606.

[46] BOGNER, S. K., FURNSTAHL, R. J., RAMANAN, S., AND A., S. Low-momentum interactions with smooth cutoffs. *Nucl. Phys. A 784* (2007), 79.

[47] BOHR, A., MOTTELSON, B. R., AND PINES, D. Possible Analogy between the Excitation Spectra of Nuclei and Those of the Superconducting Metallic State. *Phys. Rev. 110* (1958), 936–938.

[48] BORDERIE, B., AND RIVET, M. Nuclear multifragmentation and phase transition for hot nuclei. *Prog. Part. Nucl. Phys. 61*, 2 (2008), 551–601.

[49] BORUMAND, M., JOYNT, R., AND KLUŹNIAK, W. Superfluid densities in neutron-star matter. *Phys. Rev. C 54* (1996), 2745–2750.

[50] BOURDEL, T., KHAYKOVICH, L., CUBIZOLLES, J., ZHANG, J., CHEVY, F., TEICHMANN, M., TARRUELL, L., KOKKELMANS, S. J. J. M. F., AND SALOMON, C. Experimental Study of the BEC-BCS Crossover Region in Lithium 6. *Phys. Rev. Lett. 93*, 5 (2004), 050401.

[51] BOUYSSY, A., AND MAU, N. V. Particle-hole and particle-particle RPA ground state correlations and the Green function formalism. *Nucl. Phys. A 229*, 1 (1974), 1–14.

[52] BOUYSSY, A., AND MAU, N. V. Two-paritcle RPA for oxygen and calcium. *Nucl. Phys. A 224*, 2 (1974), 331–348.

[53] BOWERS, J. A., AND RAJAGOPAL, K. Crystallography of color superconductivity. *Phys. Rev. D 66*, 6 (2002), 065002.

[54] BOŻEK, P. Superfluid nuclear matter calculations. *Nucl. Phys. A 657*, 2 (1999), 187–215.

[55] BRADLEY, C. C., SACKETT, C. A., TOLLETT, J. J., AND HULET, R. G. Evidence of Bose-Einstein Condensation in an Atomic Gas with Attractive Interactions. *Phys. Rev. Lett. 75*, 9 (1995), 1687–1690.

[56] BREY, L., JOHNSON, N. F., AND HALPERIN, B. I. Optical and magneto-optical absorption in parabolic quantum wells. *Phys. Rev. B 40* (1989), 10647–10649.

[57] BROWN, E. F., AND CUMMING, A. Mapping crustal heating with the cooling lightcurves of quasi-persistent transients. *Astrophys. J. 698* (2009), 1020–1032.

[58] BRUDER, C., AND IMRY, Y. Orbital Paramagnetism of Electrons in Proximity to a Superconductor. *Phys. Rev. Lett. 80* (1998), 5782–5785.

[59] BRUUN, G., CASTIN, Y., DUM, R., AND BURNETT, K. BCS theory for trapped ultracold fermions. *Eur. Phys. J. D 7* (1999), 433–439.

[60] BRUUN, G. M. Effects of the trapping potential on a superfluid atomic Fermi gas. *Phys. Rev. A 66*, 4 (2002), 041602.

[61] BRUUN, G. M. Low-Energy Monopole Modes of a Trapped Atomic Fermi Gas. *Phys. Rev. Lett. 89*, 26 (2002), 263002.

[62] BRUUN, G. M., AND CLARK, C. W. Hydrodynamic Excitations of Trapped Fermi Gases. *Phys. Rev. Lett. 83* (1999), 5415–5418.

[63] BRUUN, G. M., AND HEISELBERG, H. Cooper pairing and single-particle properties of trapped Fermi gases. *Phys. Rev. A 65*, 5 (2002), 053407.

[64] BRUUN, G. M., AND MOTTELSON, B. R. Low Energy Collective Modes of a Superfluid Trapped Atomic Fermi Gas. *Phys. Rev. Lett. 87*, 27 (2001), 270403.

[65] BRUUN, G. M., AND SMITH, H. Frequency and damping of the scissors mode of a Fermi gas. *Phys. Rev. A 76* (2007), 045602.

[66] BUBALLA, M. NJL model analysis of quark matter at large density. *Phys. Rep. 407* (2005), 205–376, arXiv:hep-ph/0402234.

[67] BULGAC, A., AND YU, Y. Renormalization of the Hartree-Fock-Bogoliubov Equations in the Case of a Zero Range Pairing Interaction. *Phys. Rev. Lett. 88*, 4 (2002), 042504.

[68] CAO, L. G., LOMBARDO, U., AND SCHUCK, P. Screening effects in superfluid nuclear and neutron matter within Brueckner theory. *Phys. Rev. C 74* (2006), 064301.

[69] CARLSON, B. V., AND HIRATA, D. A Dirac-Hartree-Bogoliubov approximation for finite nuclei. *Phys. Rev. C 62* (2000), 054310, arXiv:nucl-th/0006006.

[70] CARLSON, J., CHANG, S.-Y., PANDHARIPANDE, V. R., AND SCHMIDT, K. E. Superfluid Fermi Gases with Large Scattering Length. *Phys. Rev. Lett. 91*, 5 (2003), 050401.

[71] CARLSON, J., AND REDDY, S. Asymmetric Two-Component Fermion Systems in Strong Coupling. *Phys. Rev. Lett. 95*, 6 (2005), 060401, arXiv:cond-mat/0503256.

[72] CARTER, B., AND CHACHOUA, E. Newtonian mechanics of neutron superfluid in elastic star crust. *Int. J. Mod. Phys. D 15* (2006), 1329–1358, arXiv:astro-ph/0601658.

[73] CARTER, B., CHAMEL, N., AND HAENSEL, P. Effect of BCS pairing on entrainment in neutron superfluid current in neutron star crust. *Nucl. Phys. A 759* (2005), 441–464, arXiv:astro-ph/0406228.

[74] CARTER, B., AND LANGLOIS, D. Relativistic models for superconducting-superfluid mixtures. *Nucl. Phys. B 531* (1998), 478–504, arXiv:gr-qc/9806024.

[75] CARTER, B., AND SAMUELSSON, L. Relativistic mechanics of neutron superfluid in (magneto) elastic star crust. *Class. Quant. Grav. 23* (2006), 5367–5388, arXiv:gr-qc/0605024.

[76] CASALBUONI, R., AND NARDULLI, G. Inhomogeneous superconductivity in condensed matter and QCD. *Rev. Mod. Phys. 76*, 1 (2004), 263–320.

[77] CASTORINA, P., GRASSO, M., OERTEL, M., URBAN, M., AND ZAPPALÀ, D. Nonstandard pairing in asymmetric trapped Fermi gases. *Phys. Rev. A 72* (2005), 025601.

[78] CHAMEL, N., AND HAENSEL, P. Entrainment parameters in a cold superfluid neutron star core. *Phys. Rev. C 73*, 4 (2006), 045802.

[79] CHAMEL, N., AND HAENSEL, P. Physics of Neutron Star Crusts. *Living Reviews in Relativity 11* (2008), 10, arXiv:0812.3955.

[80] CHIACCHIERA, S., LEPERS, T., DAVESNE, D., AND URBAN, M. Collective modes of trapped Fermi gases with in-medium interaction. *Phys. Rev. A 79* (2009), 033613.

[81] CHIACCHIERA, S., LEPERS, T., DAVESNE, D., AND URBAN, M. Role of fourth-order phase-space moments in collective modes of trapped Fermi gases. *Phys. Rev. A 84* (2011), 043634.

[82] CHIN, C., BARTENSTEIN, M., ALTMEYER, A., RIEDL, S., JOCHIM, S., HECKER DENSCHLAG, J., AND GRIMM, R. Observation of the Pairing Gap in a Strongly Interacting Fermi Gas. *Science 305*, 5687 (2004), 1128–1130.

[83] CHODOS, A., JAFFE, R. L., JOHNSON, K., THORN, C. B., AND WEISSKOPF, V. F. A New Extended Model of Hadrons. *Phys. Rev. D 9* (1974), 3471–3495.

[84] CHOMAZ, P., COLONNA, M., AND RANDRUP, J. Nuclear spinodal fragmentation. *Phys. Rep. 389*, 5-6 (2004), 263–440.

[85] CIRIGLIANO, V., REDDY, S., AND SHARMA, R. A low energy theory for superfluid and solid matter and its application to the neutron star crust. *ArXiv Nuclear Theory e-prints* (2011), arXiv:1102.5379.

[86] COLLINS, J. C., AND PERRY, M. J. Superdense Matter: Neutrons Or Asymptotically Free Quarks? *Phys. Rev. Lett. 34* (1975), 1353.

[87] COMBESCOT, R., AND MORA, C. The low-temperature Fulde-Ferrell-Larkin-Ovchinnikov phases in 3 dimensions. *Europhys. Lett. 68*, 1 (2004), 79.

[88] COZZINI, M., AND STRINGARI, S. Fermi Gases in Slowly Rotating Traps: Superfluid versus Collisional Hydrodynamics. *Phys. Rev. Lett. 91*, 7 (2003), 070401.

[89] DAVIS, K. B., MEWES, M. O., ANDREWS, M. R., VAN DRUTEN, N. J., DURFEE, D. S., KURN, D. M., AND KETTERLE, W. Bose-Einstein Condensation in a Gas of Sodium Atoms. *Phys. Rev. Lett. 75*, 22 (1995), 3969–3973.

[90] DE GENNES, P. G. *Superconductivity of Metals and Alloys*. Benjamin, New York, 1966.

[91] DECHARGÉ, J., AND GOGNY, D. Hartree-Fock-Bogolyubov calculations with the D1 effective interaction on spherical nuclei. *Phys. Rev. C 21* (1980), 1568–1593.

[92] DEMARCO, B., AND JIN, D. S. Onset of Fermi Degeneracy in a Trapped Atomic Gas. *Science 285*, 5434 (1999), 1703–1706.

[93] DEMARCO, B., PAPP, S. B., AND JIN, D. S. Pauli Blocking of Collisions in a Quantum Degenerate Atomic Fermi Gas. *Phys. Rev. Lett. 86*, 24 (2001), 5409–5412.

[94] DI GALLO, L., OERTEL, M., AND URBAN, M. Collective excitations in the neutron star inner crust. *Phys. Rev. C 84* (2011), 045801, http://arxiv.org/abs/1107.4209.

[95] DI TORO, M., AND KOLOMIETZ, V. M. A semiclassical approach to pairing vibrations and pairing correlation effects on giant resonances. *Z. Physik A 328*, 3 (1987), 285–290.

[96] DURAND, M., SCHUCK, P., AND KUNZ, J. Semiclassical description of currents in normal and superfluid rotating nuclei. *Nucl. Phys. A 439*, 2 (1985), 263–288.

[97] ELLIOTT, J. B., MORETTO, L. G., PHAIR, L., WOZNIAK, G. J., ALBERGO, S., BIESER, F., BRADY, F. P., CACCIA, Z., CEBRA, D. A., CHACON, A. D., CHANCE, J. L., CHOI, Y., COSTA, S., GILKES, M. L., HAUGER, J. A., HIRSCH, A. S., HJORT, E. L., INSOLIA, A., JUSTICE, M., KEANE, D., KINTNER, J. C., LINDENSTRUTH, V., LISA, M. A., MATIS, H. S., MCMAHAN, M., MCPARLAND, C., MÜLLER, W. F. J., OLSON, D. L., PARTLAN, M. D., PORILE, N. T., POTENZA, R., RAI, G., RASMUSSEN, J., RITTER, H. G., ROMANSKI, J., ROMERO, J. L., RUSSO, G. V., SANN, H., SCHARENBERG, R. P., SCOTT, A., SHAO, Y., SRIVASTAVA, B. K., SYMONS, T. J. M., TINCKNELL, M., TUVÉ, C., WANG, S., WARREN, P., WIEMAN, H. H., WIENOLD, T., AND WOLF, K. Constructing the phase diagram of finite neutral nuclear matter. *Phys. Rev. C 67* (2003), 024609.

[98] ELLIOTT, J. B., MORETTO, L. G., PHAIR, L., WOZNIAK, G. J., BEAULIEU, L., BREUER, H., KORTELING, R. G., KWIATKOWSKI, K., LEFORT, T., PIENKOWSKI, L., RUANGMA, A., VIOLA, V. E., AND YENNELLO, S. J. Liquid to Vapor Phase Transition in Excited Nuclei. *Phys. Rev. Lett. 88* (2002), 042701.

[99] EPSTEIN, R. I. Acoustic properties of neutron stars. *Astrophys. J. 333* (1988), 880–894.

[100] ETHOFER, S. On the microscopic description of nuclei at high spins. *Z. Phys. A 271*, 2 (1974), 169–175.

[101] EVANS, N. J., HORMUZDIAR, J., HSU, S. D. H., AND SCHWETZ, M. On the QCD ground state at high density. *Nucl. Phys. B 581* (2000), 391–408, arXiv:hep-ph/9910313.

[102] F., G.-M., AND F., F. *Introduction to the theory of solid surfaces*. Cambridge University Press, Cambridge, 1979.

[103] FARHI, E., AND JAFFE, R. L. Strange Matter. *Phys. Rev. D 30* (1984), 2379.

[104] FARINE, M., HEKKING, F. W. J., SCHUCK, P., AND VIÑAS, X. Generic finite-size enhancement of pairing in mesoscopic Fermi systems. *Phys. Rev. B 68*, 2 (2003), 024507, arXiv:cond-mat/0207297.

[105] FARINE, M., SCHUCK, P., AND VIÑAS, X. Moment of inertia of a trapped superfluid gas of atomic fermions. *Phys. Rev. A 62*, 1 (2000), 013608.

[106] FETTER, A. L., AND WALECKA, J. D. *Quantum Theory of Many-Particle Systems*. McGraw-Hill, New York, 1971.

[107] FEYNMAN, R. Application of Quantum Mechanics to Liquid Helium. In *Progress in Low Temperature Physics* (1955), C. J. Gorter, Ed., vol. 1, North-Holland, Amsterdam, pp. 17–53.

[108] FLOQUET, G. Sur les équations différentielles linéaires à coéfficients périodiques. *Ann. Sci. École Normale Supérieure 12* (1883), 47–88.

[109] FORTIN, M., GRILL, F., MARGUERON, J., PAGE, D., AND SANDULESCU, N. Thermalization time and specific heat of the neutron stars crust. *Phys. Rev. C 82*, 6 (2010), 065804.

[110] FRAUTSCHI, S. C. Asymptotic Freedom And Color Superconductivity In Dense Quark Matter. In *Proceedings of the Workshop on Hadronic Matter at Extreme Energy Density, Erice, 1978* (1978), N. Cabibbo, Ed., Plenum Press, New York.

[111] FULDE, P., AND FERRELL, R. A. Superconductivity in a Strong Spin-Exchange Field. *Phys. Rev. 135*, 3A (1964), A550–A563.

[112] GAITANOS, T., DI TORO, M., TYPEL, S., BARAN, V., FUCHS, C., GRECO, V., AND WOLTER, H. H. On the Lorentz structure of the symmetry energy. *Nucl. Phys. A 732* (2004), 24–48.

[113] GEZERLIS, A., AND CARLSON, J. Low-density neutron matter. *Phys. Rev. C 81* (2010), 025803, arXiv:0911.3907.

[114] GILSON, E. P., AND JAFFE, R. L. Very small strangelets. *Phys. Rev. Lett. 71* (1993), 332–335, arXiv:hep-ph/9302270.

[115] GNEDIN, O. Y., YAKOVLEV, D. G., AND POTEKHIN, A. Y. Thermal relaxation in young neutron stars. *Mon. Not. R. Astron. Soc. 324* (2001), 725–736, arXiv:astro-ph/0012306.

[116] GONZÁLEZ TROTTER, D. E., SALINAS, F., CHEN, Q., CROWELL, A. S., GLÖCKLE, W., HOWELL, C. R., ROPER, C. D., SCHMIDT, D., ŠLAUS, I., TANG, H., TORNOW, W., WALTER, R. L., WITAŁA, H., AND ZHOU, Z. New Measurement of the ${}^1S_0$ Neutron-Neutron Scattering Length Using the Neutron-Proton Scattering Length as a Standard. *Phys. Rev. Lett. 83* (1999), 3788–3791.

[117] GOULKO, O., CHEVY, F., AND LOBO, C. Collision of two spin polarized fermionic clouds. *ArXiv Condensed Matter e-prints* (2011), arXiv:1106.5773.

[118] GRASSO, M., KHAN, E., AND URBAN, M. Temperature dependence and finite-size effects in collective modes of superfluid-trapped Fermi gases. *Phys. Rev. A 72* (2005), 043617.

[119] GRASSO, M., AND URBAN, M. Hartree-Fock-Bogoliubov theory versus local-density approximation for superfluid trapped fermionic atoms. *Phys. Rev. A 68*, 3 (2003), 033610.

[120] GRASSO, M., URBAN, M., AND VIÑAS, X. Microscopic description of the twist mode in normal and superfluid trapped Fermi gases. *Phys. Rev. A 71*, 1 (2005), 013603.

[121] GRÉGOIRE, C., REMAUD, B., SÉBILLE, F., VINET, L., AND RAFFRAY, Y. Semi-classical dynamics of heavy-ion reactions. *Nucl. Phys. A 465*, 2 (1987), 317–338.

[122] GREINER, M., REGAL, C. A., AND JIN, D. S. Emergence of a molecular Bose-Einstein condensate from a Fermi gas. *Nature 426* (2003), 537–540.

[123] GRIN', Y. T., AND LARKIN, A. I. Nuclear Rotational Spectra at High Momenta. *Sov. J. Nucl. Phys. 2*, 1 (1966), 27–34. translation from J. Nucl. Phys. (U.S.S.R.) 2, 40-50 (1965).

[124] GULMINELLI, F., AND SCHUCK, P. Semiclassical transport model with pairing. Unpublished notes.

[125] GUSAKOV, M. E., AND HAENSEL, P. The entrainment matrix of a superfluid neutron proton mixture at a finite temperature. *Nucl. Phys. A 761* (2005), 333–348, arXiv:astro-ph/0508104.

[126] GUSAKOV, M. E., KANTOR, E. M., AND HAENSEL, P. Relativistic entrainment matrix of a superfluid nucleon-hyperon mixture: The zero temperature limit. *Phys. Rev. C 79*, 5 (2009), 055806, arXiv:0904.3467.

[127] HAENSEL, P., ZDUNIK, J. L., AND SCHAEFFER, R. Strange quark stars. *Astron. Astrophys. 160* (1986), 121–128.

[128] HASHIMOTO, M., SEKI, H., AND YAMADA, M. Shape of nuclei in the crust of a neutron star. *Prog. Theor. Phys. 71* (1984), 320–326.

[129] HEISELBERG, H. Fermi systems with long scattering lengths. *Phys. Rev. A 63*, 4 (2001), 043606.

[130] HEYER, J., KUO, T., SHEN, J., AND WU, S. Finite-temperature density-dependent HF calculation of nuclear matter with gogny interaction. *Phys. Lett. B 202*, 4 (1988), 465–469.

[131] HOUBIERS, M., FERWERDA, R., STOOF, H. T. C., MCALEXANDER, W. I., SACKETT, C. A., AND HULET, R. G. Superfluid state of atomic ^{6}Li in a magnetic trap. *Phys. Rev. A 56*, 6 (1997), 4864–4878.

[132] HUANG, K. *Statistical Mechanics*. Wiley, New York, 1987.

[133] HUANG, M. Color superconductivity at moderate baryon density. *Int. J. Mod. Phys. E 14* (2005), 675, arXiv:hep-ph/0409167.

[134] JACKSON, B., AND ZAREMBA, E. Modeling Bose-Einstein condensed gases at finite temperatures with N-body simulations. *Phys. Rev. A 66* (2002), 033606.

[135] JAIKUMAR, P., REDDY, S., AND STEINER, A. W. The strange star surface: A crust with nuggets. *Phys. Rev. Lett. 96* (2006), 041101, arXiv:nucl-th/0507055.

[136] JIANG, M. F., HEYER, J., YANG, S. D., AND KUO, T. T. S. Collapse of Ring Diagrams and Nuclear-Matter Phase Transitions. *Phys. Rev. Lett. 61* (1988), 38–41.

[137] JIN, M., URBAN, M., AND SCHUCK, P. BEC-BCS crossover and the liquid-gas phase transition in hot and dense nuclear matter. *Phys. Rev. C 82* (2010), 024911.

[138] KHAN, E., SANDULESCU, N., AND GIAI, N. V. Collective excitations in the inner crust of neutron stars: Supergiant resonances. *Phys. Rev. C 71*, 4 (2005), 042801.

[139] KINAST, J., HEMMER, S. L., GEHM, M. E., TURLAPOV, A., AND THOMAS, J. E. Evidence for Superfluidity in a Resonantly Interacting Fermi Gas. *Phys. Rev. Lett. 92*, 15 (2004), 150402.

[140] KINAST, J., TURLAPOV, A., AND THOMAS, J. E. Breakdown of hydrodynamics in the radial breathing mode of a strongly interacting Fermi gas. *Phys. Rev. A 70* (2004), 051401.

[141] KOHN, W. Cyclotron Resonance and de Haas-van Alphen Oscillations of an Interacting Electron Gas. *Phys. Rev. 123* (1961), 1242–1244.

[142] KONTOS, T., APRILI, M., LESUEUR, J., AND GRISON, X. Inhomogeneous Superconductivity Induced in a Ferromagnet by Proximity Effect. *Phys. Rev. Lett. 86*, 2 (2001), 304–307.

[143] LAHEURTE, J. P., WILLIAMS, G. A., DANDACHE, H., AND ZOAETER, M. Boundary conditions at the liquid-vapor interface of superfluid ^{3}He-^{4}He mixtures. *Phys. Rev. B 28*, 11 (1983), 6585–6588.

[144] LANDAU, L. D., AND LIFSHITZ, E. M. *Quantum Mechanics*. No. 3 in Landau Lifshitz Course of Theoretical Physics. Pergamon, London, 1958.

[145] LANDAU, L. D., AND LIFSHITZ, E. M. *Statistical Physics, Part 1*. No. 5 in Landau Lifshitz Course of Theoretical Physics. Pergamon, Oxford, 1967.

[146] LARKIN, A. I., AND OVCHINNIKOV, Y. N. Nonuniform state of superconductors. *Sov. Phys. JETP 20* (1965), 762.

[147] LAZARIDES, A., AND VAN SCHAEYBROECK, B. Collective oscillations of trapped imbalanced fermion gases. *Phys. Rev. A 77* (2008), 041602(R).

[148] LEGGETT, A. J. Theory of a Superfluid Fermi Liquid. I. General Formalism and Static Properties. *Phys. Rev. 140*, 6A (1965), A1869–A1888.

[149] LEGGETT, A. J. Theory of a Superfluid Fermi Liquid. II. Collective Oscillations. *Phys. Rev. 147*, 1 (1966), 119–130.

[150] LEPERS, T. *Étude dynamique des modes collectifs dans les gaz de fermions froids*. PhD thesis, Université Claude-Bernard Lyon-I, 2010.

[151] LEPERS, T., DAVESNE, D., CHIACCHIERA, S., AND URBAN, M. Numerical solution of the Boltzmann equation for the collective modes of trapped Fermi gases. *Phys. Rev. A 82* (2010), 023609.

[152] LIFSHITZ, E. M., AND PITAEVSKII, L. P. *Physical Kinetics*. No. 10 in Landau Lifshitz Course of Theoretical Physics. Pergamon, Oxford, 1980.

[153] LIFSHITZ, E. M., AND PITAEVSKII, L. P. *Statistical Physics, Part 2: Theory of the Condensed State*. No. 9 in Landau Lifshitz Course of Theoretical Physics. Pergamon, Oxford, 1980.

[154] LITIM, D. F., AND MANUEL, C. Photon self-energy in a color superconductor. *Phys. Rev. D 64* (2001), 094013, arXiv:hep-ph/0105165.

[155] LIU, W. V., AND WILCZEK, F. Interior Gap Superfluidity. *Phys. Rev. Lett. 90*, 4 (2003), 047002, arXiv:cond-mat/0208052.

[156] LOMBARDO, U., NOZIÈRES, P., SCHUCK, P., SCHULZE, H.-J., AND SEDRAKIAN, A. Transition from BCS pairing to Bose-Einstein condensation in low-density asymmetric nuclear matter. *Phys. Rev. C 64*, 6 (2001), 064314.

[157] LOMBARDO, U., AND SCHULZE, H. J. Superfluidity in Neutron Star Matter. *Lect. Notes Phys. 578* (2001), 30–53, arXiv:astro-ph/0012209.

[158] MA, Y. G. Cluster emission and phase transition behaviours in nuclear disassembly. *J. Phys. G 27*, 12 (2001), 2455.

[159] MA, Y. G., NATOWITZ, J. B., WADA, R., HAGEL, K., WANG, J., KEUTGEN, T., MAJKA, Z., MURRAY, M., QIN, L., SMITH, P., ALFARO, R., CIBOR, J., CINAUSERO, M., MASRI, Y. E., FABRIS, D., FIORETTO, E., KEKSIS, A., LUNARDON, M., MAKEEV, A., MARIE, N., MARTIN, E., MARTINEZ-DAVALOS, A., MENCHACA-ROCHA, A., NEBBIA, G., PRETE, G., RIZZI, V., RUANGMA, A., SHETTY, D. V., SOULIOTIS, G., STASZEL, P., VESELSKY, M., VIESTI, G., WINCHESTER, E. M., AND YENNELLO, S. J. Critical behavior in light nuclear systems: Experimental aspects. *Phys. Rev. C 71* (2005), 054606.

[160] MADISON, K. W., CHEVY, F., WOHLLEBEN, W., AND DALIBARD, J. Vortex Formation in a Stirred Bose-Einstein Condensate. *Phys. Rev. Lett. 84*, 5 (2000), 806–809.

[161] MADISON, K. W., CHEVY, F., WOHLLEBEN, W., AND DALIBARD, J. Vortices in a stirred Bose-Einstein condensate. *Journal of Modern Optics 47*, 14–15 (2000), 2715–2723.

[162] MADSEN, J. Color-flavor locked strangelets. *Phys. Rev. Lett. 87* (2001), 172003, hep-ph/0108036.

[163] MADSEN, J. Strangelets in cosmic rays. *ArXiv Astrophysics e-prints* (2006), arXiv:astro-ph/0612784.

[164] MADSEN, J., AND LARSEN, J. M. Strangelets as Cosmic Rays beyond the Greisen-Zatsepin- Kuzmin Cutoff. *Phys. Rev. Lett. 90* (2003), 121102, arXiv:astro-ph/0211597.

[165] MARGUERON, J. *Effets du milieu sur la propagation des neutrinos dans la matière nucléaire*. PhD thesis, Université Paris-Sud XI, 2001.

[166] MARUYAMA, T., YABU, H., AND SUZUKI, T. Monopole oscillations and dampings in a boson and fermion mixture in the time-dependent Gross-Pitaevskii and Vlasov equations. *Phys. Rev. A 72* (2005), 013609.

[167] MASSIGNAN, P., BRUUN, G. M., AND SMITH, H. Viscous relaxation and collective oscillations in a trapped Fermi gas near the unitarity limit. *Phys. Rev. A 71* (2005), 033607.

[168] MENOTTI, C., PEDRI, P., AND STRINGARI, S. Expansion of an Interacting Fermi Gas. *Phys. Rev. Lett. 89*, 25 (2002), 250402, arXiv:cond-mat/0208150.

[169] MIGDAL, A. B. Superfluidity and the moments of inertia of nuclei. *Nucl. Phys. 13*, 5 (1959), 655–674.

[170] MIZUSHIMA, T., MACHIDA, K., AND ICHIOKA, M. Direct Imaging of Spatially Modulated Superfluid Phases in Atomic Fermion Systems. *Phys. Rev. Lett. 94*, 6 (2005), 060404.

[171] NASCIMBÈNE, S., NAVON, N., JIANG, K. J., CHEVY, F., AND SALOMON, C. Exploring the thermodynamics of a universal Fermi gas. *Nature 463* (2010), 1057–1060.

[172] NASCIMBÈNE, S., NAVON, N., JIANG, K. J., TARRUELL, L., TEICHMANN, M., MCKEEVER, J., CHEVY, F., AND SALOMON, C. Collective Oscillations of an Imbalanced Fermi Gas: Axial Compression Modes and Polaron Effective Mass. *Phys. Rev. Lett. 103* (2009), 170402.

[173] NEGELE, J. W., AND VAUTHERIN, D. Neutron star matter at subnuclear densities. *Nucl. Phys. A 207* (1973), 298–320.

[174] NOZIÈRES, P., AND SCHMITT-RINK, S. Bose condensation in an attractive fermion gas: From weak to strong coupling superconductivity. *J. Low Temp. Phys. 59* (1985), 195–211.

[175] NYGAARD, N., BRUUN, G. M., CLARK, C. W., AND FEDER, D. L. Microscopic Structure of a Vortex Line in a Dilute Superfluid Fermi Gas. *Phys. Rev. Lett. 90*, 21 (2003), 210402.

[176] OERTEL, M., AND URBAN, M. Surface effects in color superconducting strange-quark matter. *Phys. Rev. D 77* (2008), 074015.

[177] O'HARA, K. M., HEMMER, S. L., GEHM, M. E., GRANADE, S. R., AND THOMAS, J. E. Observation of a Strongly Interacting Degenerate Fermi Gas of Atoms. *Science 298*, 5601 (2002), 2179–2182.

[178] OHASHI, Y., AND GRIFFIN, A. Collective modes and the effect of single-particle excitations in the BCS-BEC crossover region of a trapped Fermi superfluid. *ArXiv Condensed Matter e-prints* (2005), arXiv:cond-mat/0503641.

[179] OYAMATSU, K. Nuclear shapes in the inner crust of a neutron star. *Nucl. Phys. A 561*, 3 (1993), 431–452.

[180] PAGE, D., AND USOV, V. V. Thermal Evolution and Light Curves of Young Bare Strange Stars. *Phys. Rev. Lett. 89* (2002), 131101, arXiv:astro-ph/0204275.

[181] PARIJA, B. C. Dynamical effects of quantum chromodynamics on the surface tension of a cold strange quark nugget. *Phys. Rev. C 48* (1993), 2483–2490.

[182] PARTRIDGE, G. B., LI, W., LIAO, Y. A., HULET, R. G., HAQUE, M., AND STOOF, H. T. C. Deformation of a Trapped Fermi Gas with Unequal Spin Populations. *Phys. Rev. Lett. 97* (2006), 190407.

[183] PEDRI, P., GUÉRY-ODELIN, D., AND STRINGARI, S. Dynamics of a classical gas including dissipative and mean-field effects. *Phys. Rev. A 68* (2003), 043608.

[184] PERALI, A., PIERI, P., PISANI, L., AND STRINATI, G. C. BCS-BEC Crossover at Finite Temperature for Superfluid Trapped Fermi Atoms. *Phys. Rev. Lett. 92*, 22 (2004), 220404.

[185] PERALI, A., PIERI, P., STRINATI, G. C., AND CASTELLANI, C. Pseudogap and spectral function from superconducting fluctuations to the bosonic limit. *Phys. Rev. B 66*, 2 (2002), 024510.

[186] PETHICK, C. J., CHAMEL, N., AND REDDY, S. Superfluid Dynamics in Neutron Star Crusts. *Prog. Theor. Phys. Suppl. 186* (2010), 9–16, arXiv:1009.2303.

[187] PETHICK, C. J., AND RAVENHALL, D. G. Matter at large neutron excess and the physics of neutron-star crusts. *Ann. Rev. Nucl. Part. Sci. 45* (1995), 429–484.

[188] PIERI, P., PISANI, L., AND STRINATI, G. C. Comparison between a diagrammatic theory for the BCS-BEC crossover and quantum Monte Carlo results. *Phys. Rev. B 72* (2005), 012506.

[189] PRESS, W. H., TEUKOLSKY, S. A., VETTERLING, W. T., AND FLANNERY, B. P. *Numerical Recipes in FORTRAN: The Art of Scientific Computing*, second ed. Cambridge University Press, 1992.

[190] PRIX, R. Variational description of multifluid hydrodynamics: Uncharged fluids. *Phys. Rev. D 69*, 4 (2004), 043001.

[191] RAJAGOPAL, K., AND WILCZEK, F. The Condensed Matter Physics of QCD. In *At the Frontier of Particle Physics / Handbook of QCD*, M. Shifman, Ed., vol. 3. World Scientific, 2001, ch. 35, pp. 2061–2151, arXiv:hep-ph/0011333.

[192] RAJAGOPAL, K., AND WILCZEK, F. Enforced electrical neutrality of the color-flavor locked phase. *Phys. Rev. Lett. 86* (2001), 3492–3495, arXiv:hep-ph/0012039.

[193] RAPP, R., SCHÄFER, T., SHURYAK, E. V., AND VELKOVSKY, M. Diquark Bose condensates in high density matter and instantons. *Phys. Rev. Lett. 81* (1998), 53–56, arXiv:hep-ph/9711396.

[194] RAVENHALL, D. G., PETHICK, C. J., AND WILSON, J. R. Structure of Matter below Nuclear Saturation Density. *Phys. Rev. Lett. 50* (1983), 2066–2069.

[195] RECATI, A., AND STRINGARI, S. Spin oscillations of the normal polarized Fermi gas at unitarity. *Phys. Rev. A 82* (2010), 013635.

[196] REGAL, C. A., GREINER, M., AND JIN, D. S. Observation of Resonance Condensation of Fermionic Atom Pairs. *Phys. Rev. Lett. 92*, 4 (2004), 040403.

[197] REN, H.-C. Color superconductivity of QCD at high baryon density. *ArXiv High-Energy Physics–Phenomenology e-prints* (2004), arXiv:hep-ph/0404074.

[198] RIEDL, S. A rotating strongly interacting Fermi gas. Talk given at "Joint Meeting Innsbruck-Trento on Ultracold Bose and Fermi Gases", IQOQI, Innsbruck, 2007.

[199] RIEDL, S., SÁNCHEZ GUAJARDO, E. R., KOHSTALL, C., ALTMEYER, A., WRIGHT, M. J., HECKER DENSCHLAG, J., GRIMM, R., BRUUN, G. M., AND SMITH, H. Collective oscillations of a Fermi gas in the unitarity limit: Temperature effects and the role of pair correlations. *Phys. Rev. A 78* (2008), 053609.

[200] RIEDL, S., SÁNCHEZ GUAJARDO, E. R., KOHSTALL, C., HECKER DENSCHLAG, J., AND GRIMM, R. Superfluid quenching of the moment of inertia in a strongly interacting Fermi gas. *New J. Phys. 13*, 3 (2011), 035003.

[201] RING, P., AND SCHUCK, P. *The nuclear many-body problem*. Springer-Verlag, Berlin, 1980.

[202] RIOS, A., POLLS, A., RAMOS, A., AND MÜTHER, H. Liquid-gas phase transition in nuclear matter from realistic many-body approaches. *Phys. Rev. C 78* (2008), 044314.

[203] RISCHKE, D. H. The quark-gluon plasma in equilibrium. *Prog. Part. Nucl. Phys. 52* (2004), 197–296, arXiv:nucl-th/0305030.

[204] ROBERTS, J. L., CLAUSSEN, N. R., CORNISH, S. L., DONLEY, E. A., CORNELL, E. A., AND WIEMAN, C. E. Controlled Collapse of a Bose-Einstein Condensate. *Phys. Rev. Lett. 86*, 19 (2001), 4211–4214.

[205] RÖPKE, G., SCHMIDT, M., MÜNCHOW, L., AND SCHULZ, H. Particle clustering and Mott transition in nuclear matter at finite temperature (II): Self-consistent ladder Hartree-Fock approximation and model calculations for cluster abundances and the phase diagram. *Nucl. Phys. A 399*, 2 (1983), 587–602.

[206] RYBCZYNSKI, M., WLODARCZYK, Z., AND WILK, G. Strangelets in cosmic rays. *Nucl. Phys. Proc. Suppl. 151* (2006), 341–344, arXiv:hep-ph/0410064.

[207] SÁ DE MELO, C. A. R., RANDERIA, M., AND ENGELBRECHT, J. R. Crossover from BCS to Bose superconductivity: Transition temperature and time-dependent Ginzburg-Landau theory. *Phys. Rev. Lett. 71*, 19 (1993), 3202–3205.

[208] SANDULESCU, N. Nuclear superfluidity and specific heat in the inner crust of neutron stars. *Phys. Rev. C 70*, 2 (2004), 025801.

[209] SARMA, G. On the influence of a uniform exchange field acting on the spins of the conduction electrons in a superconductor. *J. Phys. Chem. Solids 24*, 8 (1963), 1029–1032.

[210] SCHÄFER, T. Patterns of symmetry breaking in QCD at high baryon density. *Nucl. Phys. B 575* (2000), 269–284, arXiv:hep-ph/9909574.

[211] SCHÄFER, T. Quark matter. In *Mesons and Quarks* (2004), A. B. Santra, S. Kailas, and R. S. Bhalerao, Eds., Narosa Publishing House, p. 185, arXiv:hep-ph/0304281.

[212] SCHMIDT, M., RÖPKE, G., AND SCHULZ, H. Generalized Beth-Uhlenbeck approach for hot nuclear matter. *Ann. Phys. (N.Y.) 202*, 1 (1990), 57–99.

[213] SCHMITT, A., WANG, Q., AND RISCHKE, D. H. Mixing and screening of photons and gluons in a color superconductor. *Phys. Rev. D 69* (2004), 094017, arXiv:nucl-th/0311006.

[214] SCHRECK, F., FERRARI, G., CORWIN, K. L., CUBIZOLLES, J., KHAYKOVICH, L., MEWES, M.-O., AND SALOMON, C. Sympathetic cooling of bosonic and fermionic lithium gases towards quantum degeneracy. *Phys. Rev. A 64*, 1 (2001), 011402.

[215] SEDRAKIAN, A., AND LOMBARDO, U. Thermodynamics of a $n-p$ Condensate in Asymmetric Nuclear Matter. *Phys. Rev. Lett. 84*, 4 (2000), 602–605.

[216] SEDRAKIAN, A., MUR-PETIT, J., POLLS, A., AND MÜTHER, H. Deformed Fermi surfaces in ultracold Fermi gases. *ArXiv Condensed Matter e-prints* (2004), arXiv:cond-mat/0404577.

[217] SEDRAKIAN, A. D. Neutron-Phonon Interaction in Neutron Stars: Phonon Spectrum of Coulomb Lattice. *Astrophys. Space Sci. 236* (1996), 267–276.

[218] SERENE, J., AND RAINER, D. The quasiclassical approach to superfluid 3He. *Phys. Rep. 101*, 4 (1983), 221–311.

[219] SHAPIRO, S. L., AND TEUKOLSKY, S. A. *Black Holes, White Dwarfs, and Neutron Stars: The Physics of Compact Objects*. Wiley, 1983.

[220] SHIN, Y.-I., SCHUNCK, C. H., SCHIROTZEK, A., AND KETTERLE, W. Phase diagram of a two-component Fermi gas with resonant interactions. *Nature 451* (2008), 689–693.

[221] SHOVKOVY, I., AND HUANG, M. Gapless two-flavor color superconductor. *Phys. Lett. B 564*, 3–4 (2003), 205–211.

[222] SHOVKOVY, I. A. Two lectures on color superconductivity. *Found. Phys. 35* (2005), 1309–1358, arXiv:nucl-th/0410091.

[223] SHOVKOVY, I. A., AND WIJEWARDHANA, L. C. R. On gap equations and color flavor locking in cold dense QCD with three massless flavors. *Phys. Lett. B 470* (1999), 189–199, arXiv:hep-ph/9910225.

[224] SHTERNIN, P. S., YAKOVLEV, D. G., HAENSEL, P., AND POTEKHIN, A. Y. Neutron star cooling after deep crustal heating in the X-ray transient KS 1731-260. *Mon. Not. R. Astron. Soc. 382* (2007), L43–L47.

[225] SOGO, T., LAZAUSKAS, R., RÖPKE, G., AND SCHUCK, P. Critical temperature for α-particle condensation within a momentum-projected mean-field approach. *Phys. Rev. C 79* (2009), 051301.

[226] SOMÀ, V., AND BOŻEK, P. Thermodynamic properties of nuclear matter with three-body forces. *Phys. Rev. C 80* (2009), 025803.

[227] SOMMER, A., KU, M., ROATI, G., AND ZWIERLEIN, M. W. Universal spin transport in a strongly interacting Fermi gas. *Nature 472* (2011), 201–204, arXiv:1101.0780.

[228] SONG, H.-Q., ZHENG, G.-D., AND SU, R.-K. Critical phenomena in nuclear matter with Gogny interaction. *J. Phys. G 16*, 12 (1990), 1861.

[229] SPIEGELHALDER, F. M., TRENKWALDER, A., NAIK, D., KERNER, G., WILLE, E., HENDL, G., SCHRECK, F., AND GRIMM, R. All-optical production of a degenerate mixture of ^{6}Li and ^{40}K and creation of heteronuclear molecules. *Phys. Rev. A 81* (2010), 043637.

[230] STEIN, H., PORTHUN, C., AND RÖPKE, G. Liquid-gas binodal anomaly for systems with pairing transition. *Eur. Phys. J. B 2* (1998), 393–398.

[231] STEIN, H., SCHNELL, A., ALM, T., AND RÖPKE, G. Correlations and pairing in nuclear matter within the Nozières-Schmitt-Rink approach. *Z. Physik A 351* (1995), 295–299.

[232] STEINWEDEL, H., JENSEN, J. H. D., AND JENSEN, P. Nuclear Dipole Vibrations. *Phys. Rev. 79*, 6 (1950), 1019.

[233] STRINGARI, S. Collective oscillations of a trapped superfluid Fermi gas near a Feshbach resonance. *Europhys. Lett. 65*, 6 (2004), 749.

[234] SU, R. K., YANG, S. D., AND KUO, T. T. S. Liquid-gas and superconducting phase transitions of nuclear matter calculated with real time Green's function methods and Skyrme interactions. *Phys. Rev. C 35* (1987), 1539–1550.

[235] SWOPE, W. C., ANDERSEN, H. C., BERENS, P. H., AND WILSON, K. R. A computer simulation method for the calculation of equilibrium constants for the formation of physical clusters of molecules: Application to small water clusters. *J. Chem. Phys. 76*, 1 (1982), 637–649.

[236] TATSUMI, T., YASUHIRA, M., AND VOSKRESENSKY, D. N. Hadron quark mixed phase in neutron stars. *Nucl. Phys. A 718* (2003), 359–362, arXiv:nucl-th/0209091.

[237] TAYLOR, E., AND GRIFFIN, A. Two-fluid hydrodynamic modes in a trapped superfluid gas. *Phys. Rev. A 72* (2005), 053630.

[238] THOULESS, D., AND VALATIN, J. Time-dependent Hartree-Fock equations and rotational states of nuclei. *Nucl. Phys. 31*, 0 (1962), 211–230.

[239] THOULESS, D. J. Perturbation theory in statistical mechanics and the theory of superconductivity. *Ann. Phys. (N.Y.) 10*, 4 (1960), 553–588.

[240] TIMMERMANS, E., FURUYA, K., MILONNI, P. W., AND KERMAN, A. K. Prospect of creating a composite Fermi-Bose superfluid. *Phys. Lett. A 285*, 3–4 (2001), 228–233.

[241] TOLSTOY, I. *Wave Propagation*. McGraw-Hill Inc., New York, 1973.

[242] TONINI, G., WERNER, F., AND CASTIN, Y. Formation of a vortex lattice in a rotating BCS Fermi gas. *Eur. Phys. J. D 39* (2006), 283–294.

[243] TOSCHI, F., CAPUZZI, P., SUCCI, S., VIGNOLO, P., AND TOSI, M. P. Transition to hydrodynamics in colliding fermion clouds. *J. Phys. B 37*, 7 (2004), S91.

[244] TOSCHI, F., VIGNOLO, P., SUCCI, S., AND TOSI, M. P. Dynamics of trapped two-component Fermi gas: Temperature dependence of the transition from collisionless to collisional regime. *Phys. Rev. A 67* (2003), 041605(R).

[245] TRUSCOTT, A. G., STRECKER, K. E., MCALEXANDER, W. I., PARTRIDGE, G. B., AND HULET, R. G. Observation of Fermi Pressure in a Gas of Trapped Atoms. *Science 291*, 5513 (2001), 2570–2572.

[246] TYPEL, S., RÖPKE, G., KLÄHN, T., BLASCHKE, D., AND WOLTER, H. H. Composition and thermodynamics of nuclear matter with light clusters. *Phys. Rev. C 81* (2010), 015803.

[247] URBAN, M. Two-fluid model for a rotating trapped Fermi gas in the BCS phase. *Phys. Rev. A 71*, 3 (2005), 033611.

[248] URBAN, M. Coupling of hydrodynamics and quasiparticle motion in collective modes of superfluid trapped Fermi gases. *Phys. Rev. A 75* (2007), 053607.

[249] URBAN, M. Radial quadrupole and scissors modes in trapped Fermi gases across the BCS phase transition. *Phys. Rev. A 78* (2008), 053619.

[250] URBAN, M. Coupling between collective motion and quasiparticle excitations in superfluid trapped Fermi gases. *Las. Phys. 19* (2009), 655–663.

[251] URBAN, M., AND SCHUCK, P. Slow rotation of a superfluid trapped Fermi gas. *Phys. Rev. A 67*, 3 (2003), 033611.

[252] URBAN, M., AND SCHUCK, P. Dynamics of a trapped Fermi gas in the BCS phase. *Phys. Rev. A 73* (2006), 013621.

[253] URBAN, M., AND SCHUCK, P. Erratum: Dynamics of a trapped Fermi gas in the BCS phase [Phys. Rev. A 73, 013621 (2006)]. *Phys. Rev. A 75* (2007), 049903.

[254] URBAN, M., AND SCHUCK, P. Pair breaking in rotating Fermi gases. *Phys. Rev. A 78*, 1 (2008), 011601.

[255] USOV, V. V. Bare quark matter surfaces of strange stars and e^+e^- emission. *Phys. Rev. Lett. 80* (1998), 230–233, arXiv:astro-ph/9712304.

[256] USOV, V. V. Electric fields at the quark surface of strange stars in the color-flavor locked phase. *Phys. Rev. D 70* (2004), 067301, arXiv:astro-ph/0408217.

[257] VALATIN, J. G. Generalized Hartree-Fock Method. *Phys. Rev. 122*, 4 (1961), 1012–1020.

[258] VARSHALOVICH, D. A., MOSKALEV, A. N., AND KHERSONSKII, V. K. *Quantum Theory of Angular Momentum*. World Scientific, Singapore, 1988.

[259] VENTURA, J., POLLS, A., NAS, X. V., HERNANDEZ, S., AND PI, M. Thermodynamic instabilities of nuclear matter at finite temperature with finite range effective interactions. *Nucl. Phys. A 545*, 1-2 (1992), 247–257.

[260] VERLET, L. Computer "Experiments" on Classical Fluids. I. Thermodynamical Properties of Lennard-Jones Molecules. *Phys. Rev. 159* (1967), 98–103.

[261] VICHI, L., AND STRINGARI, S. Collective oscillations of an interacting trapped Fermi gas. *Phys. Rev. A 60* (1999), 4734–4737.

[262] VOLLHARDT, D., AND WÖLFLE, P. *The Superfluid Phases of Helium 3*. Taylor and Francis, London, 1990.

[263] WATANABE, G., IIDA, K., AND SATO, K. Thermodynamic properties of nuclear "pasta" in neutron star crusts. *Nucl. Phys. A 676* (2000), 455–473, arXiv:astro-ph/0001273.

[264] WATANABE, G., SATO, K., YASUOKA, K., AND EBISUZAKI, T. Structure of cold nuclear matter at subnuclear densities by quantum molecular dynamics. *Phys. Rev. C 68*, 3 (2003), 035806.

[265] WEINBERG, S. Quasiparticles and the Born Series. *Phys. Rev. 131* (1963), 440–460.

[266] WITTEN, E. Cosmic Separation of Phases. *Phys. Rev. D 30* (1984), 272–285.

[267] WRIGHT, M. J., RIEDL, S., ALTMEYER, A., KOHSTALL, C., GUAJARDO, E. R. S., DENSCHLAG, J. H., AND GRIMM, R. Finite-Temperature Collective Dynamics of a Fermi Gas in the BEC-BCS Crossover. *Phys. Rev. Lett. 99*, 15 (2007), 150403.

[268] YAKOVLEV, D. G., GNEDIN, O. Y., KAMINKER, A. D., AND POTEKHIN, A. Y. Theory of cooling neutron stars versus observations. *AIP Conf. Proc. 983* (2008), 379–387.

[269] YAMAGUCHI, Y. Two-Nucleon Problem When the Potential Is Nonlocal but Separable. I. *Phys. Rev. 95* (1954), 1628–1634.

[270] YASUI, S., AND HOSAKA, A. Chiral symmetry breaking and stability of quark droplets in the chiral bag. *Phys. Rev. D 74* (2006), 054036, arXiv:hep-ph/0604206.

[271] ZAMBELLI, F., AND STRINGARI, S. Moment of inertia and quadrupole response function of a trapped superfluid. *Phys. Rev. A 63*, 3 (2001), 033602.

[272] ZHAI, H., AND HO, T.-L. Critical Rotational Frequency for Superfluid Fermionic Gases across a Feshbach Resonance. *Phys. Rev. Lett. 97*, 18 (2006), 180414.

[273] ZIMMERMANN, R., AND STOLZ, H. The Mass Action Law in Two-Component Fermi Systems Revisited: Excitons and Electron-Hole Pairs. *Phys. Status Solidi B 131*, 1 (1985), 151–164.

[274] ZWIERLEIN, M. Observation of Fermi polarons in a tunable Fermi liquid of ultracold atoms. Talk given at the conference BEC 2009, Sant Feliu de Guixols (Spain), Sept. 5-11, 2009, 2009.

[275] ZWIERLEIN, M. W., ABO-SHAEER, J. R., SCHIROTZEK, A., SCHUNCK, C. H., AND KETTERLE, W. Vortices and superfluidity in a strongly interacting Fermi gas. *Nature 435* (2005), 1047–1051.

[276] ZWIERLEIN, M. W., HADZIBABIC, Z., GUPTA, S., AND KETTERLE, W. Spectroscopic Insensitivity to Cold Collisions in a Two-State Mixture of Fermions. *Phys. Rev. Lett. 91*, 25 (2003), 250404.

[277] ZWIERLEIN, M. W., STAN, C. A., SCHUNCK, C. H., RAUPACH, S. M. F., GUPTA, S., HADZIBABIC, Z., AND KETTERLE, W. Observation of Bose-Einstein Condensation of Molecules. *Phys. Rev. Lett. 91*, 25 (2003), 250401.

[278] ZWIERLEIN, M. W., STAN, C. A., SCHUNCK, C. H., RAUPACH, S. M. F., KERMAN, A. J., AND KETTERLE, W. Condensation of Pairs of Fermionic Atoms near a Feshbach Resonance. *Phys. Rev. Lett. 92*, 12 (2004), 120403.